Analysis of turbulent transport in Hall-effect plasma thrusters

by

Enrique Bello Benítez

A dissertation submitted in partial fulfillment of the requirements for the degree of Doctor of Philosophy in

Aersopace Engineering

Universidad Carlos III de Madrid

Advisor:
Eduardo Ahedo Galilea

Tutor:
Eduardo Ahedo Galilea

A mis abuelos, Inés y Julián.
Siempre os llevaré conmigo.

Acknowledgements

En primer lugar, quiero dar las gracias a mi director de tesis, Eduardo, por su tiempo y por su paciencia. Gracias por proponerme un tema tan alineado con lo que yo buscaba para el doctorado y por confiar en mí. También quiero agradecer a Jesús Ramos que haya aceptado ayudarnos a desentrañar los misterios de las inestabilidades locales. Sin tu ayuda aún estaría bloqueado intentando comprender algunos aspectos de este campo tan complejo.

Thank you to Laurent Garrigues, for welcoming me in Toulouse and for his support during my research stay. Your guidance was extremely helpful and enlightening. I am really proud of the improvement in the performance of the code achieved during the stay and I really enjoyed the process. Thank you also to my fellow PhD students in LAPLACE. François, Quentin, Arpan, thank you for making my working days there more fun.

En estas líneas quiero dar las gracias a todas esas personas que durante estos años han hecho el doctorado algo más fácil de llevar. Gracias, Álvaro, por recibirme con los brazos abiertos en el despacho cuando yo sólo era un jovencito asustado. Gracias, Adrián, por tu infinita sabiduría tanto en códigos PIC como en la vida. Gracias, Jesús, porque siempre que hablo contigo me reconforta saber que recorremos caminos parecidos y nos comemos la cabeza con los mismos temas. Gracias, Alberto, por todo tu apoyo durante gran parte del doctorado. Siempre que he andado perdido has estado ahí para ayudar. No podría haber deseado un mejor compañero de desarrollo. Gracias, Scherezade, por haber estado ahí para escucharme muchas veces que necesitaba desahogarme y por ser siempre tan atenta. Contigo me resulta fácil abrirme y es algo que no me suele pasar. Además, jamás olvidaré aquella tarta sorpresa de cumpleaños xD. Thank you to every other fellow PhD student of EP2. You are an amazing group of researchers and I wish you the best.

Agradecerle también a mi psicóloga, Miren, que me haya acompañado durante parte de este proceso. Me he dado cuenta de que llevo toda la vida luchando conmigo mismo. Gracias a tu ayuda, por fin me veo como realmente soy y lo acepto.

Quiero dar las gracias a mis padres. Parte de mis éxitos es vuestra. Muchas

gracias por la ayuda y por los buenos momentos que pasamos juntos. Os quiero mucho. Gracias también a mi hermano, Guille, por ser un amigo. Las risas que nos echamos haciendo el payaso son lo mejor. Me siento orgulloso de ser tu hermano. Gracias a mi pareja, Eva, por ser la persona que siempre ha estado ahí durante estos años. Gracias por tu paciencia, sé que no soy una persona especialmente fácil de acompañar. Hemos pasado de todo estos años, incluyendo una pandemia, y siempre hemos sido un equipo.

Published and submitted content

- **E. Bello-Benítez** and E. Ahedo. Axial-azimuthal, high-frequency modes from global linear-stability model of a Hall thruster. *Plasma Sources Science and Technology*, 30, 035003 (2021). DOI: 10.1088/1361-6595/abde21

  E. Bello-Benítez developed the code, prepared the simulations, processed the results and wrote the paper. E. Ahedo contributed with comments and revisions. This article has been published in the peer-reviewed journal *Plasma Sources Science and Technology* and is wholly included in Chapter 3 of this Thesis. Whenever material from this source is included in this Thesis, it is singled out with typographic means and an explicit reference.

- **E. Bello-Benítez** and E. Ahedo. Stationary axial model of the Hall thruster plasma discharge: electron azimuthal inertia and far plume effects. *Plasma Sources Science and Technology*, 32, 115011 (2023). DOI; 10.1088/1361-6595/ad066f

  E. Bello-Benítez developed the code, prepared the simulations, processed the results and wrote the paper. E. Ahedo contributed with comments and revisions. This article has been published in the peer-reviewed journal *Plasma Sources Science and Technology* and is wholly included in Chapter 2 of this Thesis. Whenever material from this source is included in this Thesis, it is singled out with typographic means and an explicit reference.

- **E. Bello-Benítez**, A. Marín-Cebrián and E. Ahedo. Effect of injection conditions on the non-linear behavior of the ECDI and related turbulent transport. Submitted to a peer-reviewed journal.

  E. Bello-Benítez and A. Marín-Cebrián developed the particle-in-cell code used in the paper. E. Bello-Benítez prepared the simulations, processed the results and wrote the paper. The rest of the authors contributed with comments and revisions. This article has been submitted in the peer-reviewed journal *Plasma Sources Science and Technology* and is wholly included in Chapter 6 of this Thesis. Whenever material from this source is included in this Thesis, it is singled out with typographic means and an explicit reference.

Other research merits

Additional peer-reviewed articles:

- **E. Bello-Benítez**, G. Sánchez-Arriaga, T. Passot, D. Laveder, and E. Siminos, Structure and evolution of magnetohydrodynamic solitary waves with Hall and finite Larmor radius effects, *Physical Review E*, 99, 023202 (2019). DOI: 10.1103/physreve.99.023202.
- J. J. Ramos, **E. Bello-Benítez**, and E. Ahedo, Local analysis of electrostatic modes in a two-fluid E x B plasma, *Physics of Plasmas*, 28, 052115 (2021). DOI: 10.1063/5.0039341.
- D. Poli, **E. Bello-Benítez**, P. Fajardo, and E. Ahedo, Time-dependent axial fluid model of the hall thruster discharge and its plume, *Journal of Physics D: Applied Physics*, 56, 415203 (2023). DOI: 10.1088/1361-6463/ace2d0
- A. Marín-Cebrián, **E. Bello-Benítez**, A. Domínguez-Vázquez and E. Ahedo. Non-Maxwellian electron effects on the macroscopic response of a Hall thruster discharge from an axial-radial kinetic model. *Plasma Sources Science and Technology*, 33, 025008 (2024), DOI: 10.1088/1361-6595/ad227c

Conference proceedings:

- **E. Bello-Benítez** and Eduardo Ahedo. Axial-azimuthal high-frequency instability modes in a Hall thruster fluid model. In *36th International Electric Propulsion Conference*. IEPC-2019-687. Vienna, Austria, 2019.
- **E. Bello-Benítez** and E. Ahedo. Advances on low-dimensionality fluid modelling of Hall thruster discharges. In *Space Propulsion Conference 2021*. paper 133. Online, March 17-19, 2021.
- D. Poli, **E. Bello-Benítez**, P. Fajardo, and E. Ahedo. Non Stationary Fluid Modelling of Plasma Discharge in Hall Thrusters. In *Space Propulsion Conference 2022*. paper 116. Estoril, Portugal, May 9-13, 2022.

- **E. Bello-Benítez**, A. Marín-Cebrián, J. J. Ramos, and E. Ahedo. Two-dimensional kinetic simulation of electrostatic instabilities in a Hall plasma. In *37th International Electric Propulsion Conference*. IEPC-2022-314. Boston, MA, June 19-23, 2022.

- D. Poli, **E. Bello-Benítez**, L. Garrigues, P. Fajardo and E. Ahedo. Fluid vs kinetic simulation of the Penning discharge. In *35th International Conference on Plasmas and Ionized Gases*. Egmond aan Zee, The Netherlands, July 9-14, 2023.

Poster sessions, workshops and other conference contributions:

- **E. Bello-Benítez**, G. Sánchez Arriaga, T. Passot, D. Laveder and E. Siminos. Structure and evolution of magnetohydrodynamic solitary waves with Hall and finite Larmor radius effects. Poster presented in *Waves Côte d'Azur*. Nice, France, June 4-7, 2019.

- A. Marín-Cebrián, **E. Bello-Benítez**, A. Domínguez-Vázquez, F. Cichocki, P. Fajardo, and E. Ahedo. Advances in full particle-in-cell codes for 2D plasma discharge simulations". In *IEPC Summer 2021 Virtual Events*. Online, July 9-16, 2021.

- **E. Bello-Benítez** and E. Ahedo. Axial equilibrium model of the Hall discharge and its far plume with electron inertia and other effects. Poster presented in *ExB plasmas Workshop*. Madrid, Spain, February 16-18, 2022.

- S. Tsikata, B. Jorns, A. Smolyakov, L. Wang, Y. Mikellides, **E. Bello-Benítez**, and K. Hara. Session 1: High-frequency, small-scale oscillations and turbulence. In *ExB plasmas Workshop*. Madrid, Spain, February 16-18, 2022.

- L. Garrigues, G. Fubiani, J.P. Boeuf, A.T. Powis, W. Villafana, I. Kaganovich, Y. Raitses, F. Petronio, A. Alvarez-Laguna, A. Bourdon, P. Chabert, G. Vigot, G. Bogopolsky, B. Cuenot, O. Vermorel, D. Sydorenko, M. Zadeh, A. Smolyakov, F. Cichocki, P. Minelli, F. Taccogna, D. Eremin, L. Xu, A. Denig, K. Hara, P. Q. Elias, **E. Bello-Benítez**, A. Marín-Cebrián, E. Ahedo, M. Merino, P. Fajardo, Z. Donko, P. Hartmann, M. Turner, M. Reza, F. Faraji, A. Knoll, P. Parodi, and T. Magin. Benchmark of particle-in-cell simulations of a Penning-type discharge: Preliminary results. Poster presented in *35th International Conference on Plasmas and Ionized Gases*. Egmond aan Zee, The Netherlands, July 9-14, 2023.

Abstract

The problem of anomalous electron transport is one of the great open questions in the physics of Hall and other $\boldsymbol{E} \times \boldsymbol{B}$ plasma discharges. Understanding and characterizing this phenomenon is fundamental to further promote the development of electron transport laws for efficient and predictive numerical simulations. From a theoretical and simulation perspective, this Thesis contributes to the current knowledge on instabilities in Hall discharges and their relevance regarding the electron transport. This problem is restricted here to the axial-azimuthal plane of the discharge and is faced using two different electron formulations, kinetic and macroscopic, which usually lead to different families of instabilities.

Using a particular macroscopic electron model, this Thesis explores the existence of axial equilibrium solutions and analyzes their global stability. For solving the equilibrium problem, an extended version of the well-known 1D-axial-stationary model of Ahedo et al. is proposed. This new model considers several additional physical phenomena: electron azimuthal inertia, gyroviscosity, a finite cathode layer and the far-plume physics. Which allows us to discuss several subjects relevant to Hall discharges, such as the possible contribution of electron inertia to electron transport. A linear perturbation global model is used to study the stability of some of these equilibrium solutions; which, compared with the existing literature, fully considers the effects from electron inertia and pressure. The stability analysis is limited to mid-to-high frequencies (100 kHz-10 MHz). Within this range two different mode families are obtained with the potential of producing a cross-field electron transport. The dominant mode develops in the near plume with 1-5 MHz and seems to be attached to regions with negative magnetic gradient. A subdominant mode with 100-300 kHz shows close to the anode and is much more dependent on the parameters.

In order to study kinetic instabilities and their non-linear behaviour, one of the main contributions of this Thesis is the development of an electrostatic 2D particle-in-cell (PIC) model that is able to simulate oscillations in several $\boldsymbol{E} \times \boldsymbol{B}$ plasma discharges. This code has been developed together with Alberto Marín-Cebrián and is also a contribution of his Thesis, which focuses in plasma-wall interaction phenomena in Hall thrusters. The PIC program has been optimized during a

research stay at LAPLACE laboratory supervised by Dr. Laurent Garrigues and participates in an international benchmark of similar codes simulating a Penning discharge. Partial results of this benchmark are shown in this Thesis in two scenarios: collisionless and with ionization collisions.

When adopting a kinetic electron formulation and wave propagation perpendicular to the magnetic field, the electron-cyclotron drift instability (ECDI) is the fundamental theoretical result obtained in the literature using a linear local approach. The in-house 2D PIC code is used to study the trigger and non-linear behaviour of the ECDI. We first try to simulate conditions as close as possible to the hypothesis of the classical dispersion relation, using a fully periodic domain. However, this kind of configuration does not yield a long-term electron cross-field transport in our simulation. Then, axial boundary conditions are replaced with injection/absorbing boundaries, being a finite scenario more similar to the Hall discharge. In this case, several regimes are possible depending on the value of the ion residence time (controlled by the injection conditions) compared to the characteristic saturation time of the ECDI. When these two times are close to each other, the plasma holds sustained oscillations and electron transport, even for long simulation times.

Contents

List of Figures

Chapter 1

Introduction

Electric propulsion (EP) comprehends several technologies for in-space applications, which is an interesting alternative to the more traditional chemical propulsion (CP) thrusters. The EP concept was firstly proposed by Robert Goddard in 1906 and Konstantin Tsiolkovsky in 1911 [4–7]; but the consolidation of modern technologies, such as the gridded-ion thruster (GIT) and the Hall-effect thruster (HET), started in the 1970s in the USA and the USSR. Today, HET and GIT devices are well consolidated in the market of space propulsion and EP is an attractive choice for many applications (e.g., station keeping of telecommunication satellites in geostationary orbit). In the field of telecommunications, European companies such as Airbus, Thales or OHB, have been using EP for station keeping in the last years. These companies have been also supporting the development of all-electric propulsion platforms. Other future commercial application, is the access to global internet broadband services offered by the Starlink (SpaceX) and OneWeb (counting with the partnership of Airbus) satellite constellations, which rely also on EP. There are also examples of EP in scientific missions, e.g.: GOCE, DAWN or Bepi-Colombo.

The advantage of EP compared to CP is readily understood when looking at the Tsiolkovsky rocket equation

$$\frac{M_{\text{final}}}{M_{\text{initial}}} = \exp\left(-\frac{\Delta v}{I_{sp}}\right), \tag{1.1}$$

which relates the initial M_{initial} and final mass M_{final} of a spacecraft with the total impulse Δv of the mission and the specific impulse I_{sp} of the thrusters (in velocity units). Maximizing the I_{sp} minimizes the propellant requirements. The I_{sp} is a measure of the exhaust velocity of the gases in the thruster; which, in CP thrusters, is limited by the energy released by the exothermal reaction of the propellant gases, leading to values in the range from 1 to 5 km/s. On the other hand, EP devices overcome this limitation using a external power source to accelerate a plasma (i.e., an ionized gas made of ions, electrons and neutral particles) using electric and magnetic

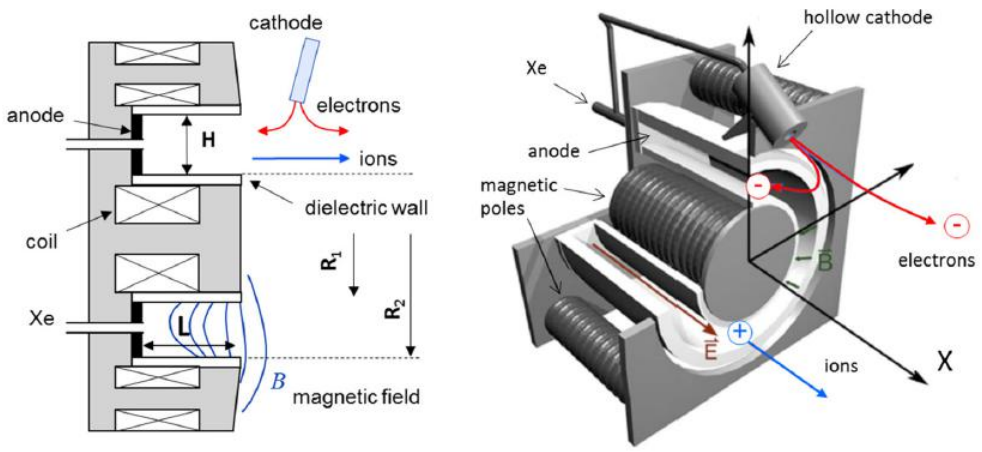

Figure 1.1: Schematic representation of a HET, taken from reference [1].

fields generated with external devices. This allows to achieve much larger I_{sp}, in the range from 10 to 100 km/s depending on the technology. If less propellant is needed, the initial weight of the spacecraft can be reduced (minimizing also the launching cost) or more ambitious Δv can be considered. However, EP devices are limited by the available power P, which limits the thrust $F = 2\eta_F P/I_{sp}$ (being η_F the thrust efficiency) to values generally smaller than with CP; making EP not eligible for every application and suitable for in-space applications only.

As already mentioned, among the EP mature technologies we find the GIT and HET devices. The GIT generates plasma inside a chamber and accelerates the ions out of the thruster using grids at different electric potential. This device shows typically [7] the greatest efficiency (40 to 80%) and specific impulse (25 to 36 km/s), but the provided F is limited. The HET technology delivers higher thrust, at the cost of lower η_F (35 to 60%) and I_{sp} (15 to 20 km/s). Moreover, HET devices are simpler from the technological point of view compared to GITs, although the plasma physics involved are very challenging.

Figure 1.1 shows a schematic representation of a conventional HET. Conventional HETs have a cylindrical shape with an annular channel. Many models exploit the axial symmetry of the HET geometry. A neutral gas (usually xenon) is injected through the anode and ionized by collision with electrons. These electrons are injected out of the chamber (in the plume) through the cathode; some of them are accelerated inwards, highly contributing to ionization, while others move outwards. The ions generated from ionization are accelerated out of the channel. The motion of electrons and ions is driven by a mainly-axial electric field $\boldsymbol{E}$, induced in the plasma by the electrical connection of the anode and the cathode with a voltage source providing the discharge voltage V_d. The counter-streaming axial flows of charged particles generate a net current I_d (i.e., the discharge current) in the plasma, which is also the current in the electrical circuit. Part of the cathode electrons naturally flow

downstream together with the ions to neutralize them, yielding a current-free plume. This process is possible because electrons are axially confined with a mainly-radial external magnetic field $\boldsymbol{B}$, which traps the electrons and increases their residence time, otherwise too small to provide significant ionization. The magnetic field is strong enough to magnetize the electron particles but ions barely feel its effect. Electrons, feeling both $\boldsymbol{E}$ and $\boldsymbol{B}$, develop a motion in the azimuthal $\boldsymbol{E}\times\boldsymbol{B}$ direction. It is the interaction between the currents of the thruster magnetic circuit and electron $\boldsymbol{E}\times\boldsymbol{B}$ motion what generates the thrust.

The electron motion can be decomposed, in a very simplistic view and accepting that $\boldsymbol{E}$ is axial and $\boldsymbol{B}$ is radial, in different contributions:

- The electrons are able to move almost free in the radial direction, parallel to $\boldsymbol{B}$, since there is no magnetic confinement in this direction.
- The gyromotion around the magnetic field lines, in the axial-azimuthal plane, perpendicular to $\boldsymbol{B}$. This is the characteristic motion of charged particles describing circular orbits under the action of a magnetic field.
- The azimuthal drift in the $\boldsymbol{E}\times\boldsymbol{B}$ direction. The combined action of $\boldsymbol{E}$ and $\boldsymbol{B}$ leads to the drift of the centre of the gyro-orbits. The only action of the fields $\boldsymbol{E}$ and $\boldsymbol{B}$ does not yield an axial drift, effectively confining the electrons.
- There is an axial drift of the electrons, in the direction opposite to $\boldsymbol{E}$. The classical explanation for the axial transport is based on collisions, i.e., when the electrons collide they are able to jump among magnetic lines, breaking the confinement. However, the experimentally measured electron transport is too large compared with what predicted by collisional diffusion only [8]. This phenomena is called the *anomalous electron transport* and is one of the great open questions in the physics of HETs.

This Thesis is intended to contribute to the understanding of anomalous transport in Hall and other $\boldsymbol{E}\times\boldsymbol{B}$ plasmas, from a simulation and theory point of view. Plasma oscillations and instabilities are one of the main candidates to explain it. As introduced by Janes and Lowder in 1966 [8], the development of correlated oscillations of plasma density and electric field in the $\boldsymbol{E}\times\boldsymbol{B}$ direction is a mechanism that could induce an axial electron drift. The number of different instabilities that have been proposed in the literature of Hall plasmas is quite extensive [8–15], being a large relative drift between electron and ions the base destabilizing requirement. Collisions or plasma inhomogeneities can also participate in the instability mechanisms. A detailed literature review on instabilities in Hall plasmas can be found in Chapters 3 and 6 of this Thesis and in reference [10], which I co-author (but is not included in the Thesis but closely related).

The simulation and theoretical study of plasmas can be faced using different types of models [16]. The plasma species can be treated statistically with a kinetic formulation, meaning that their behaviour is described with the distribution function of particles in the 6D phase space of position and velocity. The moments of the distribution function give macroscopic magnitudes commonly used in fluid dynamics; e.g., density, flows or pressure. This function is governed by the Boltzmann equation, which can be solved directly as a transport equation in phase space [17–19]. This approach is quite costly due to the high dimensionality of the problem and the modelling of collisions is challenging. The particle-in-cell (PIC) technique [20–24] is a Lagrangian-Eulerian alternative that discretizes the distribution function in macroparticles representing certain region of the phase space and their motions are solved instead, which actually coincide with the characteristic lines of the Boltzmann equation. The large number of macroparticles needed to have statistics with reasonable noise and the disparity among the smallest and biggest scales of the problem make this method still very computationally intensive.

The computationally-cheaper alternative to the kinetic description is the macroscopic or fluid formulation [16, 25–29]; which works directly on the evolution of macroscopic properties, governed by fluid equations obtained by taking the moments of the Boltzmann equation. This formulation, however, involves the problem of closure [16,30,31]: each moment of the Boltzmann equation has unknown magnitudes governed by higher-order moments. Therefore, in order to close the system, important assumptions need to be made. The usual closures are valid for species with Maxwellian-like distributions, which is not necessarily the case of low-collisional scenarios such as the Hall discharge. In addition, the macroscopic models sacrifice some kinetic effects that are relevant in the study of plasma instabilities, e.g., inverse Landau damping [32, 33] or Bernstein modes [34]. Consequently, fluid and kinetic models may predict different types of instabilities.

1.1 Thesis objectives

This Thesis is expected to contribute to the further understanding of the main instability mechanisms present in Hall (and other $\boldsymbol{E} \times \boldsymbol{B}$) discharges and their role in the anomalous electron transport, from a theoretical and simulation point of view. This knowledge is expected to guide future efforts in the development of anomalous transport laws for fast and efficient simulations with fluid electron models (e.g., with EP2's HYPHEN tool [35]). In this Thesis the problems of plasma instabilities and transport are tackled from different perspectives, including fluid and kinetic description of the electrons, which lead to different instability mechanisms.

With a macroscopic electron model, this Thesis covers the existence of

equilibrium solutions of a Hall-discharge plasma model and discusses their global stability. In the equilibrium side, the 1D-axial stationary model developed for this Thesis [28] extends previous works by Ahedo and co-workers [27, 36, 37] with a number of additional physical effects. The stability of an equilibrium solution is studied with a global linear perturbation model [38], which extends previous efforts by Escobar and Ahedo [39, 40] to fully account for electron inertia and pressure terms.

With a kinetic electron description, one of the main objectives of this Thesis has been the development, optimization and verification of a 2D particle-in-cell (PIC) code for the simulation of plasma oscillations in Hall and other $\boldsymbol{E} \times \boldsymbol{B}$ discharges. The successful development has been achieved in close collaboration with Alberto Marín-Cebrián, who is applying this code to study plasma-wall interaction phenomena in Hall thrusters as topic of his PhD Thesis. The code has been subjected to a thorough optimization process, with the valuable guidance of Dr. Laurent Garrigues during a research stay at LAPLACE laboratory and is participating in an international benchmark to compare results from Penning-discharge simulations with other groups [41].

The classical dispersion relation for propagation perpendicular to the magnetic field yields the electron-cyclotron drift instability (ECDI) [11, 12]. However, the linear theory does not capture the saturated non-linear behaviour of the plasma, which can be indeed studied with the in-house PIC code. This is used to simulate fundamental scenarios close to the hypotheses of the classical ECDI, in an attempt to characterize the non-linear behaviour of the theoretical instability and the influence of boundary conditions [24].

1.2 Thesis outline

The Thesis is organised as follows:

- Chapter 2 reproduces the peer-reviewed article [28] published in *Plasma Sources Science and Technology*. The chapter introduces the 1D-axial three-fluid equilibrium model of a Hall discharge. New effects are added to the well-known model of Ahedo and co-authors [27, 36, 37]: electron azimuthal inertia, a finite cathode-emission layer and the far-plume region. This has also allowed us to assess several aspects of interest for Hall-thruster modelling, e.g.: the role of electron inertia on cross-field transport, the relevance of gyroviscous forces and the far-plume physics.
- Chapter 3 reproduces the peer-reviewed article [38] published in *Plasma*

Sources Science and Technology. The chapter presents a 2D axial-azimuthal linear perturbation model of a Hall discharge, which is used to study the stability of equilibrium solutions using a global approach, suited to highly inhomogeneous equilibria. The model, targetting mid-to-high frequencies, keeps fully the electron pressure and inertia terms, which is the main novelty with respect to previous works [40, 42]. The dominant unstable modes develop in the near-plume region, where the magnetic-field gradient is negative, and have frequencies in the range 1-5 MHz. A subdominant mode, with lower frequencies in the range 100-300 kHz, grows close to the anode and is much more sensitive to design and operation parameters. Both of these modes have the potential to yield a cross-field electron transport.

- Chapter 4 describes the developed in-house 2D PIC code, which is a central contribution of this and A. Marín-Cebrián's Theses. The main program includes the PIC routines, a Poisson solver and a collision module. The main PIC routines are conventional and well-known but are explained for completeness. The Poisson solver may use two different schemes depending on the boundary conditions: spectral and finite-difference discretization. The collisions are treated with a Monte-Carlo collision (MCC) method.

- Chapter 5 describes the process of optimization of the PIC program, achieved during a research at stay in LAPLACE under the supervision of Dr. Laurent Garrigues. The optimization techniques applied involve: particle sorting, changing the linear solver for the Poisson module, new parallelization, the use of the Intel®Fortran compiler and exploring OpenMP parallel affinity options. Each of these aspects is analysed by comparing computational times in a simple simulation scenario. The final part of the Chapter presents results of a collisionless Penning-discharge benchmark case organized by L. Garrigues (LAPLACE) and A. T. Powis (Princeton Plasma Physics Laboratory) among many groups at international level [41]. Here, the comparison is limited to EP2 and LAPLACE results. Preliminary results for a Penning-discharge with ionization collisions are also presented.

- Chapter 6 reproduces the contents of a manuscript, currently under peer-reviewing. Preliminary results were shown in the conference paper [24]. In this chapter, we show results obtained with the 2D PIC code in scenarios close to the theoretical conditions of the ECDI. After revisiting the ECDI linear theory, the first part of the Chapter is devoted to the simulation of the non-linear evolution of the classical ECDI in a fully periodic domain. This type of configuration does not induce a long-term transport of the electrons in our simulations. The second part of the Chapter, replaces periodic axial conditions by injection/absorbing boundaries. If the ion residence time (controlled by injection conditions) is chosen to be close the ECDI characteristic saturation

time, sustained oscillations are observed that yield a significant electron transport. Other aspects discussed here are the energy conservation and the scaling with domain length and ion mass.

- Chapter 7 gathers the main conclusions of the Thesis and suggests guidelines for future steps.

Chapter 2

Fluid modelling of Hall-thruster discharges: Equilibrium

This Chapter reproduces the contents published in the peer-reviewed journal Plasma Sources Science and Technology [28]. The typography has been adapted to the style of this Thesis.

Abstract

One-dimensional axial models of the plasma discharge of a Hall thruster provide a valuable picture of its physical behaviour with a small computational effort. Therefore, they are very suitable for quick parametric analyses or as a support tool for analyzing the impact of modelling decisions. This paper extends a well-known drift-diffusion stationary, quasineutral model by adding electron azimuthal inertia (EAI), a non-zero thickness cathode layer, and the far-plume region where electrons demagnetize and cool down. The EAI dominates on the far plume and affects positively to thrust. For a small ion backstreaming current, EAI modifies much the electron velocities and density near the anode, but has no discernible effect on the electron cross-field transport. Electron axial inertia and azimuthal gyroviscosity are estimated. The thick cathode layer connects quasineutrally the near and far plumes but the coupling between these two regions is weak. The far plume region is sensitive to the decay length of the magnetic field, the downstream boundary conditions on the electron currents, and the stray electric currents.

2.1 Introduction

In a set of consecutive papers, Ahedo and co-workers [27,36,37] presented a complete stationary, axial fluid model of the Hall-effect thruster (HET) discharge between the anode and an external surface simulating the cathode electron emission. The model considered three fluids, plasma quasineutrality (except for a Debye sheath at the anode), the electron energy equation (including heat conduction), and an empirical model for wave-based anomalous electron transport. Auxiliary radial models [43–45], distinguishing primary and secondary electrons from the wall were developed to characterize, in the axial model, the source terms simulating the plasma losses to the lateral dielectric walls. The analyses with that axial model were able (i) to describe at very low computational cost, the interplay among main physical phenomena, the sonic transitions of the ion flow, the three regions of the discharge (ion-backstreaming, ionization, and acceleration), and (ii) to provide good estimates of thruster performances and the different sources of thrust inefficiency.

A stationary model is a very suitable tool for carrying out extensive studies on (i) the influence of design and operation parameters on Hall thruster performances [46], (ii) more complex HET configurations [47] and (iii) linear stability studies both local [10,42,48–51] and global [38,39] unveiling the longitudinal and azimuthal fluid self-modes developing in a HET discharge.

1D stationary solutions can be obtained also from time-dependent fluid models. Barral et al. [52] developed a model similar to reference [27] with time-dependent terms. They obtained both fully-stationary solutions and others bearing saturated breathing and ion-transit modes [53–56]. It is worth to note that (i) the time-averaged features of these last ones are similar to the fully-stationary solutions and (ii) numerical integration schemes are different for stationary and time-dependent formulations. With small variations, the model of Barral et al. continues to be amply used for longitudinal oscillations studies, such as recent references [57–60].

Both references [27, 36, 37] and [52] focused their studies on the so-called drift-diffusion approximation (DDA) [61,62], which neglects totally electron inertia (i.e. it corresponds to the limit of massless electrons). Nonetheless, reference [37] already pointed out that electron azimuthal inertia (EAI) could be relevant (in both the momentum and energy equations) and reference [52] noted that EAI could dominate in the near-anode region. Ahedo and Rus [63] extended the quasineutral DDA model by including EAI in the near-anode region and found that, at a low ion-reverse current (i.e. a few percentage of the discharge current I_d), the azimuthal velocity, u_{ye}, is upper bounded to values of the order of the electron thermal velocity. Although the axial velocity, $|u_{ze}|$, also grows, EAI makes the ratio $|u_{ye}/u_{ze}|$ to be in that region much less than the Hall parameter χ (defined as the ratio between electron cyclotron

and collisional frequencies). Their results agreed with experimental observations by Dorf et al. [64].

The above models include the electron azimuthal inertia but neglect the electron axial inertia, based on their axial velocity being much smaller than the azimuthal one. Ahedo and Escobar [65] analyzed in detail the near anode region and found that axial electron inertia becomes relevant only when the ion-reverse current becomes very small and the anode sheath transits from normal (electron-confining) to inverse (ion-confining). For xenon, this would happen for an inverse ion current at the anode equal to about 0.5% of the discharge current I_d. They also showed that in that parametric range, the bulk discharge is still quasineutral but the Bohm condition defining the anode sheath edge involves both the ion and electron axial flows. This is a consequence of a change on the mathematical structure of the problem and its singular points when including electron axial inertia.

Azimuthal electron inertia can be relevant also around the channel exit where the axial ambipolar electric field, E_z, is maximum. Haas and Gallimore [66] measured around the channel exit plane of a 5kW laboratory HET, an electron drift energy of the same order of their thermal energy. 2D simulations of a conventional HET by Domínguez-Vázquez et al. [67] have found the same result around the electron-emitting cathode for certain operation conditions. With a complementary perspective, Cappelli et al. [68, 69] speculated that a strong azimuthal shear (i.e. $\mathrm{d}u_{ye}/\mathrm{d}z$) would lead to a local suppression of the electron anomalous cross-field transport around the channel exit. They and later works [69, 70] included the shear-based effect in the empirical anomalous transport expression of a DDA model.

In a recent work, Sahu et al. [71] develop a time-dependent, non-neutral, 'full-fluid-moment' model (i.e. including both axial and azimuthal electron inertia). They analyze a stationary test case and confirm (i) the effect of inertia on limiting u_{ye} near the anode and the channel exit, and (ii) the fulfilment of the quasineutral and drift diffusion approximations away from those regions. They find the discharge current I_d (constituted mainly by the electron axial current at the anode) to be 0.5% higher with the full-fluid model than with the DDA, thus claiming that the shear component of the electron momentum contributes to the electron transport across the magnetic field lines.

This paper extends the stationary, quasineutral model with EAI of Ahedo and co-workers to the far plume by connecting the near and far plumes with an electron-emitting layer. This is a more realistic approach to electron emission by a real cathode than a surface or boundary cathode, unanimous in 1D models cited so far. In fact, in our model the surface cathode is obtained as a limit case. Other important subjects treated in the paper are: the role of EAI on cross-field transport suggested by Sahu et al. [71], the connection of the coupling plume region with the rest of

the discharge, and the possible relevance of electron azimuthal gyroviscosity in the solution.

The analysis of the far plume will highlight the central role of EAI there, linked to electron demagnetization. The discussion of far plume boundary conditions is relevant, since they substitute the boundary-cathode conditions of previous models and affect both the far and near plumes. This subject is also of interest to 2D numerical models using fluid electrons [67, 72] where computational affordability limits the extension of the simulated plume and thus the analysis of electron demagnetization and cooling.

Electron axial momentum is not included in the stationary model we propose, due again to the mathematical complexity it introduces and the limited applicability: in practice a good plasma attachment to the anode requires a normal anode sheath [73].

The fluid theory of collisionless (or weakly collisional) magnetized plasma species (here applying to electrons) demonstrates that, in the small Larmor radius (SLR) expansion, electron inertia and the electron (non diagonal) gyroviscous tensor are formally of the same order [31, 74–76]. As far as we know, in fluid models of HET discharges, gyroviscosity has been considered and found relevant only in local linear stability studies [10,51]. Here, we will assess from the results of our non-linear model the possible importance of the azimuthal electron gyroviscous force.

The paper is organized as follows. Section 2.2 presents the extended axial stationary model. Section 2.3 analyzes the solution for a reference case. Section 2.4 discusses the EAI effects, their role in cross-field transport, and evaluates the gyroviscous force. Section 2.5 deals with far-plume aspects. Section 2.6 gathers the main conclusions.

2.2 Formulation of the axial stationary model

Let us assume axial symmetry and study the axial evolution of radially-averaged plasma variables, with the divergence operator (acting on an arbitrary flux vector $\boldsymbol{v}$) expressed as

$$\nabla \cdot \boldsymbol{v} = \frac{1}{A}\frac{\mathrm{d}}{\mathrm{d}z}(Av_z) + v'_w \tag{2.1}$$

where z stands for the axial coordinate, $A(z)$ for the cross-sectional area of the plasma beam, and v'_w accounts for lateral wall fluxes, expressed as source terms in this paraxial model. As shown in figure 2.1, the quasineutral simulation domain includes the complete plasma region in-between the anode Debye sheath edge (B) and an arbitrarily far downstream boundary (∞). The point A stands (with $z_A = 0$) for the real anode wall, which (we assume) has attached an infinitely thin electron-

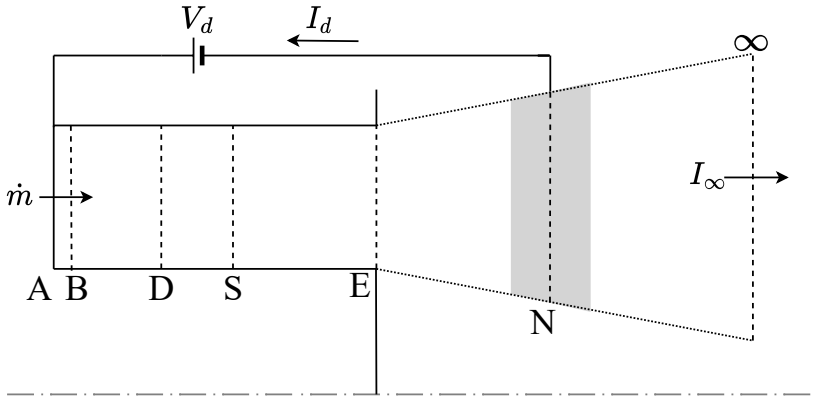

Figure 2.1: Schematic of the axial model of an annular HET. $\dot{m}$ is the (anodic) mass flow, V_d is the discharge voltage, I_d the discharge current, and I_∞ is the far-field total current. A is the anode wall, B is the anode sheath edge, D is the ion stagnation point, S is the ion sonic point, E is the chamber exit, N is the centre of the neutralizer layer, and ∞ is the far-field downstream boundary. $A(z)$ is the effective cross-section area of the plasma beam.

repelling sheath from A to B (i.e. $z_B \simeq 0$ in the quasineutral scale) accounted for through an auxiliary sheath model that gives plasma conditions at B. The thruster exit is located at point E ($z = L_\mathrm{E}$) and the electron emitting sheet (which we will name 'cathode') is centred at point N ($z = L_N$). The distance from N to the boundary ∞ of the simulated plume is $L_{\mathrm{N}\infty}$. Notice that a 1D model (either with a boundary or a volumetric cathode) cannot reproduce the 2D coupling between the cathode's electron emission and the ion beam; thus, the associated voltage coupling is neglected here.

Under these assumptions and following a standard notation, the set of quasineutral ($n_i = n_e$) macroscopic equations for the three species to be considered is

$$\frac{1}{A}\frac{\mathrm{d}}{\mathrm{d}z}\left(An_n u_{zn}\right) = -n_e(\nu_p - \nu_w), \tag{2.2}$$

$$\frac{1}{A}\frac{\mathrm{d}}{\mathrm{d}z}\left(An_e u_{zi}\right) = n_e(\nu_p - \nu_w), \tag{2.3}$$

$$\frac{1}{A}\frac{\mathrm{d}}{\mathrm{d}z}\left(An_e u_{ze}\right) = n_e(\nu_p - \nu_w) + S_c, \tag{2.4}$$

$$n_n u_{zn}\frac{\mathrm{d}u_{zn}}{\mathrm{d}z} = -n_e\nu_w(u_{zn} - u_{znw}) \tag{2.5}$$

$$m_i u_{zi}\frac{\mathrm{d}u_{zi}}{\mathrm{d}z} = -e\frac{\mathrm{d}\phi}{\mathrm{d}z} + m_i\nu_p\left(u_{zn} - u_{zi}\right), \tag{2.6}$$

$$0 = e\frac{\mathrm{d}\phi}{\mathrm{d}z} - \frac{1}{n_e}\frac{\mathrm{d}p_e}{\mathrm{d}z} + m_e\left(\omega_{ce}u_{ye} - \nu_e u_{ze}\right), \tag{2.7}$$

$$u_{ze}\frac{\mathrm{d}u_{ye}}{\mathrm{d}z} = -\omega_{ce}u_{ze} - \nu_e u_{ye}, \tag{2.8}$$

$$\frac{\mathrm{d}P_{ze}}{\mathrm{d}z} = -I_e\frac{\mathrm{d}\phi}{\mathrm{d}z} + A\left(S_c\mathcal{E}_c - n_e\nu_p\mathcal{E}_{\mathrm{inel}} - n_e\nu_w\mathcal{E}_w\right). \tag{2.9}$$

The continuity equations (2.2) to (2.4) include the production (or ionization) frequency ν_p, the wall-recombination effective frequency ν_w and the cathode source S_c of electrons around N. Two combinations of them yield, first, the conservation of the anodic mass flow

$$\dot{m} = Am_i(n_n u_{zn} + n_e u_{zi}) = \mathrm{const} \tag{2.10}$$

and, second, the evolution of the axial electric current $I = I_i + I_e \equiv eAn_e(u_{zi} - u_{ze})$ as

$$\mathrm{d}I/\mathrm{d}z = -eAS_c. \tag{2.11}$$

Equations (2.5) to (2.7) are obtained from the species axial momentum equations: ion and neutral pressure are neglected; ion magnetization is neglected; u_{znw} is the effective axial velocity of wall-born neutrals, ϕ is the electrostatic potential, $\omega_{ce}(z) = eB/m_e$ is the electron gyrofrequency, and ν_e is the total electron collision frequency. This one reads

$$\nu_e = \nu_{en} + \nu_{ei} + \nu_{wm} + S_c/n_e + \nu_t, \tag{2.12}$$

where the contributions on the right side, from left to right, are due to electron-neutral collisions, electron-ion Coulomb collisions (both with negligible effect on heavy species), lateral-wall collisionality, cathode injection, and wave-based turbulence.

Equation (2.8) derives from the electron azimuthal momentum equation, and includes on the left side the non-linear electron azimuthal inertia term. When neglecting the inertia term we get

$$-u_{ye}/u_{ze} = \chi \equiv \omega_{ce}/\nu_e, \tag{2.13}$$

with χ the Hall parameter. If ℓ_z is the typical axial gradient length, azimuthal inertia effects matter in the unmagnetized far plume and in regions with $u_{ze}/\ell_z \geq O(\nu_e)$.

The electron energy equation (2.9) has, on the right side, the work of the axial electric field, the inelastic and wall losses, and the energy injected at the cathode. Here $\mathcal{E}_c$, $\mathcal{E}_{\mathrm{inel}}$ and $\mathcal{E}_w$ stand for the characteristic energy per particle involved in cathode injection, inelastic and wall losses, respectively. The left side is the variation of the axial flow of total electron energy,

$$P_{ze} = \Big(\frac{1}{2}m_e u_{ye}^2 n_e u_{ze} + \frac{5}{2}T_e n_e u_{ze} + q_{ze}\Big)A, \tag{2.14}$$

sum of the axial flows of kinetic energy (with $u_e^2 \simeq u_{ye}^2$), thermal energy, and conduction heat. After manipulating the Fourier's law $\boldsymbol{q}_e = -\bar{\bar{\kappa}}_e \cdot \nabla T_e$ for the

heat flux vector, with $\bar{\bar{\kappa}}_e$ the thermal conductivity tensor of magnetized electrons, the axial heat flux satisfies [16, 37]

$$q_{ze} = -\kappa_{\perp e}\frac{\mathrm{d}T_e}{\mathrm{d}z}, \qquad \kappa_{\perp e} = \frac{5n_eT_e}{2m_e\nu_e}\frac{1}{1+\chi^2}. \tag{2.15}$$

The cathode electron source term S_c in equations (2.4) and (2.9) is assumed Gaussian,

$$S_c(z) = \frac{I_d - I_\infty}{eA(z)\sqrt{\pi}\ell_c}\exp\left[-\frac{(z-z_\mathrm{N})^2}{\ell_c^2}\right], \tag{2.16}$$

with $2\ell_c$ the effective emission thickness of the cathode, $I_d = I(0)$ the discharge current between anode and cathode, and $I_\infty = I(\infty)$ the electric current in the far plume. This last one is typically zero, except if the plume interaction with spacecraft surfaces drives some stray current into the anode-cathode circuit [77]. Applying equation (2.16) into (2.11) and integrating yields

$$I(z) = I_\infty + \frac{I_d - I_\infty}{2}\,\mathrm{erfc}\left(\frac{z-z_N}{\ell_c}\right). \tag{2.17}$$

If I_{iN} is the ion current crossing the cathode layer, the electron currents flowing downstream and upstream the cathode layer are $I_{iN} - I_\infty$ and $I_d - I_{iN}$ respectively. Except in section 2.5, the plume is assumed current-free, i.e. $I_\infty = 0$. Since the quasineutral model applies to the zero-Debye-length asymptotic limit, the solution is expected to be quasineutral across a cathode layer of non-zero length.

Axial inertia effects were neglected in equation (2.7) based on assuming $u_{ze}^2 \ll c_e^2$. This condition, amply fulfilled by the solutions presented later, allows to preserve the mathematical structure of the quasineutral DDA model, where it can be said that equation (2.7) solves for ϕ, the sum of equations (2.6) and (2.7) plus equation (2.3) solve for n_e and u_{zi}, and equation (2.11) solves for u_{ze},

$$u_{ze} = u_{zi} - I/Aen_e. \tag{2.18}$$

In contrast, the mathematical structure of the time-dependent, non-neutral, full-fluid model of reference [71] differs substantially from this one.

The magnetic field enters in this model exclusively in the electron momentum equations through $\omega_{ce}(z)$. A piece-wise Gaussian shape is assumed for the radial magnetic field,

$$B(z) = B_m\exp\left[-\frac{(z-z_m)^2}{\ell_m^2}\right], \tag{2.19}$$

with B_m the maximum magnetic field, z_m the location of that maximum, and ℓ_m the characteristic length of magnetic decay; different values of ℓ_m will be taken at the internal (ℓ_{m1}) and external (ℓ_{m2}) sides of z_m. It can be said that ℓ_{m1} and ℓ_{m2} are determined by the magnetic circuit of the HET, while the strength B_m can be

Table 2.1: Simulation parameters, based on a SPT-100-type thruster, for the reference cases I.

$\dot{m}$	4.75 mg s^{-1}	u_{znA}	300 m s^{-1}
V_d	300 V	I_∞	0
$T_{e\infty}$	1 eV	$\mathcal{E}_c$	7.5 eV
$A(0)$	40 cm^2	R	4.25 cm
B_m	265 G	z_m	2.5 cm
ℓ_{m1}	1.5 cm	ℓ_{m2}	1.0 cm
$2\ell_c$	1 cm	$L_{\mathrm{N}\infty}$	10 cm
L_{E}	2.5 cm	L_{N}	3.35 cm

tuned for each operation point so that $|I_{iA}|/I_d$ is relatively small and the discharge is both stable and efficient [46].

The (time-averaged) turbulent transport is modelled as the collisional contribution [36, 78] $\nu_t = \alpha_t \omega_{ce}$, where α_t is a phenomenological parameter, which is taken constant in the simulations here. Expressions for

$$\nu_p,\ \nu_w,\ \nu_{en},\ \nu_{ei},\ \nu_{wm},\ u_{znw},\ \mathcal{E}_{\mathrm{inel}},\ \mathcal{E}_{\mathrm{w}},$$

are given in Appendix 2.A.

The accumulated thrust at a cross-section $z = \text{const}$ is defined as the axial flow of axial momentum of the whole plasma,

$$F(z) \equiv \left(m_i n_e u_{zi}^2 + m_i n_n u_{zn}^2 + p_e\right) A, \tag{2.20}$$

and the total thrust is $F(\infty)$. Applying the previous equations for continuity and momentum, the accumulated thrust satisfies

$$F(z) = F_{pB} - F_w(z) + F_m(z) + F_d(z), \tag{2.21}$$

with $F_{pB} = F(z_B)$ the pressure force at B, $F_w(z) = \int_{z_B}^{z} n_e m_i \nu_w (u_{zi} - u_{znw}) A \, \mathrm{d}z$ the drag in the lateral walls, $F_d(z) = \int_{z_B}^{z} p_e (dA/dz) \, \mathrm{d}z$ the beam expansion contribution, and $F_m(z) = \int_{z_B}^{z} e n_e B u_{ye} A \, \mathrm{d}z$ the magnetic force, which is the main contribution and imprints the electromagnetic character to thrust in HETs.

This section is concluded discussing the boundary conditions. While references [27, 36, 37] used an infinitely thin cathode boundary, with the anode-cathode region decoupled from the far plume solution, all regions of the plasma are mathematically coupled with a thick cathode layer. Boundary conditions used in those works are adapted accordingly to the present model. Equations (2.3), (2.6), (2.7) and (2.15) can be combined to obtain an explicit expression for $\mathrm{d}u_{zi}/\mathrm{d}z$ free of derivatives of other plasma variables, which reads

$$m_i \left(c_s^2 - u_{zi}^2\right) \frac{\mathrm{d}u_{zi}}{\mathrm{d}z} = G, \tag{2.22}$$

Case	V_d [V]	B_m [G]	α_t	$n_{e\mathrm{B}}$ [10^{17} m^{-3}]	$\lvert u_{ze\mathrm{B}}\rvert$ [km/s]	$u_{ye\mathrm{B}}$ [km/s]	$I_{i\infty}$ [A]	$I'_{e\mathrm{N}}$ [A]	$I_{i\mathrm{A}}/I_d$ [%]	$e\phi_{\mathrm{AB}}/T_{e\mathrm{B}}$	η_{cur} [%]	η_F [%]
Ia	300	265	0.01	1.604	51.33	1130.0	3.143	1.987	2.87	1.699	61.26	53.6
Ib	300	265	0.01	2.094	39.61	604.8	3.146	1.988	3.54	1.903	61.28	55.1
IIa	300	271	0.01	0.708	113.49	2637.7	3.142	1.934	1.40	0.996	61.90	53.8
IIb	300	271	0.01	1.097	73.70	880.0	3.145	1.936	1.93	1.313	61.90	55.2
IIIa	600	406	0.01	1.684	47.89	1413.3	3.143	1.864	3.23	1.814	62.77	53.3
IIIb	600	406	0.01	2.094	38.71	717.3	3.147	1.859	3.79	1.968	62.87	55.4
IVb	300	95	0	1.918	36.05	404.2	3.073	1.193	3.86	1.985	72.03	61.8

Table 2.2: Input and output parameters for simulation cases considered in the paper. Cases with 'a' correspond to the DDA model (without EAI) and cases with 'b' correspond to the model including EAI. For all cases, input parameters not cited here are those of Table 2.1. Case IV without inertia (i.e. IVa) is not included since it does not yield a stationary solution.

with $c_s = \sqrt{T_e/m_i}$ and

$$G = T_e\left(\nu_p - \nu_w\right) + u_{zi}\left[m_i\nu_i\left(u_{zi} - u_{zn}\right) - m_e(\omega_{ce}u_{ye} + \nu_e u_{ze}) - T_e\frac{\mathrm{d}\ln A}{\mathrm{d}z} - \frac{q_{ze}}{\kappa_{\perp e}}\right]. \quad (2.23)$$

Therefore, there will be singularities of u_{zi} and other plasma variables at sonic points $u_{zi} = \pm c_s$, unless $G = 0$ there. By including electron azimuthal inertia in the model, equation (2.8) yields $u_{ze} = 0$ (within the cathode layer) as singular point unless $u_{ye} = 0$ there.

Based again on [27,36,37], boundary conditions are imposed at: the anode sheath edge B, the regular sonic point S, the cathode N, and the plume boundary ∞. At point S, we impose [BC1] $G_S = 0$ where $u_{ziS} = c_{sS}$. At the sheath edge B, located at $z \simeq z_A = 0$ in the zero Debye length limit, we impose: [BC2-BC3] the mass flow $\dot{m}$ and $u_{znB} = u_{znA}$ are known; [BC4] the Bohm condition

$$u_{ziB} = -c_{sB} \quad (2.24)$$

valid as long as $\lvert u_{ze\mathrm{B}}\rvert \ll \bar{c}_{e\mathrm{B}}$ and the axial electron inertia is negligible [65]; [BC5] the sheath potential fall

$$\phi_{\mathrm{AB}} = \frac{T_{e\mathrm{B}}}{e}\ln\frac{\bar{c}_{e\mathrm{B}}}{4\lvert u_{ze\mathrm{B}}\rvert}, \quad (2.25)$$

assuring the electron current continuity across the sheath, with $\bar{c}_e = \sqrt{8T_e/\pi m_e}$, and yielding $\phi_B = V_d + \phi_{\mathrm{AB}}$ with V_d the (known) discharge voltage; and [BC6] the heat flux

$$q_{ze\mathrm{B}} = n_{\mathrm{B}}u_{ze\mathrm{B}}\left(e\phi_{\mathrm{AB}} - T_{e\mathrm{B}}/2\right) \quad (2.26)$$

obtained from the electron energy equation across the sheath and the energy flux $2T_{eB}n_{\mathrm{B}}u_{ze\mathrm{B}}$ deposited at the anode. At the cathode centre N, $z = z_N$, it is: [BC7] $\phi_N = 0$; and [BC8] $u_{ye} = 0$ where $u_{ze} = 0$ (always within the cathode layer). At the plume boundary ∞, [BC9] $T_{e\infty}$ is known. The downstream electric current I_∞ is known too, while the discharge current I_d is an output.

In the electron inertialess model, which we will compare with the present one, equation (2.8) reduces to (2.13) and the point $u_{ze} = 0$ is no longer singular. Thus, the inertialess model does not need the boundary condition [BC8]. Still equation (2.13) assures that the inertialess solution satisfies $u_{ye} = 0$ where $u_{ze} = 0$.

From equation (2.25), the normal anode sheath vanishes for $|u_{zeB}| = \bar{c}_e/4$. Applying quasineutrality and the Bohm condition on ions at B, there is a normal anode sheath (and the model is valid) for

$$|I_{iA}|/I_d > \sqrt{2\pi m_e/m_i}. \tag{2.27}$$

Appendix B explains the numerical method implemented to integrate the set of non-linear ordinary differential equations and the benchmarking with other works and numerical approaches.

2.3 Overview of the plasma discharge

A SPT-100-type Hall thruster operating with xenon is used for the simulations. Table 2.1 summarizes the main parameters of the reference cases Ia (without EAI) and Ib (with EAI). For the purposes of this paper, the turbulent parameter $\alpha_t(z)$ is just assumed constant and equal to 0.01, and the effective cross-section of the plasma beam outside the channel follows the law [36]

$$\mathrm{d}A/\mathrm{d}z = 4\pi R c_{sE}/u_{zi}, \tag{2.28}$$

with R the channel mid-radius. The numerical method described in Appendix 2.B is applied to a grid with 1000 nodes to solve the extended model. Table 2.2 summarizes the main cases simulated here. Notice that in all cases: (1) there is a normal anode sheath, with $e\phi_{\mathrm{AB}}/T_{e\mathrm{B}}$ between 1 and 2, and scaling with $|I_{i\mathrm{A}}|/I_d$; and (2) $|u_{ze\mathrm{B}}| \ll u_{ye\mathrm{B}}$, thus justifying that axial inertia is negligible near the anode. It will be later shown that it is negligible everywhere.

Figure 2.2 depicts the axial profiles of the main plasma variables for cases Ia (red dash-dotted lines, no EAI) and Ib (black solid lines, with EAI). We start overviewing briefly the main features of the discharge for both models. [The differences between them are analyzed in Section 2.4 and far plume characteristics are commented in Section 2.5.] First, we must highlight that the location of (regular) points D ($u_{ziD} = 0$), S ($u_{ziS} = +c_{sS}$), and $u_{ye} = 0$ (this last one slightly upstream of point N) are part of the solution. The three of them mark the approximate limits of the different plasma regions [36].

In figure 2.2(a), the magnetic strength profile, $B(z)$, is an input, and $\chi(z)$ with $\chi_m \simeq 100$ shows that electrons are magnetized until beyond the cathode layer.

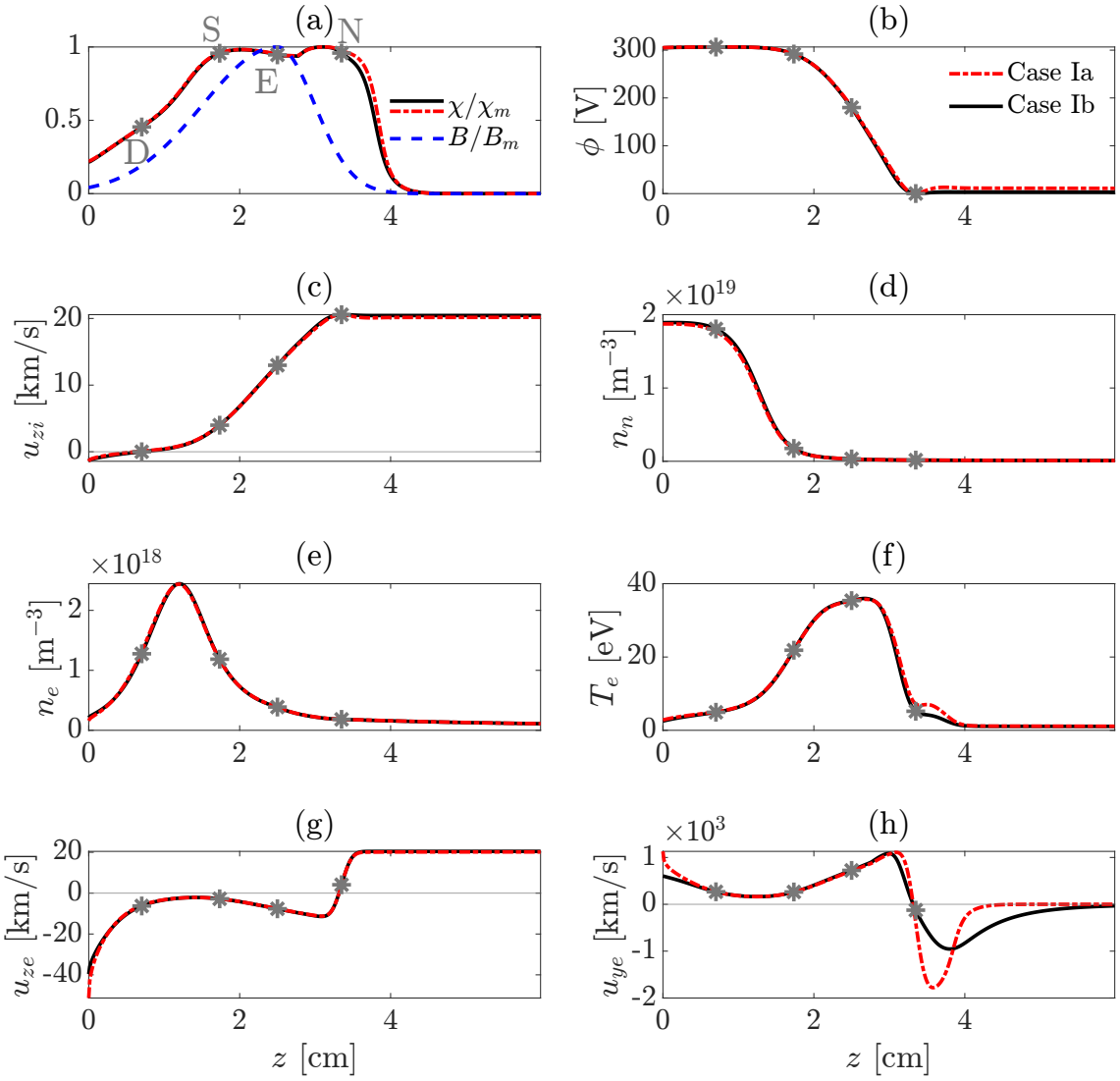

Figure 2.2: Stationary plasma response for cases Ia (dash-and-dot, red, without EAI) and Ib (solid, black, with EAI) from anode to $z = 6$ cm. Asterisks correspond to points defined in plot (a). The locations of points D, S, and $u_{ye} = 0$ are part of the solution. In (a): $B(z)$ is an input and $\chi_m = 100$.

Between S and N, $\chi \approx \chi_m = \alpha_t^{-1}$ and the electron collisionality is fully dominated by the (empirical) turbulent transport; the small decrease of χ around E is due to a high wall collisionality caused by a large SEE. The electric potential profile, ϕ in figure 2.2(b), shows that the main acceleration region is downstream of the sonic point S, it extends into the near plume, and the cathode layer is quasineutral. The profile of u_{zi} in figure 2.2(c) corresponds approximately to free acceleration under the electric potential. In the region upstream of D, backstreaming ions are driven by the small electric field, while the electron magnetic force is balanced mainly by the pressure force. Figure 2.2(d) for n_n shows that the neutral gas is depleted monotonically along the chamber, since volumetric ionization dominates wall recombination. Figure 2.2(e) for n_e shows that the main ionization region is

between points D and S.

Looking next at $T_e(z)$ in figure 2.2(f), electrons moving inwards are Joule-heated first, then they are cooled down due to both wall losses and ionization. Downstream the cathode, there is also some Joule heating but T_e tends quickly to the downstream boundary $T_{e\infty}$. In figure 2.2(g), u_{ze} follows equation(2.18). Its non-monotonic behaviour inwards the cathode is just the consequence of electron flow continuity and the creation of new electrons in the ionization region. The azimuthal electron velocity, figure 2.2(h), of outward electrons decays in the far plume, while, for inwards electrons and like for u_{ze}, is non-monotonic. Both u_{ze} and u_{ye}, change sign at a single point within the cathode layer, thus distributing correctly the fractions of electron current flowing inwards and outwards. The solution also confirms that the plasma discharge remains quasineutral while crossing the cathode layer.

Figure 2.3 provides information on the different forces and collisionalities. Figure 2.3 (a) shows the accumulated thrust, which increases both in regions D to S, and S to N. The blue line makes clear that the axial magnetic force dominates almost totally the thrust production, while the pink line shows that the axial electron momentum flow contributes to thrust only in the innermost region of the channel. Figure 2.3(b) plots the different contributions to the electron collisionality along the discharge for the reference case discussed in this section. The Hall parameter becomes 1 at $z \simeq 4.36$ cm, slightly downstream of the cathode. The region upstream of $\chi = 1$ can be considered magnetized (for electrons). There, turbulent diffusion dominates amply the electron cross-field transport; except in the near anode region, dominated by ν_{en}, and close to the cathode, where S_c/n_e is of the same order. In the far plume, with $\chi < 1$, electron-ion collisions are dominant for weakly magnetized electrons, that tend to dominate for low temperature as predicted by the well-known Spitzer law [79].

Figure 2.3(c) evaluates the different contributions to the electron axial momentum equation (2.7). Expressing formally that equation as

$$0 = f_{zm} + f_{ze} + f_{zp} + f_{zc}, \tag{2.29}$$

i.e. as the balance of, respectively, magnetic, electric, pressure, and collisional (including ν_t) force densities (with $f_{zm} = m_e\omega_{ce}n_eu_{ye}$, etcetera), the following reduced balances are found: $0 \approx f_{zm} + f_{zp}$, near the anode (i.e. u_{ye} is a diamagnetic drift); $0 \approx f_{zm} + f_{ze}$, from the main ionization region to the cathode (i.e. u_{ye} is an $E \times B$ drift); $0 \approx f_{zm} + f_{zp}$, past the cathode; and $0 \approx f_{ze} + f_{zp}$, in the far plume (i.e. the Boltzmann relation applies). Collisional forces are fully marginal in the axial direction.

Figure 2.3(c) also plots for the reference case the axial inertia force, $f_{zi} = -m_en_eu_{ze}\mathrm{d}u_{ze}/\mathrm{d}z$, computed in post-process, which is found negligible everywhere;

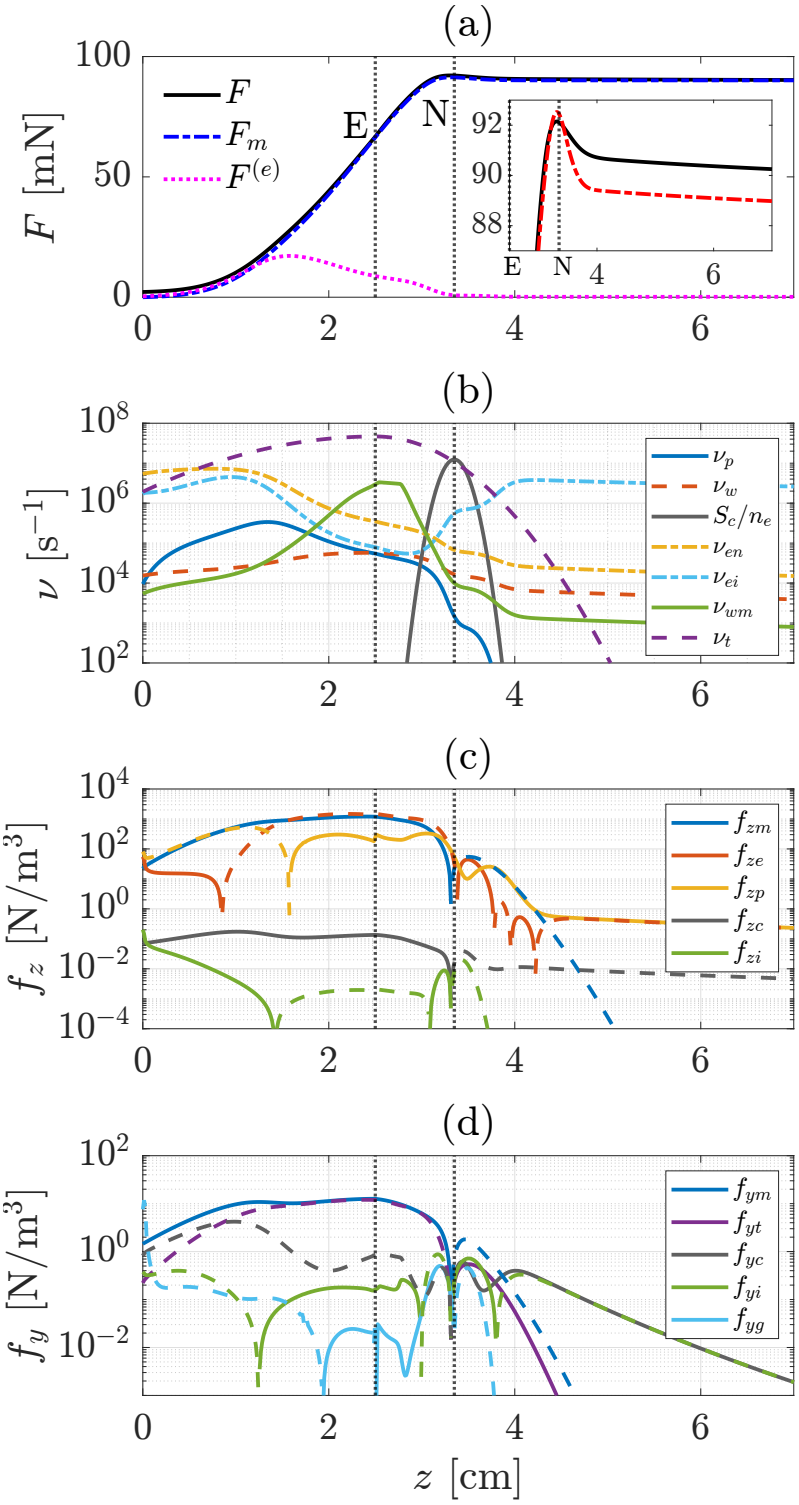

Figure 2.3: Reference case Ib. (a) Accumulated thrust, magnetic thrust contribution, and electron thrust contribution $F^{(e)} = p_e A$. (b) Main collisional frequencies. (c, d) Main axial and azimuthal forces on the electron fluid, with solid and dash-and-dot lines standing for positive and negative values, respectively. Subplot inserted in plot (a): comparison of the accumulated thrust in the far plume for cases Ia (dash-and-dot, red) and Ib (solid, black).

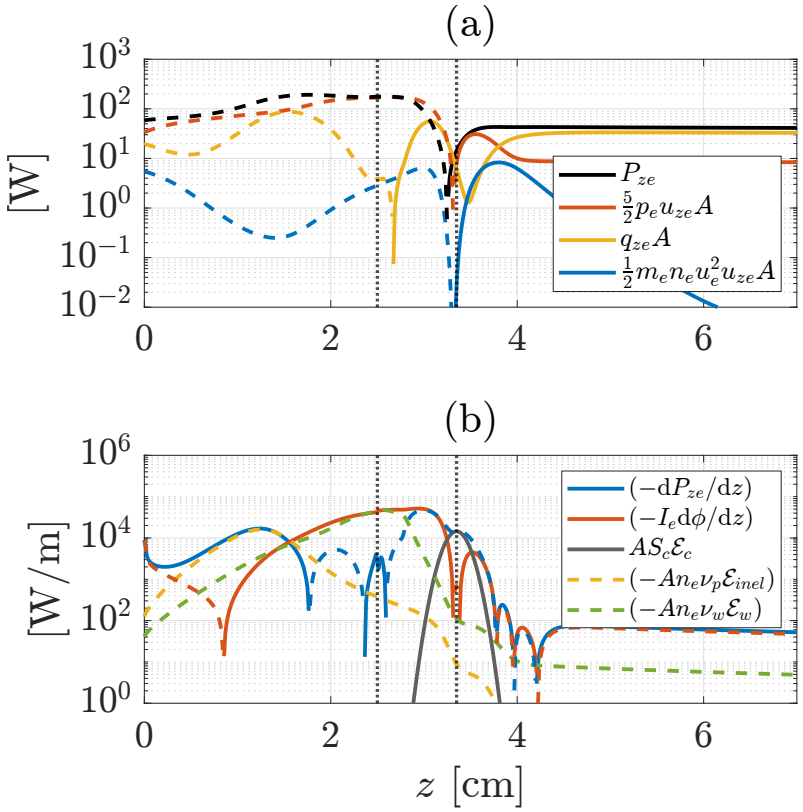

Figure 2.4: Reference case Ib. Energy balance of electrons showing: (a) the contributions to the total energy flow in equation (2.14); and (b) the different terms in the total energy equation (2.9).

the same result is found in the other cases. This completes the validation of Ahedo and Escobar's postulate [65] on axial electron inertia being negligible as long as a normal anode sheath is established. The full-fluid momentum model of Sahu et al. [71] includes the direct computation of the electron axial inertia, but all the stationary solutions they discuss bear, as long as we understand, a normal anode sheath, so axial inertia should be negligible.

Figure 2.3(d) evaluates the contributions to the azimuthal momentum equation (2.8), which we express formally as

$$0 = f_{ym} + f_{yc} + f_{yt} + f_{yi}, \tag{2.30}$$

i.e. the balance of magnetic, collisional (here excluding ν_t), turbulent, and inertial force densities (with $f_{ym} \equiv -m_e\omega_{ce}n_e u_{ze}$, etcetera); the additional gyroviscous force f_{yg} plotted in Figure 2.3(c) is discussed in a later section. The figure shows that: the full balance applies around the cathode layer; $0 \approx f_{ym} + f_{yt} + f_{yc}$ applies from the anode to the vicinity of the cathode, implying equation (2.13); $0 \approx f_{ym} + f_{yi}$ applies in the far plume, implying

$$u_{ze}\mathrm{d}u_{ye}/\mathrm{d}z \simeq -\nu_{ei}u_{ye} \tag{2.31}$$

and thus the progressive vanishing of u_{ye}. Notice that the terms of this azimuthal equation are typically χ times smaller than the ones in the axial equation. This implies that the analysis of the electron momentum vectorial equation must be done separately for each component equation.

Figure 2.4(a) shows the total axial energy flow P_{ze} and the different contributions to it. The direction of the energy flow changes at the cathode location, as expected. The contribution of the flow of kinetic energy is negligible everywhere. In the main region, inward of the cathode, P_{ze} is mainly constituted by the enthalpy (inward) flow $(5/2)p_e u_{ze} A$, while the subdominant heat flow $q_{ze}A$, changes sign at the temperature peak. In the current-free plume, the two contributions are outward, with the heat flow dominating only in the far plume where electrons are already demagnetized and thermal perpendicular conductivity is much stronger, while the remaining enthalpy is small.

Figure 2.4(b) plots the axial profiles of all the terms involved in the electron energy equation (2.9), with $\mathrm{d}P_{ze}/\mathrm{d}z$ moved to the right side. The dominant terms change along the discharge. Around the cathode there is the energy input from the injected electrons. Then, except in the ionization region where $-\mathrm{d}\phi/\mathrm{d}z$ is very small, the work of the axial electric field is a dominant contribution, which changes P_{ze} (i.e. produces electron heating or cooling) in the near and far plume and next to the anode. However, in the outer part of the channel the work of the electric field compensates mainly energy losses at the walls.

In the far, unmagnetized plume, the electron dynamics reduce approximately to the the energy conservation law $A[(5T_e/2 - e\phi)n_e u_{ze} + q_{ze}]$=const, and the electrostatic balance $en_e \mathrm{d}\phi/\mathrm{d}z \simeq \mathrm{d}p_e/\mathrm{d}z$. The weak outwards electric field there is behind the mild re-acceleration of the ions.

2.4 Electron azimuthal inertia effects on the discharge

2.4.1 Comparison with inertialess solution

The comparison of cases Ia and Ib shows that the EAI reduces the gradients of u_{ye} in three regions: across the cathode layer, in the far plume, and near the anode. At the two sides of the cathode layer, the local maximum and minimum of u_{ye} are limited by the EAI. In the far plume, EAI changes substantially the profile of u_{ye} due to the progressive cancellation of the magnetic force in equation (2.8). Once electrons are demagnetized, electron-ion or electron-neutral collisions there, damp

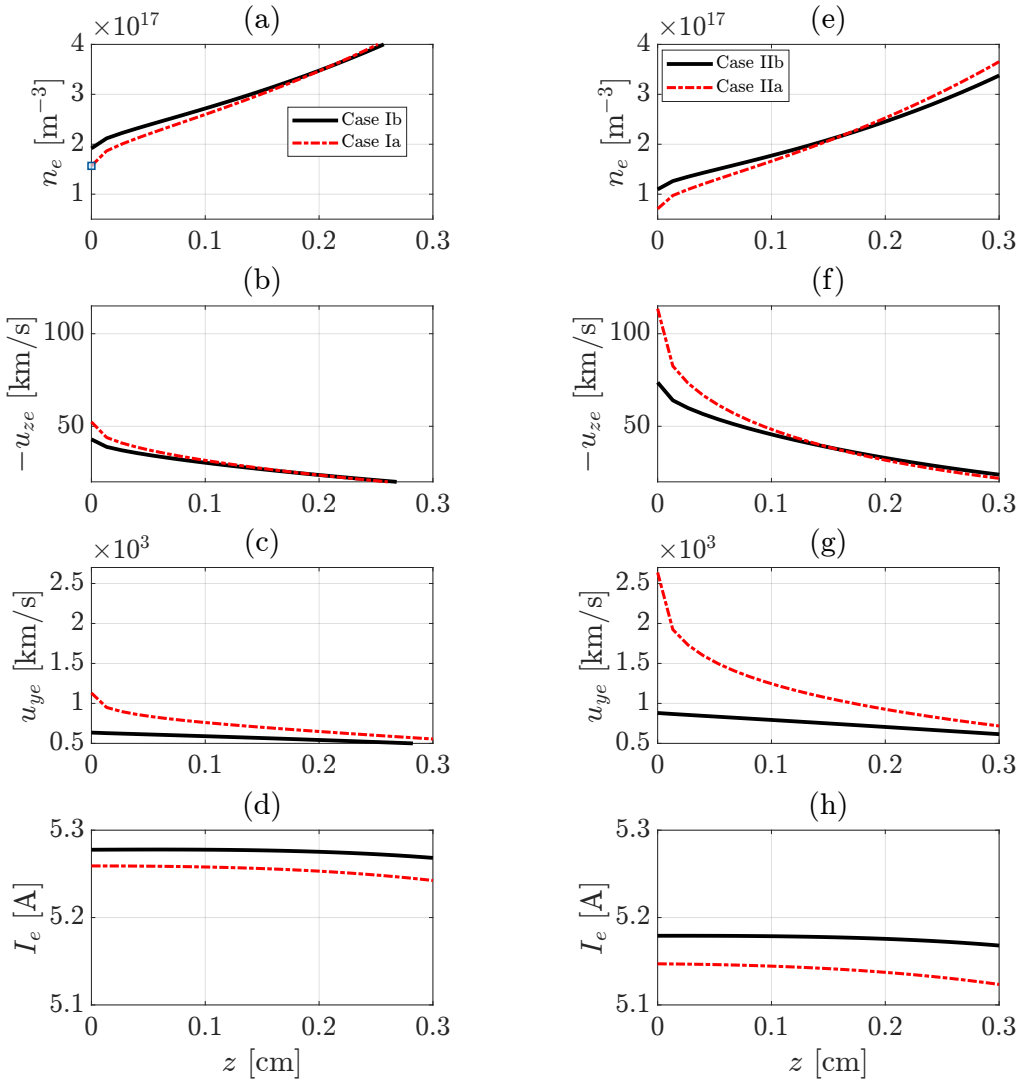

Figure 2.5: Profiles of several magnitudes in the near-anode region for cases I and II (left and right plots, respectively).

u_{ye} to zero. The change of sign of u_{ye} in the far plume makes the magnetic thrust contribution negative there. This penalty is smaller in the EAI model due to a milder force density $|Bu_{ye}|$. This effect is well illustrated in the zoom inserted in figure 2.3(a), where the accumulated thrust for cases Ia and Ib is shown, with the EAI model yielding a total thrust about 1.4% higher.

Figure 2.5 (left) depicts the near-anode region of some of the variables of figure 2.2. As in reference [71], the EAI reduces the growth of both u_{ye} and $-u_{ze}$ towards the anode, but in a different proportion: while the inertialess solution yields a velocity ratio $u_{ye}/|u_{ze}|$ equal to the Hall parameter, the EAI-modified solution yields $u_{ye}/|u_{ze}|$ lower than χ. The EAI also reduces the decay of n_e in such a proportion that $j_{ze} = -en_eu_{ze}$ and thus I_e are practically unaffected by the EAI. [This last point, essential to discuss the cross-field transport, is absent in reference [71].] Table 2.2 shows that for cases Ia and Ib, the EAI reduces by 87% the value of u_{yeB} and

modifies by 30% the values of u_{zeB} and n_{eB}, while $|I_{eA}|$ in figure 2.5 increases by a mere 0.5% with EAI, in agreement with reference [71].

The effects of the EAI around the anode are more pronounced the higher is u_{yeB}. This is illustrated by cases IIa and IIb of Table 2.2 and figure 2.5 (right) with $B_m = 271$ G instead of 265 G (i.e. just an increase of 2.2%). Now, the EAI reduces by 300% the value of u_{yeB} and by 54% the value of u_{zeB}. Looking for a situation with higher axial electric fields around the thruster exit E (and thus larger u_{ye} there) cases IIIa and IIIb with $V_d = 600V$ (and an adjusted B_m) of Table 2.2 were run. No appreciable differences were observed with respect to previous cases.

Hence we can conclude that, the electron azimuthal inertia, which is simple to add to the DDA model, has relevant effects on the discharge and should not be disregarded. On the contrary, the electron axial inertia, which, in addition, requires a more complex mathematical model, is negligible for all cases considered here: post-processing the solution for case IIb, the most critical one for this matter, yields that the axial momentum inertia is below 1% of the dominant (electric or magnetic) force along the whole discharge.

2.4.2 On cross-field transport

The electron cross-field transport determines the axial electron current density j_{ze} in the main discharge (from A to N) and its integral over the beam cross section, I_e. The absolute and relative parameters most suitable to measure the intensity of the (global) cross-field transport are, respectively, $I'_{eN} = I_d - I_{i\infty}$, which (for $I_{i\infty} \simeq I_{iN}$) is the cathode electron current drifting inwards, or the current efficiency

$$\eta_{cur} = \frac{I_{i\infty}}{I_d} \equiv \frac{I_{i\infty}}{I_{i\infty} + I'_{eN}}. \tag{2.32}$$

Table 2.2 for Cases I to III show that these parameters have variations of ± 0.1-0.2 % when adding EAI, so the global effect of the EAI on the cross-field transport (when this is dominated by the presence of the turbulent force) is negligible. Nonetheless, the same Table shows that including EAI increases the thrust efficiency, $\eta_F = F^2/(2\dot{m}I_dV_d)$ by 1-1.5 %. This increase is due to the lower (negative) magnetic thrust in the plume with EAI commented previously.

References [68,69,71] claim a 'shear-induced' electron transport based on du_{ye}/dz in equation 2.8, which can be expressed as

$$\frac{u_{ye}}{-u_{ze}} = \left(1 + \frac{\mathrm{d}u_{ye}/\mathrm{d}z}{\omega_{ce}}\right)\chi.$$

We have seen that the presence *and sign* of $\mathrm{d}u_{ye}/\mathrm{d}z$ modify certainly the local velocity ratio, and as a result, the electron velocities and density, but not the (global)

cross-field transport. This same result leads us to opine that there is no basis to introduce $|\mathrm{d}u_{ye}/\mathrm{d}z|$ as a contribution to the turbulent parameter α_t, as proposed in reference [68].

According to the azimuthal balance equation (2.30), the inclusion of the azimuthal turbulent force f_{yt} increases the azimuthal magnetic force $f_{ym} = Bj_{ze}$ and thus j_{ze} in the main discharge. The empirical selection of α_t is indeed based on fitting experimental values for I'_{eN}. In order to complete the analysis of EAI effects on cross-field transport, we consider the hypothetical case IVb of Table 2.2 without an azimuthal turbulent forces (i.e. $\alpha_t = 0$), and B_m reduced to 95G, in order to keep n_{eB} similar to case Ib. Figure 2.6(a)-(d) and Table 2.2 compare the plasma solutions for cases Ib and IVb. As expected, the most important difference is the reduced cross-field transport with I'_{eN} decaying from 1.9A to 1.1A and η_{cur} increasing from 61% to 72%. As a result η_F increases from 55% to 62%. In spite of the smaller magnetic field the maximum Hall parameter has increased from $\chi_m = 100$ to $\chi_m = 2300$. However, the maxima of u_{ye} increase only four times due, partially to a smaller u_{ze} and mainly to inertial effects, which tend to set $u_{ye} = O(c_e)$. Since our fluid model also considers anomalous thermal conductivity, $\kappa_{\perp e}$ decreases much in case IVb, explaining the larger gradients of T_e around its maximum. In turn, the new T_e profile explains the shift in the location of the ionization region. Finally, figure 2.6(d) analyze the relative importance, in the absence of the turbulent force, of electron inertia and collisionality in the cross-field transport inward from the cathode. While in the balance of Figure 2.3(c) for case Ib, inertial effects where marginal (except perhaps very locally at the cathode), in case IVb electron inertia dominates in the near plume while collisions (with ions and neutrals) dominate inside the channel. The gyroviscous force continues to be globally modest compared to inertia.

The effects of EAI on cross-field transport have been discussed, but this paper is not on cross-field transport in itself. This explains that the analysis has been limited to simple cases with $\alpha_t(z)$ constant. In the literature there are many examples of tailoring $\alpha_t(z)$ to best fit an experimental plasma profile (e.g., ϕ and u_{zi}) or some performances figures [72, 80]. In some of these cases, inertial effects could have a less marginal role in cross-field transport.

2.4.3 Effect of cathode thickness

A cathode with non-zero thickness $2\ell_c$ allows to connect continuously the main discharge (from point B to N^-) and the far plume (from point N^+ to ∞), and how conditions at infinity influence the main discharge, both in the inertial and inertialess models.

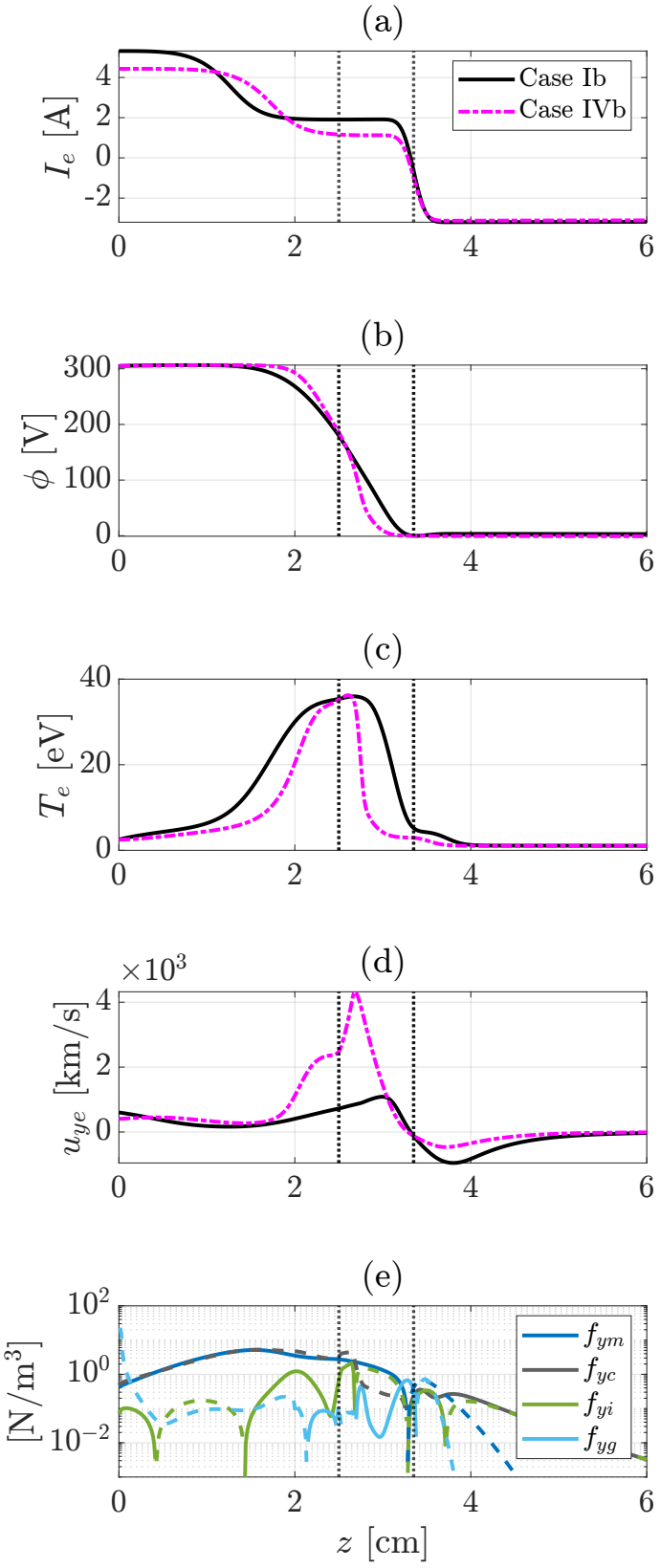

Figure 2.6: Effect of suppressing turbulent transport. (a)-(d) Several plasma profiles for cases Ib and IVb. (e) Electron azimuthal momentum balance for case IVb to be compared with figure 2.3(d).

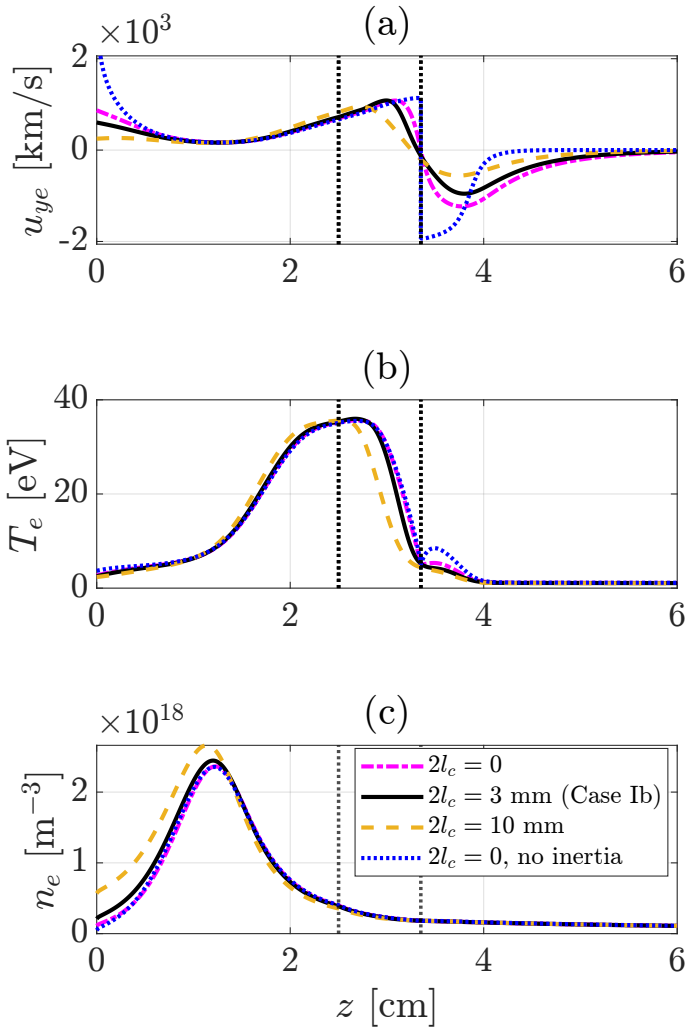

Figure 2.7: Effect of the cathode thickness for reference case Ib.

Instead, the widely-used boundary cathode model separates sharply the main discharge and the far plume, and the solution of both regions are solved independently. Since all electron emission is concentrated in a discontinuity surface, $S_c = 0$ is used in the equations of section 2.2. In the main discharge, boundary conditions are the same as in the previous section, except for: the regularizing boundary condition [BC8] at the electron stagnation point (i.e., $u_{ye} = 0$ when $u_{ze} = 0$) is not required and, in the inertial model, is substituted by $u_{yeN^-} = 0$ (note that $u_{zeN^-} \neq 0$); and (2) the condition [BC9] is substituted by the value of T_{eN^-}. The main plume is solved with boundary conditions at N^+ that guarantee the continuity at point N of every plasma variable, (in particular $u_{yeN^+} = 0$, $T_{eN^+} = T_{eN^-}$), except for u_{ze} and q_{ze}. The resultant curves are, however, not differentiable at N. The value of u_{zeN+} is set according to equation (2.18) and I_∞. The value of q_{zeN^+} is such that the far-field boundary condition is satisfied.

Figure 2.7 compares the plasma solution for zero-thickness cathode and two different non-zero thickness cases. There is a continuity on the plasma response with

parameter ℓ_c. A thicker cathode smooths the gradients of u_{ze} and u_{ye} in the vicinity of N. The rest of variables, as n_e illustrates in plot (c) are practically unaffected around the cathode. Figure 2.7 also compares the inertial and inertialess models for $\ell_c = 0$: the only observation is that the inertial model allows the continuity of u_{ye} across the cathode, which mitigates the role of inertia in the solution.

Apart from the local behaviour close to point N, Figure 2.7 shows that the cathode thickness has some secondary effects on the plasma behaviour near the anode, where the evolution of u_{ye} and u_{ze} are also smoothed when increasing ℓ_c. This behaviour seems to be a side effect of ℓ_c on the ionization region, that seems to be shifted towards the anode when increasing ℓ_c. The result is a larger anode density (and ion current) that mitigates the effect of the anode sheath-edge singularity.

2.4.4 Gyroviscosity

As pointed out in the Introduction, the inclusion of azimuthal electron inertia term raises the question of whether gyroviscous part of the electron pressure tensor, $\bar{\bar{p}}^{GV}$, could also be relevant, transforming equation (2.8) into

$$u_{ze}\frac{\mathrm{d}u_{ye}}{\mathrm{d}z} = -(\omega_{ce}u_{ze} + \nu_e u_{ye}) - \frac{(\nabla\cdot\bar{\bar{p}}^{GV})_y}{m_e n_e}. \tag{2.33}$$

With the postulates used in our model, the fast-dynamics ordering approximation [31, 74] estimates the force produced by the non-gyrotropic part of the pressure tensor as [10]

$$\nabla\cdot\bar{\bar{p}}^{GV} = \nabla\times\left[(\nabla\cdot\boldsymbol{u}_e)\frac{m_e p_e}{2eB^2}\boldsymbol{B}\right] + \nabla\left[\frac{m_e p_e}{2eB^2}\boldsymbol{B}\cdot(\nabla\times\boldsymbol{u}_e)\right] - \left\{\left[\nabla\times\left(\frac{m_e p_e}{eB^2}\boldsymbol{B}\right)\right]\cdot\nabla\right\}\boldsymbol{u}_e, \tag{2.34}$$

where we assume a purely radial magnetic field and disregard heat flow, particle flows, and gradients in the parallel direction. This expression was already considered in Hall-thruster linear stability studies [10, 51].

For the one-dimensional case under consideration, the only azimuthal contribution comes from the first term of the right-hand side of equation (2.34) and reads

$$f_{yg} \equiv \left(\nabla\cdot\bar{\bar{p}}^{GV}\right)_y = \frac{\mathrm{d}}{\mathrm{d}z}\left(\frac{m_e p_e}{2eB}\frac{\mathrm{d}u_{ze}}{\mathrm{d}z}\right). \tag{2.35}$$

If $c_e = \sqrt{T_e/m_e}$, $r_{Le} = c_e/\omega_{ce}$, and ℓ_z is characteristic length of axial gradients, the ratio of gyroviscous versus inertial azimuthal forces is

$$\frac{f_{yg}}{f_{yi}} \sim \frac{r_{Le}}{\ell_z}\frac{c_e}{u_{ye}}. \tag{2.36}$$

This ratio is $O(1)$ if $u_{ye}/c_e = O(r_{Le}/\ell_z)$, as assumed by the small Larmor radius theory. Here, figures 2.3(d) and 2.6(e) show f_{yg} along the discharge, calculated by post-process from the solution without gyroviscosity. In general, it can be said that: azimuthal inertia and gyroviscosity are of the same order between anode and cathode; both are negligible except locally around anode and cathode, where large gradients develop; and, in the far plume, the azimuthal inertia is the dominant force while the azimuthal gyroviscosity is fully negligible.

Taking into account that the gyroviscous force introduces second-order derivatives of u_{ze} and products of first order derivatives, which complicate much the mathematical model to be solved, the above behaviour of the forces justifies including inertia and neglecting gyroviscosity in the fluid model. (Still, the gyroviscous force could be included as a source term in the present first-order model and iterate until convergence.)

2.5 Far plume behaviour

The plasma discharge in the far plume (downstream the cathode) presents different characteristics from the main discharge: it is current-free (or almost), variations of the electric potential are much milder (of the order of T_e there), and the azimuthal electron inertia takes a major role, as electrons become demagnetized. Some aspects related to the far plume are investigated here.

The first one is numerical, related to the length $L_{N\infty}$ of the simulated plume domain. In an expansion to free-space the plume is infinite, but in our numerical model it is necessarily bounded. The second aspect, related to this one, is the condition on T_e at the end of the domain. Two standard possibilities have been tested: we can set either $T_{e\infty}$ (as done up to here in the paper) or $(\mathrm{d}T_e/\mathrm{d}z)_\infty$.

Figure 2.8(a)-(c) analyzes the sensitivity of the solution, at a point P, 5 cm downstream the cathode (i.e. $z_\mathrm{P} = 8.35$ cm) to both $L_{\mathrm{N}\infty}$ (from 5 cm to 40 cm) and the boundary condition on T_e. When we set $T_{e\infty} = 1$eV, ϕ_P is nearly invariant and $(\mathrm{d}T_e/\mathrm{d}z)_\mathrm{P}$ can be considered small: about 1eV/m, smaller than $T_{e\infty}/L_{N\infty}$. When, instead, we set $(\mathrm{d}T_e/\mathrm{d}z)_\infty = 0$, there is about a 14% of variation in ϕ_P and a 40% in $T_{e\mathrm{P}}$ as $L_{\mathrm{N}\infty}$ goes from 5 cm to 40 cm; also, $T_{e\infty} \simeq T_{e\mathrm{P}}$ (about 3-5 eV) is larger than expected in real far plumes. Figure 2.8(d) shows the influence of the boundary condition and plume size on $u_{ye}(z)$, where again the sensitivity of the solution to $L_{N\infty}$ when imposing $(\mathrm{d}T_e/\mathrm{d}z)_\infty$ is observed. The conclusion is that imposing the boundary condition on $T_{e\infty}$ seems more adequate. Furthermore, we have studied the response for $T_{e\infty}$ between 1 and 5 eV, and found no special sensitivity to that value, with electron-ion collisions dominating the far plume for the whole range. Since ν_{ei}

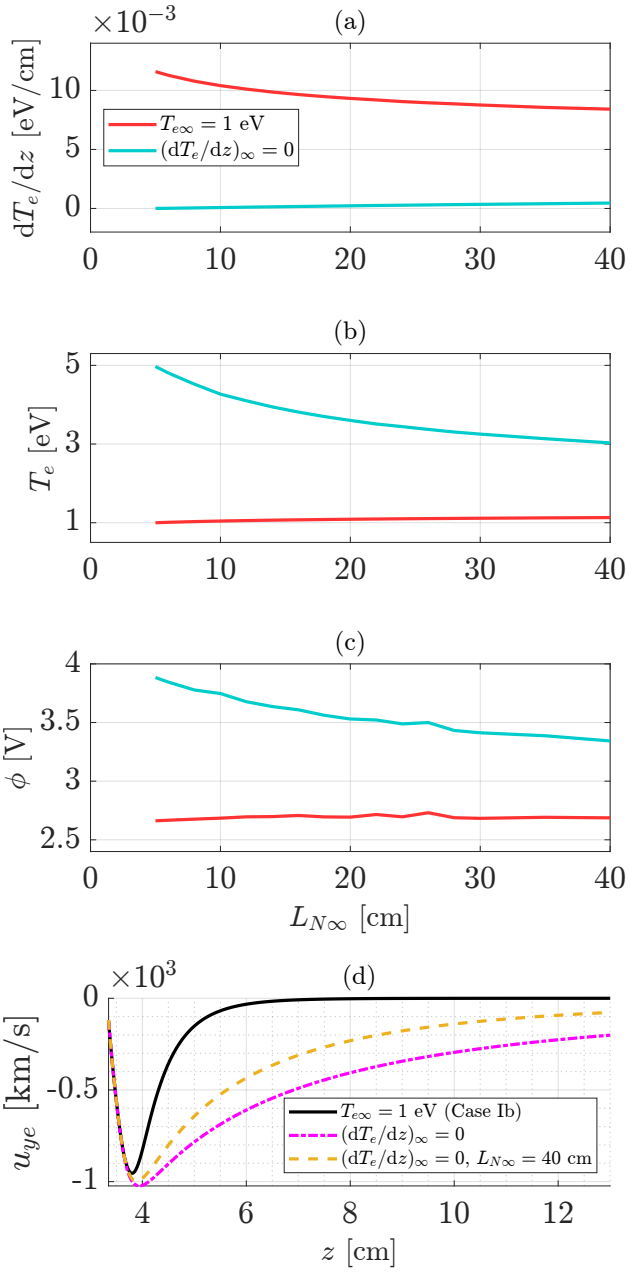

Figure 2.8: Variation with the far plume length of: (a) (dT_e/dz) (b) T_e, and (c) ϕ, evaluated at $z = 8.35$ cm, when using different downstream boundary conditions. Rest of parameters as in reference case Ib.

scales as $T_e^{-3/2}$, the azimuthal velocity decays much faster the lower T_e is.

While the type of downstream condition on T_e is important in the far plume, it has been checked for the cases of figure 2.8, that it has little effect on the main discharge and performance figures, even when the cathode layer is relatively thick. The same is true for the other downstream condition we can impose in the model: the electric-current I_∞ driven by the far plume. This current circulates just in a loop between N and ∞ and modifies only electron magnitudes there. As I_∞ increases, $|u_{ze}|$ increases according to equation (2.18), u_{ye} increases with $|u_{ze}|$ [equation (2.13)],

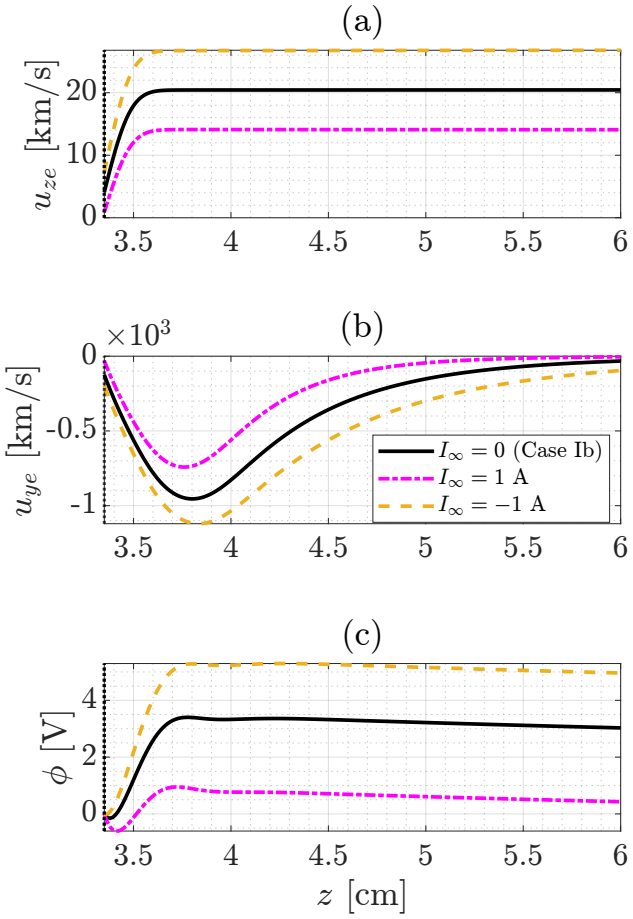

Figure 2.9: Effect of a far-plume current I_∞ in the far-plume profiles. Point N is located at the left end. Rest of parameters as in reference case Ib.

and the same is true for ϕ_∞ [equation (2.7)]. Figure 2.9 illustrates these behaviours.

To end this investigation on the quasi 1D-plume, we show that the decay length of the magnetic field has a strong effect on the far plume. Figure 2.10 illustrates this. In the case of reference $\ell_{m2} = 0.7$ cm, it was $B_N = 58$ G, the demagnetization went quite fast and there was not a significant electron heating at the beginning of the far plume. However, for $\ell_{m2} = 1$ cm (and $B_m = 260$ G to help convergence of the solution), it is $B_N = 126$ G and, similarly to the electron behaviour in the near plume, electron heating and increase of ϕ develop downstream the cathode, which can decelerate much the ion beam and thus reduce thrust. This heating is related to the degree of magnetization at the cathode injection region, because of the reversal in the electron flows across the cathode. Cathode injection with relatively big B_N leads to more energetic plumes that hold larger q_{ze} in the far-field region, being the enthalpy flow $(5/2)T_e n_e u_{ze}$ limited by the far-plume boundary condition. Nonetheless, it must be noted that such large electron heating past the cathode is partially an exaggeration of the 1D model, caused by whole plasma beam crossing the electron injection surface. This large heating is not observed in 2D simulations [67] where the injection region only covers a small fraction of the beam cross-section.

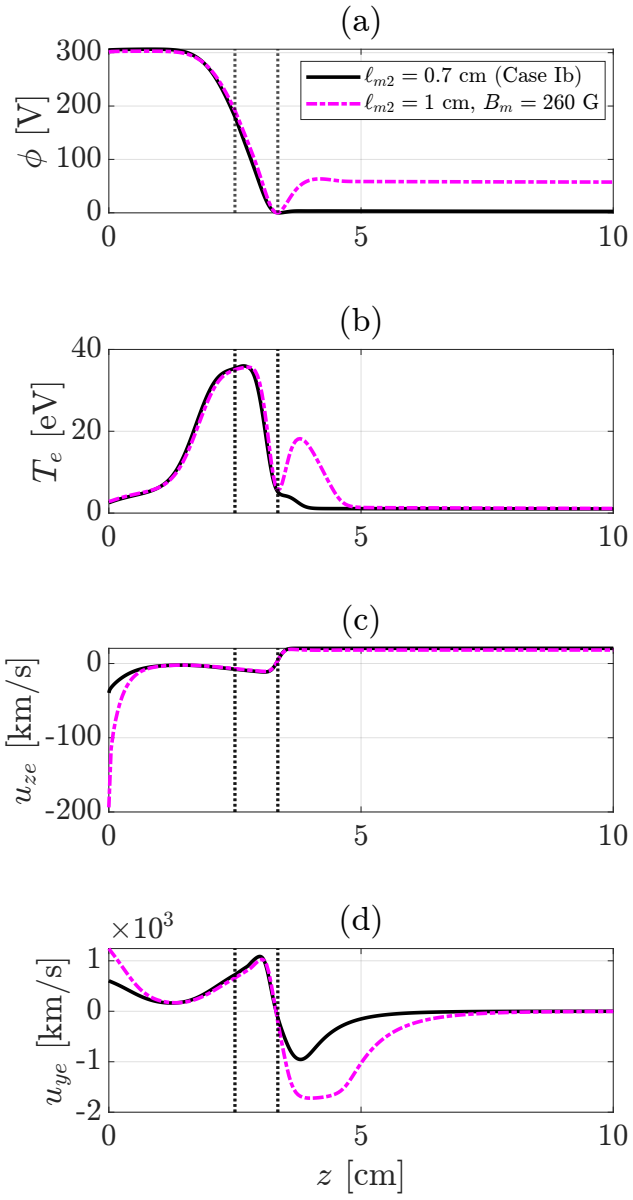

Figure 2.10: Effect of the outer axial magnetic gradient in the plasma discharge. Rest of parameters as in reference case Ib.

An interesting remark observing figure 2.10 and also figure 2.7 is that changes in plume related-parameters, seem to affect little the main ionization region, but end affecting the plasma discharge near the anode, which indicates that the near anode region is a very sensitive one, and can be more prone to oscillatory behaviours (outside of the scope of this model).

2.6 Conclusions

A 1D, stationary, drift-diffusion, quasineutral model of the plasma discharge in a HET has been extended by adding the effects of electron azimuthal inertia and

gyroviscosity, a finite thickness cathode emission layer, and the far-plume region. These additions affect the mathematical formulation of the problem, by: adding singular points when accounting for EAI; the coupling between the main and far-plume regions when considering a finite-thickness cathode, and the displacement of boundary conditions to the far-plume boundary. The plasma remains quasineutral within the cathode layer.

For the several cases analyzed, the solutions of the extended model in the main region (chamber and near-plume) are very similar except for EAI having a smoothing effect on u_{ye} across the cathode layer and near the anode. In this last region EAI can produce large variations of the two electron velocities and the plasma density but the electron axial current density remains practically unaffected. In the far plume, the EAI becomes always relevant since the electron fluid demagnetizes, leading to the progressive vanishing of the azimuthal drift. This reduces the negative magnetic thrust in the far plume and has a non negligible effect on the thrust efficiency (around 1-1.5 percentage points in our simulations).

While EAI affects the local plasma response and dynamics, it has been shown that its inclusion leads to no discernible effect on the (global) electron cross-field transport, measured for instance with the current efficiency (or alternatively, with the inwards flow of electrons from the cathode). Instead, a test simulation without an azimuthal turbulent force confirms both a large improvement on the current efficiency and a minor role of electron azimuthal inertia on cross-field transport. This leads us to conclude that there is not a 'shear-induced' effect on cross-field transport.

The effect of axial electron inertia in the plasma response has been estimated. It has been found negligible in all the simulations presented here. This advises against using a full-fluid model, due to its higher mathematical complexity, unless necessary (e.g. for anode sheath vanishing). The azimuthal gyroviscous force has been estimated too. In some regions of the discharge it could be of the same order than azimuthal inertia. Since gyroviscosity involves second order derivatives of the velocity, which would modify drastically the mathematical model, it is suggested to include them as a source-like, small term.

The plasma response in chamber and near-plume is found to be little sensitive to far-plume conditions, such as the downstream boundary condition on the electron temperature, the presence of stray currents, the thickness of the cathode layer, the decay length of the magnetic field. On the contrary, regarding the far-plume response: a far-field boundary condition based on T_e (and not on its gradient) provides solutions much less sensitive to the plume size; the stray currents change the potential drop; and a stronger magnetic field in the plume does lead to significant electron heating and ion deceleration in the near plume past the cathode, with

the corresponding detriment of performance, although the comparison with 2D simulations suggests that this is probably a consequence of the 1D nature of the model.

Future work could use the stationary solutions of the present model as the equilibrium plasma state in global linear stability analyses. This was achieved in reference [38] with a domain including the anode-to-cathode region only. Including the far plume in the stability analysis is doubly interesting. First, cathode emission in a thin layer induces strong gradients of u_{ye} that could lead to Kelvin-Helmholtz-type instabilities [48]. Second, such a stability analysis would check the reliability of dominant near-plume instability modes found in reference [38], with oscillations concentrated in a very thin region close to the cathode.

Acknowledgements

This research was started under Grant Y2018/NMT-4750 (project PROMETEO) funded by Comunidad de Madrid, and completed under Grant PID2019-108034RB-I00 (project ESPEOS) funded by MCIN/AEI/10.13039/501100011033.

E. Bello-Benítez thanks the financial support by MCIN/AEI/10.13039/501100011033 under Grant FPU18/03686. This work is part of his PhD thesis, under development, and it will be included as a chapter within it.

Appendices

2.A Auxiliary collisional models

The models introduced in this section are a summary of those used in references [27, 36, 37]. Such an overview was already given in [38].

The ionization or production frequency, ν_p, is modelled as $\nu_p = n_n \bar{c}_e \bar{\sigma}_{\text{ion}}$, with

$$\bar{\sigma}_{\text{ion}} = \sigma_{\text{ion},0} \left[1 + \frac{T_e E_{\text{ion}}}{(T_e + E_{\text{ion}})^2}\right] \exp\left(-\frac{E_{\text{ion}}}{T_e}\right) \tag{2.37}$$

where E_{ion} stands for the primary ionization energy. For xenon: $E_{\text{ion}} = 12.1$ eV, $\sigma_{\text{ion},0} = 5 \times 10^{-20}$ m^2. The effective energy loss due to ionization, E_{inel}, satisfies

$$\frac{E_{\text{inel}}}{E_{\text{ion}}} = 2 + \frac{1}{4} \exp\left(\frac{2E_{\text{ion}}}{3T_e}\right) \tag{2.38}$$

The elastic electron-neutral collisions frequency is $\nu_{en} = n_n \bar{c}_e \sigma_{en}$. Here, the cross-section σ_{en} is taken approximately constant and equal to $\sigma_{en} = 27 \times 10^{-20}$ m^2 for xenon.

The electron-ion (Coulomb) collision frequency is $\nu_{ei} = n_e R_{ei}$, with R_{ei} given by

$$\frac{R_{ei}}{10^{-12}\text{m}^3\text{s}^{-1}} = 2.9 \cdot \left(\frac{1\text{ eV}}{T_e}\right)^{3/2} \ln\Lambda \tag{2.39}$$

and

$$\ln\Lambda \approx 9 + \frac{1}{2} \ln\left[\left(\frac{10^{18}\text{ m}^{-3}}{n_e}\right)\left(\frac{T_e}{1\text{ eV}}\right)^3\right]. \tag{2.40}$$

The ion-neutral (charge-exchange) collision frequency is $\nu_{in} = n_n c_{in} \sigma_{in}$, with $c_{in} = |u_{zi} - u_{zn}|$ and

$$\sigma_{in} = \sigma_{in0} \left[1 - 0.2 \log_{10} \frac{c_{in}}{1\text{ km/s}}\right]^2 \tag{2.41}$$

and $\sigma_{in0} = 81 \cdot 10^{-20}$ m^2 for xenon.

The wall-loss frequency of particles is

$$\nu_w = \tilde{\nu}_w \frac{2\pi R}{A} c_s \tag{2.42}$$

with $\tilde{\nu}_w$ being a constant. The value $\tilde{\nu}_w = 0.17$ is used here, based on the parametric analysis of reference [27]. The effective axial velocity of wall-born neutrals from ion recombination is

$$u_{znw} = a_w u_{zn} + (1 - a_w) u_{zi} \tag{2.43}$$

where a_w is a velocity accommodation factor; $a_w = 0.85$ is used here. The wall-loss frequency for momentum and energy are $\nu_{wm} = \beta_m \nu_w$ and $\nu_{we} = \beta_e \nu_w$, respectively with

$$\beta_m = \frac{\delta_w}{1 - \delta_w}, \qquad \beta_e = 5.62 + \frac{1.65}{1 - \delta_w}, \tag{2.44}$$

for xenon. Here, δ_w is the effective secondary electron emission yield from the wall, which is modelled as

$$\delta_w(T_e) = \sqrt{T_e/T_1} \quad \text{if} \quad T_e < T_e^* \tag{2.45}$$

and $\delta_w = \delta_w^* = \sqrt{T_e^*/T_1}$ if $T_e \geq T_e^*$, where T_1 is the temperature leading (theoretically) to a 100% yield (which depends on the wall material) and T_e^* is the temperature where the charge-saturation limit is reached at the wall. Here: $T_e^*/T_1 = 0.967$, $\delta_w^* = 0.983$, and $T_1 = 37$ eV.

2.B Numerical integration method

The numerical method used here to solve a boundary-value problem (BVP) on a system of non-linear ordinary differential equations (ODEs) is a basic finite-difference approach, as similarly done in reference [38] for a linear system but adapted to solve non-linear equations by using also a Newton solver. The method has been verified to show numerical stability and provide a solution to the discretized system that satisfy the fluid equations within certain tolerance. The system of stationary axial fluid equations (and any other auxiliary differential expression) can be written in the form of a general system of non-linear ODEs

$$\frac{\mathrm{d}\boldsymbol{x}}{\mathrm{d}\boldsymbol{z}} = \boldsymbol{g}_f(\boldsymbol{x}), \tag{2.46}$$

where $\boldsymbol{x} = \boldsymbol{x}(z)$ is the vector of states, of length m, that contains the macroscopic variables. In our case, $\boldsymbol{x}$ generally contains the variables ϕ, n_n, n_e, u_{zn}, u_{zi}, u_{ze}, u_{ye}, T_e, q_{ze} and A. In addition, we have m boundary-condition equations

$$\boldsymbol{g}_{bc}(\boldsymbol{x}) = 0. \tag{2.47}$$

The method benefits from the use of conservation laws, such as the conservation of $\dot{m}$ that can be obtained by combining equations (2.2) and (2.3). One of the

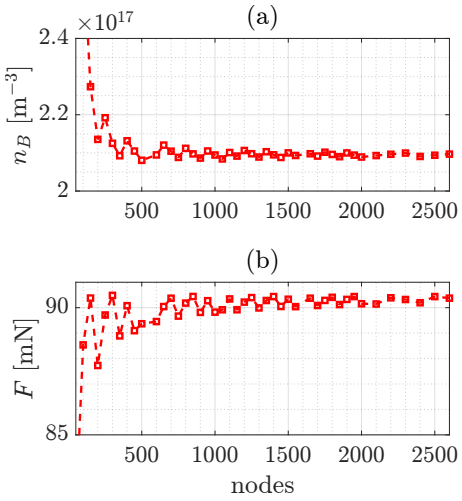

Figure 2.11: Grid convergence study on: (a) anode density (b) thrust.

plasma unknown variables can be directly computed in terms of $\dot{m}$, other variables and parameters. For example

$$u_{zi} = \frac{\dot{m} - Am_i n_n u_{zn}}{Am_i n_e}. \tag{2.48}$$

The conservation of $\dot{m}$ allows to eliminate one variable from the system, reducing the dimensionality of the system and thus the computational workload. Moreover, this approach has been seen to produce better quality solutions by eliminating ripples that appear otherwise. When doing so, u_{zi} is no longer an independent unknown and can be left out of $\boldsymbol{x}$. The differential ion continuity equation (2.3) is substituted by the algebraic expression (2.48). Also, the use of (2.48) guarantees that the mass flow is conserved and, thus, [BC2] can be removed from the set $\boldsymbol{g}_{bc}$.

The system (2.46) is discretized in an axial grid with n nodes at constant spacing Δz. The vector of unknowns $\boldsymbol{X}$ of the discretized problem gathers the values of $\boldsymbol{x}$ at the grid points and has a length mn. The discrete system to be solved is achieved by evaluating (2.46) on the $n-1$ midpoints between nodes, that yields

$$\frac{\mathrm{d}\boldsymbol{X}^*}{\mathrm{d}\boldsymbol{z}} = \boldsymbol{G}_f(\boldsymbol{X}^*), \tag{2.49}$$

where $\boldsymbol{X}^*$ stands for a vector of $m(n-1)$ elements gathering the state vector $\boldsymbol{x}$ evaluated at every midpoint and $\boldsymbol{G}_f$ is defined equivalently for the right-hand side $\boldsymbol{g}_f$. The values in $\boldsymbol{X}^*$ are approximated by those in $\boldsymbol{X}$ through

$$\boldsymbol{x}_{j+1/2} = \frac{\boldsymbol{x}_{j+1} + \boldsymbol{x}_j}{2}, \tag{2.50}$$

which can be used to compute the coefficients of an averaging matrix $\bar{\mathbf{M}}$ such that $\boldsymbol{X}^* = \bar{\mathbf{M}} \cdot \boldsymbol{X}$. Similarly the scheme for gradients at midpoints is

$$\left(\frac{\mathrm{d}\boldsymbol{x}}{\mathrm{d}z}\right)_{j+1/2} = \frac{\boldsymbol{x}_{j+1} - \boldsymbol{x}_j}{\Delta z}, \tag{2.51}$$

which determines the coefficients of a finite difference matrix $\bar{\mathbf{F}}$ such that $\mathrm{d}\boldsymbol{X}^*/\mathrm{d}z = \bar{\mathbf{F}} \cdot \boldsymbol{X}$.

The finite difference scheme converts the ODEs (2.49) into the algebraic system of $m(n-1)$ equations

$$\boldsymbol{G}_\epsilon(\boldsymbol{X}) \equiv \bar{\mathbf{F}} \cdot \boldsymbol{X} - \boldsymbol{G}_f(\bar{\mathbf{M}} \cdot \boldsymbol{X}) = 0 \tag{2.52}$$

that together with the m boundary conditions $\boldsymbol{g}_{bc}(\boldsymbol{X}) = 0$ can be solved for the n unknowns in $\boldsymbol{X}$. The system formed by $\boldsymbol{G}_\epsilon(\boldsymbol{X}) = 0$ and $\boldsymbol{g}_{bc}(\boldsymbol{X}) = 0$ is solved in MATLAB with the built-in Newton solver `fsolve` with function tolerance 10^{-5}. The two regularizing conditions [BC1] and [BC8], included in $\boldsymbol{g}_{bc}(\boldsymbol{X})$, are evaluated on the sonic and $u_{ze} = 0$ points taking their temporary positions at each iteration of the Newton method. To start the method, an initial guess has to be carefully selected close enough to the final solution to facilitate convergence of the solver. Convergence of the solution with the number of nodes is shown in figure 2.11 for several plasma parameters.

As aforementioned, sometimes it has been found convenient to have a fixed anode-sheath-edge density n_{eB} while freeing B_m. In this case, the equation

$$n_e(0) - n_{eB} = 0, \tag{2.53}$$

with given n_{eB}, is added to the system. The parameter B_m becomes an unknown and it is added to $\boldsymbol{X}$.

As already mentioned, the stationary problem considered here is a BVP on a system of non-linear ODEs, which is the same exact type of mathematical model as in previous works by Ahedo et al. [27, 36, 37]. In those papers, the stationary problem was numerically solved by integrating the regularized set of ODEs with a Runge-Kutta scheme, while using shooting techniques to match boundary conditions and ensure continuity of variables and derivatives across the sonic point. While still applicable to the present case, this approach becomes cumbersome when including azimuthal electron inertia due to the additional singularity on the $u_{ze} = 0$ point. For this reason, we opted for the finite-difference Newton-solver approach.

The MATLAB code implementing the method described in this Appendix has been doubly benchmarked, what gives confidence on the validity of the results presented. First, without the electron inertia term, solutions from the finite-difference approach have been verified to yield the same solution as the former Runge-Kutta shooting method in references [27, 36, 37]. And second, with EAI included and fixed operation conditions, solutions of the present stationary model have been successfully compared with stationary solutions from a time-dependent model [29].

This second verification case is specially interesting, since time-dependent models work with the absolutely different framework of partial differential equations (PDEs) and, thus, numerical methods used in this work can be hardly compared with those in, e.g., references [29, 71]. An evidence of the different mathematical nature of steady and time-dependent problems is that working with PDEs avoids the problem of dealing with internal singularities, which is one of the main challenges of the stationary model. Even if the two problems are mathematically different, when the same physics are considered, solutions from both the time-dependent [29] and stationary models are in excellent agreement.

Chapter 3

Fluid modelling of Hall-thruster discharges: Global stability

This Chapter reproduces the contents published in the peer-reviewed journal Plasma Sources Science and Technology [38]. The typography has been adapted to the style of this Thesis.

Abstract

Axial-azimuthal instabilities of a Hall-thruster plasma discharge are investigated using fluid model and a linear global stability approach, appropriate to the large axial inhomogeneity of the equilibrium solution. Electron pressure and electron inertia are considered in both the equilibrium and perturbed solutions. Fourier transform in time and azimuth are taken and the dispersion relation for the resultant Sturm-Liouville problem governing the axial behaviour of the modes is numerically obtained. The analysis, focused in mid-to-high frequencies and large wavenumbers identifies two main instability types. The dominant mode develops in the near plume at 1-5 MHz and azimuthal mode numbers $\sim$ 10-50, has a weak ion response and seems to be triggered by negative gradients of the magnetic field. The subdominant mode develops near the anode at 100-300 kHz and azimuthal mode numbers $\sim$ 1-10, and seems of the rotating-spoke type. Both instabilities are well characterized by investigating their oblique propagation, the influence of design and operation parameters, and the effects of anode-cathode electric connection, electron inertia, and temperature perturbations. The possible impact of these instabilities on electron cross-field transport is estimated through a quasilinear approach, which yields a spatially-rippled turbulent force.

3.1 Introduction

Instabilities and their role in electron cross-field transport is the main open problem in Hall-effect thruster (HET) discharges. Although oscillations modes within a large range of frequencies and wavevectors have been observed in experiments and simulations [82] there is not yet a fully established classification and characterization of them. Among all oscillation modes, azimuthal ones are potential candidates to contribute to cross-field transport through, at least, a net azimuthal electric force coming from correlated oscillations of plasma density and azimuthal electric field [1, 8].

Among the different lines of research, linear stability analyses provide the basic stage in order to identify the instability modes and characterizing them physically. Linear stability studies can be based on either kinetic or fluid formulations, and they can be local (generally limited to a given axial section of the HET discharge) or global (dealing with the whole extension of the discharge). Kinetically based studies are generally local, due to their high complexity, and, in the context of HET plasmas, lead to dispersion relations for the electron-cyclotron drift instability [3, 11, 83, 84] and the modified two-stream instability [85–87]. Fluid formulations are amenable to local and global studies and the modal families resulting are quite diverse. Global analyses, which take into account the large inhomogeneity of the plasma discharge, are more consistent and localize the regions where instabilities develop.

A stationary axial model of the inhomogeneous HET discharge [27, 46] was used by Escobar and Ahedo to carry out linear global stability studies at both low-frequencies (the 10-100 kHz range, say) and high-frequencies (the 1-10 MHz range, say), with azimuthal wavemodes of order unity [39, 40]. The papers included an extensive literature review on the subject, that we, thus, omit here. The low-frequency global analysis [39] was quite extensive: equilibrium and perturbation models kept all relevant terms, the central role of ionization instabilities was highlighted, as well as the relation with experimental evidence, and the comparison with a previous local analysis [50] was made.

The high-frequency global analysis [40], centred in the MHz range, was more limited in scope. First, several simplifications were applied to the perturbation model in order to recover the global dispersion relations of previous studies on Rayleigh and lower-hybrid instabilities by Litvak and Fisch [48] and Kapulkin et al. [88, 89]. Second, the analysis was limited to low azimuthal mode numbers. And third, electron pressure was ignored, which is now believed an important shortcoming inside the HET chamber. More recently, Sorokina et al. [42] discussed the existence of drift-gradient, near-anode modes using typical plasma-parameter profiles and a global dispersion relation that coincides with the collisionless limit of reference [40]

except for the treatment of the compressibility of the electron velocity field; both models ignore the electron pressure. Marusov et al. [90] apply the same logic as in references [40] and [42] to a magnetron-type geometry with a constant magnetic field. Romadanov et al. [91] have also discussed a global perturbation model aiming at the regimes of drift-gradient and lower-hybrid instabilities [13, 92]. The model has the peculiarity of being applied to a fully empirical equilibrium solution, where 7/8 of the domain corresponds to the external plume, and, similarly to references [40, 42, 90], the perturbation problem is simplified into a second-order differential equation for the electric potential perturbation.

The present work analyzes global fluid instabilities of the inhomogeneous HET discharge in the mid-to-high ranges of both frequency and azimuthal wavenumber, but always respecting the limits of validity of the multi-fluid formulation, i.e. frequencies and wavenumbers much smaller, respectively, than the electron gyrofrequency and the inverse of the electron gyroradius. Compared to the previously mentioned global analyses, the axial-azimuthal model considered here keeps fully the effects of: (i) the electron pressure, in order to cover both the subsonic and supersonic regions of the discharge; and (ii) the electron inertia, in order to assess their relevance in equilibrium and perturbation solutions, and turbulence-based forces. In references [40, 42, 90, 91], electron inertia was included directly as a small correction to the leading $E \times B$ drift velocity in the final mathematical model.

Several studies with non-linear particle-in-cell simulations are proposing the turbulent electric force generated by electron-drift kinetic instabilities as the main driver of the anomalous cross-field transport of electrons in HET discharges [1, 84, 93–95]. The fluid instabilities discussed here develop in a frequency range not far from the above kinetic ones. This has motivated us to consider the quasilinear extension of the global fluid model, based on estimating the quadratically correlated terms in the electron momentum equation, in order to speculate on the possible contribution to anomalous transport of the electric and inertia forces generated by those fluid instabilities.

The zeroth and first-order formulations of the axial-azimuthal model, and the equilibrium solution are presented in Sec. 2. The fluid model assumes quasineutrality except at the anode sheath. The inclusion of electron azimuthal inertia in the equilibrium solution is rather novel. Since the low frequency range is out of the scope here, neutral dynamics are disregarded in the first-order problem.

Sections 3 and 4 analyze the eigenvalues and eigenmodes of the global dispersion relation of a 'nominal model', with no electron inertia effects in equilibrium and no temperature perturbations. This case is very comparable with the majority of local analyses in the literature [13, 14, 51] and shows a manageable number of unstable branches. A dominant near-plume and a subdominant near-anode instabilities are

identified. The quasineutrality and axial-wavenumber spectrum of these instabilities are checked, and an investigation of design and operation parameters is conducted in order to assure the robustness of the characterization of these instabilities.

Section 5 investigates how the dispersion relation and the resulting eigenmodes are modified in 'off-nominal models', in particular when zeroth-order electron inertia is included or when electron temperature perturbations are allowed. Section 6 analyzes the dominant perturbation forces in the electron momentum equation and attempts to estimate the relevance of the instabilities studied here in the electron cross-field transport.

3.2 Model Formulation

A time-dependent, axial-azimuthal, fluid model of a Hall thruster is considered. Since the radial direction is excluded, plasma magnitudes will be in fact radially-averaged values, while the plasma interaction with radial walls is included as source terms in the axial-azimuthal model. In particular, for a generic vector variable $\boldsymbol{v}(z, y, t)$, its divergence will be expressed as

$$\nabla \cdot \boldsymbol{v} = \hat{\nabla} \cdot \boldsymbol{v} + v'_w, \qquad \hat{\nabla} \cdot \boldsymbol{v} = \frac{\partial v_y}{\partial y} + \frac{1}{A_c}\frac{\partial}{\partial z}\left(A_c v_z\right), \tag{3.1}$$

where: $y = R\theta$ is the azimuthal arc (with R the annular channel mid-radius), z is the axial coordinate, A_c is the cross-sectional area of the plasma beam, and v'_w is the radial wall contribution to magnitude $\boldsymbol{v}(z, y, t)$. As sketched in figure 3.1, the plasma domain goes from the anode A (at $z = 0$) to the chamber exit E (at $z = L_\mathrm{E}$) and the external cathode (at $z = L_\mathrm{N}$), which is treated here as an infinitely-thin source of electrons. This assumption decouples the current-free region downstream of the plume, which is here left out of the analysis. Since the radial direction is omitted, the plasma is quasineutral everywhere except at the infinitely-thin Debye sheath next to the anode, B being the sheath edge in figure 3.1.

The plasma is constituted of neutrals, singly-charged ions and electrons, with subscripts n, i, and e, respectively. The equations for the quasineutral plasma are based in previous works by Ahedo and co-workers [27]. Using conventional notation, they are the following:

$$\frac{\partial n_n}{\partial t} + \hat{\nabla} \cdot (n_n \boldsymbol{u}_n) = -n(\nu_p - \nu_w), \tag{3.2}$$

$$\frac{\partial n}{\partial t} + \hat{\nabla} \cdot (n \boldsymbol{u}_i) = n(\nu_p - \nu_w), \tag{3.3}$$

$$\frac{\partial n}{\partial t} + \hat{\nabla} \cdot (n \boldsymbol{u}_e) = n(\nu_p - \nu_w), \tag{3.4}$$

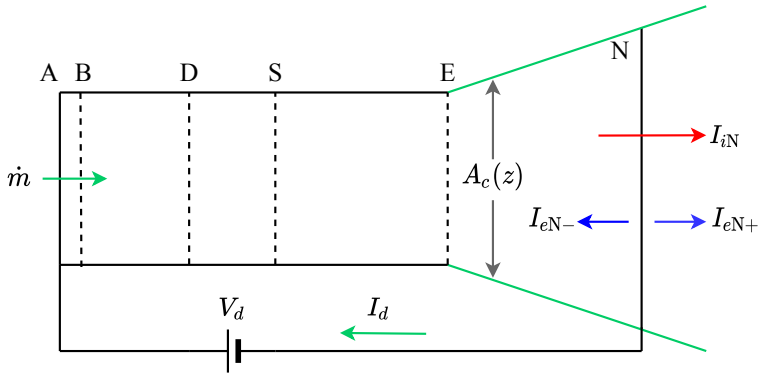

Figure 3.1: Schematic representation of the plasma discharge in a Hall thruster. $\dot{m}$ is the mass flow, V_d is the discharge voltage, I_d the discharge current, and $I_{i\mathrm{N}}$ is the ion current flowing downstream. The electron current flowing from anode A to neutralizer N, $-I_d$, splits into the downstream neutralizing current, $I_{\mathrm{N}+} = I_{i\mathrm{N}}$, and the upstream ionizing current $I_{e\mathrm{N}-} = I_d - I_{i\mathrm{N}}$. E is the chamber exit, B is the anode sheath edge, D is the ion stagnation point, and S is the ion sonic point. $A_c(z)$ is the effective cross-section area.

$$m_i n_n \left(\frac{\partial \boldsymbol{u}_n}{\partial t} + \boldsymbol{u}_n \cdot \nabla \boldsymbol{u}_n \right) = m_i n [\nu_w \left(\boldsymbol{u}_{nw} - \boldsymbol{u}_n \right) + \nu_{in} \left(\boldsymbol{u}_i - \boldsymbol{u}_n \right)] \tag{3.5}$$

$$m_i n \left(\frac{\partial \boldsymbol{u}_i}{\partial t} + \boldsymbol{u}_i \cdot \nabla \boldsymbol{u}_i \right) = -en\nabla\phi + m_i n \nu_i \left(\boldsymbol{u}_n - \boldsymbol{u}_i \right), \tag{3.6}$$

$$m_e n \left(\frac{\partial \boldsymbol{u}_e}{\partial t} + \boldsymbol{u}_e \cdot \nabla \boldsymbol{u}_e \right) = -\nabla \left(nT_e \right) + en \left(\nabla\phi - \boldsymbol{u}_e \times \boldsymbol{B} \right) - m_e n \nu_e \boldsymbol{u}_e, \tag{3.7}$$

$$\frac{\partial}{\partial t} \left(\frac{3}{2} n T_e \right) + \hat{\nabla} \cdot \left(\frac{5}{2} n T_e \boldsymbol{u}_e + \boldsymbol{q}_e \right) = \boldsymbol{u}_e \cdot \nabla \left(nT_e \right) - n\nu_p E_{\mathrm{inel}} - n\nu_{we} T_e + m_e n \nu_e u_e^2, \tag{3.8}$$

$$0 = \frac{5}{2} n T_e \nabla T_e + e\boldsymbol{q}_e \times \boldsymbol{B} + m_e \nu_e \boldsymbol{q}_e. \tag{3.9}$$

In equations (3.2)-(3.4): ν_p is the plasma production (i.e., ionization) frequency, and $n\nu_w$ is the source term for particle losses at radial walls. Equations (3.5)-(3.7) are a combination of the corresponding species momentum and particle conservation equations. In equation (3.5): $\boldsymbol{u}_{nw}$ is the effective neutral velocity from plasma recombination at lateral walls, ν_{in} is the frequency of charge-exchange collisions, and neutral pressure has been neglected. In equation (3.6): ϕ is the electrostatic potential, ion pressure and magnetization have been neglected, and $\nu_i = \nu_{in} + \nu_p$ is the total collision frequency for ions. In equation (3.7): $\boldsymbol{B}$ is the applied magnetic field and

$$\nu_e = \nu_{en} + \nu_{ei} + \nu_{wm} + \nu_t \tag{3.10}$$

is an effective collision frequency for electrons, which includes contributions from electron-neutral collisions (ν_{en}), electron-ion collisions (ν_{ei}), effective wall-collisionality (ν_{wm}), and turbulent transport (ν_t). In equation (3.8): E_{inel} is the effective ionization-plus-excitation energy cost per ionization event, and $n\nu_{we}T_e$

accounts for energy losses at lateral walls. The closure heat equation (3.9) for the electrons derives from Boltzmann equation [16], after assuming: negligible dynamical terms, Maxwellian distribution and a Krook collisional operator. Appendix A compiles the auxiliary models for all the collisionality terms included in the model. The effective cross-section area of the beam, A_c, is taken constant inside the channel and follows $\mathrm{d}A_c/\mathrm{d}z = 4\pi R(T_{eE}/m_i)^{1/2}/u_{zi}$ in the plume.

Azimuthal fluxes are considered relevant only for electrons, so that

$$\boldsymbol{u}_n = u_{zn}\mathbf{1}_z, \quad \boldsymbol{u}_i = u_{zi}\mathbf{1}_z, \quad \boldsymbol{u}_e = u_{ye}\mathbf{1}_y + u_{ze}\mathbf{1}_z,$$

and the electron heat flux is $\boldsymbol{q}_e = q_{ye}\mathbf{1}_y + q_{ze}\mathbf{1}_z$. The magnetic field is approximated as

$$\boldsymbol{B}(z) = \mathbf{1}_r \; B_m \exp\left[-\frac{(z-z_m)^2}{L_m^2}\right], \tag{3.11}$$

where z_m (generally at the thruster exit $z_m = L_\mathrm{E}$) is the location of the maximum field B_m, and L_m determines the rate of decay of the magnetic field in the thruster, which is generally different inside ($L_{m,\mathrm{in}}$) and outside ($L_{m,\mathrm{out}}$) the thruster.

Axial-azimuthal oscillatory modes in a Hall thruster discharge are studied as small perturbations of the axisymmetric equilibrium solution of the above model. Under this approach, the plasma variables are expressed as

$$\varphi(y,z,t) = \varphi_0(z) + \tilde{\varphi}_1(y,z,t), \tag{3.12}$$

where φ represents every plasma variable, φ_0 is the equilibrium part and $\tilde{\varphi}_1$ is the perturbation part, satisfying $|\tilde{\varphi}_1| \ll |\varphi_0|$. When expanding equations (3.2)-(3.8) in this way, the leading (or zeroth) order yields a system of ordinary differential equations that determines the axial equilibrium solution. The next order yields the set of linear perturbation equations with axially-varying coefficients, which depend on the equilibrium solution. Since the equilibrium solution is azimuthally homogeneous, the Fourier transform in both t and y of the perturbation equations can be taken, which is equivalent to write every first-order variable as

$$\tilde{\varphi}_1(z,y,t) = \mathrm{Re}\{\varphi_1(z,k_y,\omega)\exp\left(-\mathrm{i}\omega t + \mathrm{i}k_y y\right)\}, \tag{3.13}$$

where k_y is the real azimuthal wavenumber, $\omega = \omega_r + \mathrm{i}\gamma$ is the complex (angular) frequency, and $\varphi_1(z,k_y,\omega)$ is the complex amplitude of the perturbations, which keeps the axial dependence. Formally, due to azimuthal periodicity only integer mode numbers $k_y R$ can exist, but this restriction will add nothing relevant to the analysis hereafter.

3.2.1 Equilibrium solution

The stationary ($\partial/\partial t = 0$) axisymmetric ($\partial/\partial y = 0$) form of the set of equations (3.2)-(3.8), governing the plasma equilibrium solution, reads

$$-\frac{\mathrm{d}}{\mathrm{d}z}\left(A_c n_{n0} u_{zn0}\right) = \frac{\mathrm{d}}{\mathrm{d}z}\left(A_c n_0 u_{zi0}\right) = \frac{d}{dz}\left(A_c n_0 u_{ze0}\right) = A_c n_0 \left(\nu_p - \nu_w\right), \tag{3.14}$$

$$m_i n_{n0} u_{zn0} \frac{\mathrm{d}u_{zn0}}{\mathrm{d}z} = m_i n_0 \left[\nu_w \left(u_{znw} - u_{zn0}\right) + \nu_{in}\left(u_{zi0} - u_{zn0}\right)\right], \tag{3.15}$$

$$m_i n_0 u_{zi0} \frac{\mathrm{d}u_{zi0}}{\mathrm{d}z} = -e n_0 \frac{\mathrm{d}\phi_0}{\mathrm{d}z} + m_i n_0 \nu_i \left(u_{zn0} - u_{zi0}\right), \tag{3.16}$$

$$0 = -\frac{\mathrm{d}}{\mathrm{d}z}\left(n_0 T_{e0}\right) + e n_0 \frac{\mathrm{d}\phi_0}{\mathrm{d}z} + e n_0 u_{ye0} B - m_e n_0 \nu_e u_{ze0}, \tag{3.17}$$

$$m_e n_0 u_{ze0} \frac{\mathrm{d}u_{ye0}}{\mathrm{d}z} = -e n_0 u_{ze0} B - m_e n_0 \nu_e u_{ye0}, \tag{3.18}$$

$$\begin{aligned}\frac{\mathrm{d}}{\mathrm{d}z}\left(\frac{5}{2} n_0 T_{e0} u_{ze0} + q_{ze0}\right) = {} & u_{ze0}\frac{\mathrm{d}}{\mathrm{d}z}\left(n_0 T_{e0}\right) - n_0 \nu_p E_{\mathrm{inel}} - n_0 \nu_{we} T_{e0} \\ & + m_e n_0 \nu_e u_{e0}^2 - \left(\frac{5}{2} n_0 T_{e0} u_{ze0} + q_{ze0}\right)\frac{\mathrm{d}\ln A_c}{\mathrm{d}z},\end{aligned} \tag{3.19}$$

$$q_{ze0} = -\frac{5 n_0 T_{e0}}{2 m_e}\frac{\nu_e}{\nu_e^2 + \omega_{ce}^2}\frac{\mathrm{d}T_{e0}}{\mathrm{d}z}. \tag{3.20}$$

In equation (3.17), axial electron inertia has been discarded since it is always negligible. However, azimuthal electron inertia can be relevant and has been kept in equation (3.18). In equation (3.20), $\omega_{ce} = eB/m_e$ stands for the electron gyrofrequency and the azimuthal heat flow equation has been used in order to eliminate q_{ye0} from the system. The continuity equations (3.14) can be combined by pairs and integrated to yield

$$A_c m_i \left(n_{n0} u_{zn0} + n_0 u_{zi0}\right) = \mathrm{const} = \dot{m}, \tag{3.21}$$

$$A_c e n_0 \left(u_{zi0} - u_{ze0}\right) = \mathrm{const} = I_d, \tag{3.22}$$

being $\dot{m}$ and I_d, the total mass flow and the electric current flowing between anode and cathode, respectively. The discharge current is also the current flowing through the external anode-cathode circuit, since the plume downstream of point N is assumed current-free.

The rearrangement of the above ordinary differential problem, shows the possible existence of singularities at sonic points, defined by $u_{zi0} = \pm c_{s0}$, with $c_{s0} = \sqrt{T_{e0}/m_i}$. For instance, the equation for the derivative of the ion velocity reads

$$\left(T_{e0} - m_i u_{zi0}^2\right)\frac{\mathrm{d}u_{zi0}}{\mathrm{d}z} = G_0, \tag{3.23}$$

with

$$G_0 = T_{e0}\left(\nu_p - \nu_w\right) - u_{zi0}T_{e0}\frac{\mathrm{d}\ln A_c}{\mathrm{d}z} - eBu_{zi0}u_{ye0} + m_i\nu_i u_{zi0}\left(u_{zi0} - u_{zn0}\right) - \frac{2m_e}{5n_0T_{e0}}\frac{\nu_e^2 + \omega_{ce}^2}{\nu_e}u_{zi0}q_{ze0}. \quad (3.24)$$

The axial boundary conditions for the equilibrium problem are the following.

1. The total mass flow $\dot{m}$ injected at the anode is known.
2. The injection velocity of neutrals at the anode $u_{zn0\mathrm{A}}$ is known and the sheath is transparent for neutrals.
3. The ion velocity is backwards and sonic at the anode sheath edge, $u_{zi0\mathrm{B}} = -c_{s0\mathrm{B}}$.
4. The electric potential is set zero at the cathode, $\phi_{\mathrm{N}} = 0$.
5. Taking then $\phi_{0\mathrm{A}} = V_d$, the electric potential at the anode sheath edge is

$$\phi_{0\mathrm{B}} = V_d + \phi_{0\mathrm{AB}}, \quad \phi_{0\mathrm{AB}} = \frac{T_{e0\mathrm{B}}}{e}\ln\frac{\bar{c}_{e0\mathrm{B}}}{4|u_{ze0\mathrm{B}}|}, \quad (3.25)$$

   where $\bar{c}_e = \sqrt{8T_e/\pi m_e}$ is the electron thermal velocity.
6. The heat flux at the anode sheath edge is [37]

$$q_{ze0\mathrm{B}} = n_{0\mathrm{B}}u_{ze0\mathrm{B}}\left(e\phi_{0\mathrm{AB}} - \frac{1}{2}T_{0e\mathrm{B}}\right). \quad (3.26)$$

7. There is a regular forward sonic transition inside the channel, at an unknown location S, satisfying

$$u_{zi0\mathrm{S}} = c_{s0\mathrm{S}}, \qquad G_{0\mathrm{S}} = 0. \quad (3.27)$$

8. The temperature of injected electrons at the cathode N, $T_{e0\mathrm{N}}$, is known.
9. The electrons are emitted at N with null azimuthal velocity, i.e. $u_{ye0\mathrm{N}} = 0$.

Since V_d is an input, the discharge current I_d is an output. The opposite choice is valid too. The circuit boundary condition does not change the equilibrium solution but it does on the perturbation modes, as it will be shown later.

Table 3.1: Nominal simulation case parameters, based on a SPT-100-type Hall thruster, used in this work and defined in the main text. $A_{c,\mathrm{in}}$ is the chamber cross-section area.

$\dot{m}$	4.75 mg s^{-1}	V_d	300 V
B_m	251 G	z_m	2.5 cm
L_E	2.5 cm	L_N	3.35 cm
$A_{c,\mathrm{in}}$	40 cm^2	R	4.25 cm
$T_{e\mathrm{N}}$	5 eV	$u_{zn\mathrm{B}}$	300 m s^{-1}
$L_{m,\mathrm{in}}$	1.5 cm	$L_{m,\mathrm{out}}$	0.5 cm

The parameters of the nominal simulation case, based on previous works [39,40], are gathered in table 3.1. The resulting stationary solution is plotted in figure 3.2. The main features of this solution were thoroughly discussed in [27, 36, 37]. The only interesting novelty here is the inclusion of azimuthal electron inertia. This is motivated by consistency, since electron azimuthal inertia is known to be important in high-frequency, short wavelength perturbation modes, such as lower-hybrid oscillations [13, 96]. To assess the relevance of electron azimuthal inertia in the stationary solution, figure 3.2 plots the solution for two different models. First, there is Model 0A excluding the azimuthal electron inertia, when the electron azimuthal momentum equation (3.18) reduces to the algebraic relation

$$u_{ye0} = -\frac{\omega_{ce}}{\nu_e} u_{ze0}, \tag{3.28}$$

(and the ninth boundary condition above is not applied). Then, there is Model 0B, which includes the electron azimuthal inertia term. The comparison of Models 0A and 0B shows that, in Model 0B, unmagnetized electrons emitted from the cathode with zero azimuthal velocity adapt, within a thin region, to the solution of Model 0A. Also, close to the anode, the near singularity of $\mathrm{d}u_{ye0}/\mathrm{d}z$ makes u_{ye0} significantly lower when inertia is considered; this reduction near the anode affects u_{ze0} too. For the rest of regions and plasma variables, Models 0A and 0B yield practically the same solution.

Neglecting the small collisional contribution to the axial momentum equation (3.17), this states that azimuthal electron velocity is approximately the sum of the $E \times B$ and diamagnetic drifts,

$$u_{ye0} = -\frac{1}{B}\left[\frac{\mathrm{d}\phi}{\mathrm{d}z} + \frac{1}{en_0}\frac{\mathrm{d}p_{e0}}{\mathrm{d}z}\right] > 0.$$

Figure 3.2(g) shows that each of these contributions dominates in separated regions of the discharge and both yield an azimuthal current along $+y$ (notice that both drifts are negative only in regions where they are not dominant). The dominance

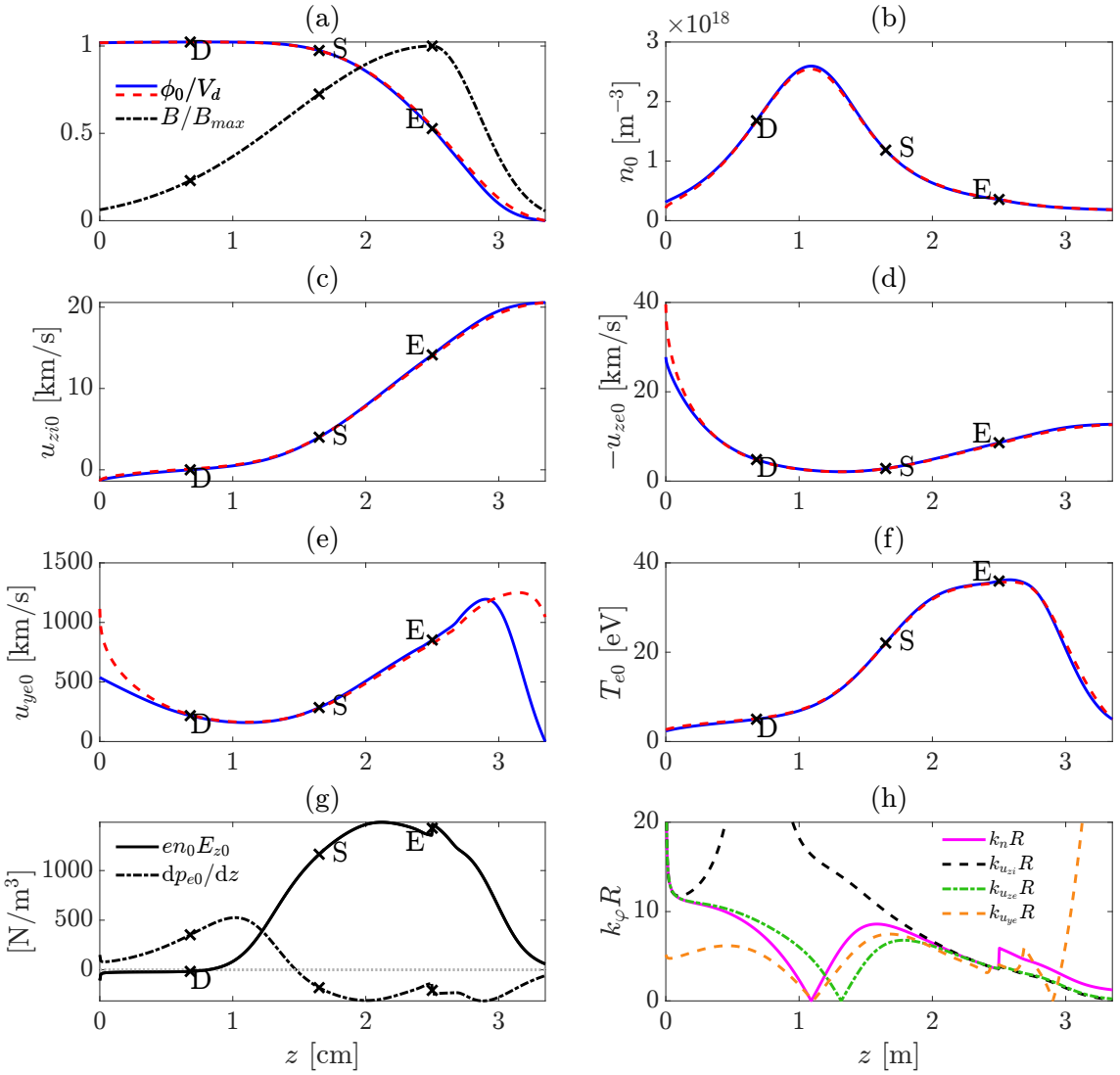

Figure 3.2: Stationary axial response of Model 0B for parameters in Table 3.1. Ion-stagnation (D), ion-sonic (S) and channel exit (E) are marked with crosses. Only $B(z)$ is an input, its maximum being at E. In (a)-(f), red dashed lines correspond to the inertialess-electron Model 0A. In (g): the two forces contributing to the azimuthal electron drift. In (h): relative gradient lengths of n, u_{zi}, u_{ze}, and u_{ye}.

of pressure gradients over the electric field in the inner part of the chamber, and the ion sonic transition there are two clear features highlighting the importance of electron pressure effects in a stability analysis of the global discharge.

A second aspect highlighting the importance of a global analysis is the high inhomogeneity of the equilibrium solution. Figure 3.2 (h) depicts the inverse of the local gradient length of main plasma magnitudes,

$$k_\varphi(z) = \left| \frac{1}{\varphi_0} \frac{\mathrm{d}\varphi_0}{\mathrm{d}z} \right| \tag{3.29}$$

for a generic plasma variable at equilibrium, φ_0. Leaving apart the singular behaviours near the anode sheath edge and the ion stagnation point ($u_{zi0} = 0$),

the plasma profiles have $k_\varphi R = O(10)$. A local stability analysis is fully justifiable only for perturbation modes with axial wavenumbers k_z satisfying the Boussinesq approximation $k_z R \gg k_\varphi R = O(10)$. Otherwise only the global analysis of stability is fully consistent.

In order to evaluate spatial and time scales in the perturbation modes, typical values of the equilibrium solution are: $n_{e0} \sim 10^{18}$ m^{-3}, $T_{e0} \sim 20$ eV, $B \sim 150$ G, ion sound velocity $c_{s0} \sim 3.8$ km s^{-1}, electron thermal velocity $\bar{c}_{e0} \sim 1900$ km s^{-1}, cyclotron frequency $f_{ce} = \omega_{ce}/2\pi \sim 400$ MHz, lower-hybrid frequency $f_{lh} \sim 0.86$ MHz, axial-transit frequency $f_z \sim u_{zi0}/2\pi L_{\rm N} \sim 90$ kHz, azimuthal transit frequency $f_\theta \sim u_{ye0}/2\pi R \sim 3.5$ MHz, Debye length $\lambda_{\rm D} \sim 33$ μm, and electron gyroradius $\ell_e \sim 720$ μm. This yields $R/\ell_e \sim 60$ and $\ell_e/\lambda_{\rm D} \sim 22$.

3.2.2 Linear perturbation model

As aforementioned, the evolution of small perturbations to an equilibrium plasma is governed by the first-order expansion of equations (3.2)-(3.8). Nonetheless, perturbations of collision frequencies have been ignored (which is not fully consistent in all cases), as well as, the perturbations of neutral variables (which is correct for the high-frequency range of interest here). Then, the first order equations for continuity and momentum of ions and electrons are

$$u_{zi0}\frac{\mathrm{d}n_1}{\mathrm{d}z} + n_0\frac{\mathrm{d}u_{zi1}}{\mathrm{d}z} = \left(\mathrm{i}\omega - \frac{\mathrm{d}u_{zi0}}{\mathrm{d}z} + \nu_p - \nu_w\right) n_1 - \frac{\mathrm{d}n_0}{\mathrm{d}z}u_{zi1} \equiv F_1, \tag{3.30}$$

$$u_{ze0}\frac{\mathrm{d}n_1}{\mathrm{d}z} + n_0\frac{\mathrm{d}u_{ze1}}{\mathrm{d}z} = \left(\mathrm{i}\omega - \mathrm{i}k_y u_{ye0} - \frac{\mathrm{d}u_{ze0}}{\mathrm{d}z} + \nu_p - \nu_w\right) n_1 - \frac{\mathrm{d}n_0}{\mathrm{d}z}u_{ze1} - \mathrm{i}k_y n_0 u_{ye1} \equiv F_2, \tag{3.31}$$

$$u_{zi0}\frac{\mathrm{d}u_{zi1}}{\mathrm{d}z} + \frac{e}{m_i}\frac{\mathrm{d}\phi_1}{\mathrm{d}z} = \left(\mathrm{i}\omega - \frac{\mathrm{d}u_{zi0}}{\mathrm{d}z} - \nu_i\right) u_{zi1} \equiv F_3, \tag{3.32}$$

$$u_{ze0}\frac{\mathrm{d}u_{ze1}}{\mathrm{d}z} + \frac{T_{e0}}{m_e n_0}\frac{\mathrm{d}n_1}{\mathrm{d}z} - \frac{e}{m_e}\frac{\mathrm{d}\phi_1}{\mathrm{d}z} + \frac{1}{m_e}\frac{\mathrm{d}T_{e1}}{\mathrm{d}z} = \left(\mathrm{i}\omega - \mathrm{i}k_y u_{ye0} - \frac{\mathrm{d}u_{ze0}}{\mathrm{d}z} - \nu_e\right) u_{ze1} + \frac{eB}{m_e}u_{ye1} + \frac{T_{e0}}{m_e n_0^2}\frac{\mathrm{d}n_0}{\mathrm{d}z}n_1 - \frac{1}{m_e n_0}\frac{\mathrm{d}n_0}{\mathrm{d}z}T_{e1} \equiv F_4, \tag{3.33}$$

$$u_{ze0}\frac{\mathrm{d}u_{ye1}}{\mathrm{d}z} = \left(\mathrm{i}\omega - \mathrm{i}k_y u_{ye0} - \nu_e\right) u_{ye1} - \left(\frac{\mathrm{d}u_{ye0}}{\mathrm{d}z} + \frac{eB}{m_e}\right) u_{ze1} - \mathrm{i}k_y\frac{T_{e0}}{m_e n_0}n_1 + \mathrm{i}k_y\frac{e}{m_e}\phi_1 - \mathrm{i}k_y\frac{1}{m_e}T_{e1}, \tag{3.34}$$

and the energy equations for electrons are

$$\frac{\mathrm{d}q_{ze1}}{\mathrm{d}z}+\frac{3}{2}u_{ze0}n_0\frac{\mathrm{d}T_{e1}}{\mathrm{d}z}+\frac{3}{2}u_{ze0}T_{e0}\frac{\mathrm{d}n_1}{\mathrm{d}z}+\frac{5}{2}n_0T_{e0}\frac{\mathrm{d}u_{ze1}}{\mathrm{d}z}=\left(\mathrm{i}\omega\frac{3}{2}T_{e0}-\mathrm{i}k_y\frac{3}{2}u_{ye0}T_{e0}\right.$$
$$\left.-\frac{3}{2}u_{ze0}\frac{\mathrm{d}T_{e0}}{\mathrm{d}z}-\frac{5}{2}T_{e0}\frac{\mathrm{d}u_{ze0}}{\mathrm{d}z}-\nu_pE_{\mathrm{inel}}-\nu_{we}T_{e0}+m_e\nu_eu_{ye0}^2\right)n_1$$
$$+\left(-\frac{3}{2}\frac{\mathrm{d}n_0T_{e0}}{\mathrm{d}z}+2m_e\nu_en_0u_{ze0}\right)u_{ze1}+\left(-\mathrm{i}k_y\frac{5}{2}n_0T_{e0}+2m_e\nu_en_0u_{ye0}\right)u_{ye1}$$
$$+\left(\mathrm{i}\frac{3}{2}\omega-\mathrm{i}k_y\frac{3}{2}u_{ye0}-\frac{3}{2}\frac{u_{ze0}}{n_0}\frac{\mathrm{d}n_0}{\mathrm{d}z}-\frac{5}{2}\frac{\mathrm{d}u_{ze0}}{\mathrm{d}z}-\nu_{we}-\frac{5}{2}\frac{T_{e0}}{m_e\nu_e}k_y^2\right)n_0T_{e1}$$
$$+\mathrm{i}k_y\frac{\omega_{ce}}{\nu_e}q_{ze1},\quad(3.35)$$

$$\frac{5}{2}n_0T_{e0}\frac{\mathrm{d}T_{e1}}{\mathrm{d}z}=-\frac{5}{2}T_{e0}\frac{\mathrm{d}T_{e0}}{\mathrm{d}z}n_1-\frac{5}{2}n_0\left(\frac{\mathrm{d}T_{e0}}{\mathrm{d}z}+\mathrm{i}k_y\frac{\omega_{ce}}{\nu_e}T_{e0}\right)T_{e1}$$
$$-m_e\frac{\nu_e^2+\omega_{ce}^2}{\nu_e}q_{ze1}\equiv F_5,\quad(3.36)$$

Under the limits of cold electrons (implying hypersonic ions) and

$$\mathrm{d}u_{zi0}/\mathrm{d}z,\ k_zu_{zi0},\ k_zu_{ze0}\ll\omega,\ k_yu_{ye0},\ \nu_e\ll\omega_{ce}$$

(with k_z an effective axial wavenumber) the mathematical complexity of the problem gets significantly reduced and the perturbation problem resembles the one by Escobar and Ahedo [40]. Furthermore, if electron collisions are assumed to be even smaller (i.e., $\nu_e\ll\omega, k_yu_{ye0}\ll\omega_{ce}$) the perturbation problem becomes collisionless and similar to that of Sorokina et al. [42].

The boundary conditions for the perturbation model are perturbations of those for the equilibrium problem, and are homogeneous for the stability analysis. They are the following.

1. The ion velocity satisfies the Bohm condition at B,

$$u_{zi1\mathrm{B}}=-\frac{c_{s0\mathrm{B}}}{2T_{e0\mathrm{B}}}T_{e1\mathrm{B}}=-\frac{1}{2m_ic_{s0\mathrm{B}}}T_{e1\mathrm{B}}.\quad(3.37)$$

   As it will be shown, the first-order problem is singular at the anode-sheath edge. This condition ensures the validity of the small-perturbation assumption close to the anode singularity [97]. The numerical solution of the perturbation problem verifies that this is required for moderate growths of perturbations around B and for good convergence behaviour with a suitable number of grid points.

2. The potential perturbation is zero at the anode, $\phi_{1\mathrm{A}} = 0$. Then, assuming an instantaneous response of the anode sheath to perturbation, the linearized sheath potential-fall condition yields

$$\phi_{1\mathrm{B}} = \phi_{1\mathrm{A}} + \left(\frac{e\phi_{0\mathrm{AB}}}{T_{e0\mathrm{B}}} + \frac{1}{2}\right)\frac{T_{e1\mathrm{B}}}{e} - \frac{T_{e0\mathrm{B}}}{eu_{ze0\mathrm{B}}}u_{ze1\mathrm{B}}. \tag{3.38}$$

3. The heat flux at the sheath edge satisfies

$$\begin{aligned} q_{ze1\mathrm{B}} = &\left(e\phi_{0\mathrm{AB}} - \frac{1}{2}T_{e0\mathrm{B}}\right)u_{ze0\mathrm{B}}n_{1\mathrm{B}} \\ &+ \left(e\phi_{0\mathrm{AB}} - \frac{3}{2}T_{e0\mathrm{B}}\right)n_{0\mathrm{B}}u_{ze1\mathrm{B}} + \frac{e\phi_{0\mathrm{AB}}}{T_{e0\mathrm{B}}}n_{0\mathrm{B}}u_{ze0\mathrm{B}}T_{e1\mathrm{B}}. \end{aligned} \tag{3.39}$$

4. A regularizing boundary condition at point S is required to ensure smooth behaviour close to the sonic point, similarly to the equilibrium problem. The system of first order fluid equations written in the form of equations (3.30)-(3.36) hides the role played by sonic points in the model. From equations (3.30)-(3.33) and (3.36), the derivative of u_{zi1} satisfies

$$n_0\left(T_{e0} - m_i u_{zi0}^2\right)\frac{\mathrm{d}u_{zi1}}{\mathrm{d}z} = G_1,$$

$$G_1 = T_{e0}F_1 + m_e u_{ze0}u_{zi0}F_2 - n_0 u_{zi0}\left(m_i F_3 + m_e F_4 - \frac{2}{5}\frac{F_5}{n_0 T_{e0}}\right),$$

where $u_{ze0} \ll \bar{c}_{e0}$ was used, and functions F_1 to F_5 are defined in equations (3.30)-(3.33) and (3.36), respectively. Thus

$$G_{1\mathrm{S}} = 0 \tag{3.40}$$

is required to avoid a singularity at the zeroth-order interior sonic point in the perturbation problem (the anode-sheath edge is, however, singular). The interior sonic point of the perturbed plasma is shifted with respect to the zeroth-order position [97] but this displacement is not needed to solve the perturbation problem and can be computed in post-processing.

5. The perturbation of the discharge current is zero at the cathode,

$$I_{d1\mathrm{N}} \equiv A_{c\mathrm{N}}e\left[(u_{zi0\mathrm{N}} - u_{ze0\mathrm{N}})n_{1\mathrm{N}} + n_{0\mathrm{N}}u_{zi1\mathrm{N}} - n_{0\mathrm{N}}u_{ze1\mathrm{N}}\right] = 0. \tag{3.41}$$

The alternative case of zero perturbation of the cathode potential, $\phi_{1\mathrm{N}} = 0$, will be treated later too.

6. The azimuthal electron velocity perturbation is zero at the cathode, $u_{ye1\mathrm{N}} = 0$.

7. The temperature of electrons injected at N is known, yielding $T_{e1\mathrm{N}} = 0$.

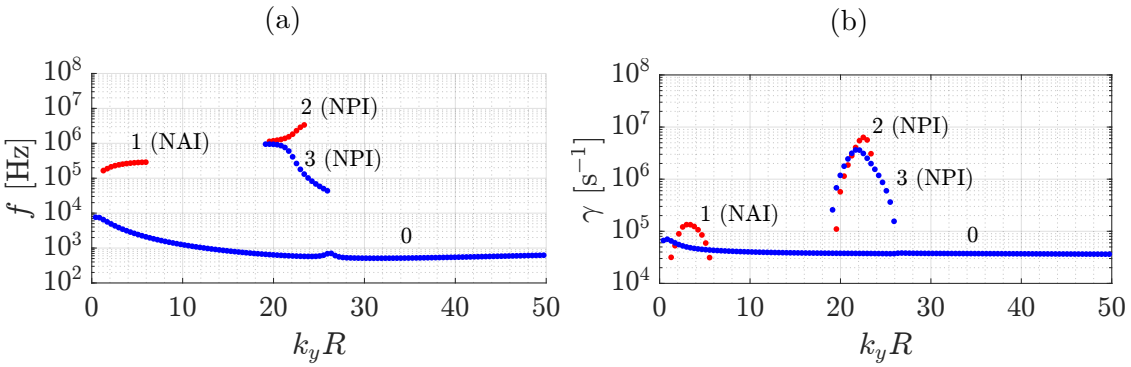

Figure 3.3: Nominal model. Main eigenvalues of global dispersion relation. Each unstable branch is tagged with a number and an instability type. Red and blue colours denote propagation along $+y$ and $-y$, respectively.

For a given equilibrium solution, the parameters of the linear perturbation problem (defined in the complex plane) are the real wavenumber k_y and the complex frequency $\omega \equiv \omega_r + \mathrm{i}\gamma$. For each k_y, the problem admits eigenvalues ω and eigenmodes (i.e. non-trivial solutions) in the form of the perturbation magnitudes $\varphi_1(z, k_y, \omega)$ in equation (3.13). Eigenmodes with $\gamma > 0$ are unstable. Modes with phase velocity $\omega_r/k_y > 0$ propagate in the $+u_{ye0}$ (i.e $+y$) direction. It is enough to analyze the parametric region $k_y > 0$ since, as demonstrated in Appendix 3.B, the region $k_y < 0$ yields the same perturbation modes. The numerical method to solve this eigenvalue (or Sturm-Liouville) problem is explained in the Appendix 3.C.

3.3 Near-plume and near-anode instabilities

Stability results will be hereafter analyzed for several simulation settings. This and next section discuss a, say, *nominal model* (or Model I) consisting of (i) the stationary, inertialess-electron Model 0A, and (ii) the perturbation model with zero electron temperature perturbations (i.e. $T_{e1} = 0$), thus consisting of equations (3.30)-(3.34), and (iii) the perturbed boundary conditions defined before. Parameters of table 3.1 will be used, except in sections 3.4.3 and 3.4.4, devoted to parametric investigation where the effects of varying the magnetic field slope, the discharge voltage, the mass flow and the channel length, are analyzed. Three off-nominal models (II, II, and IV) are defined and discussed in Section 3.5.

In Sturm-Liouville problems, such as the present one, the number of eigenvalues of the global dispersion relation can be, in principle, infinite. The interest is, of course, in the most unstable modes. The instability analysis here will be centred in unstable modes with: (real) frequencies $f = |\omega_r|/2\pi \sim 0.5 - 50$ MHz, well below

the electron gyrofrequency ($\omega_{ce}/2\pi \sim 400$ MHz); and azimuthal mode numbers $k_y R < 50$ (i.e azimuthal wavelengths down to $\lambda_y \equiv 2\pi/k_y \sim 5$ mm), also within the applicability range of the present fluid formulation.

The unstable solutions of the dispersion relation for the nominal model are plotted in figure 3.3. There are up to 3 families of high-frequency unstable modes plus a low-frequency ($f \sim 7.5$ kHz) unstable family. This last one [branch 0 in figure 3.3] is characterized by intense density oscillations in the ionization region, which correspond to the breathing and rotating-spoke modes of Ref. [39] but incompletely characterized in the present mid-to-high frequency model (which neglects neutral density perturbations). Hereafter that low-frequency mode will be omitted from figures and discussions.

Then, in the range $f > 100$ kHz of interest, there are three branches of unstable modes. Based on the region where these modes develop preferentially, they are named Near-Anode Instability (NAI) [branch 1 in figure 3.3] and Near-Plume Instability (NPI) [branches 2 and 3]. Figure 3.3 states that the global perturbation response of the nominal model is dominated by the NPI mode in branch 2 with $k_y R = 23$ (i.e. $\lambda_y = 1.16$ cm) and $f = 2.87$ MHz. In addition, the NAI mode of branch 1 with $k_y R = 3$ (i.e. $\lambda_y = 8.90$ cm) and $f = 241$ kHz is considered a subdominant mode, since it develops in a different region of the discharge and thus can still be present in the long-time response. Branch 3 is just a second NPI mode, likely overshadowed by branch 2 in the long-time response.

3.3.1 The subdominant Near-Anode Instability

The NAI in figure 3.3 presents low azimuthal mode numbers, $k_y R = 1.3$-6.0 ($\lambda_y \sim 4.4$-21 cm), and mid-frequencies $f = 160$-290 kHz. Instantaneous 2D spatial profiles of the main NAI mode ($k_y R = 3$) are shown in figure 3.4. The plots represent perturbation solutions, i.e. the eigenmodes defined in equation (3.13). They scale linearly with, say,

$$\tilde{\phi}_{1,\max} = \max\{\tilde{\phi}_1(y,z,t)\}\ \forall y,z. \tag{3.42}$$

which has been set to equal to 1 volt in figure 3.4.

It is clearly observed that the NAI develops mainly in the near-anode region (from B to D in figure 3.2), but some remnants are observed in the rest of the discharge, in particular for $\tilde{\phi}_1$ around the thruster exit E. Azimuthally, the NAI propagates with an azimuthal phase velocity $\omega_r/k_y = 21.5$ km/s for $k_y R = 3$ in the $+u_{ye0}$ direction; remind that this velocity is a diamagnetic drift near the anode. The axial propagation of the NAI is not identical for all plasma variables as the change of inclination of the wavefronts in figure 3.4 illustrates. A Fast Fourier transform

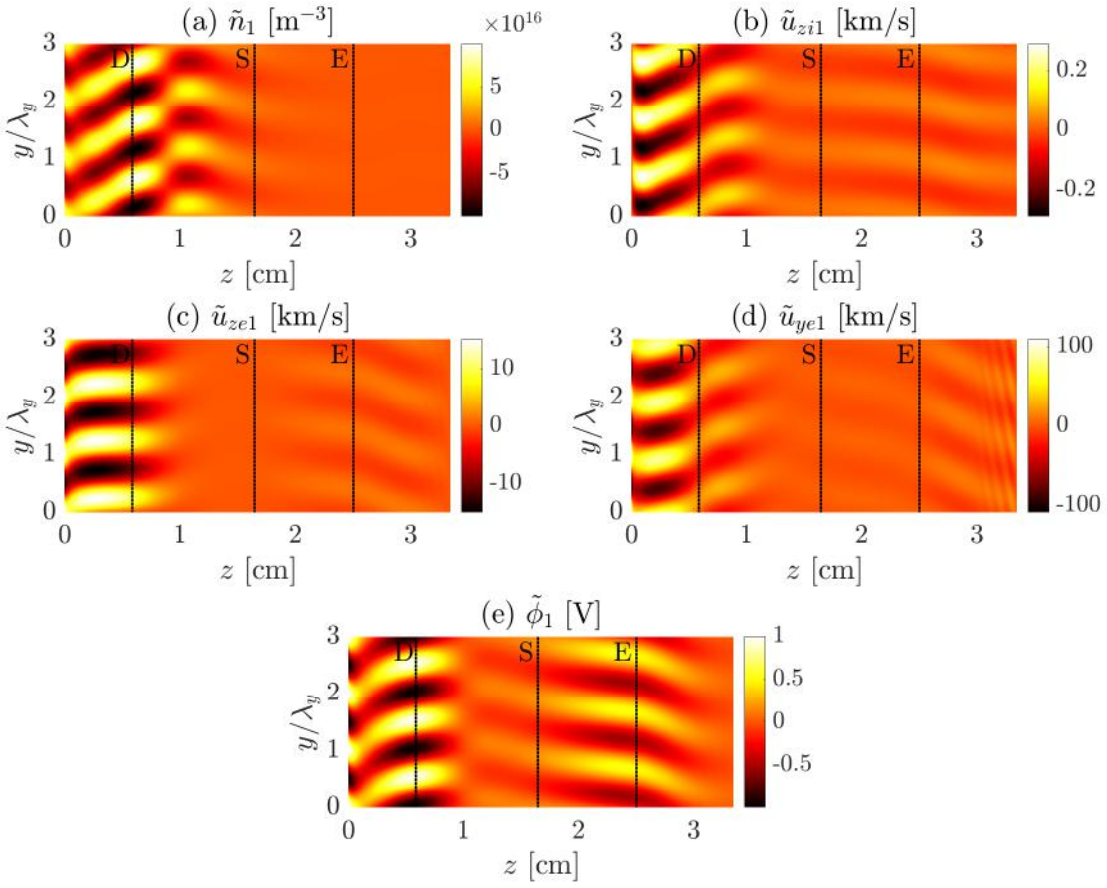

Figure 3.4: Nominal model. Instantaneous spatial response for the subdominant NAI mode, with $k_y R = 3$ (i.e. $\lambda_y = 8.90$ cm) and $f = 241$ kHz. In this and similar figures, only three azimuthal wavelengths are plotted; which in this specific case coincide with the azimuthal length $2\pi R$. Perturbations amplitudes correspond to $\tilde{\phi}_{1,\max} = 1$ volt.

(FFT) analysis discussed later will identify the main axial wavenumbers k_z of the perturbed variables. Near the anode, $\tilde{n}_1$, $\tilde{u}_{zi1}$, and $\tilde{\phi}_1$ propagate axially outwards (i.e., the dominant term in the FFT has $k_z < 0$), while electron velocities do not propagate. Around the chamber exit, the propagation of $\tilde{\phi}_1$ has changed and is directed towards the plume (i.e. $k_z > 0$).

The high-frequency global analysis by Sorokina et al. [42] discusses the existence of a near-anode modes with $k_y R$ from 1 to 5, frequencies of 260-670 kHz and propagation in the $+u_{ye0}$ direction. There are however differences with the present case, that could be related to model limitations (some of them also common to the global models of [40] and [90]), such as the lack of pressure forces on both the equilibrium and perturbation problems and the assumption of marginal electron inertia effects. Also, the local analysis by Marusov et al. [98] predicts near-anode instabilities within similar frequency range and suggests that pressure force has a non-negligible impact on the resultant wavelengths, frequencies and growth rates of

the unstable modes.

Rotating-spoke instabilities are also near-anode oscillations propagating in the $+u_{ye0}$ direction with similar λ_y but generally at frequencies below 100 kHz [8, 99]. An exception are rotating spokes with $f \sim$ 79-210 kHz observed in a cylindrical HET [100]. This discrepancy with respect to experimentally observed frequencies of near-anode modes was already noted in reference [42]. The formation of wave packets with a reduced envelope frequency, when unstable modes with similar ω_r and γ co-exist, was identified as a possible explanation.

3.3.2 The dominant Near-Plume Instability

For the nominal model, figure 3.3 shows that the main NPI branch [number 2 in figure 3.3] develops at higher mode numbers and frequencies than the NAI. It has $k_y R \sim$ 19-23 (i.e., $\lambda_y \sim$ 1.40-1.16 cm), and $f \sim$ 1.1-3.3 MHz. The azimuthal propagation is along $+u_{ye0}$, which is now due to the $E \times B$ drift. Instantaneous 2D spatial profiles of the dominant NPI mode, with $k_y R \sim 23$ and $f = 2.87$ MHz (thus, $\omega/k_y \simeq 45.9$km/s) are shown in figure 3.5. The oscillations develop almost exclusively in the near plume, which coincides here with the region having $\mathrm{d}B/\mathrm{d}z < 0$. Concerning the direction of propagation of the waves, $\tilde{n}_1$ and $\tilde{u}_{zi1}$ propagate obliquely inwards (i.e. with positive k_z). The propagation of $\tilde{\phi}_1$, $\tilde{u}_{ze1}$ and $\tilde{u}_{ye1}$ is azimuthal. For $\tilde{u}_{ye1}$, there is an abrupt change of phase, close to 180°, at the mid-plume. This event takes place when $\mathrm{d}\tilde{\phi}_1/\mathrm{d}z$ changes sign, due to the inversion of the azimuthal $E \times B$ drift component in the perturbation problem. Additionally, $\tilde{u}_{ye1}$ presents small-amplitude short-wavelength axial waves.

The NPI modes of branch 3 in figure 3.3 propagate azimuthally along $-y$. Since they develop in the same discharge region of branch 2 with a smaller γ they will not be observed in the long-term perturbed plasma response, so they are dropped from the discussion here.

The NAI and NPI modes present interesting differences on the relative perturbations of the different plasma magnitudes. First, $\tilde{n}_1/\tilde{\phi}_1$ and $\tilde{u}_{zi1}/\tilde{\phi}_1$ decrease by two orders of magnitudes from the NAI to the NPI, suggests that the NPI is mainly an 'electron mode'. Second, $\tilde{n}_1/n_0 \ll e\tilde{\phi}_1/T_{e0}$ for the NPI mode, which has consequences on fulfilling quasineutrality (see Sec. 3.4.1). Third, while the NAI has $\tilde{u}_{ze1} \ll \tilde{u}_{ye1}$, the NPI has $\tilde{u}_{ze1} \sim \tilde{u}_{ye1}$, implying that $\tilde{u}_{ze1}/u_{ze0} \gg \tilde{u}_{ye1}/u_{ye0}$, so that the perturbed axial electron inertia is as relevant as the azimuthal one for the NPI mode (see Sec. 3.6.1).

The development of oscillations in the discharge region where $\mathrm{d}B/\mathrm{d}z < 0$ suggest a connection of the (global) NPI with (local) high-frequency drift-gradient

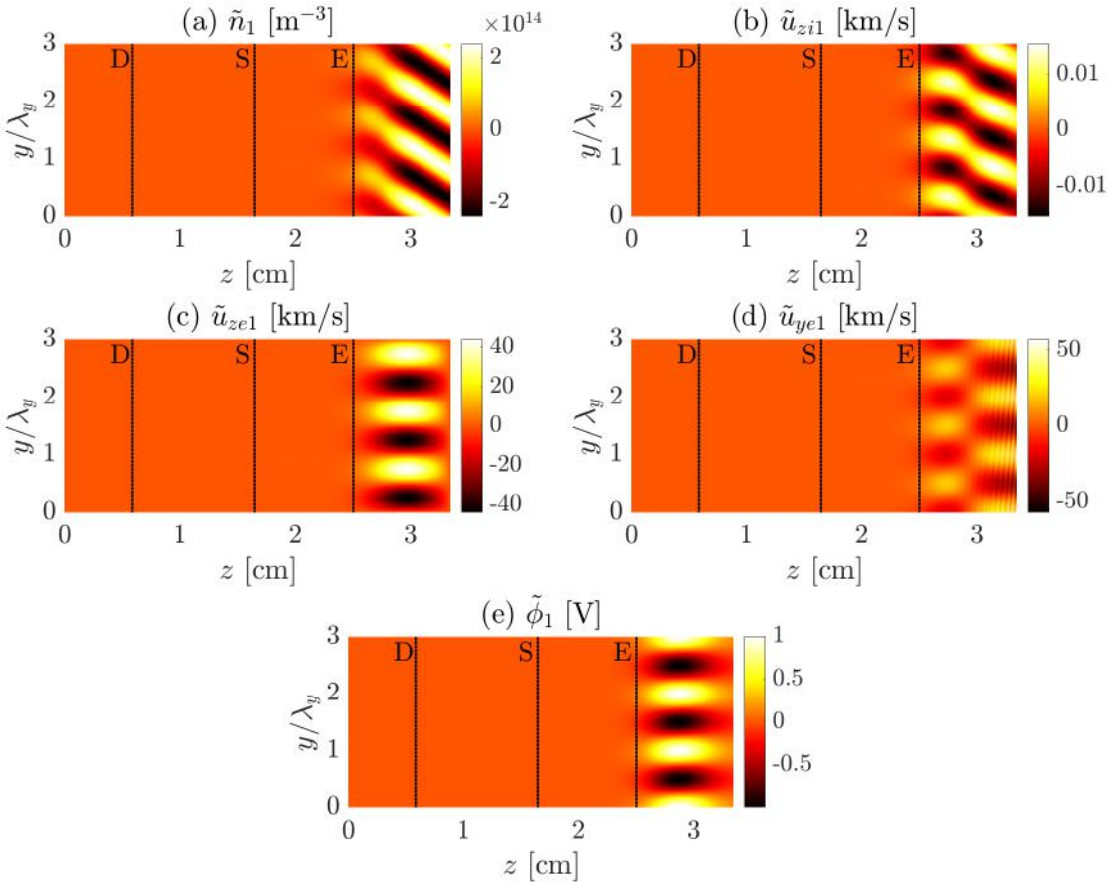

Figure 3.5: Nominal model. Instantaneous spatial response for the dominant NPI mode: $k_y R = 23$ (i.e. $\lambda_y = 1.16$ cm) and $f = 2.87$ MHz.

instabilities [13, 51, 98], originally analyzed by Esipchuk and Tilinin [96]. The dispersion relation for these waves points at density and magnetic gradients as the main instability mechanisms. In the local stability analyses, the values of $\mathrm{d}B/\mathrm{d}z$ and $\mathrm{d}n_0/\mathrm{d}z$ leading to instabilities do not follow simple criteria and depend on the model assumptions and other local properties of the plasma. For example, the local analysis by Marusov et al. [98] shows near-plume drift-gradient modes, within the wide frequency range 0.01-12.16 MHz, that are only unstable when accounting for finite electron temperature. The effect of the magnetic field shape on the NPI modes is further investigated later.

Finally, counter-propagating azimuthal oscillations have been observed in some empirical results in the literature [101], which resemble the main and secondary NPI modes here. These observations have been made in the frequency range 0.9-6 MHz, but in the context of the electron-cyclotron drift instability. The azimuthal scales are smaller, generally satisfying $k_y \ell_e \geq O(1)$, outside the range of analysis of the fluid models here.

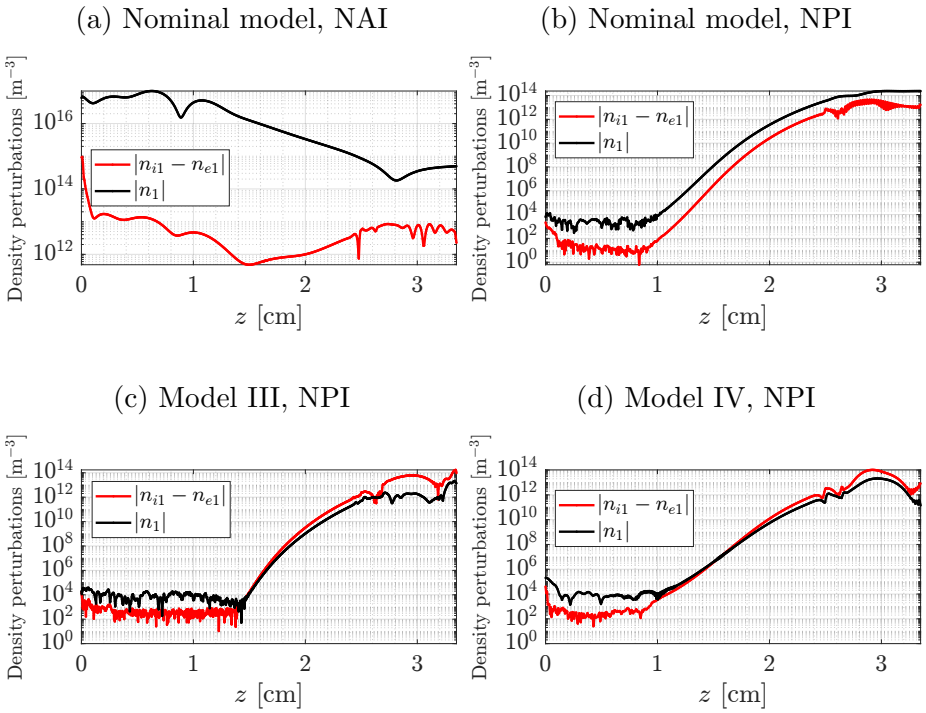

Figure 3.6: Assessment of quasineutrality in main instability modes. (a) Subdominant NAI in nominal model. (b) Dominant NPI in nominal model. (c) Dominant NPI in Model III, having $k_y R = 37.4$ and $f = 27.2$ MHz. (d) Dominant NPI in Model IV, having $k_y R = 25.1$, $f = 14.2$ MHz. The noise in the electric charge is due to the numerical second derivative of ϕ_1 used for its computation.

3.4 Further investigation of the NAI and NPI instabilities

This section analyzes more in detail the characteristics of the NAI and NPI modes for the nominal model.

3.4.1 Plasma quasineutrality

The perturbation model has assumed the zero-Debye length limit, so perturbations are quasineutral except in the perturbed anode sheath. Once the solution is known, the level of compliance with quasineutrality can be assessed. The perturbed Poisson equation allows to estimate the charge separation as

$$e\left(n_{i1} - n_{e1}\right) = \varepsilon_0 \left(k_y^2 \phi_1 - \frac{\mathrm{d}^2 \phi_1}{\mathrm{d}z^2}\right), \tag{3.43}$$

and to compare it with the quasineutral estimated charge density, en_1. A value of λ_D, based on n_0 and T_{e0}, very small compared to any other characteristic length

of the problem is enough to ensure the validity of the quasineutral assumption in the equilibrium solution. For the k_yR range considered in this work, $k_y\lambda_D$ is always very small. However, in the first-order problem, and assuming $k_z \leq O(k_y)$, quasineutrality requires

$$k_y\sqrt{\varepsilon_0\phi_1/en_1} \ll 1, \tag{3.44}$$

which is a more severe condition than $k_y\lambda_D \ll 1$ when $n_1/n_0 \ll e\phi_1/T_{e0}$, a situation happening for the dominant NPI.

For the NAI and the NPI modes of the nominal model, figure 3.6 (a) and (b) plot both $(n_{i1} - n_{e1})$ and n_1, showing that $|n_{i1} - n_{e1}| \ll |n_1|$, thus validating the modes are quasineutral. However, figures 3.6(c)-(d) for off-nominal models discussed in section 3.5, will show that the dominant NPI modes present non-neutral effects, which should be included in the global perturbation model. That inclusion is far from immediate since the perturbation model is built upon a stationary solution which is quasineutral, except for the anode sheath.

3.4.2 Axial wavenumbers

A standard *local* stability analysis solves the complex eigenfrequency for given azimuthal and axial wavenumbers, that is $\omega(k_y, k_z)$. The present global stability analysis provides the complex eigenfrequency for each azimuthal wavenumber $\omega(k_y)$ and the complex eigenmodes as functions of z. These eigenmodes do not correspond generally to normal modes with a single k_z. Indeed, the analysis of the NAI and the NPI in figures 3.4 and 3.5, respectively, showed that the axial propagation is dependent on both the variable and the region within the discharge.

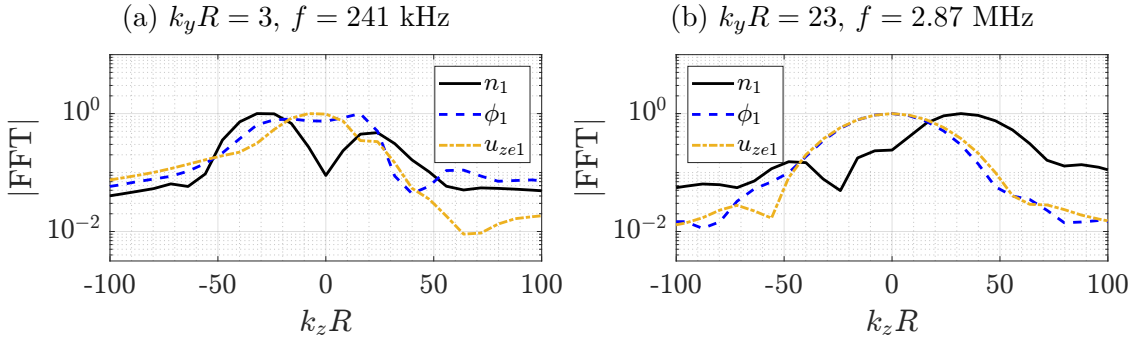

Figure 3.7: Nominal model. Axial wavenumbers of n_1, ϕ_1 and u_{ze1} from the (normalized) axial FFT of the perturbed solution, for (a) the subdominant NAI mode and (b) the dominant NPI mode.

The dominant axial wavenumbers of the instability modes can be obtained from

the axial FFT. The k_zR-spectrum goes from a minimum of $2\pi R/L_{\rm N} \simeq 8$ to a maximum of $\pi R/\Delta z \approx 4000$, where $\Delta z \approx L_{\rm N}/1000$ is the cell size used here to solve the Sturm-Liouville problem. The axial FFTs of the modes of figures 3.4 and 3.5 are plotted in figure 3.7. The FFTs are done on complex amplitudes and yield, in general, nonsymmetrical spectra on k_z for each k_y. The sign of the dominant k_z determines the principal direction of axial propagation. The FFTs in figure 3.7 for each global mode show that the dominant k_z is different for several perturbation variables. The trends already identified in figures 3.4 and 3.5 are confirmed here: for the NAI, the negative oblique propagation of $\tilde{n}_1$, the positive and negative oblique propagations of $\tilde{\phi}_1$, and the purely-azimuthal propagation of $\tilde{u}_{ze1}$; for the NPI, the positive oblique propagation of $\tilde{n}_1$, a secondary high-k_z mode on electron velocities (out of the k_zR limits of the figure), etcetera. The comparison of figures 3.2(h) and 3.7, yields that the Boussinesq approximation, $k_z \gg k_\varphi$, that could justify a local axial analysis, is not satisfied.

3.4.3 Influence of the magnetic field slope

The previous analysis has shown that the NPI develops only outside point E, which, for the chosen configuration, is both the thruster chamber exit and the location of the maximum magnetic field. In this subsection the location of B_m is shifted away from the chamber exit (still point E) in order to elucidate whether the change of the plasma jet area and collisionality or, more likely, the slope of $B(z)$ are driving the NPI. All the equilibrium plasma variables are recomputed in every case according to the equilibrium equations in section 3.2.1. Figure 3.8 shows the dominant NPI mode for two magnetic profiles with $z_m = 1.5$ cm, i.e. 1 cm inwards of E. The left case keeps constant the axial decay length $L_{m,\rm out}$, and the right one smooths that decay. The corresponding dominant NPI modes have (k_yR, f) equal to (25.1, 2.36 MHz) and (15.3, 1.46 MHz), respectively. In the first row, together with $B(z)$, $u_{ye0}(z)$ is depicted, showing a maximum to the right of z_m. The other three rows plot the perturbation solution for the dominant NPI mode showing that while $\tilde{n}_1$ and (unplotted) $\tilde{u}_{zi1}$ oscillations spread all over the $\mathrm{d}B/\mathrm{d}z < 0$ region, the electron-related oscillations are bounded approximately between the maxima of $B(z)$ and and $u_{ye0}(z)$. The eigenvalue spectrum of the case with the slowest decay of $B(z)$ (unplotted), shows a significant shift of the NPI to smaller wavelengths $k_yR \sim$ 13-19. The behaviour of the NPI under variations of $B(z)$ reinforces the idea that these modes are strongly related with $\mathrm{d}B/\mathrm{d}z$ being negative. Local fluid instabilities, in the same order of frequencies, driven by negative gradients of B (and n_0) were studied by Esipchuk and Tilinin [96] and have been recently revisited by several authors [13, 51].

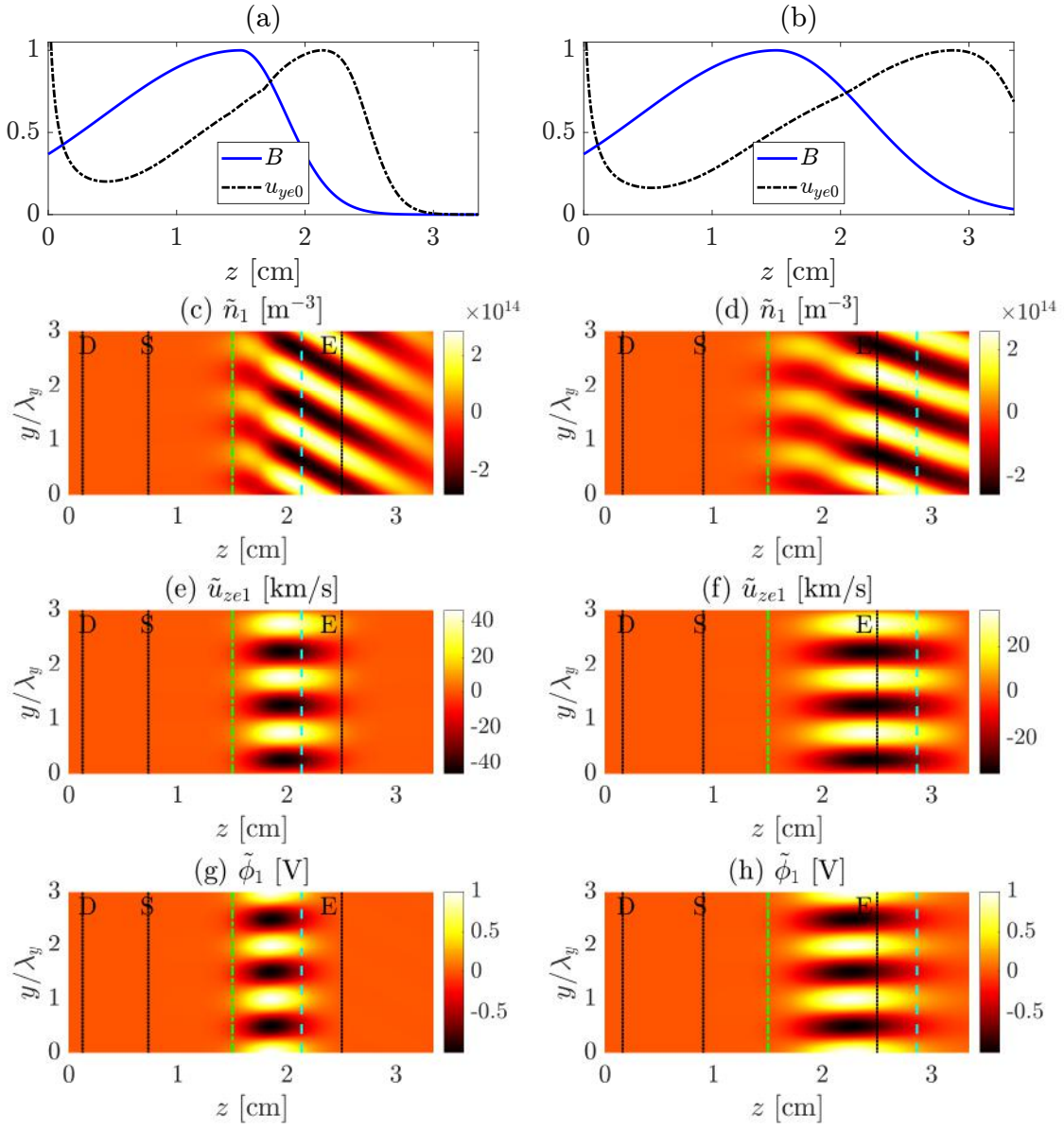

Figure 3.8: Nominal model. Variation of the magnetic field profiles. In left plots, the magnetic field has $(z_m, L_{m,\text{out}}) = (1.5 \text{ cm}, 0.5 \text{ cm})$, and the dominant NPI eigenmode has $(k_y R, f) = (25.1, 2.36 \text{ MHz})$. In right plots, one has $(z_m, L_{m,\text{out}}) = (1.5 \text{ cm}, 1 \text{ cm})$ and $(k_y R, f) = (15.3, 1.46 \text{ MHz})$. First row: Axial profiles of B and the stationary azimuthal electron velocity. Rows 2 to 4: instantaneous profiles of the dominant mode. Green dash-dotted and cyan dashed vertical lines indicate the locations of the maxima of B and u_{ye0}, respectively.

3.4.4 Investigation of operation and geometrical parameters

In order to check the dependence of the NAI and NPI on the zeroth-order solution, the perturbation problem is solved for different equilibrium solutions, obtained by modifying discharge voltage, mass flow, or channel length. In order to have in each case an optimal magnetic strength (with the plasma well attached to the anode) the maximum amplitude of the magnetic field is tuned according to conditions of reference [46]. In each case, the rest of parameters are as in table 3.1.

Figure 3.9 (top row) plots the influence of the discharge voltage, through cases $V_d = 200$ V, 300 V and 700 V. The NAI is favoured by a low V_d, when its range of $k_y R$ is wider and the growth rate is larger; its frequency increases slightly with V_d. The NAI is practically absent for $V_d = 700$ V. As suggested before, those features are typical of rotating spoke instabilities, as reported experimentally [102] and numerically [39]. With respect to the NPI modes, as V_d increases, there is a shift on $k_y R$ toward higher wavenumbers but both the amplitude of the $k_y R$-range and the maximum growth rate do not change practically. The frequency increases slightly with V_d, which agrees with empirical evidence on high-frequency oscillations in Hall thrusters [103].

Figure 3.9 (middle row) plots the influence of the mass flow rate, simulating three different flows. For the NAI, the $k_y R$ range is very sensitive to $\dot{m}$: at low values, the NAI disappears; at high values, the range becomes wide and can even overlap the one of the NPI. At low mass flows, the frequency of the oscillations decreases mildly. Similar trends were identified in reference [39] for rotating spokes due to the displacement of the ionization region. Nonetheless, NPI continues to be the dominant mode and presents a mild shift of $k_y R$ with mass flow changes.

Figure 3.9 (bottom row) plots the influence of the channel length, L_E, while keeping constant the distance from exit to cathode (i.e. $L_\mathrm{N} - L_\mathrm{E}$). The ratio $B(0)/B_m$ is also kept constant throughout the cases, by adjusting $L_{m,\mathrm{in}}$, in order to prevent the long-channel case from having unrealistically low magnetic field close to the anode. The NAI gets less unstable as the channel is shorter and, indeed, that unstable branch disappears for $L_\mathrm{E} = 1.4$ cm. This is coherent with findings on the rotating spoke: they were observed originally in a long-channel (~ 10 cm) thruster [8] and PIC simulations suggest that they appear if the anode-cathode distance is large enough [1]. The frequency and growth rate of the dominant NPI do not change much with the chamber length but the mode number $k_y R$ shifts towards higher values when reducing L_E as a consequence of modifying the decay of $B(z)$ inside the channel. This points out that the near-plume instability is not totally alien to gradients inside the chamber. An interesting novelty is the presence, for the shortest channel, of a new pair of NPI branches with lower wavenumbers ['new NPI' in figure 3.9(bottom row)]. Interestingly, their dominant mode has a growth rate

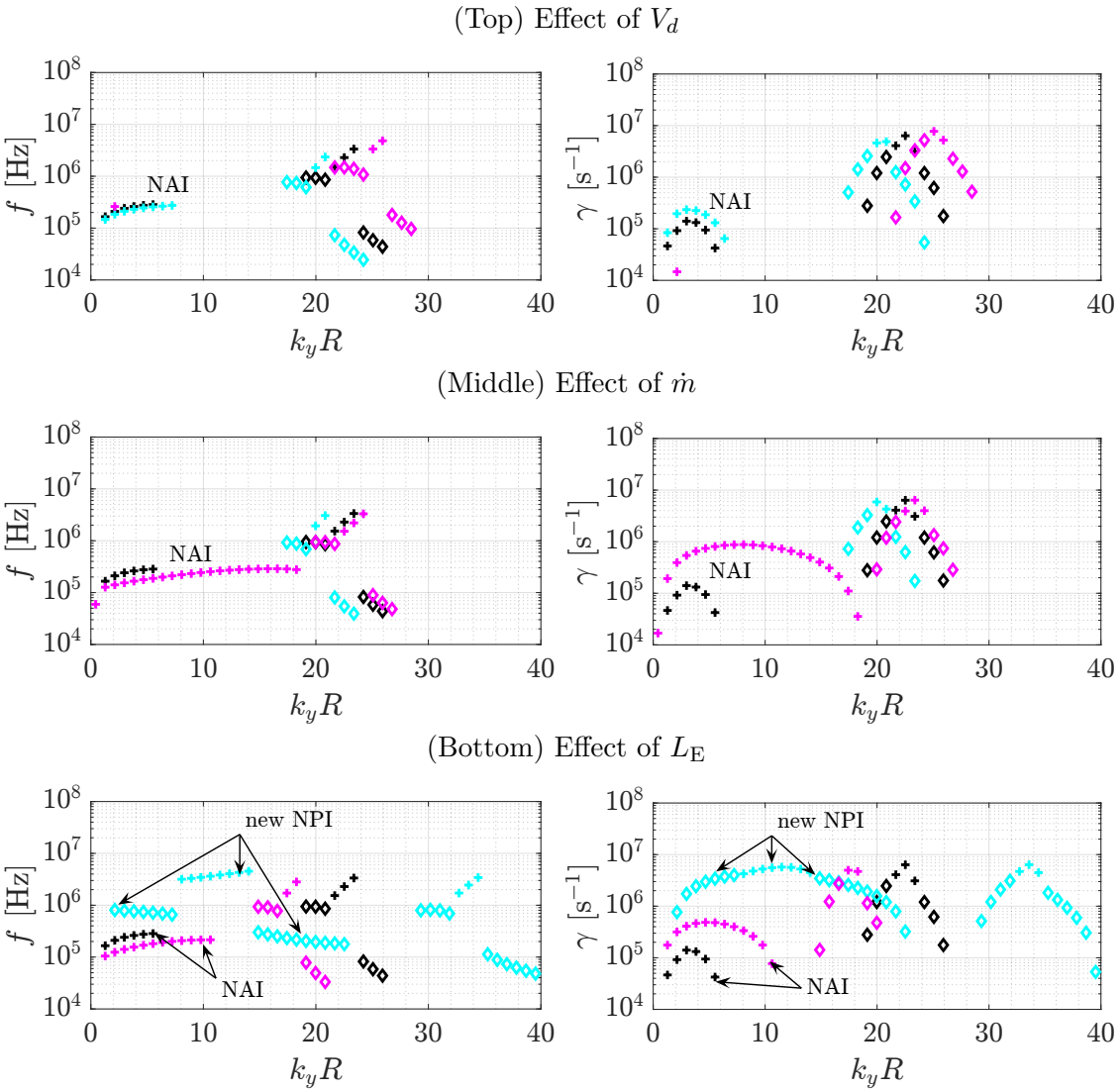

Figure 3.9: Nominal model. Effects on the dispersion relation of parametric variation. In each case, parameters of table 3.1 are used except those explicitly specified below. Contrary to other similar figures, for each case, only the most unstable mode at each k_yR is plotted. All eigenvalues correspond to NPI modes, except those specifically marked. Cross and diamond markers account for azimuthal propagation in the $+y$ and $-y$ directions, respectively. (Top) Effect of discharge voltage: $V_d = 200$ V, $B_m = 194$ G (cyan); $V_d = 300$ V, $B_m = 251$ G (black, nominal case); and $V_d = 700$ V, $B_m = 416$ G (magenta). (Middle) Effect of node mass flow: $\dot{m} = 3.1$ mg/s, $B_m = 224$ G (cyan); $\dot{m} = 4.75$ mg/s, $B_m = 251$ G (black, nominal case); and $\dot{m} = 6.3$ mg/s, $B_m = 265$ G (magenta). (Bottom) Effect of the channel length: $L_E = 1.4$ cm, $B_m = 245$ G (cyan); $L_E = 2.5$ cm, $B_m = 251$ G (black, nominal case); and $L_E = 3.3$ cm, $B_m = 251$ G (magenta).

very close to the one of the original pair of NPI branches, and will also be found again next.

3.5 Changes in the global fluid models

The following off-nominal models, named II, III and IV, are considered here. In section 3.5.1, Model II corresponds to the nominal one except for a change of a boundary condition in the perturbation model. In section 3.5.2, Model III corresponds to the nominal one except for the stationary Model 0B being used instead of the (electron inertialess) Model 0A. And in section 3.5.3, Model IV corresponds to the nominal one except that T_{e1} perturbations are admitted in the perturbation model.

3.5.1 Model II: Change of the circuit boundary condition

Depending on the anode-to-cathode electric circuit coupled to the plasma, the discharge current or the discharge voltage are controlled. When solving the stationary problem, this is not an issue, since results will be the same as long as the operational point in the current-voltage curve of the thruster model is the same. However, fixing the current or voltage does affect time-dependent perturbations and the global stability dispersion relations can present differences. The nominal model here has considered a current-controlled response with $I_{d1\mathrm{N}} = 0$, equation (3.41). Model II here changes from the boundary condition $I_{d1\mathrm{N}} = 0$ to $\phi_{1\mathrm{N}} = 0$ (which together with $\phi_{1\mathrm{A}} = 0$, guarantees $V_{d1} = \phi_{1\mathrm{A}} - \phi_{1\mathrm{B}} = 0$).

Figure 3.10 depicts main eigenvalues of the global dispersion relation for this voltage-controlled case. The known branches 1 to 3 of the nominal model are just shifted moderately, with no qualitative changes in the NAI and NPI modes. The most unstable mode in branch 2 has now $k_y R = 25.5$, $f = 2.04$ MHz, $\gamma = 5.73 \cdot 10^6$ s^{-1}. Beyond that, two additional branches, 4 and 5, of NPI type, appear, qualitatively identical to the ones found in figure 3.9(bottom) for the short-channel. The main NPI mode in branch 4, has $k_y R = 11.0$, $f = 3.0$ MHz, and $\gamma = 6.16 \cdot 10^6$ s^{-1}. Therefore it is narrowly the globally dominant mode for Model II. The eigenmodes of branch 4 (none of them depicted here) are very similar to those in branch 2 except for slightly shorter axial wavelengths and a phase change in $\tilde{u}_{ze1}$ similar to that of $\tilde{u}_{ye1}$ in figure 3.5(d).

An important conclusion of this particular study is that global instabilities are not determined exclusively by the intrinsic plasma dynamics but also by the particular set of homogeneous boundary conditions, an aspect out of the capabilities

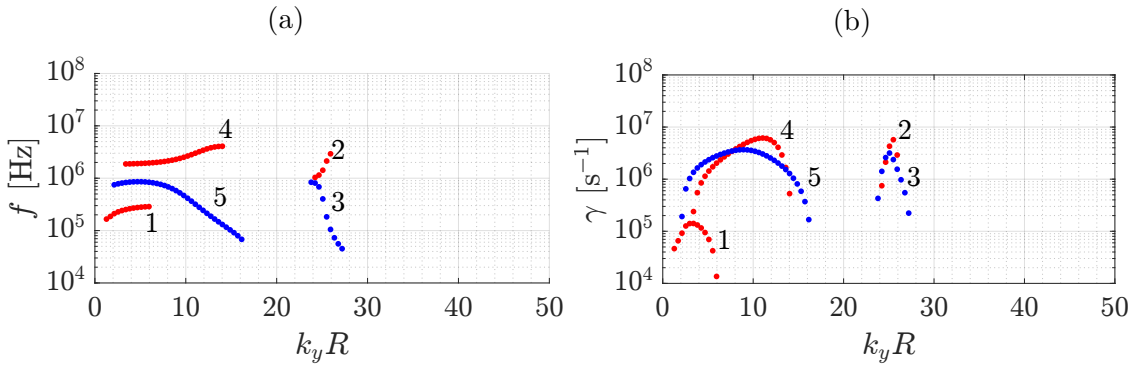

Figure 3.10: Model II (imposing $\phi_{1N} = 0$). Main eigenvalues. Red and blue colours denote azimuthal propagation in the $+y$ and $-y$ directions, respectively. Branches 4 and 5 are new NPI modes.

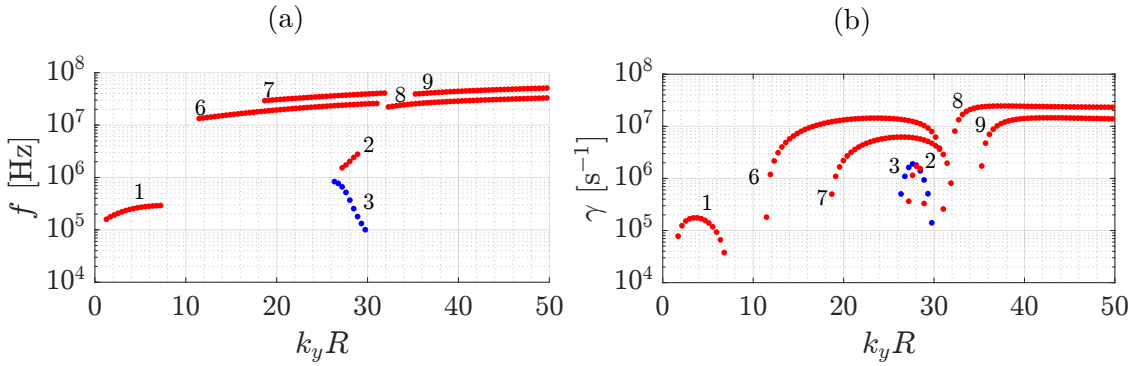

Figure 3.11: Model III (using the stationary Model 0B). Main eigenvalues. Red and blue colours denote azimuthal propagation along $+y$ and $-y$, respectively. Branches 6 to 9 are new NPI modes.

of local stability analyses.

3.5.2 Model III: Inclusion of zeroth-order electron inertia

Model III considers, as stationary model, the more general Model 0B, instead of the electron-inertialess Model 0A, both being depicted in Fig. 3.2. The main eigenvalues of the resulting global dispersion relation are shown in figure 3.11. Branches 1 to 3 are just shifted versions of those of the nominal model in figure 3.3. Interestingly, the dominant modes in NPI branches 2 and 3 (which counterstream azimuthally) have now very similar growth rates. However, these two branches are now overshadowed by branches 6 to 9, all of NPI type, with significantly higher frequencies. The dominant mode of Model III belongs to branch 8, having $k_yR = 37.4$ and $f = 27.2$ MHz. The eigenmodes are shown in figure 3.12. However, there are two facts that

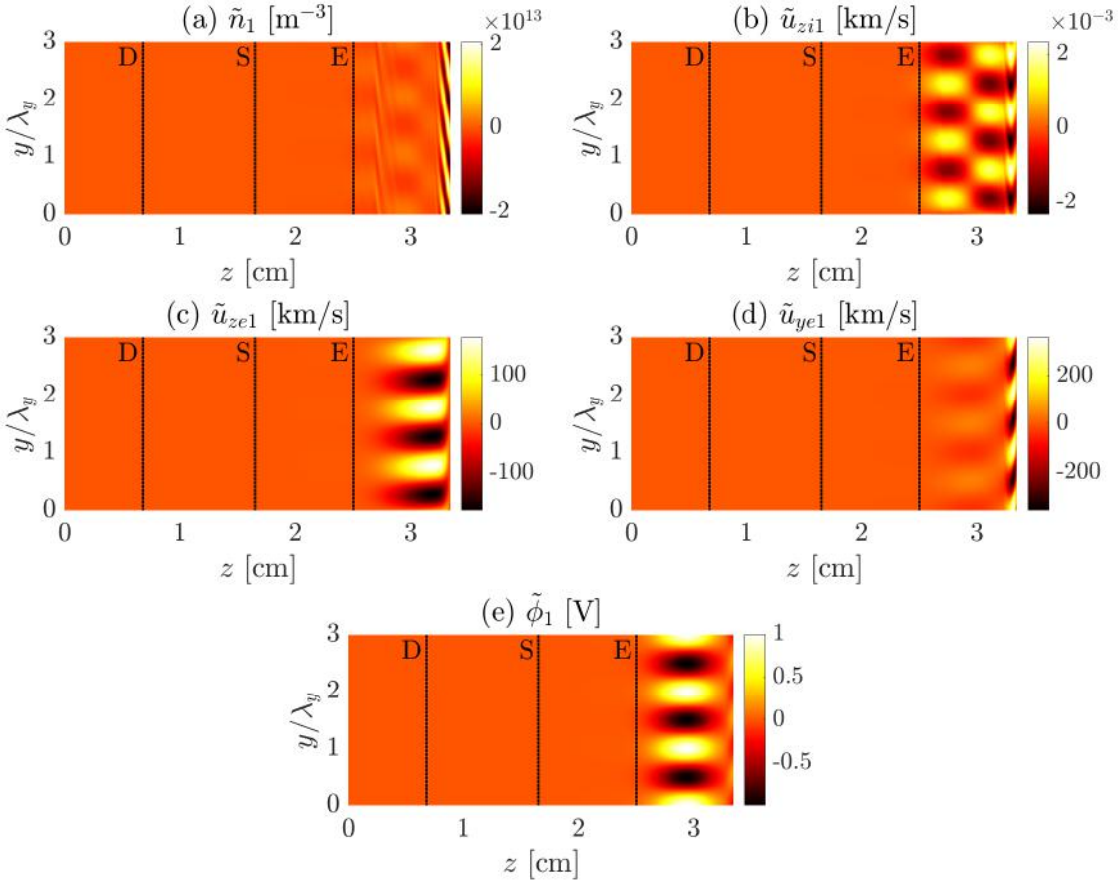

Figure 3.12: Model III. Instantaneous spatial response for the dominant NPI mode: $k_y R = 37.4$ (i.e. $\lambda_y = 0.71$ cm) and $f = 27.2$ MHz.

make not reliable these modes. The first one are the the particular behaviour of the instability in the very thin region close to the neutralizer, with very small axial wavelengths. These could be induced by the large values of $\mathrm{d}u_{ye0}/\mathrm{d}z$ there and the boundary conditions at the infinitely thin cathode location. The second one, partially related to the first one, is the failure of the quasineutrality condition, as shown in figure 3.6(c). Therefore, a consistent stability analysis of Model 0B is going to require considering a finite thickness cathode, the extension to the downstream plume, and the consideration of non-neutral effects in the global perturbation model.

3.5.3 Model IV: Inclusion of temperature perturbations

This subsection analyzes the effect of allowing perturbations of the electron temperature and the heat flux, i.e. $T_{e1}, q_{ze1} \neq 0$. The system of perturbed equations comprises equations (3.30)-(3.36), with the corresponding boundary conditions. The stationary inertialess Model 0A is used.

The corresponding eigenvalues are represented in Figure 3.13. The subdominant

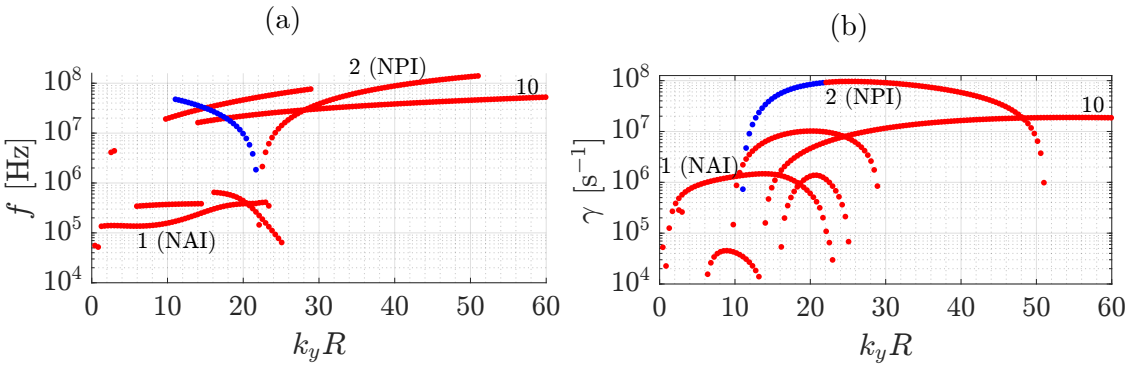

Figure 3.13: Model IV (allowing temperature perturbations). Main eigenvalues. Red and blue colours denote azimuthal propagation along $+y$ and $-y$, respectively.

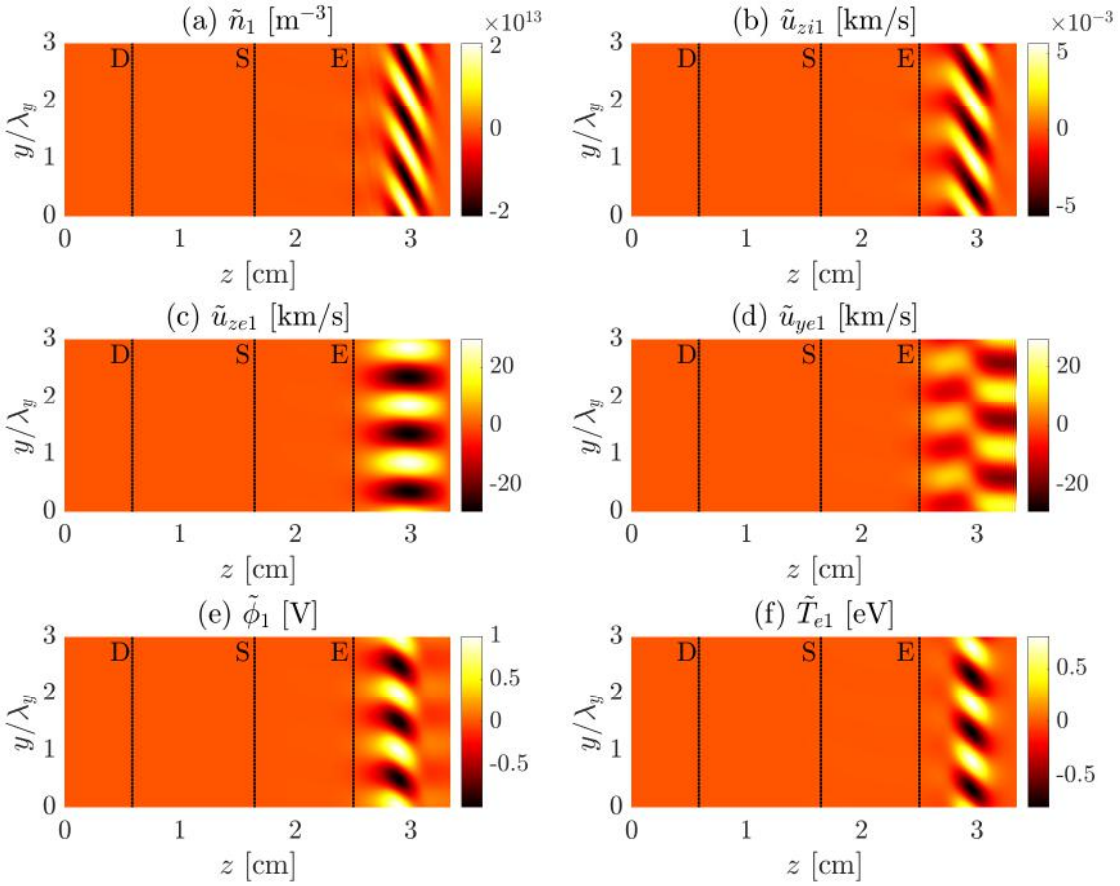

Figure 3.14: Model IV. Instantaneous spatial response for the dominant NPI mode: $k_yR = 25.1$ and $f = 14.2$ MHz.

NAI [in branch 1] and the dominant NPI [in branch 2] modes are still identifiable. There are several new NPI branches [untagged], but the long-term behaviour is expected to be dominated, in the near plume, by the dominant NPI mode in branch 2. This branch is unstable within a much wider interval of k_yR and its frequency has increased considerably, up to $f \lesssim 140$ MHz. The fork structure in f with a main and secondary NPI modes has been substituted by a more involved coexistence

of instability modes. For instance, now the frequency of the main NPI branch shows a sign change at $k_y R \approx 22$. The dominant NPI mode of Model IV has now $k_y R = 25.1$ and $f = 14.2$ MHz. The corresponding eigenmodes are plotted in figure 3.14. Compared to the dominant NPI mode of the nominal model (figure 3.5), this one shows: an attenuation of the fast axial oscillations of $\tilde{u}_{ye1}$, shorter axial wavelengths (i.e., larger k_z) of $\tilde{n}_1$, $\tilde{\phi}_1$ and $\tilde{u}_{zi1}$, and a decrease by one order of magnitude of the relative amplitude of $\tilde{n}_1/\tilde{\phi}_1$. The two last effects lead to an increase of non-neutrality and, indeed, 3.6(d) shows that non-neutral effects should be included for a correct characterization of the NPI instability with temperature perturbations.

Another feature of Model IV to stand out is that the NAI branch 1 is no more a subdominant mode. This role is taken by branch 10 in figure 3.13, in particular by the eigenmode with $k_y R = 54.8$ and f =49 MHz. This mode is not of NAI or NPI type, since it develops between the ion-stagnation point D and the point with n_0 maximum in figure 3.2(b), i.e in a region with downstream ion flow and $\mathrm{d}n_0/\mathrm{d}z > 0$. This subdominant mode presents significant non-neutral effects too.

3.6 Analysis of the electron momentum equations

The analysis here is limited to the nominal model.

3.6.1 Dominant perturbation forces

Equations (3.33) and (3.34) for the axial and azimuthal components of the first-order, electron momentum, are analysed in order to identify the main perturbation forces. Figures 3.15(a) and (b) plot the relative contributions of (I) inertia terms, (P) pressure gradients, (E) electric forces, (M) magnetic forces, and (C) collisional terms, for the subdominant NAI and dominant NPI modes of the nominal model. The first observation is that the electric and magnetic perturbation forces are the main contributions, as expected. The second one is that collisional effects are very marginal for both the NAI and the NPI 'high-frequency' modes (and this is true either keeping or neglecting the turbulent contribution ν_t to the total collision rate ν_e in the perturbation model). Therefore, these two instabilities would pertain to the drift-gradient instability class. Third, the perturbed pressure gradient is totally negligible for the NPI –due to the small (relative) perturbation of plasma density–, but is an important contribution in the inner (subsonic) region of the discharge for the NAI.

Finally, the perturbed inertial forces provide mild local contributions to the

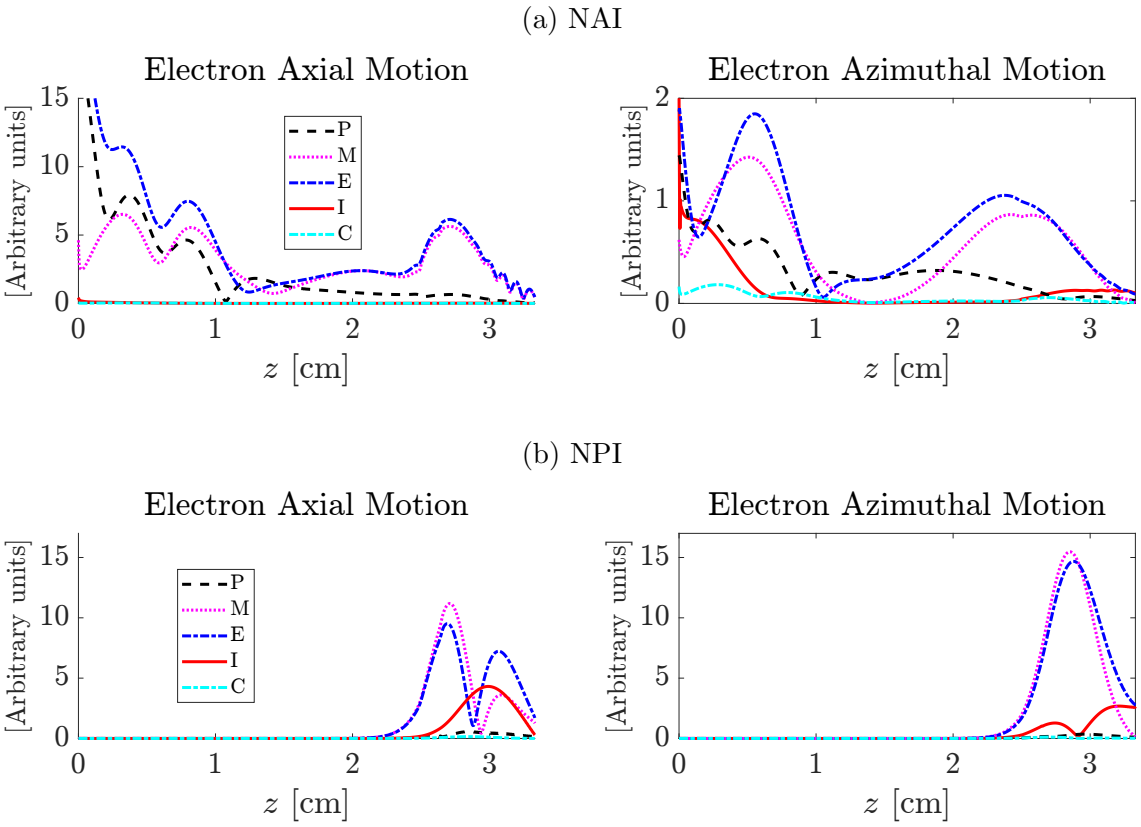

Figure 3.15: Nominal model. Contributions to the axial and azimuthal components of the first-order electron momentum equations (3.33) and (3.34) for the (a) subdominant NAI and (b) dominant NPI modes. P, M, E, I, and C represent pressure, magnetic, electric, inertial, and collisional terms. Complex moduli in arbitrary units are shown. Small-wavelength axial oscillations (mainly due to u_{ye1}) have been filtered out.

azimuthal force balance, in the regions of development of each instability mode, where the stationary azimuthal inertia was already important. In fact, these contributions are partially connected to the fulfilment of the boundary conditions. While in the equilibrium solution only the azimuthal electron inertia has some contribution of interest, in the perturbed NPI modes, the axial electron inertia is as relevant as the azimuthal one. Neglecting smaller contributions, the perturbed electron momentum equations (3.33) and (3.34) for the NPI and NAI modes, can be simplified into

$$\mathrm{i}k_y m_e u_{ye0} u_{ze1} \simeq eBu_{ye1} + e\frac{\mathrm{d}\phi_1}{\mathrm{d}z} - \frac{T_{e0}}{n_0}\frac{\mathrm{d}n_1}{\mathrm{d}z}, \tag{3.45}$$

$$\mathrm{i}k_y m_e u_{ye0} u_{ye1} \simeq -eBu_{ze1} + \mathrm{i}k_y e\phi_1 - \mathrm{i}k_y \frac{T_{e0}}{n_0} n_1, \tag{3.46}$$

with the (mild) inertial terms are grouped on the left side. The inertia contribution in the perturbed axial equation is of interest only for the NPI since $u_{ze1} = O(u_{ye1})$ (Fig. 3.5). The pressure terms are only important for the NAI.

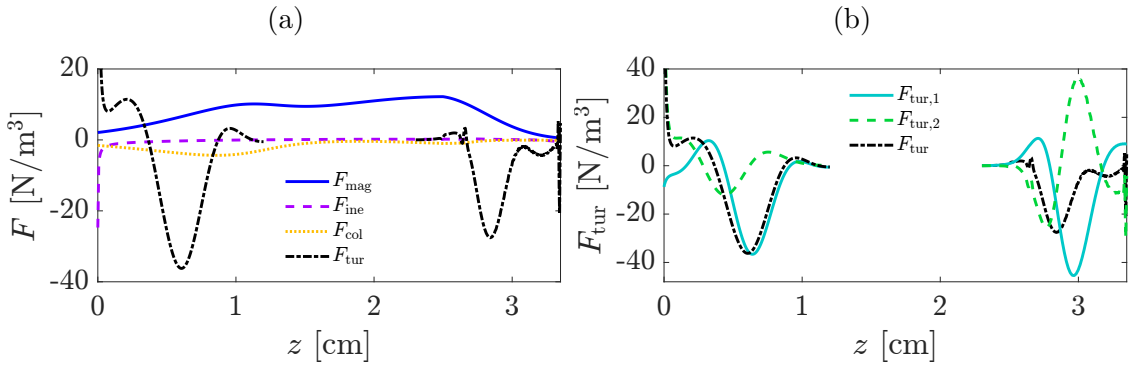

Figure 3.16: Nominal model. Azimuthal electron momentum balance including turbulent forces. (a) Magnetic force, and turbulent force arising from the dominant NPI mode with $\tilde{\phi}^{NPI}_{1,\max} = 71$V plus the subdominant NAI mode with $\tilde{\phi}^{NAI}_{1,\max} = 10.5$V. (b) Individual contributions of the electric and inertial forces to the previous NPI and NAI turbulent forces. These are proportional to $(\tilde{\phi}^{NPI}_{1,\max})^2$ and $(\tilde{\phi}^{NAI}_{1,\max})^2$, respectively. Small-wavelength axial oscillations (mainly due to u_{ye1}) have been filtered out.

3.6.2 On electron cross-field transport

The quasilinear extension of the fluid model is considered now to analyze quadratically correlated effects of the NPI and NAI modes. The key equation for cross-field electron transport is the stationary azimuthal momentum equation (3.18), which can be formally expressed as the force balance

$$0 = F_{\rm mag} + F_{\rm ine} + F_{\rm col} + F_{\rm tur}, \tag{3.47}$$

with $F_{\rm mag} = -eBn_0u_{ze0}$, $F_{\rm ine} = -m_en_0u_{ze0}\mathrm{d}u_{ye0}/\mathrm{d}z$, $F_{\rm col} = -m_e(\nu_{e0} - \nu_t)n_0u_{ye0}$, and $F_{\rm tur}$, respectively, the magnetic, inertial, collisional (excluding the empirical contribution of turbulence), and turbulence-based forces. The magnetic force is undoubtedly the dominant force and must be balanced by the combination of the rest of forces. Figure 3.16(a) plots $F_{\rm mag}$, $F_{\rm ine}$, and $F_{\rm col}$, and, as expected, inertial and collisional forces cannot balance $F_{\rm mag}$ except at very localized regions. In this case, the compensation comes from the crude and common expression used for the turbulent force, $F_{\rm tur} = -\alpha_t eBn_0u_{ye0}$, according to equation (3.60).

Let us analyze now, based on the quadratic time-and-azimuth averaged contributions of the dominant NAI and NPI modes, how the resulting azimuthal turbulent force would be. Since the linear perturbation analysis does not predict the saturation level of the instability modes, we will speculate on which saturation levels can lead to $F_{\rm tur}$ balance $F_{\rm mag}$ globally. The time- and azimuth- averaging operator on a quadratic magnitude Φ is defined as

$$\langle\Phi\rangle(z) = \frac{\omega k_y}{4\pi^2}\int_t^{t+2\pi/\omega}\mathrm{d}t\int_y^{y+2\pi/k_y}\mathrm{d}y \quad \Phi(t,y,z). \tag{3.48}$$

For complex, first-order variables $\tilde{\varphi}_1$ and $\tilde{\psi}_1$, fulfilling (3.13), the correlated product satisfies $\left\langle \tilde{\varphi}_1 \tilde{\psi}_1 \right\rangle = \mathrm{Re}\{\varphi_1 \psi_1^*\}/2$, with ψ_1^* the complex conjugate of ψ_1.

Departing from equation (3.7), the turbulent force is $F_{\mathrm{tur}} = F_{\mathrm{tur},1} + F_{\mathrm{tur},2}$ with

$$F_{\mathrm{tur},1} = -e\langle \tilde{n}_1 \tilde{E}_{y1} \rangle, \tag{3.49}$$

$$F_{\mathrm{tur},2} = -m_e \left[n_0 \left\langle \tilde{u}_{ze1} \frac{\partial \tilde{u}_{ye1}}{\partial z} \right\rangle + u_{ze0} \left\langle \tilde{n}_1 \frac{\partial \tilde{u}_{ye1}}{\partial z} \right\rangle + u_{ye0} \left\langle \tilde{n}_1 \frac{\partial \tilde{u}_{ye1}}{\partial y} \right\rangle + \frac{\partial u_{ye0}}{\partial z} \langle \tilde{n}_1 \tilde{u}_{ze1} \rangle + \left\langle \tilde{n}_1 \frac{\partial \tilde{u}_{ye1}}{\partial t} \right\rangle \right], \tag{3.50}$$

the contributions from electric and inertial forces, respectively (the pressure azimuthal gradient does not contribute, on average, to turbulent transport because of its azimuthal periodicity).

The shapes of $F_{\mathrm{tur}}(z)$ generated by the dominant NPI and the subdominant NAI modes are depicted in Figure 3.16 (a) too. The contributions are proportional to $(\tilde{\phi}_{1,\max}^{NPI})^2$ and $(\tilde{\phi}_{1,\max}^{NAI})^2$, respectively for each mode. As commented above, the saturation values of the electric potential, $\tilde{\phi}_{1,\max}^{NPI}$ and $\tilde{\phi}_{1,\max}^{NAI}$, are out of reach of the linear model, and those selected for the plots, $\tilde{\phi}_{1,\max}^{NPI} = 71\mathrm{V}$ and $\tilde{\phi}_{1,\max}^{NAI} = 10.5\mathrm{V}$, correspond just to those making F_{tur} to compensate globally F_{mag} in the last and first centimetre of the domain, where, respectively, the NPI and NAI are significant. The associated amplitudes of the azimuthal electric fields are $\tilde{E}_{y1,\max} = \mathrm{Re}\{\mathrm{i}k_y \phi_{1,\max}\}$ are 390 V/cm and 7.4 V/cm for the NPI and NAI modes, respectively. These magnitudes of the perturbations fields are comparable to those of the local zeroth-order electric field, thus suggesting that the NPI and NAI modes must develop well into the non-linear regime in order to contribute to the cross-field transport.

Figure 3.16(b) depicts the electric and inertial contributions to F_{tur}. The inertial contribution, $F_{\mathrm{tur},2}$, is small for the NAI, but it is of the same order as the electric one, $F_{\mathrm{tur},1}$, for the NPI. This result is not immediate since, within first order, electron inertia ($m_e u_{ye0} u_{ye1}$) is generally small compared to the electric force ($e\phi_1$). However, for the second-order forces,

$$\frac{m_e n_0 u_{ze1} \partial u_{ye1}/\partial z}{e k_y n_1 \phi_1} \sim \frac{m_e u_{ye0} u_{ye1}}{e\phi_1} \cdot \frac{n_0 u_{ze1}}{n_1 u_{ye0}} \geq O(1), \tag{3.51}$$

since $n_0 u_{ze1}/n_1 u_{ye0} \sim 100$ for the NPI (as for the quasineutrality condition, the extremely low n_1 disrupts the expected natural orderings). This, and a mildly higher correlation level on the electric force, explain that $F_{\mathrm{tur},2} \sim F_{\mathrm{tur},1}$ for the NPI.

Next, while $\int_{z_A}^{z_N} F_{\mathrm{tur}} \mathrm{d}z < 0$, is negative (and, thus, contributes positively to cross-field transport), the profile of $F_{\mathrm{tur}}(z)$ is very rippled spatially, F_{tur} becoming even positive in certain subregions. This is natural to the oscillatory character of modes

generating $F_{\rm tur}$ but is far different from the gentle profile of $F_{\rm tur} = -\alpha_t eBn_0 u_{ye0}$, used to construct the equilibrium solution (although this one could be interpreted as a spatially-averaged force). An iterative scheme can be set up to obtain a solution consistent with the rippled $F_{\rm tur}(z)$ up to second order. This is out of the scope of this work and a challenging problem anyway. A spatially rippled $F_{\rm tur}(z)$ enhances the relevance of the electron inertia force in the equilibrium solution, since it is the first term reacting to variations of $F_{\rm tur}(z)$, and likely leads to some rippling in the rest of plasma variables at equilibrium and to changes in the linear perturbation modes. Furthermore, the non-negligible role of electron inertia in the instability analysis here, implies that gyroviscous effects, of the same order as inertia effects in the standard finite-Larmor-radius ordering [13,81], should be included in the model to strengthen its consistency. But the gyroviscous tensor introduces second-order axial derivatives, implying a major change in the mathematical formulation, which here is first-order in axial derivatives.

To conclude it is worth observing that a spatially rippled $F_{\rm tur}(z)$ is also found in the non-linear kinetic simulations of a HET discharge [94], although instabilities there were attributed to kinetic electron-drift instabilities. A fully non-linear fluid model would be needed to a more solid comparison of kinetic and fluid contributions to cross-field transport.

3.7 Summary and conclusions

The plasma discharge in a HET from the anode to the external cathode is highly inhomogeneous, so the linear stability analysis of a stationary response must consider the discharge globally. Departing from a fluid model of the discharge that ignores the radial direction, and is quasineutral except for the anode sheath, a perturbation scheme is applied to define (i) a zeroth-order axisymmetric stationary axial model plus (ii) a first-order model of small perturbations. Both pressure effects and electron inertia effects are kept in the two models, with the interest of assessing their relevance.

Fourier transforms are applied only in time and the azimuthal direction, so the perturbation model constitutes a set of ordinary differential equations in z for each azimuthal wavenumber k_y and frequency ω. The stability analysis of the perturbation model considers homogeneous boundary conditions at the anode, the cathode, and the internal sonic point. Given k_y, the problem admits non-trivial solutions only at specific values of ω. A discretization method in a uniform grid has been implemented to transform the differential Sturm-Liouville problem into an algebraic eigenvalue problem. For each real k_y, complex eigenvalues ω are found; the corresponding eigenvectors build up the perturbation solution.

The analysis is focused in the mid-to-high frequency range (say, $f > 100$ kHz) and high-wavenumber range (i.e. $k_y R$ large) but still within the fluid-formulation validity range. Two well-distinguished instability types are found under a broad range of conditions. There is first a dominant instability mode (NPI) developing in the near-plume. It has frequencies in the ranges $f \sim$ 1-30 MHz and azimuthal mode numbers $k_y R \sim$ 10-40. It involves electron perturbations almost exclusively and travels in the $+u_{ye0}$ direction. By modifying $B(z)$ it is shown that the NPI development is related to the region where $\mathrm{d}B/\mathrm{d}z$ is negative, thus suggesting that the NPI could be related to the classical drift-gradient instability of Esipchuk and Tilinin. There is, then, a subdominant instability mode (NAI) developing mainly near the anode. This mode has lower frequencies ($f \sim$ 100-300 kHz) and mode numbers ($k_y R \sim$ 1-10) and involves both perturbations of electrons and ions. This mode could be a high-frequency manifestation of a rotating spoke.

For the nominal model (the main one studied here) there is a second counterstreaming NPI branch (i.e. travelling along $-u_{ye0}$) which could be related to some experimental observations but it is never dominant in the analyses here. For a short channel or a certain anode-to-cathode electric connection, a second pair of NPI branches develop at lower wavenumbers, and one of their modes can even become the dominant mode. When zeroth-order electron inertia (mostly significant close to the anode and cathode boundaries) or electron temperature perturbations are included in the analysis, the number of unstable eigenvalue branches of the dispersion relation increase much, and the discussion is more involved. Still, there is a dominant NPI mode but mode number and frequency have shifted to higher values.

Both NPI and NAI are not simple normal waves since, for each k_y and ω, a fast Fourier transform shows that different axial wavenumbers k_z characterize the propagation of the different plasma variables, which means that the oblique propagation is different for each of them, contrary to local analyses based on setting both wavenumbers, and obtaining $\omega(k_y, k_z)$. The two perturbation modes are nearly collisionless, pressure effects matter only for the NAI (developing in the subsonic region of the plasma beam), and first-order electron inertia is a small correction to them. Quasineutrality is satisfied by the NAI but not always by the NPI: non-neutral effects appear, even with $k\lambda_D \ll 1$, due to the very low perturbations of the ions in the NPI.

The last part of the paper has been devoted to a speculative analysis on the possible contribution of the NPI and the NAI to the electron cross-field transport, through quadratically-correlated electric and inertia forces. The conclusions have been that: (1) a fully non-linear development of the modes is required to obtain a significant turbulent azimuthal force, (2) the contribution of electron inertia to the net turbulent force is not small for the NPI (because of the small density perturbation

and the resulting quadratic electric force), and (3) the turbulent force is highly rippled axially.

This last feature has important consequences on the stationary mathematical model. First, it makes electron inertia a key mechanism to control spatial rippling on the equilibrium solution. Second, the gyroviscous effects, cannot be further ignored, mainly if dealing with a rippled solution, but these imply major changes to the present first-order mathematical formulation. Finally, since the NPI develops close to the cathode boundary, the extension of the global discharge model beyond the cathode, into the current-free plume, is another interesting direction of research.

Acknowledgements

This research was funded by the Comunidad de Madrid (Spain), under PROMETEO-CM project, with grant number Y2018/NMT-4750. Enrique Bello-Benítez is supported by Spain's Ministerio de Ciencia, Innovación y Universidades, under grant FPU18/03686. The authors acknowledge useful discussions on this work with J. J. Ramos and P. Fajardo.

Appendices

3.A Expressions for collision-related parameters

This Appendix compiles the expressions for the collision-related terms of equations (3.2)-(3.9) and the values selected in the simulations for some of the constants. The expressions come from previous papers on the same model by Ahedo and co-workers.

The ionization or production frequency, ν_p, is modelled as $\nu_p = n_n \bar{c}_e \bar{\sigma}_{\text{ion}}$, with

$$\bar{\sigma}_{\text{ion}} = \sigma_{\text{ion},0} \left[1 + \frac{T_e E_{\text{ion}}}{(T_e + E_{\text{ion}})^2} \right] \exp\left(-\frac{E_{\text{ion}}}{T_e} \right) \tag{3.52}$$

where E_{ion} stands for the primary ionization energy. For xenon: $E_{\text{ion}} = 12.1$ eV, $\sigma_{\text{ion},0} = 5 \times 10^{-20}$ m^2. The effective energy loss due to ionization, E_{inel}, satisfies

$$\frac{E_{\text{inel}}}{E_{\text{ion}}} = 2 + \frac{1}{4} \exp\left(\frac{2E_{\text{ion}}}{3T_e} \right) \tag{3.53}$$

The elastic electron-neutral collisions frequency is $\nu_{en} = n_n \bar{c}_e \sigma_{en}$. Here, and for xenon the cross-section σ_{en} is taken approximately constant and equal to $\sigma_{en} = 27 \times 10^{-20}$ m^2.

The electron-ion (Coulomb) collision frequency is $\nu_{ei} = nR_{ei}$, with R_{ei} given by

$$\frac{R_{ei}}{10^{-12}\text{m}^3\text{s}^{-1}} = 2.9 \cdot \left(\frac{1 \text{ eV}}{T_e} \right)^{3/2} \ln\Lambda \quad \text{and} \quad \ln\Lambda \approx 9 + \frac{1}{2} \ln\left[\left(\frac{10^{18} \text{ m}^{-3}}{n_e} \right) \left(\frac{T_e}{1 \text{ eV}} \right)^3 \right]. \tag{3.54}$$

The ion-neutral (charge-exchange) collision frequency is $\nu_{in} = n_n c_{in} \sigma_{in}$, with $c_{in} = |u_{zi} - u_{zn}|$ and

$$\sigma_{in} = \sigma_{in0} \left[1 - 0.2 \log_{10} \frac{c_{in}}{1 \text{ km/s}} \right]^2 \tag{3.55}$$

and $\sigma_{in0} = 81 \cdot 10^{-20}$ m^2 for xenon.

The wall-loss frequency of particles is

$$\nu_w = \tilde{\nu}_w \frac{2\pi R}{A_c} c_s \tag{3.56}$$

with $\tilde{\nu}_w$ a constant (accounting for plasma density decrease near the wall); $\tilde{\nu}_w = 0.17$ is used here. The effective axial velocity of wall-born neutrals from ion recombination is

$$u_{znw} = a_w u_{zn} + (1 - a_w) u_{zi} \tag{3.57}$$

where a_w is a velocity accommodation factor; $a_w = 0.85$ is used here. The wall-loss frequency for momentum and energy are $\nu_{wm} = \beta_m \nu_w$ and $\nu_{we} = \beta_e \nu_w$, respectively with

$$\beta_m = \frac{\delta_w}{1 - \delta_w}, \qquad \beta_e = 5.62 + \frac{1.65}{1 - \delta_w}. \tag{3.58}$$

Here, δ_w is the effective secondary electron emission yield from the wall, which is modelled as

$$\delta_w(T_e) = \sqrt{T_e/T_1} \quad \text{if} \quad T_e < T_e^* \tag{3.59}$$

and $\delta_w = \delta_w^* = \sqrt{T_e^*/T_1}$ if $T_e \geq T_e^*$, where T_1 is the temperature leading (theoretically) to a 100% yield (which depends on the wall material) and T_e^* is the temperature where the charge-saturation limit is reached at the wall. Here: $T_e^*/T_1 = 0.967$, $\delta_w^* = 0.983$, and $T_1 = 37$ eV.

Turbulent transport in the stationary solution is introduced through an effective collisional frequency

$$\nu_t = \alpha_t \omega_{ce} \tag{3.60}$$

with α_t a constant equal to 0.0094 in the simulations here.

3.B Symmetry of the perturbation problem

As noted in the main text, the parametric region with $k_y < 0$ yields the same perturbation modes as those obtained for $k_y > 0$. Analytical evidence is provided here by, first, proving that the perturbation problem satisfies the symmetry condition

$$\omega_r(-k_y) = -\omega_r(k_y), \quad \gamma(-k_y) = \gamma(k_y), \quad \varphi_1(z, -k_y, -\omega^*) = \varphi_1^*(z, k_y, \omega), \tag{3.61}$$

for every first-order variable φ_1, with the asterisk denoting the complex conjugate. The solutions, for k_y and $-k_y$, complying with (3.61) do not generally belong to the same branch (meaning by 'branch' the continuous curves in, e.g., figure 3.3).

According to the symmetry condition (3.61), every perturbation equation, that can be expressed as $f(k_y, \omega, \boldsymbol{\varphi}_1) = 0$ (being $\boldsymbol{\varphi}_1$ the vector of first-order variables), complies with

$$f^*(k_y, \omega, \boldsymbol{\varphi}_1) = f(-k_y, -\omega^*, \boldsymbol{\varphi}_1^*). \tag{3.62}$$

In that case, if there exists a solution for k_y, ω and $\boldsymbol{\varphi}_1$ obeying $f(k_y, \omega, \boldsymbol{\varphi}_1) = 0$; there must exist another solution fulfilling $f(-k_y, -\omega^*, \boldsymbol{\varphi}_1^*) = 0$ for $-k_y$, $-\omega^*$ and $\boldsymbol{\varphi}_1^*$. Let us now demonstrate that (3.62) is satisfied by the perturbation equations (3.30)-(3.36). It is enough with providing proof for electron-related equations, since those for ions are simplified versions of these. Also, for the sake of conciseness, we will work on the case with $T_{e1} = 0$; but the property (3.62) remains valid for the more general case with non-zero T_{e1} and q_{ze1}.

If k_y, ω and $\boldsymbol{\varphi}_1$ are substituted by $-k_y$, $-\omega^*$ and $\boldsymbol{\varphi}_1^*$ in the first-order electron continuity equation (3.31), the result is

$$u_{ze0}\frac{\mathrm{d}n_1^*}{\mathrm{d}z} + n_0\frac{\mathrm{d}u_{ze1}^*}{\mathrm{d}z} = \left(-\mathrm{i}\omega^* + \mathrm{i}k_y u_{ye0} - \frac{\mathrm{d}u_{ze0}}{\mathrm{d}z} + \nu_p - \nu_w\right) n_1^* - \frac{\mathrm{d}n_0}{\mathrm{d}z}u_{ze1}^* + \mathrm{i}k_y n_0 u_{ye1}^*, \tag{3.63}$$

that can be easily proved to be equal to the complex conjugate of equation (3.31), thus fulfilling (3.62). Similarly, the same substitution for the electron momentum equations (3.33) and (3.34), yields

$$\begin{aligned} u_{ze0}\frac{\mathrm{d}u_{ze1}^*}{\mathrm{d}z} + \frac{T_{e0}}{m_e n_0}\frac{\mathrm{d}n_1^*}{\mathrm{d}z} - \frac{e}{m_e}\frac{\mathrm{d}\phi_1^*}{\mathrm{d}z} = \left(-\mathrm{i}\omega^* + \mathrm{i}k_y u_{ye0} - \frac{\mathrm{d}u_{ze0}}{\mathrm{d}z} - \nu_e\right) u_{ze1}^* \\ + \frac{eB}{m_e}u_{ye1}^* + \frac{T_{e0}}{m_e n_0^2}\frac{\mathrm{d}n_0}{\mathrm{d}z}n_1^*, \end{aligned} \tag{3.64}$$

$$\begin{aligned} u_{ze0}\frac{\mathrm{d}u_{ye1}^*}{\mathrm{d}z} = \left(-\mathrm{i}\omega^* + \mathrm{i}k_y u_{ye0} - \nu_e\right) u_{ye1}^* - \left(\frac{\mathrm{d}u_{ye0}}{\mathrm{d}z} + \frac{eB}{m_e}\right) u_{ze1}^* \\ + \mathrm{i}k_y\frac{T_{e0}}{m_e n_0}n_1^* - \mathrm{i}k_y\frac{e}{m_e}\phi_1^*, \end{aligned} \tag{3.65}$$

which are equal to complex conjugate of equations (3.33) and (3.34), respectively. The same procedure can be followed to demonstrate the compliance with (3.62) of the general system with non-zero T_{e1} and q_{ze1}; and including electron energy and heat flow equations.

Following the definition (3.13), for every complex perturbation solution, only the real part has physical meaning. It happens that the modes satisfying the proposed symmetry also fulfil

$$\tilde{\varphi}_1(z, y, t) = \mathrm{Re}\{\varphi_1(z, k_y, \omega)\exp\left(-\mathrm{i}\omega t + \mathrm{i}k_y y\right)\} = \mathrm{Re}\{\varphi_1^*(z, k_y, \omega)\exp\left(\mathrm{i}\omega^* t - \mathrm{i}k_y y\right)\} \tag{3.66}$$

and, thus, they are the same mode.

3.C Numerical method for the perturbation problem

The system of linearized macroscopic equations can be written formally as a general homogeneous system of ordinary differential equations

$$\bar{\mathbf{A}} \cdot \frac{\mathrm{d}\boldsymbol{x}_1}{\mathrm{d}z} = \left(\bar{\mathbf{B}} + \mathrm{i}\omega\bar{\mathbf{C}} + \mathrm{i}k_y\bar{\mathbf{D}} + k_y^2\bar{\mathbf{D}}_2\right) \cdot \boldsymbol{x}_1 \tag{3.67}$$

with $\boldsymbol{x}_1 = \boldsymbol{x}_1(z)$ being the vector of perturbation variables and having length m, say. The coefficients of matrices $\bar{\mathbf{A}}$, $\bar{\mathbf{B}}$, $\bar{\mathbf{C}}$, $\bar{\mathbf{D}}$ and $\bar{\mathbf{D}}_2$ are functions of just z and the equilibrium solution $\boldsymbol{x}_0 = \boldsymbol{x}_0(z)$. Similarly, each boundary condition of the problem is homogeneous and can be expressed as a linear combination of the perturbation variables at the corresponding point of application (since the boundary conditions do not involve axial gradients).

The global linear stability problem, or Sturm-Liouville problem, described by equation (3.67) and its set of homogeneous boundary conditions consists of finding non-trivial solutions $\boldsymbol{x}_1(z)$ (eigenfunctions) at specific values of the complex frequency ω (eigenvalues) for given k_y and background plasma state $\boldsymbol{x}_0(z)$.

Equation (3.67) is solved in a discrete way on an uniform grid with p points covering the distance from the anode sheath edge (B) to the neutralizer (N). The unknowns of the discrete problem, $\boldsymbol{X}_1$, are the values of the first order variables, $\boldsymbol{x}_1$, at the grid points. Let j be the index, going from 1 to p, denoting the grid point. This means a total of mp unknowns, which satisfy m boundary conditions and $m\,(p-1)$ macroscopic equations. These come from evaluating equations (3.67) at p different axial positions of the domain. These do not need to coincide with the grid points. After checking different possibilities to proceed, the method identified as the most numerically robust has been selected.

This method evaluates the first-order system (3.67) at intermediate points in between grid points; the non-integer index $j + 1/2$ denotes the midpoint between grid points j and $j+1$. This directly yields $m(p-1)$ equations, which can be written, analogously to equation (3.67), as the system

$$\bar{\mathbf{A}}_g \cdot \frac{\mathrm{d}\boldsymbol{X}_1^*}{\mathrm{d}z} = \left(\bar{\mathbf{B}}_g + \mathrm{i}\omega\bar{\mathbf{C}}_g + \mathrm{i}k_y\bar{\mathbf{D}}_g + k_y^2\bar{\mathbf{D}}_{2,g}\right) \cdot \boldsymbol{X}_1^* \tag{3.68}$$

where $\boldsymbol{X}_1^*$ stands for the vector of first order quantities at midpoints, which is $m(p-1)$ elements long. The matrices in the previous expression are squared with column length $m(p-1)$, and are global versions of those in equation (3.67). Their coefficients come from evaluating the local matrices at each midpoint. The specific arrangement of these coefficients within global matrices depends on the order used for the elements in vector $\boldsymbol{X}_1^*$.

Equation (3.68) has to be expressed in terms of the unknown vector $\boldsymbol{X}_1$. First, the derivatives at midpoints (collected in $\mathrm{d}\boldsymbol{X}_1^*/\mathrm{d}z$) are estimated, using grid-point values, with the centred finite difference formula

$$\left.\frac{\mathrm{d}\boldsymbol{x}_1}{\mathrm{d}z}\right|^{j+1/2} \approx \frac{\boldsymbol{x}_1^{j+1} - \boldsymbol{x}_1^{j}}{\Delta z} \tag{3.69}$$

where Δz is the grid step. Using this equation it is possible to build a finite difference matrix $\bar{\mathbf{F}}$ such that

$$\frac{\mathrm{d}\boldsymbol{X}_1^*}{\mathrm{d}z} \approx \bar{\mathbf{F}} \cdot \boldsymbol{X}_1. \tag{3.70}$$

Second, the values of perturbations at midpoints (collected in $\boldsymbol{X}_1^*$) can be estimated as the mean of the values at the two nearest grid points, i.e

$$\boldsymbol{x}_1^{j+1/2} \approx \frac{\boldsymbol{x}_1^{j} + \boldsymbol{x}_1^{j+1}}{2} \tag{3.71}$$

This expression can be used to build an averaging matrix $\bar{\mathbf{M}}$ such that $\boldsymbol{X}_1^* \approx \bar{\mathbf{M}} \cdot \boldsymbol{X}_1$. The size of matrices $\bar{\mathbf{F}}$ and $\bar{\mathbf{M}}$ is $m(p-1) \times mp$.

Using these discretizations in equation (3.68) yields the algebraic equation

$$\bar{\mathbf{A}}_g \cdot \bar{\mathbf{F}} \cdot \boldsymbol{X}_1 = \left(\bar{\mathbf{B}}_g + \mathrm{i}\omega\bar{\mathbf{C}}_g + \mathrm{i}k_y\bar{\mathbf{D}}_g + k_y^2\bar{\mathbf{D}}_{2,g}\right) \cdot \bar{\mathbf{M}} \cdot \boldsymbol{X}_1 \tag{3.72}$$

The size of the matrices multiplying $\boldsymbol{X}_1$ is $m(p-1) \times mp$. The set of linear homogeneous boundary conditions can be expressed as linear combinations of the the discrete unknowns of the problem in the form $\bar{\mathbf{G}} \cdot \boldsymbol{X}_1 = \mathbf{0}$.

Then, the complete discrete system of equations that gives an approximate solution to the Sturm-Liouville problem of equation (3.67) reads

$$\left[\begin{pmatrix} \bar{\mathbf{A}}_g \cdot \bar{\mathbf{F}} - \left(\bar{\mathbf{B}}_g + \mathrm{i}k_y\bar{\mathbf{D}}_g + k_y^2\bar{\mathbf{D}}_{2,g}\right) \cdot \bar{\mathbf{M}} \\ \bar{\mathbf{G}} \end{pmatrix} - \begin{pmatrix} \bar{\mathbf{C}} \cdot \bar{\mathbf{M}} \\ \bar{\mathbf{0}} \end{pmatrix} \mathrm{i}\omega \right] \cdot \boldsymbol{X}_1 = \mathbf{0} \tag{3.73}$$

This is a generalized algebraic eigenvalue problem with ω and the corresponding $\boldsymbol{X}_1$ being the eigenvalues and eigenvectors, respectively. Once solved, the axial evolution of the perturbation plasma variables is obtained in the complex plane.

This scheme has shown good numerical convergence and, for simple equilibrium solutions, the discrete solution has been verified with analytical solutions. An alternative discretization scheme would have been to evaluate the first order fluid equations at grid points (instead of at midpoints) and use forward, centred, and backward finite difference schemes for estimating axial gradients at left boundary, interior points and right boundary, respectively. However, the complete system (3.67) cannot be evaluated at every grid point, since this would provide mp equations, and m boundary conditions should still be added. This implies that m fluid equations must be disregarded, but that selection is not at all trivial when boundary conditions are set at different points (B, S and N).

Chapter 4

Particle-in-cell modelling of electrostatic plasmas

4.1 Kinetic theory

At the microscopic level, plasmas are formed by charged and neutral particles that interact among each other. Solving and tracking the state (position and velocity) of each particle in time would give an exact representation of the plasma behaviour, but this is not practical due to the large number of particles. Instead, the kinetic theory uses a statistical approach to solve the evolution of the distribution function $f_s(\boldsymbol{x}, \boldsymbol{v}, t)$ of a species s in time and in the six-dimensional phase space $(\boldsymbol{x}, \boldsymbol{v})$ formed by position $\boldsymbol{x}$ and velocity $\boldsymbol{v}$. The individual particles, with certain position $\boldsymbol{x}_p$ and velocity $\boldsymbol{v}_p$ can be represented as points in phase space. At a given time t, the value $f_s(\boldsymbol{x}, \boldsymbol{v}, t)$ is defined as the density of particles with $\boldsymbol{x}_p$ and $\boldsymbol{v}_p$ lying inside the infinitesimal volume from $(\boldsymbol{x}, \boldsymbol{v})$ to $(\boldsymbol{x} + \mathrm{d}\boldsymbol{x}, \boldsymbol{v} + \mathrm{d}\boldsymbol{v})$. The distribution function is governed by the Boltzmann equation [16]

$$\frac{\partial f_s}{\partial t} + \boldsymbol{v} \cdot \nabla f_s + \frac{q_s}{m_s} (\boldsymbol{E} + \boldsymbol{v} \times \boldsymbol{B}) \cdot \nabla_v f_s = \left(\frac{\delta f_s}{\delta t} \right)_{\text{coll}}, \tag{4.1}$$

where ∇_v is the gradient operator in the velocity space, m_s and q_s are the mass and charge of the species particles, and $(\delta f_s / \delta t)_{\text{coll}}$ accounts for the effect of collisions. The term dot-multiplying $\nabla_v f_s$ is the acceleration vector, that has been particularized for our case of interest where the only forces on the plasma come from the macroscopically smoothed electric $\boldsymbol{E}(\boldsymbol{x}, t)$ and magnetic $\boldsymbol{B}(\boldsymbol{x}, t)$ fields.

The distribution function contains all the information from each species behaviour, and the more meaningful macroscopic properties can be computed from it by taking moments in the velocity space from $-\infty$ to $+\infty$. The macroscopic

density $\varphi_s(\boldsymbol{x},t)$ of certain property $\Phi_s(\boldsymbol{x},\boldsymbol{v},t)$ can be computed as

$$\varphi_s(\boldsymbol{x},t) = n_s\langle\Phi_s\rangle_v = \iiint_v \Phi_s f_s \ \mathrm{d}^3v \tag{4.2}$$

where $\langle\Phi_s\rangle_v(\boldsymbol{x},t)$ is the average of $\Phi_s(\boldsymbol{x},\boldsymbol{v},t)$ in velocity space (or through particles at given $\boldsymbol{x}$) and $n_s(\boldsymbol{x},t)$ is the number density. Some interesting macroscopic magnitudes, used in fluid formulations of Chapters 2 and 3, are:

- The number density ($\Phi_s = 1$)

$$n_s = \iiint_v f_s \ \mathrm{d}^3v. \tag{4.3}$$

- The particle flow vector ($\Phi_s = \boldsymbol{v}$)

$$\boldsymbol{g}_s = n_s \left\langle \boldsymbol{v} \right\rangle_v = \iiint_v \boldsymbol{v} f_s \ \mathrm{d}^3v. \tag{4.4}$$

  Defining the fluid or macroscopic average velocity vector as $\boldsymbol{u}_s = \left\langle \boldsymbol{v} \right\rangle_v$, the particle flow can be expressed as $\boldsymbol{g}_s = n_s\boldsymbol{u}_s$. The particle velocity $\boldsymbol{v}$ can be decomposed as $\boldsymbol{v} = \boldsymbol{u}_s + \boldsymbol{w}$, where $\boldsymbol{w}$ is the random velocity satisfying $\left\langle \boldsymbol{w} \right\rangle_v = 0$.

- The momentum flow tensor ($\Phi_s = m_s\boldsymbol{v}\boldsymbol{v}$)

$$\bar{\boldsymbol{M}}_s = n_s \left\langle m_s\boldsymbol{v}\boldsymbol{v} \right\rangle_v = m_s \iiint_v \boldsymbol{v}\boldsymbol{v} f_s \ \mathrm{d}^3v. \tag{4.5}$$

  By using $\boldsymbol{v} = \boldsymbol{u}_s + \boldsymbol{w}$, this tensor can be alternatively expressed as $\bar{\boldsymbol{M}} = m_s n_s \boldsymbol{u}_s\boldsymbol{u}_s + \bar{\boldsymbol{p}}_s$, where the first term is the contribution of macroscopic velocity and $\bar{\boldsymbol{p}}_s = m_s n_s \left\langle \boldsymbol{w}\boldsymbol{w} \right\rangle$ is the pressure tensor accounting for the momentum flow due to random particle motion. The scalar pressure definition is $p_s = \frac{1}{3}\mathrm{trace}(\boldsymbol{p}_s) = \frac{1}{3}m_s n_s \left\langle \boldsymbol{w}\cdot\boldsymbol{w} \right\rangle$. Similarly the absolute temperature is $T_s = p_s/n_s$.

- The energy flow vector ($\Phi_s = \frac{1}{2}m_s v^2\boldsymbol{v}$)

$$\boldsymbol{P}_s'' = n_s \left\langle \frac{1}{2}m_s v^2 \boldsymbol{v} \right\rangle_v = \frac{1}{2}m_s \iiint_v v^2\boldsymbol{v} f_s \ \mathrm{d}^3v, \tag{4.6}$$

  which, using previous definitions, can be decomposed as

$$\boldsymbol{P}_s'' = \frac{1}{2}m_s n_s u_s^2 \boldsymbol{u}_s + \frac{3}{2}p_s\boldsymbol{u}_s + \boldsymbol{u}_s\cdot\bar{\boldsymbol{p}}_s + \boldsymbol{q}_s;$$

  being the last term the heat flow vector $\boldsymbol{q}_s = \frac{1}{2}m_s n_s \left\langle w^2\boldsymbol{w} \right\rangle$.

In a similar way, moments of the Boltzmann equation (4.1) can be taken, yielding the macroscopic transport equations [16]. Each new moment introduces, however, an

additional unknown macroscopic variable that is governed by higher order moments. To avoid solving infinitely many equations, the fluid approach accounts for the first moments of the Boltzmann equations and takes a closure assumption. For example, in chapter 2, the electron model considers moments up to the energy equation and the system is closed with a Fourier law for the heat flow $\boldsymbol{q}_e = -\bar{\boldsymbol{\kappa}}_{\perp e} \cdot \nabla T_e$. Typical closures imply cold, Maxwellian or bi-Maxwellian distribution functions; which may not be suitable in unmagnetized and/or low collisionality conditions, such as those in the Hall discharge. Also, in the context of plasma oscillations, the macroscopic models may miss kinetic effects in particle-wave interaction that can lead, e.g., to Landau or inverse-Landau damping [16, 32, 33], some instabilities such as the electron-cyclotron drift instability (ECDI) [11, 12] or particle-wave trapping.

The numerical treatment of the Boltzmann equation may involve several modules:

- Solving the electric and magnetic fields ($\boldsymbol{E}$ and $\boldsymbol{B}$), which have a collective contribution from the particle interactions in the plasma and, thus, depend on the particles distribution in space. Therefore, they have to be solved together with the distribution functions. In Hall plasmas, it is usually assumed that the fields are electrostatic; with negligible self-induced $\boldsymbol{B}$ and $\boldsymbol{E} = -\nabla\phi$ coming from an electric potential ϕ, solution to Poisson's equation

$$\nabla^2\phi = -\frac{\rho_c}{\varepsilon_0}. \tag{4.7}$$

  Here, ε_0 is the permittivity of free space and $\rho_c = \sum_s q_s n_s$ is the net electric charge density. The value of $\boldsymbol{B}$ comes from sources external to the system and is given.

- Solving the transport of f_s in the six-dimensional space $(\boldsymbol{x}, \boldsymbol{v})$ and time. This is, dealing with the left-hand side of equation (4.1). If collisions are disregarded, f_s is conserved along the streamlines in the phase space. Numerical approaches can be divided, very generally, in [20] Vlasov solvers and particle-in-cell (PIC) codes. Vlasov codes use an Eulerian description to directly solve the the evolution of f_s in the phase space on a given grid. On the other hand, PIC codes use a Lagrangian description to follow the motion of macroparticles along characteristic lines that conserve f_s. The characteristics can be solved from the equations of motion

$$\frac{\mathrm{d}\boldsymbol{x}_p}{\mathrm{d}t} = \boldsymbol{v}_p \tag{4.8}$$

  and

$$\frac{\mathrm{d}\boldsymbol{v}_p}{\mathrm{d}t} = \frac{q_s}{m_s}\left(\boldsymbol{E} + \boldsymbol{v}_p \times \boldsymbol{B}\right) \tag{4.9}$$

  of the macroparticles. Each macroparticle represents certain number W_p of real particles (this is the macroparticle weight or clumping factor). The

distribution function (or its moments) can be reconstructed statistically from the macroparticle states. The main drawback of the PIC approach is the inherent statistical noise compared to the almost noise-free Vlasov solutions. However, Vlasov codes can be very demanding due to the high dimensionality of the problem and more prone to numerical stability issues [104]. Due to its conceptual simplicity and the background of EP2 [105–107], the PIC approach is the preferred option in this thesis.

- Solving for the effect of collisions, which break the conservation of f_s along characteristics. Within the PIC framework, collisions are simulated with the Monte-Carlo Collisions (MCC) [108] or Direct Simulation Monte-Carlo (DSMC) [109] methods. The MCC technique simulates the effects on the macroparticles of a certain species colliding with a background cloud and it is accurate when the collisions have a negligible effect on the target background species (e.g, an electron colliding with a heavy species). In the DSMC approach, macroparticles are collided with other actual macroparticles in the simulation. Collisions may imply creation/removal of particles (e.g, ionization event), as well as changes in velocities of the colliding particles.

4.2 Structure of the in-house developed PIC code

In order to study kinetic instabilities and other effects not captured by conventional macroscopic formulations, PIC and Poisson solvers have been developed in the context of the theses of Enrique Bello Benítez and Alberto Marín Cebrián. The optimization of the codes was tackled during a research stay at LAPLACE laboratory and is described in the next chapter.

Due to the excessive computational workload, three-dimensional PIC codes are not very extended for Hall thruster simulation (although there are some attempts [110–112]). The developed codes are kept two-dimensional in physical space (but three-dimensional in velocity i.e., a 2D3V model) and operates on a uniform Cartesian mesh. The model is able to work with several species of ions, electrons and neutrals (the simulations shown in this thesis account for two species: singly-charged ions and electrons). The development of the PIC code has taken advantage of previous developments of EP2 and has adapted some of the routines and algorithms used in the PIC module of the hybrid model HYPHEN [35] by Adrián Domínguez Vázquez.

The whole code is divided in three big blocks that are executed independently and communicate through files in HDF5 format: input generation, core program and post-processing. In the next subsections, the most relevant features and algorithms

are summarized.

4.2.1 Input generation

The input generation is done in Python. The input parameters of the simulation are gathered in Python files that contain the information about: physical constants, mesh, boundary conditions, macroparticle populations, collision processes, time steps, print-outs and other simulation settings. Those inputs are used to generate the mesh, surface elements, initial populations and collision data; which are saved in a HDF5 file called *SimState.hdf5*.

Uniform Cartesian mesh

The PIC and Poisson codes operate on a 2D rectangular domain with sides $L_{x,y}$, discretized in a uniform Cartesian mesh with coordinates (x, y) and grid spacing Δx and Δy. The cell size should be small enough to resolve the local Debye length in order to capture the non-neutrality at small scales and prevent the numerical heating caused by the finite-grid instability [113,114]. In each direction, the numbers of used nodes are $N_{x,y}$. Similarly, there are $(N_{x,y} - 1)$ cells in each direction. Nodes and cells indexes are i and j, in x and y coordinates respectively. The node (i, j) is the left-bottom corner of cell (i, j) and has position

$$x_i = x_1 + i\Delta x \tag{4.10}$$

$$y_j = y_1 + j\Delta y. \tag{4.11}$$

where x_1 and y_1 stand for the coordinates of the left-bottom corner of the domain. In the uniform mesh, all cells have the same volume $\Delta V = \Delta x \Delta y \Delta z$ (since the domain is 2D, $\Delta z = 1$ m is taken for area and volume computations always). For calculation of macroscopic magnitudes at the nodes, each one has an associated volume $\Delta V_{i,j}$; which will be different for interior ($\Delta V_{i,j} = \Delta V$), boundary ($\Delta V_{i,j} = \Delta V/2$) and corner nodes ($\Delta V_{i,j} = \Delta V/4$). The cell surfaces corresponding to boundaries constitute *important* surface elements and their information is also generated and stored: coordinates, normal vector, area and type of interaction with particles (e.g., periodic or absorbing).

Routines and algorithms used in the PIC module of HYPHEN [35] were generalized for non-uniform meshes. By using constant grid spacing, some steps and calculations of the code are simplified and performed more efficiently. The most relevant is the use of computational coordinates, which are an alternative coordinate system (ξ, η) that is convenient since they take values between 0 and $(N_{x,y} - 1)$ in a uniform computational mesh with grid spacing $\Delta\xi = \Delta\eta = 1$. The computational

position of a macroparticle $\boldsymbol{\xi}_p = (\xi_p, \eta_p)$ is very useful since $(\lfloor \xi_p \rfloor + 1, \lfloor \eta_p \rfloor + 1)$ gives the indexes of the cell where the macroparticle is contained. This is crucial, e.g., to detect macroparticles out of domain or to know surrounding nodes for volumetric weighting. When the physical mesh is not uniform, the calculation of $\boldsymbol{\xi}_p$ given the physical one $\boldsymbol{x}_p$ may not be analytical and involves an iterative computation. When both meshes are uniform, the relation between $\boldsymbol{\xi}_p$ and $\boldsymbol{x}_p$ is simply

$$\xi_p = \frac{x_p - x_1}{\Delta x} \tag{4.12}$$

$$\eta_p = \frac{y_p - y_1}{\Delta y}, \tag{4.13}$$

and there is no need to iterate, which alleviates computationally some steps in the PIC code.

Generation of the initial population

The initial populations can be generated directly from macroparticle states or sampling randomly particles from a Maxwellian VDF

$$f_s(\boldsymbol{x}, \boldsymbol{v}) = n_s(\boldsymbol{x}) \left[\frac{m_s}{2\pi T_s(\boldsymbol{x})} \right]^{3/2} \exp\left[-\frac{m_s w^2}{2T_s(\boldsymbol{x})} \right], \tag{4.14}$$

with $w^2 = [\boldsymbol{v} - \boldsymbol{u}_s(\boldsymbol{x})] \cdot [\boldsymbol{v} - \boldsymbol{u}_s(\boldsymbol{x})]$, given the evolution of macroscopic properties at the mesh nodes. The sampling process is done cell by cell, being $n_s(\boldsymbol{x}_k)\Delta V / W_p$ the number of particles to be injected; with $n_s(\boldsymbol{x}_k)$ being average density at the k^{th} cell and given the macroparticle weight W_p. In many cases, a uniform density $n_s(\boldsymbol{x}) = n_s$ is used to start and it is convenient to fix the initial number of particles per cell N_{cell}, which determines the macroparticle weight $W_p = n_s \Delta V / N_{\text{cell}}$ used in the simulation.

Macroparticles are loaded uniformly in each cell. For an arbitrary cell element k with indexes (i, j), positions are given by

$$x_p = x_i + \Delta x R_1 \tag{4.15}$$

and

$$y_p = y_j + \Delta y R_2, \tag{4.16}$$

where $\boldsymbol{x}_k = (x_i, y_j)$ are the coordinates of the left-bottom node of the cell and $R_{1,2} \sim U(0, 1)$ [i.e, they are random numbers uniformly distributed in the interval (0,1)].

The velocities of the particles should reproduce the Maxwellian distribution (4.14). The normalized distribution function reads

$$\bar{f}_s(w) = \frac{f_s(w)}{n_s} = \left(\frac{1}{\sqrt{2\pi}\sigma} \right)^3 \exp\left(-\frac{w^2}{2\sigma^2} \right) \tag{4.17}$$

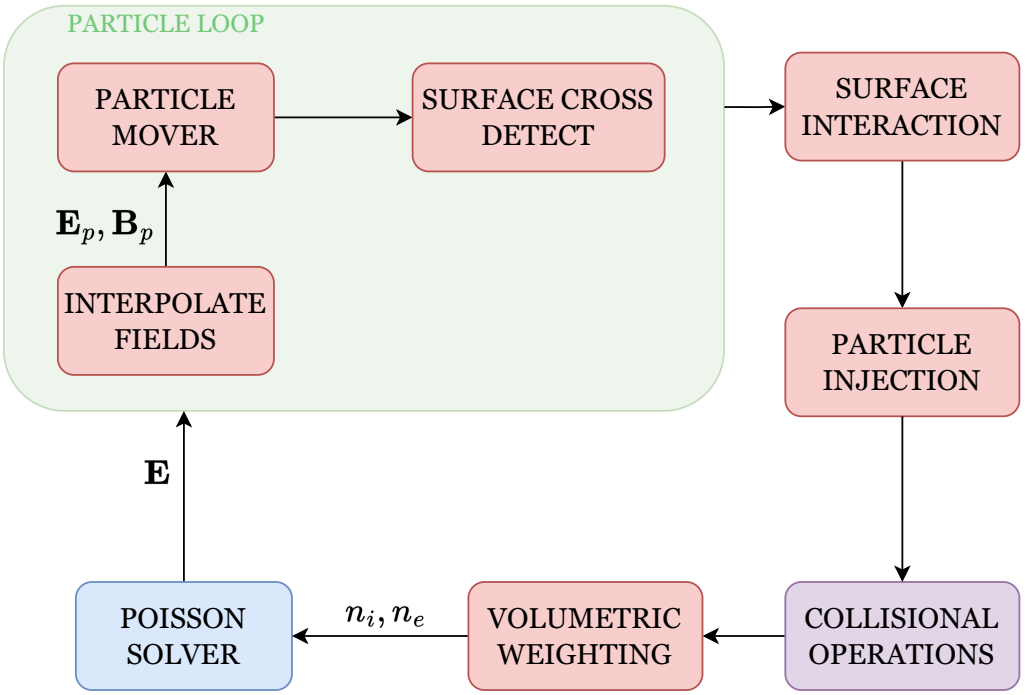

Figure 4.1: Diagram with the structure of the temporal loop the core program. Red boxes are PIC routines. The green box denotes operations that are repeated for every macroparticle in the simulation.

with fixed macroscopic properties and $\sigma = \sqrt{T_s/m_s}$ being the standard deviation or thermal velocity of the species. The previous expression can be factorized in three 1D VDFs as $\bar{f}_s(w) = \bar{f}_{xs}(w_x)\bar{f}_{ys}(w_y)\bar{f}_{zs}(w_z)$, being

$$\bar{f}_{\alpha s}(w_k) = \frac{1}{\sqrt{2\pi}\sigma} \exp\left(-\frac{w_k^2}{2\sigma^2}\right). \tag{4.18}$$

with $\alpha = x, y, z$. The inverse cumulative method [115] is used in the three directions to sample the random velocities, according to

$$w_\alpha = \sqrt{2}\sigma \ \mathrm{erf}^{-1}(2R_\alpha - 1), \tag{4.19}$$

where, again, $R_k \sim U(0, 1)$. For each species, a *particle list* is generated gathering $\boldsymbol{\xi}_p$, $\boldsymbol{x}_p$, $\boldsymbol{v}_p$ and W_p. The index or position of each particle in the list is what we call the particle ID or k_p.

4.2.2 Core program

The core program is coded in Fortran90. All the information from the SimState file is loaded into the PIC program. In figure 4.1, the main operations done each time step Δt are summarized. The value of Δt must be small enough so that particles travel less than one cell per step and to resolve properly all the relevant

time scales of the problem (gyromotion, plasma oscillations and collisions); being the most restrictive condition in Hall plasmas $\omega_{Pe}\Delta t$, based on the value of the electron plasma frequency $\omega_{Pe} = \sqrt{n_e e^2/m_e\varepsilon_0}$ (where e is the electron charge). Starting in the *volumetric weighting*, the steps summarized in figure 4.1 are:

1. Volumetric weighting. From the states of the macroparticles, this operation calculates on the nodes: macroscopic magnitudes (n_s, $\boldsymbol{g}_s$, $\bar{\boldsymbol{M}}_s$ and $\boldsymbol{P}_s''$) and distribution functions (f_s, only in some prescribed nodes) for each species, and charge density (ρ_c). This is done by adding up the contribution of each macroparticle to these magnitudes in the nodes, using a weighting scheme. Many of these calculations are not strictly required for the PIC method and are calculated for the post-processing. The only mandatory magnitude is ρ_c (at the current state of the program), which is needed to solve the Poisson equation.

2. Poisson solver. It is coded in Fortran90 as an in-house library that is called by the core PIC program. It uses either finite-difference or spectral methods (depending on the problem) to numerically solve the Poisson equation (4.7) for $\phi(\boldsymbol{x})$ and $\boldsymbol{E}(\boldsymbol{x})$ on the nodes.

3. Particle loop. It includes operations that are repeated for each macroparticle in the simulation:

   (a) Interpolate fields. The values of $\boldsymbol{E}(\boldsymbol{x})$ and $\boldsymbol{B}(\boldsymbol{x})$ are interpolated to the particle position $\boldsymbol{x}_p$, yielding the local values $\boldsymbol{E}_p$ and $\boldsymbol{B}_p$.

   (b) Particle mover. It updates $\boldsymbol{x}_p$ and $\boldsymbol{v}_p$ one Δt, solving the equations of motion (4.8) and (4.9) with the values of $\boldsymbol{E}_p$ and $\boldsymbol{B}_p$ from the interpolation. This is numerically accomplished using the Boris method [116, 117], quite standard in PIC modelling of magnetized plasmas.

   (c) Surface cross detect. Here, crosses of particles with important surface elements (i.e, those on boundaries) are detected. If any, information about the cross is recorded in a *hit list*: ID of the crossing particle, surface element crossed, position and velocity at the crossing point.

4. Surface interaction. In this module, the hit list is traversed and boundary conditions are applied to macroparticles that crossed boundaries. For the simulations shown in this thesis, boundary conditions can be periodic or absorbing. If further boundary crosses happen in the same Δt (e.g, a particle goes through a periodic boundary and then cross an absorbing one), they are detected and resolved here. At this point, *surface weighting* is also done, which computes surface fluxes by adding up the contributions of crossing particles.

5. Particle injection. It is the operation of adding new particles in the domain and can be either volumetric or surface injection.

6. Collisional operations. Here the effect of scattering and collision events of particles species with other particles or background species are simulated. At the moment, only simple scattering with given frequency and ionization MCC are implemented.

The main results obtained from the simulations are: evolution of the macroscopic properties and electric field, distribution functions at selected nodes or fluxes through boundaries. These data at certain print-out steps are stored in a HDF5 file *PostData.hdf5*. At the end of the simulation (or at some intermediate steps), another SimState file is generated (having the same structure as the one created in the input generation) with the final state of the macroparticles and any data required to relaunch simulations. In the post-processing, the PostData file is loaded in Python or MATLAB programs to generate figures and produce results. This block is very simulation specific (e.g, Hall or Penning discharges).

4.3 PIC model

In this section, the main PIC routines (red boxes in figure 4.1) are described in detail, with emphasis in those that have been modified or simplified with respect to HYPHEN [35].

4.3.1 Particle loop

This subsection describes routines that are applied to every particle present in the simulation at the beginning of the time step. As aforementioned, the particles data are stored in a particle list matrix. Since the number of particles can vary significantly along a simulation, the list is allocated for a maximum number of particles $N_{p,\max}$, of which $N_p \leq N_{p,\max}$ are actual particles in the simulation at a certain time step. The other $N_{p,\max} - N_p$ entries of the list are empty.

Field interpolation

The field interpolation to the local value seen by a particle uses $\boldsymbol{\xi}_p$ to pinpoint the cell where the particle is. Then, $\boldsymbol{E}$ is bi-linearly interpolated to $\boldsymbol{\xi}_p$ according to

$$\boldsymbol{E}_p = \sum_{k=1}^{4} \boldsymbol{E}(\boldsymbol{x}_k) S_k(\boldsymbol{\xi}_p), \tag{4.20}$$

where the bilinear weight function reads [118]

$$S_k(\boldsymbol{\xi}) = (1-|\xi-\xi_k|)(1-|\eta-\eta_k|) \quad \text{if } \{\xi_k, \eta_k\} \in \{[\xi_k-1, \xi_k+1], [\eta_k-1, \eta_k+1]\} \tag{4.21}$$

and $S_k(\boldsymbol{\xi}) = 0$ otherwise. The index k loops through the surrounding nodes (the four corners of the current cell). The calculation of $\boldsymbol{B}_p$ is done similarly.

Particle mover

The update of $\boldsymbol{x}_p$ and $\boldsymbol{v}_p$ is done with the standard Boris method [116,117]. In this approach, the values of $\boldsymbol{x}_p$ and $\boldsymbol{v}_p$ stored in the simulation at a given time step n are shifted $\Delta t/2$. This is, $\boldsymbol{x}_p$ and $\boldsymbol{v}_p$ are known at times t and $t-\Delta t/2$, respectively. Only for this subsection, let us add superscripts to the particle position $\boldsymbol{x}_p^n$ and velocity $\boldsymbol{v}_p^{n-1/2}$ to denote the $\Delta t/2$ shift and the update (elsewhere in this chapter, they are called $\boldsymbol{x}_p$ and $\boldsymbol{v}_p$).

The update of $\boldsymbol{v}_p^{n-1/2}$ to $\boldsymbol{v}_p^{n+1/2}$ undergoes three phases. First, half the acceleration due to the electric field is added, such that

$$\boldsymbol{v}_1 = \boldsymbol{v}_p^{n-1/2} + \frac{q_s \boldsymbol{E}_p}{m_s}\frac{\Delta t}{2}. \tag{4.22}$$

Second, the rotation of the velocity due to the magnetic field is accounted for, through expressions

$$\boldsymbol{v}_2 = \boldsymbol{v}_1 + \boldsymbol{v}_1 \times \tilde{\boldsymbol{\omega}}_{cs} \tag{4.23}$$

and

$$\boldsymbol{v}_3 = \boldsymbol{v}_1 + \frac{2}{1+\tilde{\omega}_{cs}^2}(\boldsymbol{v}_2 \times \tilde{\boldsymbol{\omega}}_{cs}), \tag{4.24}$$

being $\tilde{\boldsymbol{\omega}}_{cs} = q_s \boldsymbol{B}_p \Delta t/2m_s$. The updated velocity is obtained by adding the other half acceleration, yielding

$$\boldsymbol{v}_p^{n+1/2} = \boldsymbol{v}_3 + \frac{q_s \boldsymbol{E}_p}{m_s}\frac{\Delta t}{2}. \tag{4.25}$$

A centred scheme on $n+1/2$ is used to update the position

$$\boldsymbol{x}_p^{n+1} = \boldsymbol{x}_p^n + \boldsymbol{v}_p^{n+1/2}\Delta t. \tag{4.26}$$

Cross detect

The detection of crosses with boundary surface elements has been also simplified with respect to that of HYPHEN, which is an axisymmetric code intended to simulate the Hall-thruster chamber and near plume with a domain having internal boundaries and corners. For this reason, they found convenient to follow every particle along

the time step in search of crosses with boundaries. The simulations shown in this thesis work always on simple rectangular domains. For this reason, it is easier to detect what particles are out of the domain at the end of the step and apply the cross-detect algorithm only to those particles.

The cross detect algorithm is as described in reference [35]. The particle trajectory during the time step is simplified an straight segment from $\boldsymbol{x}_p^n$ to $\boldsymbol{x}_p^{n+1}$, travelled with velocity $\boldsymbol{v}_p^{n+1/2}$. Along the trajectory, it is the goal of the cross-detect algorithm to track the particle during the step in order to determine what cell faces are crossed and detect if any is an important surface element. The crossing time, measured with respect to the beginning of the step, with a certain surface element is

$$\Delta t_{\text{cross}} = \frac{(\boldsymbol{x}_k - \boldsymbol{x}_p^n) \cdot \mathbf{1}_\perp}{\boldsymbol{v}_p^{n+1/2} \cdot \mathbf{1}_\perp}, \tag{4.27}$$

where $\boldsymbol{x}_k$ is the physical position of one of the nodes limiting the considered surface and $\mathbf{1}_\perp$ is an unit vector perpendicular to the surface pointing inwards from the domain. For each travelled cell, this formula can be applied to measure the Δt_{cross} with each cell face. In the initial cell, the crossed face would be that with the minimum positive Δt_{cross}. In subsequent cells, if any, the crossed face would be that with the second minimum positive Δt_{cross} (the minimum one is the entrance point).

The algorithm stops whenever a cross with an important surface element is detected. Having identified the element and the corresponding Δt_{cross}, the crossing point and velocity are approximated as $\boldsymbol{x}_p^n + \boldsymbol{v}_p^{n+1/2}\Delta t_{\text{cross}}$ and $\boldsymbol{v}_p^{n+1/2}$. The information about the cross and the involved particle ID are stored in a *hit list*.

4.3.2 Surface interaction

At the end of the particle loop, all particles out of the domain should have been detected and the hits with the boundary surface elements noted in the hit list. Boundary conditions have to be applied to these particles, since any particle out of the domain will raise errors in the program in future steps. Similarly to the particle one, the hit list matrix is allocated for a maximum of $N_{p,\max}$ hits, of which $N_{\text{hit}} \leq N_{p,\max}$ happen at a certain time step. In the surface interaction model, a loop goes across the hit list, applies boundary conditions and updates fluxes through boundaries.

Boundary conditions

In the simulations shown in this thesis, two types of boundary conditions are used: absorbing and periodic. Those macroparticles hitting absorbing boundaries are

removed from the simulation by deleting the corresponding entry k_p from the particle list. This is done by copying the last active macroparticle in the list (that one with ID N_p) to position k_p. Then the last entry of the list is removed and the number of active macroparticles in the simulation is updated to $N_p - 1$.

On the other hand, periodic boundary conditions conserve the number of particles in the simulation but modify the state of particles at the end of the step. Using an asterisk to denote state after periodic conditions, the velocity is kept $\boldsymbol{v}_p^* = \boldsymbol{v}_p$ and the position is updated to $\boldsymbol{x}_p^* = \boldsymbol{x}_p + L_{x,y}\mathbf{1}_\perp$; using L_x for left/right (vertical) boundaries and L_y for top/bottom (horizontal) ones. Moreover, if the particle leaves the domain through an element k_S with indexes (i_S, j_S), the particle will enter after periodic conditions through element k_S^* with new indexes (i_S^*, j_S^*).

After periodic conditions, the algorithm checks for further hits with boundaries within the same time step (which can happen, e.g., close to corners) following the same logic as in section 4.3.1. The only difference is that additional hits, if any, are not noted in the hit list but the surface interaction is directly solved.

Surface weighting

Each hit with an important surface element updates the fluxes of particles and energy through that element. Fluxes are computed for each element individually, separating inward and outward fluxes. The net fluxes through certain boundary can be computed in the post processing of results. The outwards fluxes of particles and energy of certain species through element k_S read [119, 120]

$$g_{s,k_S}^{(\mathrm{out})} = \frac{1}{\Delta t \Delta A_{k_S}} \sum_p W_p \tag{4.28}$$

and

$$P_{s,k_S}^{''(\mathrm{out})} = \frac{1}{\Delta t \Delta A_{k_S}} \sum_p \frac{1}{2} m_s v_p^2 W_p, \tag{4.29}$$

with the sum across all particle IDs participating in the hit list. Particles hitting periodic boundaries will contribute also to the inward fluxes $g_{s,k_S^*}^{(\mathrm{in})}$ and $P_{s,k_S^*}^{''(\mathrm{in})}$ through element k_S^*.

4.3.3 Particle injection

Volume injection

In volumetric injection, new particles are added to the simulation in the middle of the domain. This can be done, for example, to mimic ionization by injecting the

same amount of ion and electron particles. The code considers several ways to deal with volume injection. The most general approach requires as input a volumetric source $S_s(\boldsymbol{x})$ that gives the number of real particles injected per unit time and volume, together with injection properties $\boldsymbol{u}_s^{(\mathrm{inj})}(\boldsymbol{x})$ and $T_s^{(\mathrm{inj})}(\boldsymbol{x})$. The generated particles follow a Maxwellian VDF.

As an approximation, injection is done cell-wise. For the k^{th} injection cell, injection properties are evaluated at the cell centre $\boldsymbol{x}_k^{(\mathrm{cell})}$. In the initial step, the target number of macroparticles to be injected is $N_p^{(\mathrm{tg})} = S_s(\boldsymbol{x}_k^{(\mathrm{cell})})\Delta V \Delta t / W_p$, where W_p is a prescribed generation weight. The target $N_p^{(\mathrm{tg})}$ does not have to be an integer number. The injection of the non-integer part $N_p^{(\mathrm{tg})} - \lfloor N_p^{(\mathrm{tg})} \rfloor$ is treated probabilistically. With $R \sim U(0,1)$; if $R < N_p^{(\mathrm{tg})} - \lfloor N_p^{(\mathrm{tg})} \rfloor$ the the number of injected particles is $N_p^{(\mathrm{inj})} = \lfloor N_p^{(\mathrm{tg})} \rfloor + 1$. On the other hand, if $R > N_p^{(\mathrm{tg})} - \lfloor N_p^{(\mathrm{tg})} \rfloor$, then $N_p^{(\mathrm{inj})} = \lfloor N_p^{(\mathrm{tg})} \rfloor$. In either case, this injection is introducing an error with respect to the target $N_p^{(\mathrm{err})} = N_p^{(\mathrm{inj})} - N_p^{(\mathrm{tg})}$ in the current time step. This error is accounted for in the next step, with the target being $N_p^{(\mathrm{tg})} = S_s(\boldsymbol{x}_k)\Delta V \Delta t / W_p + N_p^{(\mathrm{err})}$. This process is repeated and $N_p^{(\mathrm{err})}$ updated each time, complying with the intended injection source on average. The sampling of particle positions and velocities is done as explained in section 4.2.1.

Surface injection

This injection is done through boundary surface elements. The number of real particles to be injected per unit time and area is $g_s^{(\mathrm{inj})}(\boldsymbol{x})$, where $\boldsymbol{x}$ is restricted to positions along the boundary. Injection properties $\boldsymbol{u}_s^{(\mathrm{inj})}(\boldsymbol{x})$ and $T_s^{(\mathrm{inj})}(\boldsymbol{x})$ need to be also given. The injection is done element-wise, evaluating $g_s^{(\mathrm{inj})}(\boldsymbol{x})$ at the element centres. In a similar way to volumetric injection, in the first step, the target number of injected particles at the k^{th} element is $N_p^{(\mathrm{tg})} = g_s^{(\mathrm{inj})}(\boldsymbol{x}_k^{(\mathrm{surf})})\Delta A_k \Delta t / W_p$, where $\boldsymbol{x}_k^{(\mathrm{surf})}$ is the position of the centre. The calculation of $N_p^{(\mathrm{inj})}$ and $N_p^{(\mathrm{err})}$ follows the same logic as for volume injection.

The sampling of $\boldsymbol{x}_p$ and $\boldsymbol{v}_p$ shows however some differences with respect to volumetric generation. Regarding $\boldsymbol{v}_p = v_\perp \mathbf{1}_\perp + v_\parallel \mathbf{1}_\parallel + v_z \mathbf{1}_z$, the velocity sampling is done directly from a Maxwellian (see section 4.2.1) in the out-of-plane (v_z) and in-plane surface-parallel ($v_\parallel$) directions. In the direction perpendicular to the surface ($v_\perp$), sampling works differently. If we imagine that a Maxwellian population exist next to the injection surface out of the domain, the particles that are able to cross the boundary and to enter the domain are those injected. Clearly, the probability of a particle crossing the boundary cannot follow a Maxwellian distribution (e.g., a particle with $v_\perp = 0$ must have zero probability of crossing the boundary, even if the Maxwellian shows a maximum at $v_\perp = 0$). Instead, the probability density function of $v_\perp$ is proportional to $v_\perp \bar{f}_{\perp s}(v_\perp)$, with $\bar{f}_{\perp s}$ being a Maxwellian VDF

(4.18) [20, 35, 121]. The sampling of $v_\perp$ can be done with the acceptance-rejection method, as explained in [35].

The value of $\boldsymbol{x}_p$ is computed in two steps: (i) sampling of the entry point $\boldsymbol{x}_0$ and (ii) propagation according to the sampled $\boldsymbol{v}_p$. The entry point is chosen randomly such that

$$\boldsymbol{x}_0 = \boldsymbol{x}_k + R_1|\boldsymbol{x}_{k+1} - \boldsymbol{x}_k|\mathbf{1}_\parallel \tag{4.30}$$

being $\boldsymbol{x}_k$ and $\boldsymbol{x}_{k+1}$ the positions of the surface-element edge nodes and $R \sim U(0,1)$. The position after injection is propagated such that $\boldsymbol{x}_p = \boldsymbol{x}_0 + \boldsymbol{v}_p R_2 \Delta t$. The random time step $R_2\Delta t < \Delta t$ accounts for the fact that injection may happen anytime within the time step.

4.3.4 Volume weighting

Macroscopic properties can be calculated from the state of the particles in the simulation using certain weighting scheme. This is, a discrete version of equation (4.2) that approximates the integral of $f_s(\boldsymbol{x}, \boldsymbol{v}, t)$ in the velocity space at the mesh nodes. In our PIC formulation, this is done directly by summing the contribution of macroparticles to the macroscopic properties. The values of macroscopic properties at the nodes are stored in 2D matrices. At the k^{th} node,

$$\varphi_s(\boldsymbol{x}_k, t) = \frac{1}{\Delta V_k} \sum_p \Phi_{s,p} W_p S_k(\boldsymbol{\xi}_p), \tag{4.31}$$

where $\Phi_{s,p}$ is the value of Φ_s for particle k_p and $S_k(\boldsymbol{\xi}_p)$ is the bilinear computational weight function given by (4.21). The particular version of this equation for the main magnitudes are:

- The number density

$$n_s = \frac{1}{\Delta V_k} \sum_p W_p S_k(\boldsymbol{\xi}_p). \tag{4.32}$$

- The particle flow vector

$$\boldsymbol{g}_s = n_s \boldsymbol{u}_s = \frac{1}{\Delta V_k} \sum_p \boldsymbol{v}_p W_p S_k(\boldsymbol{\xi}_p). \tag{4.33}$$

- The momentum flow tensor

$$\bar{\boldsymbol{M}}_s = m_s n_s \boldsymbol{u}_s \boldsymbol{u}_s + \bar{\boldsymbol{p}}_s = \frac{m_s}{\Delta V_k} \sum_p \boldsymbol{v}_p \boldsymbol{v}_p W_p S_k(\boldsymbol{\xi}_p). \tag{4.34}$$

- The energy flow vector

$$\boldsymbol{P}_s'' = \frac{1}{2} m_s n_s u_s^2 \boldsymbol{u}_s + \frac{3}{2} p_s \boldsymbol{u}_s + \boldsymbol{u}_s \cdot \bar{\boldsymbol{p}}_s + \boldsymbol{q}_s = \frac{m_s}{2\Delta V_k} \sum_p v_p^2 \boldsymbol{v}_p W_p S_k(\boldsymbol{\xi}_p). \tag{4.35}$$

For the conventional PIC method, only the calculation of n_s is strictly necessary (although other magnitudes could be required depending on the collision approach or other algorithms), in order to compute ρ_c. Having the particle densities of every species, the electric charge density reads

$$\rho_c = \sum_s q_s n_s. \tag{4.36}$$

Other moments of the VDF are only computed for producing results. Since the volumetric weighting is computationally expensive, the calculation of unnecessary moments can be restricted to print steps to lighten the simulations.

After HYPHEN [35], a extended time-averaged version of these magnitudes can be computed to reduce the noise intrinsic to the PIC. At time step n, this is done according to

$$\tilde{\varphi}(\boldsymbol{x}_k, t_n) = \frac{(\Delta t_{\mathrm{EW}} - \Delta t)\ \tilde{\varphi}(\boldsymbol{x}_k, t_{n-1}) + \Delta t\ \varphi(\boldsymbol{x}_k, t_n)}{\Delta t_{\mathrm{EW}}}, \tag{4.37}$$

where Δt_{EW} is the time window used for extended weighting magnitudes. If Δt_{EW} is tuned properly, the extended variables can be representative of the instantaneous behaviour. This approach requires to compute the instantaneous magnitudes at every time step (and not only at print steps).

Calculation of the velocity distribution function

Apart from the moments of the VDF, computed with equations (4.32) to (4.35), the VDFs themselves at a certain node k can be also approximated from the state of particles in the simulation. The developed code has the possibility of computing 1D VDFs in some prescribed nodes. To do so, the velocity space is discretized in N_v bins of width Δv, with the minimum captured velocity being v_{min}. A good choice of these parameters is fundamental to accurately reconstruct the VDF.

The computational velocity coordinate in the $\alpha = x, y, z$ direction is defined, analogously to space coordinates (4.12) and (4.13), as

$$\xi_{\alpha p}^{(v)} = \frac{v_\alpha - v_{\mathrm{min}}}{\Delta v}. \tag{4.38}$$

If $\xi_{\alpha p}^{(v)} < 0$ or $\xi_{\alpha p}^{(v)} > N_v$, the particle is discarded and does not contribute to the VDF computation. The bin index to which the particle contributes is $i_v = \lfloor \xi_{\alpha p}^{(v)} \rfloor + 1$. The 1D VDF in the velocity coordinate α on the k^{th} node and ${i_v}^{\mathrm{th}}$ velocity bin is approximated as

$$f_{\alpha s}^{i_v}(\boldsymbol{x}_k, t) = \frac{1}{\Delta V_k \Delta v} \sum_p W_p S_k(\boldsymbol{\xi}_p). \tag{4.39}$$

4.4 Monte-Carlo collisions

For the purpose of this thesis, focused on the physics of instabilities, simple collisions are considered since they do not seem to be an important actor on the main instabilities found in the literature in the context of anomalous transport. Some of the simulations in this work use the MCC approach to model the collisions of particles with a background cloud. Two types of phenomena are considered: (*i*) elastic scattering and (*ii*) ionization collisions.

An efficient implementation of MCC collisions is the null-collision approach, whose steps and reasoning are summarized here based on references [108, 117, 122]. The total probability of collision (several types of collisions may be involved) of a particle from species s with a background species, say neutrals, is given by

$$P_p = 1 - \exp[-\Delta t v_p \sigma_T(\mathcal{E}_p) n_n(\boldsymbol{x}_p)], \tag{4.40}$$

being $n_n(\boldsymbol{x}_p)$ the neutral density at the particle position and $\sigma_T(\mathcal{E}_p)$ the total cross section (including all collision types), which is a function of the particle kinetic energy $\mathcal{E}_p = \frac{1}{2} m_s v_p^2$. The total collision frequency is $\nu_T(\boldsymbol{x}, \mathcal{E}) = \sigma_T(\mathcal{E}) n_n(\boldsymbol{x})$. The particle is considered to experience a collision if $R < P_p$, with $R \sim U(0,1)$. A second random-number sampling can be used to decide the collisional process that actually happens according to the individual probabilities. In the MCC methods collisions are evaluated once per time step; this is accurate for $\nu_T \Delta t \ll 1$, condition amply satisfied by Hall-plasma PIC modelling.

Repeating the computation of P_p for every particle in the simulation can be computationally expensive. The null-collision approach overcomes this drawback by introducing an additional collisional type that is null (i.e., no collision). The null collision has a frequency such that, when added to ν_T, it makes the total collision frequency equal to

$$\nu^* = \max_{\mathcal{E}}(\sigma_T v) \max_{\boldsymbol{x}}(n_n) \tag{4.41}$$

and constant for every $\boldsymbol{x}$ and $\mathcal{E}$. For a constant frequency ν^*, the maximum number of particles experiencing a collision relative to the total number of particles is

$$P^* = 1 - \exp(-\nu^* \Delta t) \approx \nu^* \Delta t, \tag{4.42}$$

where the last approximation holds for $\nu^* \Delta t \ll 1$. This means that collisions will be evaluated for a number of times $P^* N_p$, instead of N_p times in the standard approach, reducing significantly the computational cost. The collision candidates are selected randomly among the macroparticles. Using an example with two real collision types (with frequencies ν_1 and ν_2) plus the null collision, for each candidate, a random number $R \sim U(0,1)$ is sampled and the type of interaction is decided according to:

1. If $R \leq \nu_1(\mathcal{E}_p)/\nu^*$, the particle undergoes collision type 1.

2. If $\nu_1(\mathcal{E}_p)/\nu^* < R \leq [\nu_1(\mathcal{E}_p) + \nu_2(\mathcal{E}_p)]/\nu^*$, the particle undergoes collision type 1.

3. If $[\nu_1(\mathcal{E}_p) + \nu_2(\mathcal{E}_p)]/\nu^* < R$, the particle undergoes a null collision meaning that it does not experience a real collision.

In the following subsections, scattering and ionization interactions are described as implemented in the code.

4.4.1 Elastic scattering

This is a simple approach to introduce some collisionality by directly giving a scattering frequency distribution $\nu_{\text{sct}}(\boldsymbol{x})$ in the domain. In this simplified case, the collision frequency depends only on the particle position and no models for cross-sections are needed. Moreover, there is a single particle involved in each collision event. We consider that this scattering conserves the energy, mimicking elastic collisions; although the algorithm could be easily adjusted to have some inelastic losses. The elastic scattering has been used to model the anomalous transport in Hall-thruster PIC simulations that omit the azimuthal dimension [107].

Particles that undergo this interaction experience a random rotation of their velocity vectors keeping the norms intact. The velocity components after the scattering read

$$v'_{xp} = v_p \sin\beta_1 \cos\beta_2, \tag{4.43}$$

$$v'_{yp} = v_p \sin\beta_1 \sin\beta_2 \tag{4.44}$$

and

$$v'_{zp} = v_p \cos\beta_1, \tag{4.45}$$

with the prime denoting the state after the scattering event. The angles β_1 and β_2 are randomly sampled from

$$\beta_1 = \arccos(2R_1 - 1) \quad \text{and} \quad \beta_2 = 2\pi R_2 \tag{4.46}$$

with $R_{1,2} \sim U(0,1)$.

4.4.2 Ionization

Here we consider the collision of electrons with a background cloud of neutrals. Each ionization event involves the collision of an incoming electron and a target neutral; which yields an ejected (new) electron, a new ion and the scattered incoming electron. In the MCC approach, the neutral particle is sampled from a Maxwellian

VDF, as in subsection 4.2.1, knowing the properties $n_n(\boldsymbol{x})$, $\boldsymbol{u}_n(\boldsymbol{x})$ and $T_n(\boldsymbol{x})$ of the background neutral cloud. Auxiliary models are needed for the ionization cross-section σ_{ion} and the scattering of the electron particles, which depend on the type of neutral species (e.g., helium, argon or xenon).

Since the neutral and ion particles are much heavier than the electrons, the generated ion is assumed to have the same velocity as the sampled neutral particle. The incoming electron has initially a kinetic energy $\mathcal{E}_{e,\text{inc}}$ that should be greater than the ionization energy $\mathcal{E}_{\text{ion}}$ for the ionization event to be feasible. The remaining energy after the collision is split between the scattered incoming electron $\mathcal{E}'_{e,\text{inc}}$ and the ejected new one $\mathcal{E}_{e,\text{ej}}$, thus satisfying

$$\mathcal{E}'_{e,\text{inc}} + \mathcal{E}_{e,\text{ej}} = \mathcal{E}_{e,\text{inc}} - \mathcal{E}_{\text{ion}}. \tag{4.47}$$

What fraction of the remaining energy is assigned to $\mathcal{E}'_{e,\text{inc}}$ and $\mathcal{E}_{e,\text{ej}}$ is a modelling decision. Let us introduce the energy splitting factor $F \in [0, 1]$, such that

$$\mathcal{E}'_{e,\text{inc}} = F(\mathcal{E}_{e,\text{inc}} - \mathcal{E}_{\text{ion}}), \tag{4.48}$$

which combined with (4.47) yields

$$\mathcal{E}_{e,\text{ej}} = (1 - F)(\mathcal{E}_{e,\text{inc}} - \mathcal{E}_{\text{ion}}). \tag{4.49}$$

By deciding the value of F, the values of $\mathcal{E}'_{e,\text{inc}}$ and $\mathcal{E}_{e,\text{ej}}$ can be computed. The simplest approach is to set $F = 0.5$, thus diving the energy evenly between the two electrons. Another possibility is to take random values of F. Other authors [108, 123, 124] propose more complex approaches.

The kinetic energies $\mathcal{E}'_{e,\text{inc}}$ and $\mathcal{E}_{e,\text{ej}}$ can be used to compute the modules $v_p = \sqrt{2\mathcal{E}_p/m_e}$ of the velocity vectors of electrons after the ionization event. The direction of such vectors is determined by the scattering model. Reference [122] suggests a random isotropic scattering, such as that in subsection 4.4.1. In references [108, 125] more intricate expressions are proposed.

4.5 Poisson solver

The Poisson solver is independent from the PIC method and, given the charge density and boundary conditions, solves equation (4.7) for $\phi(\boldsymbol{x})$. It also computes the electric field from $\boldsymbol{E}(\boldsymbol{x}) = -\nabla\phi$. Two methods are considered depending on the boundary conditions. For fully periodic conditions on every boundary, a spectral solver is used. Otherwise, central finite differences are used.

4.5.1 Finite-difference method

At the k^{th} internal node with indexes (i, j), the Poisson equation is discretized with centred finite differences as

$$\frac{\phi_{i+1,j} - 2\phi_{i,j} + \phi_{i-1,j}}{\Delta x^2} + \frac{\phi_{i,j+1} - 2\phi_{i,j} + \phi_{i,j-1}}{\Delta y^2} = -\frac{1}{\varepsilon_0}\rho_c(\boldsymbol{x}_k), \tag{4.50}$$

where $\phi_{i,j}$ is the electric potential evaluated at node (i, j).

At boundary nodes, the discrete equations depend on the boundary conditions. For the simulations shown in this thesis, two cases are considered: Dirichlet and periodic conditions. Dirichlet conditions are the simplest case, since the value of the potential is given as

$$\phi_{i,j} = \phi_0(\boldsymbol{x}_k). \tag{4.51}$$

For periodic conditions, let us use the example of top/bottom boundaries being periodic. Node at this boundaries have either $j = 1$ or $j = N_y$. We consider periodicity along this direction to happen every L_y. For the pair $\phi_{i,1}$ and ϕ_{i,N_y}, two equations are provided. First, periodic conditions imply that these two potentials must be equal so that $\phi_{i,1} - \phi_{i,N_y} = 0$. And second, one of these two nodes is treated as internal and the discrete Poisson equation (4.50) is evaluated, taking into account the periodicity of the solution when potential values are of the domain appear in the expression. If evaluated at node (i, N_y), equation (4.50) reads

$$\frac{\phi_{i+1,j} - 2\phi_{i,j} + \phi_{i-1,j}}{\Delta x^2} + \frac{\phi_{i,2} - 2\phi_{i,N_y} + \phi_{i,N_y-1}}{\Delta y^2} = -\frac{1}{\varepsilon_0}\rho_c(\boldsymbol{x}_k), \tag{4.52}$$

where the second term in the left-hand side applies periodicity. Periodic conditions on left/right boundaries are treated in a similar way.

After discretization, the Poisson problem becomes a linear system

$$\bar{\boldsymbol{A}} \cdot \boldsymbol{\phi} = \boldsymbol{b}, \tag{4.53}$$

by gathering equations (4.50), (4.51) and (4.52) into matrix form. The coefficients of $\bar{\boldsymbol{A}}$ and $\boldsymbol{b}$ are given by the left and right-hand sides of these equations. The vector $\boldsymbol{\phi}$ collects the unknowns of the problem, i.e., the potential values at every node. External solvers are used to solve the linear system, taking advantage of the sparsity of $\bar{\boldsymbol{A}}$. We have used the iterative solver of LIS [126–129] and direct solvers of PARDISO project [130–132] and Intel®, obtaining the best results with the version of PARDISO in the Intel® Math Kernel Library (MKL).

Once the potential is known, the electric field at internal nodes is approximated using, again, the central-finite differences expressions

$$E_x(\boldsymbol{x}_k) = \frac{\phi_{i+1,j} - \phi_{i-1,j}}{2\Delta x} \tag{4.54}$$

and

$$E_y(\boldsymbol{x}_k) = \frac{\phi_{i,j+1} - \phi_{i,j-1}}{2\Delta x}. \tag{4.55}$$

On boundary nodes, second order backwards or forward differences are used when necessary. For example, on left/right boundaries, the calculation of E_x when $i = 1$ uses the forward scheme

$$E_x(\boldsymbol{x}_k) = \frac{-\phi_{i+2,j} + 4\phi_{i+1,j} - 3\phi_{i,j}}{2\Delta x}. \tag{4.56}$$

When $i = N_x$, the backwards scheme

$$E_x(\boldsymbol{x}_k) = \frac{\phi_{i-2,j} - 4\phi_{i-1,j} + 3\phi_{i,j}}{2\Delta x} \tag{4.57}$$

is used. The computation of E_y at top/bottom boundaries (i.e., when $j = 1$ or $j = N_y$) uses similar expressions.

4.5.2 Spectral method

When all the four boundaries are periodic, the finite difference method in the previous subsection shows some difficulties. The linear system (4.53) under such conditions is ill-posed, being the matrix $\bar{\boldsymbol{A}}$ singular. The physical explanation is that ϕ is only meaningful when measured with respect to a reference potential value ϕ_0. If no Dirichlet conditions are imposed anywhere, such reference does not exist. The problem can be made well-posed by setting a the reference ϕ_0 at an arbitrary point $\boldsymbol{x}_0$.

In addition, periodic conditions set some constraints on the net charge contained in the domain. The Gauss law for the electric field

$$\nabla \cdot \boldsymbol{E} = \frac{\rho_c}{\varepsilon_0} \tag{4.58}$$

can be integrated in the domain volume to get the integral version

$$\oiint_S \boldsymbol{E} \cdot \mathrm{d}\boldsymbol{S} = \frac{Q}{\varepsilon_0} \tag{4.59}$$

where $\mathrm{d}\boldsymbol{S}$ is the vector normal to the boundary with magnitude of a differential surface and $Q = \iiint_V \rho_c \, \mathrm{d}V$ is the net charge. The left-hand side is a closed integral in the domain boundaries and represents the net flux of $\boldsymbol{E}$. Clearly, periodic conditions imply that the net flux of $\boldsymbol{E}$ through boundaries should be zero and so must be Q. This last point is problematic in the PIC method: even if the number of charged particles in the domain should satisfy the zero net charge, it may be the case that $Q \neq 0$ due to PIC noise and the error made in volume weighting. When solving with finite differences, this residual charge usually leads to a large error concentrated at the reference potential location $\boldsymbol{x}_0$ that ruins the Poisson solution.

This issue justifies the need of an spectral solver (even if a workaround may exist with finite differences), which avoids this problem as it will be shown in this section.

The spectral method applied to the Poisson problem on a periodic bounded mesh, applies the discrete Fourier transform (DFT) to the Poisson equation (4.7) and works on a spectral domain, where coordinates are given in terms of the wavevector $\boldsymbol{k} = k_x\mathbf{1}_x + k_y\mathbf{1}_y$ (instead of $\boldsymbol{x} = x\mathbf{1}_x + y\mathbf{1}_y$ in the real space). The real grid spacing Δx and Δy determine the maximum wavenumbers $k_x^{(\max)} = \pi/\Delta x$ and $k_y^{(\max)} = \pi/\Delta y$ that are captured. On the other hand, the real domain lengths $L_{x,y}$ give the spectral grid spacing (i.e., the minimum measurable $k_{x,y}$) $\Delta k_x = 2\pi/L_x$ and $\Delta k_y = 2\pi/L_y$. The spectral mesh includes $k_{x,y}$ in the interval $[-k_{x,y}^{(\max)}, k_{x,y}^{(\max)}]$with spacing $\Delta k_{x,y}$.

Under the DFT framework, ϕ is expanded in terms of functions $\hat{\phi}(\boldsymbol{k})\exp(i\boldsymbol{k}\cdot\boldsymbol{x})$, being $\hat{\phi}(\boldsymbol{k})$ the Fourier transform of $\phi(\boldsymbol{x})$. The same can be done with $\rho_c(\boldsymbol{x})$. These functions are periodic in the real domain and directly satisfy the periodic conditions. Introducing these definition in (4.7) allow us to solve Poisson for each mode and $\boldsymbol{k}$ independently. In the Fourier space the operator ∇ becomes $i\boldsymbol{k}$ and, thus, the Laplacian ∇^2 is $-k^2$. The DFT of equation (4.7) yields

$$k^2\hat{\phi}(\boldsymbol{k}) = \frac{\hat{\rho}_c(\boldsymbol{k})}{\varepsilon_0}, \tag{4.60}$$

so the solution for the potential in the Fourier space is just $\hat{\phi}(\boldsymbol{k}) = \hat{\rho}_c(\boldsymbol{k})/k^2\varepsilon_0$. The electric field is $\hat{\boldsymbol{E}}(\boldsymbol{k}) = i\boldsymbol{k}\hat{\phi}(\boldsymbol{k})$ The potential solution and electric fields in real space [$\phi(\boldsymbol{x})$ and $\boldsymbol{E}(\boldsymbol{x})$] can be recovered from the inverse DFT. The DFT and inverse operations are performed with the FFTW3 external library [133].

Chapter 5

Optimization and benchmark of the particle-in-cell code

This chapter describes the optimization and benchmark of the PIC and Poisson codes. These tasks were accomplished in a three-month research stay in LAPLACE laboratory (Université Paul Sabatier, Toulouse, France) under the supervision of Dr. Laurent Garrigues.

5.1 Optimization of the PIC code

The optimization of the PIC code involves two different areas. The first is a major change in the parallelization approach with respect to HYPHEN's PIC module [35]: using a multiple-particle list approach instead of a single list. The second one is oriented to improve the usage of the processors cache memory by using particle sorting algorithms.

Along sections 5.1 and 5.3, a simple simulation case is run to compare numerical performance of the code when implementing these and other techniques. This simple simulation considers a grid with $N_x = 200$ and $N_y = 50$, with 200 macroparticles per cell (i.e., a total of 4×10^6 macroparticles). Unless said otherwise, the multiple-list version of the code is used with particle sorting every 10 time steps, the program is compiled with the Intel® Fortran compiler and the OpenMP thread affinity is set to 'spread' (the concept of *thread affinity* is introduced in section 5.3).

5.1.1 Parallelization

As discussed in the previous chapter, PIC codes involve many mathematical operations that are repeated for every macroparticle. A typical simulation usually involves several millions of particles. Even if computationally expensive, the fact that most of the operations on macroparticles are independent from each other makes PIC code very suitable for an efficient parallel computing. This is, several macroparticles can be processed at the same time in parallel computing threads. The implementation of the parallelization in the PIC code can have a large impact on the numerical performance and the proper scalability with number of threads. Some decisions that can affect the development of the code are the type of decomposition used (particle or domain decomposition) and the memory management (shared or distributed memory). As for the last point, the code is prepared to work on shared-memory architectures using the OpenMP interface.

Decomposition strategy

Regarding how particles are distributed among parallel threads, in the literature [134] we find PIC codes with domain and particle decomposition approaches. Figure 5.1 shows diagrams for the two strategies. The domain decomposition divides the domain in parallel regions, each one assigned to a thread that processes the particles within. Under this approach, the code has to deal with internal boundaries and transfer between the corresponding threads those macroparticles that cross from one parallel region to another. Moreover, serious thread-load unbalancing can happen if some parallel regions are much more crowded with macroparticles than others (which may be the case with constant W_p in the highly inhomogeneous Hall and Penning discharge simulations), leading to an inefficient parallelization and poor scaling. The unbalancing can be avoided by dynamically changing the size of the parallel regions, as several groups do in reference [134].

Particle decomposition directly distribute portions of the particle list among threads, without taking into account their physical position in the domain. No internal boundaries are required and we can have direct control on the load of each thread. From my point of view, internal boundaries and load balancing make domain decomposition less attractive than particle decomposition for our application. This is the reason why this last strategy is used in our PIC code. In the next part of the subsection, two approaches to particle decomposition are introduced and their numerical performance compared.

(a) Domain decomposition

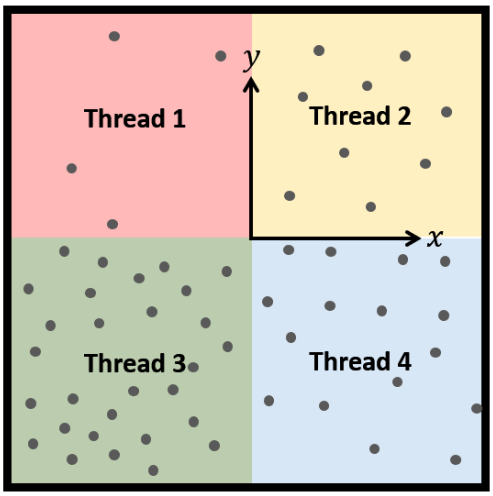

(b) Particle decomposition

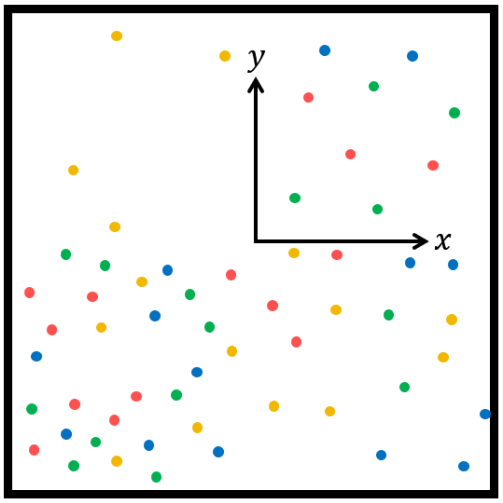

Figure 5.1: Diagrams with the logic behind (a) domain and (b) particle decomposition approaches to distribute particles among threads. Colours represent threads: (a) each thread manages certain region of the domain and (b) each thread manages a number of particles.

Multiple-list particle decomposition

Particle decomposition can be tackled in several ways. During the development of the code, two strategies were followed: single-particle-list (after HYPHEN's PIC module) and multiple-lists (after LAPLACE's PIC code [135–137]).

Before the research stay at LAPLACE, per species, one single particle list (i.e., a matrix with the macroparticles data) and one single matrix per macroscopic property were used. When moving particles, solving surface interaction or injecting new particles, all the parallel threads worked on the same shared particle list. When weighting particles to nodes or surface elements, all the parallel threads updated the same shared matrices. This way of working is, however, very prone to *race conditions*; this is, conflicts when two or more threads try to update the same element at the same time. Race conditions may happen when removing or adding particles in parallel to the shared list, or when two threads try to update the value of certain property in a node at the same time. There are two ways to avoid race conditions: (i) use of `atomic` or `critical` OpenMP clauses to avoid simultaneous reading and writing and (ii) use workaround algorithms, more convoluted than those valid in sequential calculations, that avoid race conditions. In either case, the solution comes at the price of a computational overhead, even in single-thread computations.

On the other hand, in the multiple-list strategy each thread has their own private particle lists and matrices of properties. Since most variables in the code

participating in race conditions are now private to each thread, race conditions are completely avoided. OpenMP special clauses are no longer required and algorithms valid in sequential computing are also valid in parallel. An additional operation called *reduction* is necessary to add up the contribution from each thread to the macroscopic properties. As an illustration, after the weighting is done in parallel by each thread, the total density is

$$n_s = \sum_{k_{\text{th}}} n_s^{(k_{\text{th}})} \tag{5.1}$$

where the superscript k_{th} is the thread index and, thus, $n_s^{(k_{\text{th}})}$ is the density computed by the thread k_{th}. In shared-memory systems, this operation is computationally cheap. Since matrices of properties are duplicated once per thread, this multiple-list approach is much more memory intensive than single-list or domain decomposition and we have found bottlenecks in the parallel scaling for large problems with many nodes. We suspect that the issues we have found are related to the size of the problem compared with the available cache memory. This bottleneck could be overcome by using a cluster of workstations with a distributed-memory parallelization, increasing the available memory; and/or changing the parallel approach to domain decomposition, which is less memory intensive. Fortunately, the simulations shown in this thesis are small enough and not affected by this issue and perform well with the particle-decomposition multiple-list parallelization.

The computational performance of single and multiple-list parallelization approaches is compared in table 5.1 for the simulation described at the beginning of the section. Let us note that the exact numbers and computational savings discussed here are very simulation dependent, but they serve as an illustration. Already in single-thread calculations, the savings in computational time when using the multiple-list version of the code are close to 15% because of the use of simpler algorithms and less OpenMP directives. The scalability of the speed-up, defined as the ratio over the single-core time, with the number of threads is also much better (an ideal speed-up being equal to the number of threads). For 40 threads, the time saving is about 40%, showing the clear advantages of the multiple-list parallelization. Savings are even greater (up to 57%) in percentage if particle sorting is omitted, as it is shown in the next subsection.

Time [s] (speed-up)	**1 thread**	**20 threads**	**40 threads**
Single list	1652	107 (15.4)	77.6 (21.3)
Multiple lists	1410	77.2 (18.3)	46.3 (30.5)

Table 5.1: Comparison of computational times (and speed-up) when using the single-list and multiple-list parallelization.

5.1.2 Particle sorting

The idea behind particle sorting algorithms is to keep macroparticles that are close in the domain also close in the particle list. This can potentially lead to computational time savings due to a more efficient use of the processor cache memory [2], much faster to access than RAM but also much scarcer. Two steps that benefit from sorting are field interpolation and volume weighting.

When interpolating fields to the particle position (see section 4.3.1), the values of $\boldsymbol{E}$ and $\boldsymbol{B}$ on the four vertexes nodes of the cell containing the particle are required. On the other hand, during the volumetric weighting (see section 4.3.4) the values of macroscopic properties at those nodes are updated with the contribution of each particle. These values at the vertexes are loaded from the RAM to the cache memory to be used in the calculations. If particles that are contiguous in the list belong to the same cell, the values stored in the cache memory can be reused and do not need to be reloaded when processing consecutive particles. The saving of skipping the loading step can be significant if the number of macroparticles per cell is high enough (in our experience above 100).

Our PIC code implements an algorithm based on Bowers' paper [2]. The algorithm takes advantage of the fact that the order of particles within the same cell can be ignored, to sort particles in passing only twice through the particle list. The main steps of the algorithm are summarized in figure 5.2 for a small example of 6 particles and 4 cells.

1. Panel 5.2(a) shows the particle list before sorting, with consecutive particles in the list not within the same cell.

2. During the 1^{st} pass across the unsorted list, the number of particles in each cell is counted as shown in panel 5.2(b). Having the number of particles in each cell, we can determine what particles IDs of the sorted list belong to each of the cells. In our small example, we know that the 1^{st} particle ID belong to cell 1, the 2^{nd} and 3^{rd} IDs belong to cell 2, the 4^{th} and 5^{th} IDs belong to cell 3 and the 6^{th} ID belongs to cell 4.

3. The 2^{nd} pass is devoted to the actual sorting of the particles as shown in panel 5.2(b), using the information from the previous step. Again, in the example, particle 1 is located in cell 2 and can be assigned to the 2^{nd} ID of the sorted list, which we know it corresponds to cell 2 and it is free. The same is done for every particle in the unsorted list. When it is the turn of particle 4, it will be assigned to the 3^{rd} ID of the sorted list, since the 2^{nd} ID is already taken by particle 1.

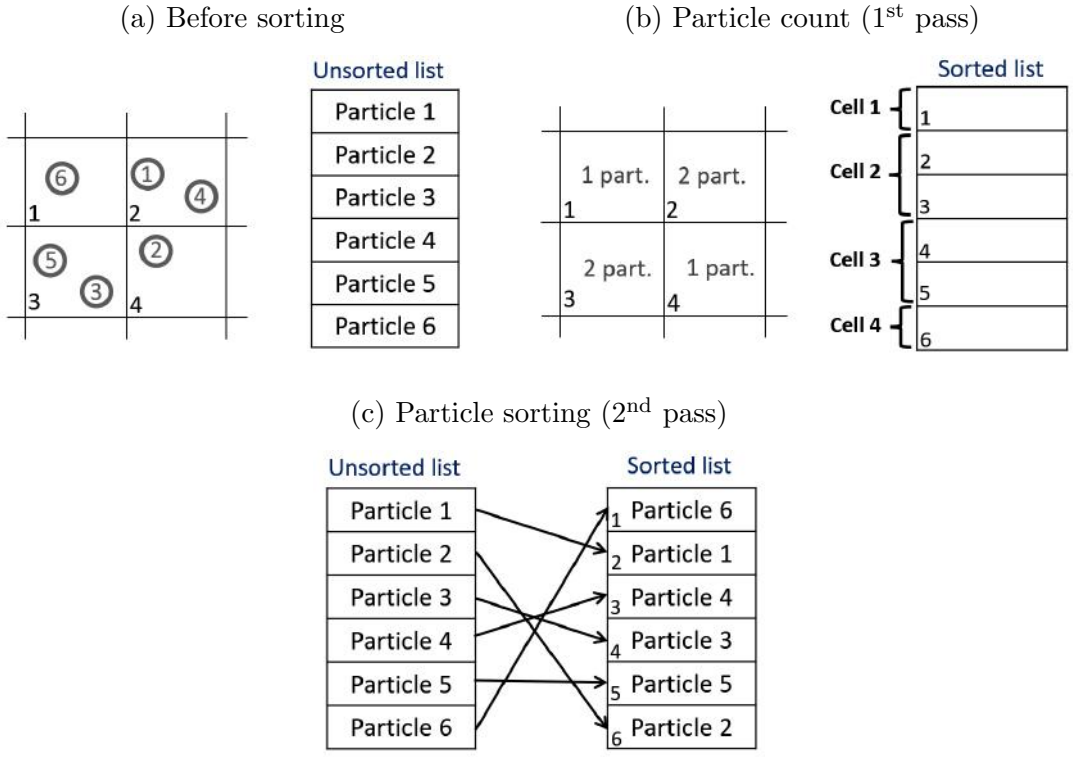

Figure 5.2: Diagram with the steps of the particle-sorting algorithm based on reference [2].

The sorting operation is computationally expensive and, thus, the computational savings of having a sorted list may not be enough to overcome the extra cost of sorting, depending on the case. However, particles should move in each step a distance lower than the cell size to comply with the CFL condition. Therefore, sorting does not need to be done in every step and it is possible to minimize its computational impact while still seeing an improvement in performance.

Tables 5.2 and 5.3 compares computational times (and speed-up) when not sorting particles and when doing it every 1, 10 or 40 steps (in single and parallel computing). Since we observed different behaviours depending on the parallelization approach, results for single (table 5.3) and multiple-list (table 5.2) approaches are included. In both cases, the additional cost of doing a particle sorting every step is not compensated by the better use of cache memory, leading to greater computational times. If sorting is done every 10 time steps, the cost of the sorting operation itself is mitigated and we start seeing a reduced computational time compared with no-sorting. There is an optimum number of steps for sorting that minimizes the computational cost, but in general 10 to 40 steps have been found to work reasonably well.

In the case of multiple-list parallelization (table 5.2), even if some savings due to sorting are observed, the impact is small, of the order of 2.5 to 4% (sorting every 40 steps, which is the best case considered). On the other hand, the single-list version

of the code shows significant improvement about 45% in the parallel cases with 10 and 20 threads. This is not the case of single-thread calculations, where the saving drops close to 1%. These results (together with the better scalability of the speed-up) seem to indicate that particle sorting mitigates partially the inefficiencies of the single-list parallelization. That would also explain why the impact of sorting on the more efficient multiple-list approach are not so important and why computational savings are similar in the single-thread case.

Time [s] (speed-up)	1 thread	10 threads	20 threads
No sorting	1423	147 (9.68)	78.0 (18.2)
Every step	1726	178 (9.70)	108 (16.0)
Every 10 steps	1410	143 (9.86)	77.2 (18.3)
Every 40 steps	1385	141 (9.82)	75.3 (18.4)

Table 5.2: Comparison of computational times (and speed-up) when using particle sorting and a multiple-list parallelization.

Time [s] (speed-up)	1 thread	10 threads	20 threads
No sorting	1671	320 (5.22)	183 (9.13)
Every step	2175	345 (6.30)	250 (8.70)
Every 10 steps	1652	184 (9.00)	107 (15.4)
Every 40 steps	1647	206 (8.00)	115 (14.3)

Table 5.3: Comparison of computational times (and speed-up) when using particle sorting and a single-list parallelization.

5.2 Optimization of the Poisson solver

Here we focus on the finite-difference solver described in section 4.5.1. First, different libraries to solve the Poisson linear system (4.53) are compared in terms of computational time. Then, we consider an alternative Monte-Carlo method to solve the Poisson problem, whose main advantage is much more efficient parallelization.

5.2.1 Linear solvers

As explained in section 4.5.1, after discretization, the Poisson problem becomes a linear system. Having a computationally efficient linear solver is key to minimize the impact of the Poisson solver to the total workload of the code. Two types of methods are considered:

- Iterative. They solve the system iteratively in a certain number of steps until the solution complies with the required tolerance. Starting from an initial guess $\boldsymbol{\phi}_0$, the residual $|\bar{\boldsymbol{A}} \cdot \boldsymbol{\phi}_0 - \boldsymbol{b}|$ can be calculated. If it does not fall below the tolerance, then $\boldsymbol{\phi}_0$ is updated and the process is repeated. The step of updating the approximate solution is the most computationally intensive. The matrix of coefficients $\bar{\boldsymbol{A}}$ is used indirectly. The iterative solver LIS [126–129] is used in our program.

- Direct. These methods factorize the coefficient matrix (e.g., LU factorization) and implement some type of elimination to get the exact solution to the linear system. In contrast with iterative methods, direct solvers work directly on the matrix of coefficients. We use the direct solver within the PARDISO project [130–132] and Intel® MKL PARDISO. These solvers have three different separate stages:

  1. Analysis. Features of $\bar{\boldsymbol{A}}$ that can be used to accelerate calculations are detected (e.g., symmetry).
  2. Factorization. The matrix $\bar{\boldsymbol{A}}$ is decomposed in a product of simpler matrices. For example, the LU-factorization yields $\bar{\boldsymbol{A}} = \bar{\boldsymbol{L}}\bar{\boldsymbol{U}}$ as the product of a lower-triangular ($\bar{\boldsymbol{L}}$) and an upper-triangular ($\bar{\boldsymbol{U}}$) matrix.
  3. Solution. The exact solution is obtained by using certain substitution formula. For example, in the LU-factorization this stage takes advantage of the triangular structure of $\bar{\boldsymbol{L}}$ and $\bar{\boldsymbol{U}}$ to get the solution.

  Most of the computational time is devoted to stages 1 and 2.

In general, for large matrices such as those in this thesis, iterative methods are much faster than direct ones, if we account for the three-stages of direct methods. However, the matrix of coefficients $\bar{\boldsymbol{A}}$ of the Poisson problem does not change in time (it is the right-hand side $\boldsymbol{b}$ what changes from one time step to the other) , which means that, if a direct solver is used, the analysis and factorization stages could be done only once at the beginning of the simulation. A fair comparison of methods for our case should consider the iterative method vs. the solution stage of the direct solvers.

In table 5.4, computational times are compared using LIS, PARDISO project and PARDISO Intel® MKL solvers. These times have been obtained for a single step of Poisson on a 257x257 grid and a tolerance for LIS equal to 10^{-5}. Also, two different Fortran compilers are used: GNU and Intel®. If only the solution phase is taken into account, direct solvers (PARDISO project and MKL) are much more competitive than the iterative one (LIS) and give also a more accurate solution. Comparing between PARDISO project and MKL, they are not far from each other but PARDISO MKL with the Intel® Fortran compiler is the most efficient solver available according to our tests and the one that scales the best when increasing

Time [ms] (speed-up)	1 thread	10 threads	20 threads	40 threads
LIS (GNU Fortran)	230	70 (3.3)	62 (3.7)	66 (3.5)
LIS (Intel® Fortran)	230	65 (3.5)	58 (4.0)	57 (4.0)
PARDISO project (GNU Fortran)	9.8	4.1 (2.4)	4.7 (2.1)	5.9 (1.7)
PARDISO MKL (Intel® Fortran)	9.0	3.3 (2.7)	2.8 (3.2)	2.7 (3.3)

Table 5.4: Comparison of computational times (and speed-up) among the different solvers (using GNU and Intel® Fortran compilers) on a 257x257 grid. Tolerance for LIS solutions is 10^{-5}. Only the solution phase is considered in PARDISO project and PARDISO MKL solutions.

the number of parallel threads. Nevertheless, scalability of the time with the number of threads is quite poor (e.g., using 40 threads the greatest speed-up is 4), which is a known issue of the Poisson and other elliptic problems. In some cases, the computational time even increases when using more threads. Regarding the compiler, Intel® Fortran seems to behave better than GNU, but this is further discussed in coming section 5.3

5.2.2 Monte-Carlo method

Results in the previous subsection show that parallelization of the finite-difference solver is not very efficient. This issue is common to elliptic problems, in which the solution on a node is coupled to every other node so that the domain cannot be easily decomposed. In order to overcome this problem, we explore in this section the potential of Monte-Carlo methods.

The Monte-Carlo (MC) method applied differential-equation solving is based on running *discrete random walks* (DRW) starting on each node and ending on an *absorbing node* (which are, in principle, on Dirichlet boundaries). Here, we summarize the method that is explained in further detail in reference [138]. Each step in the DRWs implies a jump from the current node to a surrounding node based on certain probabilities. The jump probabilities are found from the discretized Poisson equation. The same centred finite-difference scheme as in section 4.5.1 can be used to discretize the Laplace operator on an uniform grid. Isolating the potential at the k^{th} node $\phi_{i,j}$ in equation (4.50) yields

$$\phi_{i,j} = p_x(\phi_{i+1,j} + \phi_{i-1,j}) + p_y(\phi_{i,j+1} + \phi_{i,j+1}) + \frac{\Delta x^2 \Delta y^2}{2(\Delta x^2 + \Delta y^2)} \frac{\rho_c(\boldsymbol{x}_k)}{\varepsilon_0}, \tag{5.2}$$

where

$$p_x = \frac{\Delta y^2}{2(\Delta x^2 + \Delta y^2)} \quad \text{and} \quad p_y = \frac{\Delta x^2}{2(\Delta x^2 + \Delta y^2)} \tag{5.3}$$

are the probabilities of jumping in x and y directions, respectively. The coefficients resulting from the chosen scheme must satisfy two basic properties to be mirrored as probabilities: (i) the addition of all coefficients must be 1 and (ii) they must be positive. The reader can verify that $2p_x + 2p_y = 1$ and $p_{x,y} > 0$.

Once we know the jump probabilities, the method to compute the potential at the k^{th} node works as follows:

1. Starting on this node, each step of each DRW is decided by sampling a random number $R \sim U(0,1)$ with a uniform probability distribution. A possible way to decide the jump direction and satisfy probabilities (5.3) is:

   - If $0 < R \leq p_x$ the next node is $(i+1, j)$.
   - If $p_x < R \leq 2p_x$ the next node is $(i-1, j)$.
   - If $2p_x < R \leq (2p_x + p_y)$ the next node is $(i, j+1)$.
   - If $(2p_x + p_y) < R \leq 1$ the next node is $(i, j-1)$.

   The DRW continues, computing subsequent steps in the same way, until an absorbing node is reached with known potential ϕ_{w0}. Periodic boundaries are not absorbing and DRW can travel through them applying periodicity [e.g., if the next node has indexes $(N_x + 1, j)$ out of the domain, periodicity tells us that the DRW can continue to node $(2, j)$ inside the domain].

2. Each DRW gives an approximate value of the potential

$$\phi_w = \phi_{w0} + \sum_r \frac{\Delta x^2 \Delta y^2}{2(\Delta x^2 + \Delta y^2)} \frac{\rho_c(\boldsymbol{x}_r)}{\varepsilon_0}, \tag{5.4}$$

   where ϕ_{w0} is the potential of the ending absorbing node and the sum is done on the source term of equation (5.2) across each node r travelled during the DRW.

3. The process is repeated to have a number N_w of DRWs, starting on the same node. The potential on this node is estimated as the average of all DRWs, i.e. $\phi_{i,j} = \sum_w \phi_w / N_w$.

This has to be repeated for every single node to have a complete solution on the domain. The quality of the solution relies on statistical convergence, which depends on the number N_w. Even for a moderate number (e.g, $N_w = 100$), the computational cost for a typical problem size can be prohibitive with a single thread. However, it is clear that the calculation of the potential on each node is uncoupled from the rest, what makes the MC method very suitable for efficient parallelization. The approach followed here is to distribute nodes among parallel threads.

Two alternative algorithms are considered

1. MC method I: this is done exactly as described previously, with every DRW starting on the node the potential is wanted and ending on a Dirichlet boundary.

2. MC method II: in this approach we let nodes where the potential has been already computed to become internal absorbing nodes, meaning that DRWs can either end on a Dirichlet boundary or in an internal absorbing node. In this way, nodes where the solution is known help to reduce the length of DRWs from next nodes.

Verification

The two methods are tested on a problem with analytical solution to compare accuracy and numerical performance. The test problem is

$$\nabla^2\phi = \frac{256}{(L_x L_y)^4}\left\{2y^2(y-L_y)^2\left[x^2+(x-L_x)^2+4x(x-L_x)\right]\right. \\ \left. 2x^2(x-L_x)^2\left[y^2+(y-L_y)^2+4y(y-L_y)\right]\right\} \quad (5.5)$$

with homogeneous Dirichlet conditions in all boundaries. The analytical solution of such problem is

$$\phi_{\text{an.}}(\boldsymbol{x}) = x^2y^2(x-L_x)^2(y-L_y)^2. \quad (5.6)$$

Figure 5.3 shows the analytical solution together with the numerical solution obtained with MC methods 1 and 2 on a numerical grid with 257x257 nodes. The two methods give solutions that successfully approximate the analytical solution. The noise intrinsic to such statistical approaches is very evident in the solution of MC method I. This noise seems to be smoothed when using MC method 2, probably because of the coupling among nearby nodes introduced by the addition of new absorbing nodes. When looking at the numerical error with respect to $\phi_{\text{an.}}$, the two methods yield error of the same order. In method I the error distributes more homogeneously due to each node being independent from the rest. The error in method II, shows some patterns due to the mentioned coupling, which are related to the number of parallel threads and the order in which nodes are solved.

Numerical performance

For a problem with 257x257 nodes (the same size as that considered in table 5.4 for finite differences) solved with 40 parallel threads, the computational time measured in MC method I is 34 and 38 s when using Intel® and GNU Fortran compilers, respectively. This high computational cost is several orders of magnitude above that of the finite-difference methods and makes MC method I unaffordable to use.

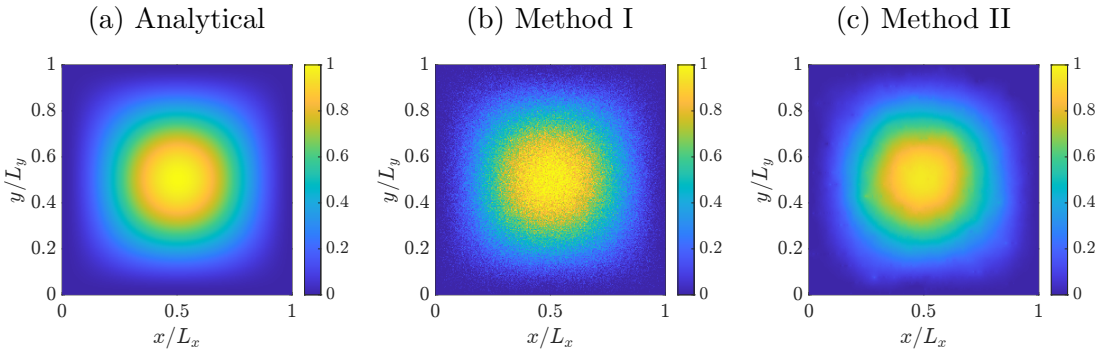

Figure 5.3: Solution to Poisson equation (5.5) with (a) analytical and MC methods (b) I and (c) II, on a 257x257 grid and $N_w = 100$.

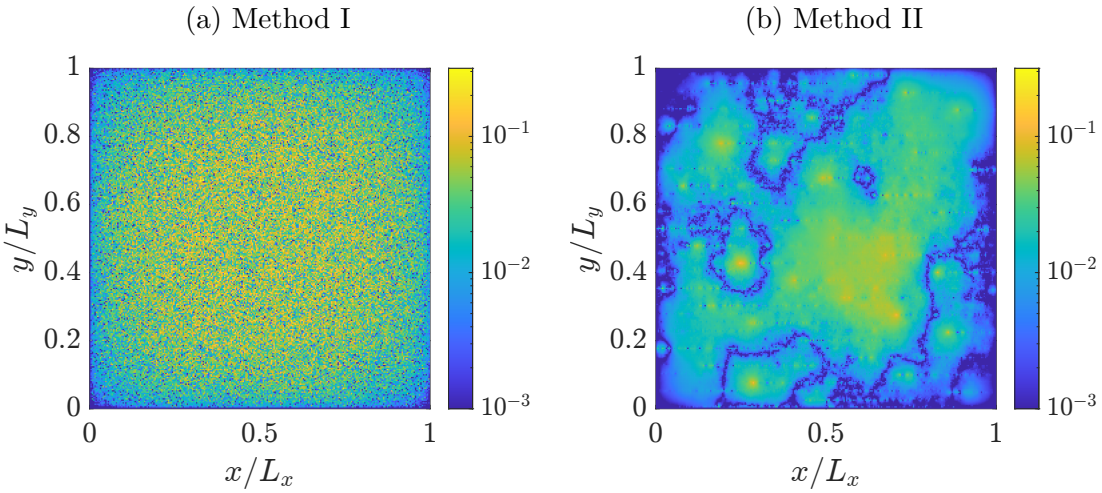

Figure 5.4: Numerical error $|\phi - \phi_{\text{an.}}|$ of MC methods (a) I and (b) II, on a 257x257 grid and $N_w = 100$.

The same problem with same number of threads takes about 122 ms using MC method II (with both Intel® and GNU Fortran), what makes this method much more interesting than I from a computational perspective. However, the computational time is still greater than finite-difference solvers and with the inconveniences of less accuracy and more noise (apart from the intrinsic PIC noise).

Even so, let us further explore the potential of MC methods. Figure 5.5(a) compares the single-thread performance of methods I and II varying the number of nodes. The results support that MC method II provides a lower computational time, which also scales much better with the size of the problem.

Figure 5.5(b) compares the scaling of the speed-up with the number of threads of the two methods. In both methods the obtained speed-up is much greater than those obtained with the finite-difference solver in table 5.4, which is the main advantage of MC methods. For reference, the ideal speed-up is represented as a black-dotted line. In general we would expect the measured speed-up to be smaller than ideal.

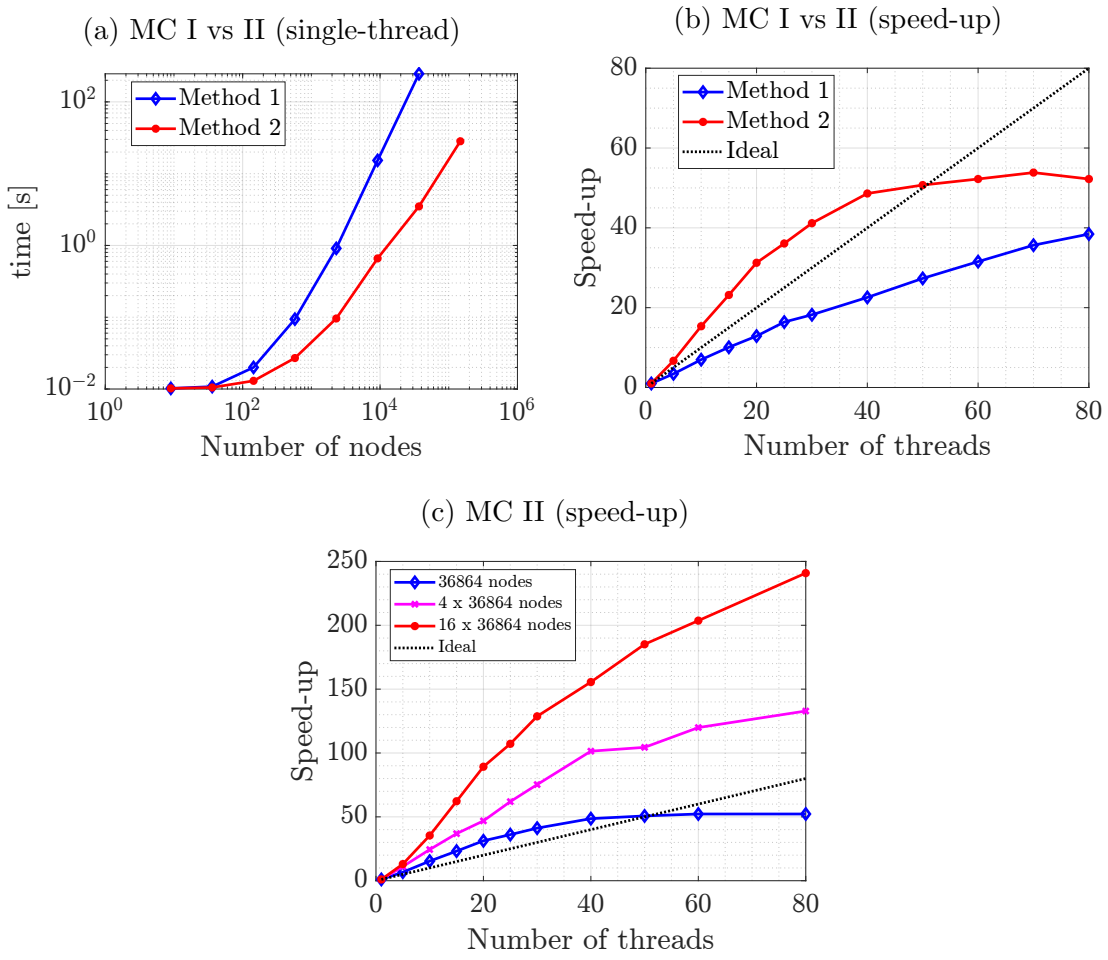

Figure 5.5: Numerical performance analyses on MC methods I and II, using Intel® compiler. (a) Single-thread computational cost comparison in a 192x192 grid with $N_w = 100$. (b) Parallelization scaling comparison in a 192x192 grid with $N_w = 100$. (c) Parallelization scaling performance of MC method II with increasing number of nodes. The black-dotted line in (b) and (c) depicts the ideal speed-up.

MC method I complies with this expectation. MC method II performs much better and in some cases better than the ideal speed-up. This unexpected finding is the result of having a higher rate of creation of absorbing nodes when in parallel, which helps next DRWs to shorten. For example, the calculation of the 100^{th} node in single-thread calculations benefits from the previous 99 nodes which have become absorbing. In parallel, the calculation of the 100^{th} node of certain thread takes advantage from previous nodes computed by itself and every other thread (which will be always greater than 99). With this example, it is clearly shown that the computational workload of each thread gets reduced with the action of other parallel threads, which explains the speed-up above ideal values. In this graph, however, the speed-up of method II seems to saturate at some point. Two possible explanations are: (i) above 40 threads, hyper-threading is used and two threads may share the same physical core of the processor (see coming section 5.3); and (ii) the number of threads is, at some point, excessive for the current problem size.

In order to check if the problem size affect the saturation of the speed-up, we have repeated calculations in figure 5.5 increasing the number of nodes, only with method II. These results confirm that the saturation is delayed with larger problems. In addition, the speed-up seems to depend also significantly on the size of the problem. The greatest case (red line) show speed-ups significantly above the ideal curve.

In order to summarize, we have seen that for a typical problem size, MC methods cannot overcome the performance of finite differences. Also, the MC approaches would introduce additional noise in the simulations apart from that intrinsic to PIC. However, increasing the size of the problem, MC method II has been seen to yield a great parallel speed-up. This point suggest that there could be potential for using MC method II in the future for larger problems than those considered in this thesis. As future work, the MC method should be tested together with a PIC simulation to analyse how the additional statistical noise affects the results.

5.3 Other numerical performance concerns

Apart from the optimization of the numerical methods, there are some aspects that can boost performance with little or no coding effort. This is the case of using a different compiler and parallelization settings.

5.3.1 Compiler

The simulations are meant to run on workstations with two sockets, each one mounting a processor Intel® Xeon® Silver 4316 @ 2.30 GHz with 20 physical cores. This processors use the hyper-threading technology that locates 2 logical threads in each physical core. Of course, the performance of two threads sharing a physical core is not equivalent to two cores with a single thread, but a small performance boost may be obtained. While the code was originally compiled with the GNU Fortran compiler, it is reasonable to think that the Intel® processor may benefit from the use of the Intel® Fortran compiler.

Time [s] (speed-up)	**1 thread**	**20 threads**	**40 threads**	**80 threads***
GNU Fortran	1570	92.6 (17.0)	60.5 (26.0)	68.1 (23.0)
Intel® Fortran	1410	77.2 (18.3)	46.3 (30.5)	40.0 (35.2)

Table 5.5: Comparison of computational times when using GNU and Intel® Fortran compilers (*) This case uses hyper-threading.

Computational times for the usual test case are shown in table 5.5 using GNU

and Intel® compilers. Let us emphasize again that the conclusions here are not only simulation but computer dependent. If the program is expected to run in a workstation with very different components (e.g., AMD processor), it would be advisable to repeat this analysis. As expected, the program uses the computer resources more efficiently when compiled with Intel®. For this particular simulation and workstation, the single-thread savings are around 10% with respect to GNU times. The computational time scales also better with the number of threads with Intel®, providing greater speed-ups. With 40 threads, the savings are greater than in single-thread and close to 23% with respect to GNU. Finally, the case in table 5.5 with 80 threads uses hyper-threading to assign two threads to each physical core, expecting a small performance boost with respect to the 40-thread case. The program compiled with Intel® does take advantage of hyper-threading. However, the GNU-compiled program seems to be unable to manage hyper-threading efficiently and times with 80 threads are actually worse than with 40. The results suggest that the Intel® compiler should be used

5.3.2 OpenMP thread affinity

The concept of *thread affinity* stands for the strategy used by OpenMP to bind processes in the program to threads in the processor. This can have a significant impact in the computational times if not all threads in the computer are used. The affinity behaviour of OpenMP can be controlled by changing the value of the environment variables `KMP_AFFINITY` and `OMP_PROC_BIND` in Intel® and GNU compilers, respectively (other environment variables can also play a role in fine tuning of the affinity). Thread affinity can be configured to a fine level of detail, we consider here the simple cases:

- No affinity: the binding of processes to threads is decided internally by OpenMP, which are allowed to migrate across different threads in the system. Hyper-threading can be used or not depending on the binding settings decided internally by OpenMP. Apart from being inefficient, this option is less predictable and computational times may have some variability from run to run, even for the same simulation settings.

- Spread: processes are assigned to system threads as far as possible from each other. This means that binding happens, preferentially, to different physical cores and to different sockets. If the number of used threads exceeds the number of physical cores, only then hyper-threading is used. In our configuration, e.g., if parallelization uses 40 threads, each socket will host 20 of them in separate physical cores. In our workstation, hyper-threading comes into place only if more than 40 threads are used. The values of the environment variables yielding this behaviour are `KMP_AFFINITY = granularity = fine,`

`scatter` (with Intel®) or `OMP_PROC_BIND = spread` (with GNU).

- Compact: processes are bound as close as possible in the system. This is, preferentially, in the same socket and in the same physical core. Using the same example, if parallelization uses 40 threads, they will be all hosted by the same socket and each of the 20 cores will manage 2 threads. The values of the environment variables yielding this behaviour are `KMP_AFFINITY = granularity = fine, compact` (with Intel®) or `OMP_PROC_BIND = close` (with GNU).

Time [s]	5 threads	10 threads	20 threads	40 threads
No affinity	284	150	82.8	66.3
Spread	283	143	77.2	46.3
Compact (*)	433	221	120	74.9

Table 5.6: Comparison of computational times when using different OpenMP affinity settings and the Intel® Fortran compiler. (*) These cases use hyper-threading.

Results of computational times for the usual test simulation are shown in table 5.6 for these affinities on the PIC program compiled with Intel®. For the same number of threads, the spread affinity always provides shorter computational times than the other two options. This affinity behaviour ensures that threads are placed in different physical cores, so that every thread benefits from the full computational power of a physical core. On the other hand, the compact affinity always provides the longest computational times for equal thread number. However, this comparison is not fair since, under the compact strategy, threads are bound to the same physical core when possible, actively using hyper-threading. It is fairer to compare results that use the same number of physical cores (e.g., compare time with 20 threads and compact affinity with 10 threads and spread affinity). As concluded in section 5.3, this comparison shows a better performance of the compact affinity compared to others and supports that hyper-threading can give a performance boost while using the same number of physical cores. Therefore, the compact affinity is useful when the user wants to use the full potential of a certain number of physical cores (e.g., if there are 10 physical cores available, the user may want to use 20 threads and compact affinity). The hyper-threading boost seems to be more significant when using a smaller number of cores. Setting no affinity can lead to unexpected behaviour and the resources of the processor are not efficiently used, specially when the number of threads increases. Using spread or compact affinities, depending on the needs, is almost always a preferable choice.

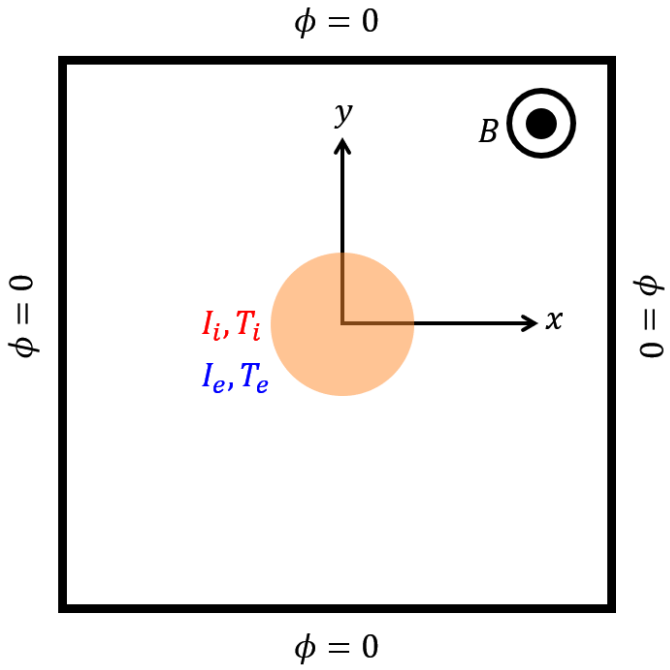

Figure 5.6: Diagram of the Penning-discharge simulation settings. The orange-shadowed region represents the circular injection area with radius R_{inj}.

5.4 Penning discharge benchmark

As demonstrated in chapters 4 and 5, even if conceptually simple to understand, PIC, MCC and Poisson codes involve many different algorithms and can easily become very complex. Verifying that every part of the code is working as expected is one the challenges faced during the development and it can be quite time consuming. The different modules have been verified during development by modular tests, which check the proper operation of individual routines, and integrated tests, which involves the interaction of several modules. Some of the tests used for the PIC code are described in [35] for the PIC-module of HYPHEN.

A complementary approach to verification is by comparing results coming from similar codes. In our group, there are a few examples of benchmarking of in-house codes. This is the case of the benchmark of the 2D HYPHEN [35] and the 3D EP2PLUS [139, 140] hybrid codes, simulating the expansion of a plasma plume. A more recent example is the comparison of stationary [28] and time-dependent [29] 1D-axial models of a Hall thruster, which involves the stationary code of chapter 2.

In the literature, we find also collective efforts of the plasma community to benchmark codes among different research groups [122, 141, 142]. In the context of 2D PIC codes intended to analyse oscillations and anomalous transport, two recent benchmark works are those of Charoy et al. [134] and Villafana et al. [143]; simulating the axial-azimuthal and radial-azimuthal planes of a Hall discharge, respectively.

In this section we benchmark the in-house 2D PIC code comparing with results from the LAPLACE 2D PIC model [135–137]. The simulation case is the plane perpendicular to the plasma column of a Penning discharge, inspired in previous works by Carlsson et al. [144] and Powis et al. [145]. In this type of simulations the formation of a rotating spoke is observed with a clearly identifiable rotation frequency. Two benchmark cases are considered: (*i*) collisionless and (*ii*) with ionization collisions. The results shown on the collisionless case are part of a larger international benchmark involving 15 groups, organized by A.T Powis (Princeton Plasma Physics Laboratory) and L. Garrigues (LAPLACE) [41].

5.4.1 Collisionless benchmark case

A diagram with the main characteristics of the simulation is provided in figure 5.6. The domain has squared shape, with sides $L_{x,y}$ and the origin of coordinates at the geometrical centre. The boundaries are perfectly conducting and grounded to a potential $\phi_0 = 0$. Particles hitting the boundaries are perfectly absorbed. There is an uniform magnetic field $\boldsymbol{B}_0$ that is perpendicular to the domain (i.e., in the axial direction) and tends to confine the plasma in the middle. Starting with an empty domain, constant currents of ions I_i and electrons I_e are injected distributed in a circular region, centred in the domain and with radius R_{inj}. The two populations are assumed to have a Maxwellian distribution of velocities with temperatures $T_i^{(\text{inj})}$ and $T_e^{(\text{inj})}$. The main physical and numerical parameters of the benchmark simulation are gathered in table 5.7. A total of 500 μs of time are simulated, giving enough time for the initial transient, formation and several cycles of the rotating spoke. Snapshots of several magnitudes are printed out every Δt_{print}. This benchmark case disregards collisions.

Volumetric injection in a circular region

The benchmark simulation has a volumetric injection of certain ion I_i and electron I_e currents in a circular region with radius R_{inj}, centred in the squared domain. The currents are distributed uniformly in the circular region. Instead of discretizing the injection region and inject cell-wise as explained in section 4.3.3, the injection is done directly sampling particle positions inside the circle. The sampling of velocities from a Maxwellian distribution follows section 4.2.1. The target number of macroparticles of species s to be injected per time step is

$$N_{p,s}^{(\text{tg})} = \frac{I_s \Delta t}{q_s W_p}, \tag{5.7}$$

which yields $N_{p,e}^{(\text{tg})} = 49.932$ for electrons and $N_{p,i}^{(\text{tg})} = 19.973$ for ions, using the values of table 5.7.

Type	Description and symbol	Value and units
Species settings	Ion mass, m_i	4 u
	Electron injection current, I_e	-20 mA
	Ion injection current, I_i	8 mA
	Electron injection temperature, $T_e^{(\mathrm{inj})}$	6 eV
	Ion injection temperature, $T_i^{(\mathrm{inj})}$	0.025 eV
System parameters	Magnetic field, B_0	100 G
	Domain length in x, L_x	5 cm
	Domain length in y, L_y	5 cm
	Injection radius, R_{inj}	0.5 cm
Numerical parameters	Number of nodes in x, N_x	257
	Number of nodes in y, N_y	257
	Macroparticle weight, W_p	10^5
	Time step, Δt	4×10^{-11} s
	Number of time steps, N_t	12.5×10^6
	Print-out step, $\Delta t_{\mathrm{print}}$	5×10^{-8} s

Table 5.7: Parameters of the Penning discharge simulation benchmark.

If thinking in polar coordinates, to distribute particles uniformly within a circle, the probability distribution of positions is independent of the polar angle θ but must depend on the radial coordinate r. To be precise, in order to keep constant the average distance among macroparticles, it must be proportional to r. It can be easily proved that the position distribution function is $f_r(r) = 2r/R_{\mathrm{inj}}^2$. By using the inverse-cumulative method [115], the sampling formula that provides the radial distance of particles to the centre is $r_p = R_{\mathrm{inj}}\sqrt{R_1}$, being $R_1 \sim U(0,1)$. The polar angle is uniformly distributed in the interval $(0, 2\pi)$, i.e., $\theta_p = 2\pi R_2$ also with $R_2 \sim U(0,1)$. The transformation to Cartesian coordinates yields

$$x_p = r_p \cos\theta_p = R_{\mathrm{inj}}\sqrt{R_1}\cos(2\pi R_2) \tag{5.8}$$

and

$$y_p = r_p \sin\theta_p = R_{\mathrm{inj}}\sqrt{R_1}\sin(2\pi R_2) \tag{5.9}$$

Temporal and averaged behaviour

In figure 5.7 the evolution of the number of macroparticles in the simulation is represented. These curves give an idea of the time needed for the initially empty simulation to reach global a stationary state. At the beginning of the simulation,

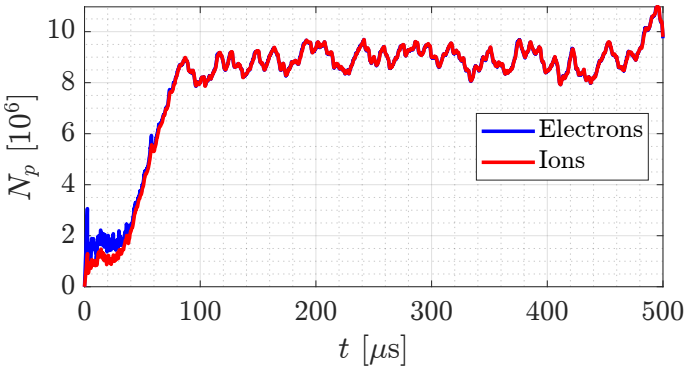

Figure 5.7: Time evolution of the total number of ion and electron macroparticles in the collisionless Penning simulation benchmark.

due to $|I_e| > |I_i|$, there is an imbalance in the number of electrons and ions. After 40 μs global quasineutrality is approximately reached. The number of macroparticles does not show a stationary behaviour until 100 μs, when $N_{p,e}$ and $N_{p,i}$ stabilize around 9×10^6. Even so, the values of $N_{p,e}$ and $N_{p,i}$ keep oscillating during the rest of the simulation between 8×10^6 and 11×10^6.

Figure 5.8 shows the average of snapshots of several plasma variables in the time interval 200 μs $\leq t <$ 500 μs, which provide a good qualitative picture of the plasma behaviour in the Penning discharge. When injection satisfies $|I_e| > |I_i|$ (i.e., the amount of electrons injected is greater than ions), the shape of ϕ tend to be a potential well such that it tries to confine ions in the middle and accelerate electrons out, as figure 5.8(b) depicts. Therefore, the induced $\boldsymbol{E}$ will be mainly radial and pointing towards the centre. This electric field, combined with the axial $\boldsymbol{B}_0$ induces an azimuthal $\boldsymbol{E} \times \boldsymbol{B}$ in both ions and electrons. As demonstrated by figure 5.8(c), only electrons are effectively magnetized and confined since the ion Larmor radius is of the order of the system dimensions. In figure 5.8(a), the averaged n_i is represented, which tends to be maximum in the centre, close to the injection region. The behaviour of n_i and n_e (not included) is equivalent and representative of the plasma density $n \approx n_i \approx n_e$, since the plasma tends to satisfy local quasineutrality. Regarding temperature in figures 5.8(e) and (f), electrons heat up close to the injection area and then cool down towards the boundaries. Ion temperature increases from the centre to the walls.

In equilibrium conditions, denoted by a '0' subscript, the figure 5.8 shows that $\boldsymbol{E}_0 \cdot \nabla n_0 > 0$ is satisfied, which is the local criterion behind the collisionless Simon-Hoh instability [10, 13, 146, 147]. It is believed that this instability mechanism is the main actor leading to the formation of rotating spokes [144, 145]. In the absence of collisions, the plasma oscillations are the main actor in the radial transport of electrons. Of course, spokes are filtered out when averaging in figure 5.8 but can be seen in figure 5.9, which shows several snapshots along one rotation period. Under this configuration, one single spoke is formed that can be best seen in the evolution

of n_i in figure 5.9(a) The behaviour of other variables (e.g., ϕ, $\boldsymbol{u}_e$ and $\boldsymbol{u}_i$) is more intricate and different from the averaged behaviour. While $\boldsymbol{u}_e$ stills shows the $\boldsymbol{E} \times \boldsymbol{B}$ drift, its evolution is turbulent. The rotating spoke observed in n_i shows as a large scale vortex structure in $\boldsymbol{u}_e$, but other smaller vortexes also co-exist.

It is not the goal of this section to give an in-depth physical discussion of the Penning-discharge simulation. The next section is devoted to the comparison of results with those obtained by the PIC code of LAPLACE.

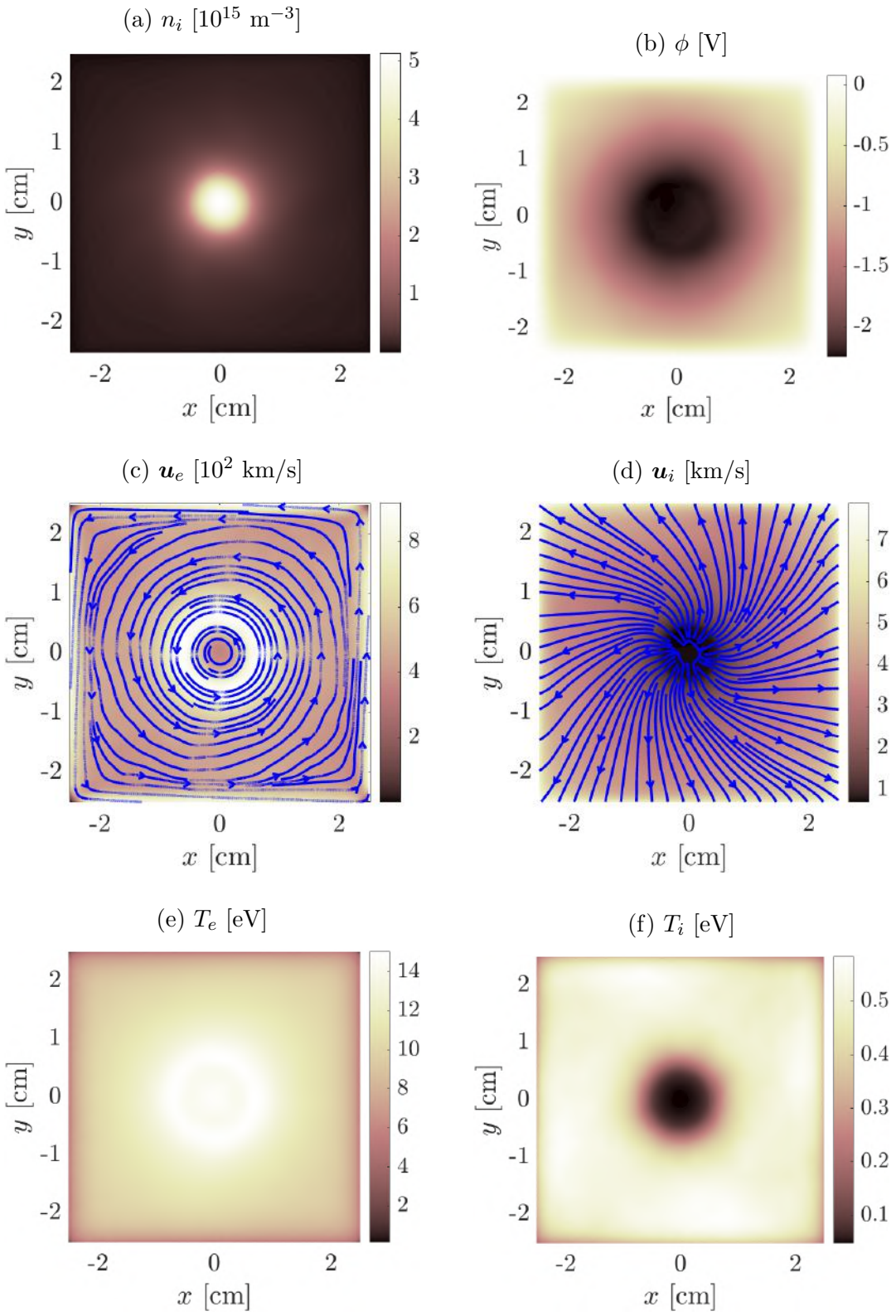

Figure 5.8: Time average of snapshots of several variables in the interval 200 μs $\leq t <$ 500 μs. Panels (c,d) represent streamlines together with a colour map of the local velocity norms.

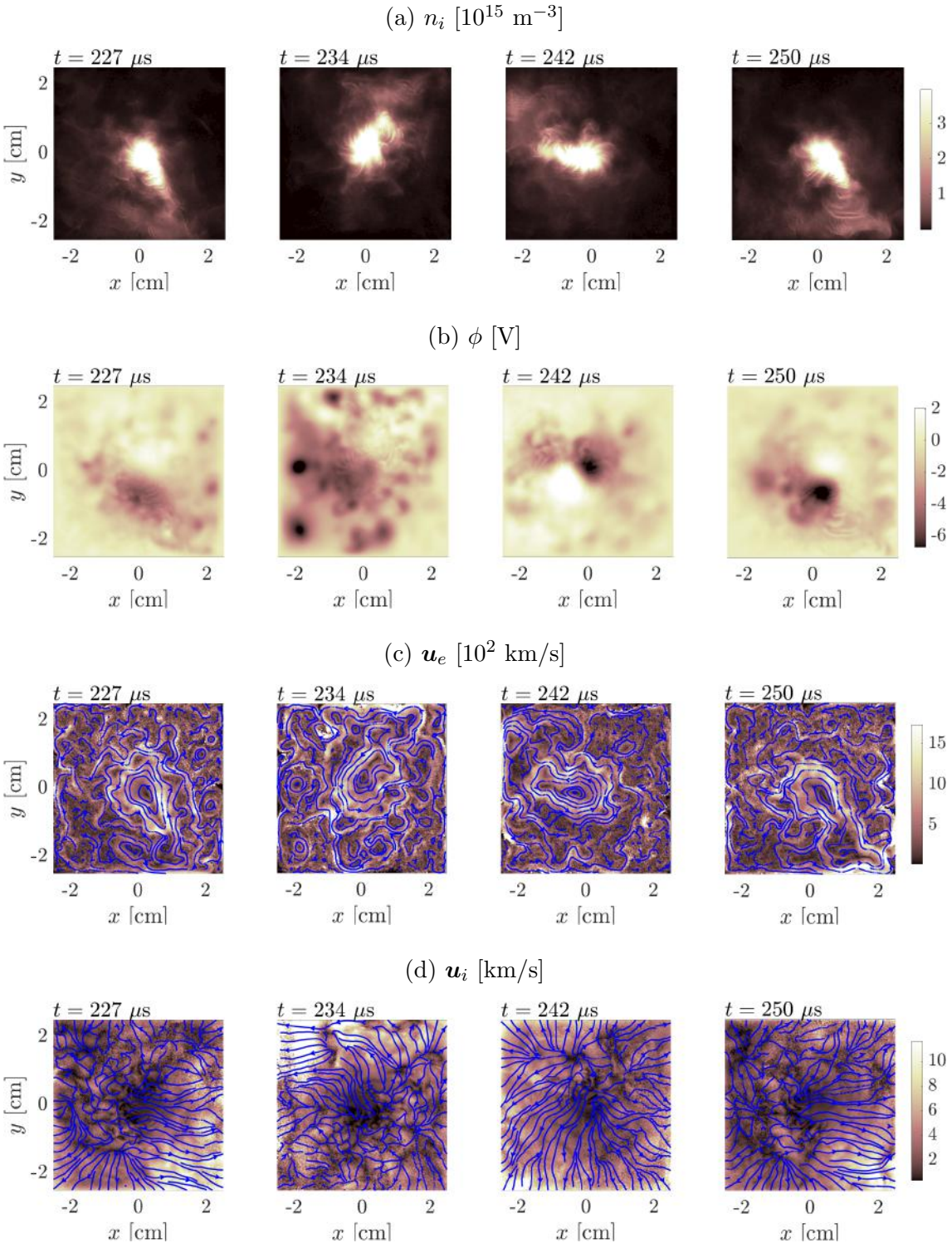

Figure 5.9: Evolution of several plasma variables and electric potential along one period of the rotating spoke. Panels (d,e) represent streamlines together with a colour map of the local velocity norms.

Benchmark

The LAPLACE's 2D3V PIC code [135–137] works with Cartesian coordinates and a structured mesh. As EP2's code, the motion of macroparticles is solved with the standard Boris method [116] and the Poisson solver uses the direct solver of PARDISO included in Intel® MKL. The parallelization of the PIC code uses a particle decomposition approach (which has inspired EP2's multiple-list parallelization described in section 5.1.1) and a hybrid strategy combining OpenMP and MPI (*message passing interface*).

The benchmark of the two codes is based on two types of results: (i) rotation frequency of the spoke and (ii) average cross-section plasma profiles at $y = 0$. The frequency is computed from density-probe measurements of n_i at the location $x = L_x/4$ and $y = 0$. The time evolution of n_i measured by the probe is depicted in figure 5.10. A peak-finder algorithm is used to locate the relative maxima in the density time evolution over the last 10 periods, which are marked with red crosses in the figure. It takes 233.75 μs for the spoke to complete 10 full cycles, which gives an average rotation frequency of 42.8 kHz. The frequency measured by LAPLACE is approximately 43.3 kHz. This is a difference of less than 1.2%, which is satisfactory.

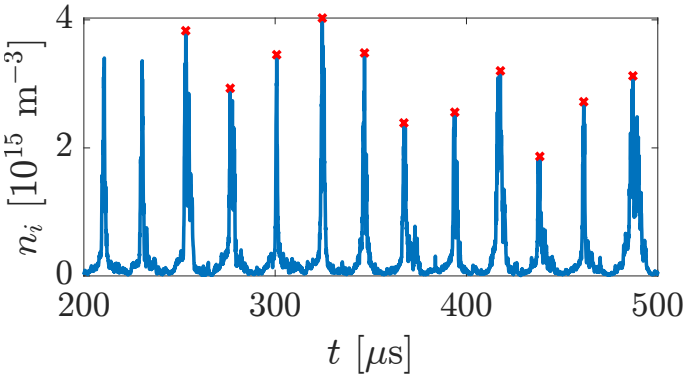

Figure 5.10: Collisionless case. Time evolution of n_i measured with a density probe located at $x = L_x/4$ and $y = 0$.

The cross-sections $y = 0$ of ϕ, n_i and T_e are averaged in the interval 200 μs $\leq t <$ 500 μs (i.e., the average of 6,000 snapshots), and compared also between codes (the 2D average maps are shown in figure 5.8). Such a comparison is shown in figure 5.11, where it seems clear that the two codes give result that match quantitatively and follow the same trends. The match of n_i profiles is almost perfect in every region of the x-domain. The differences in T_e and ϕ are more evident. The error in ϕ with respect to LAPLACE's result is close to 3.2% in the centre of the domain. On the other hand, there is a difference in T_e of 1.6% in the centre and 3.6% to 4.5% in the peaks. These errors are acceptable and similar in magnitude to those observed in recent benchmark of 2D PIC codes [134, 143].

The EP2 and LAPLACE's PIC codes have been seen to yield very similar results and the benchmark can be considered successful. This is a very important verification milestone for our PIC code that gives credibility to future results.

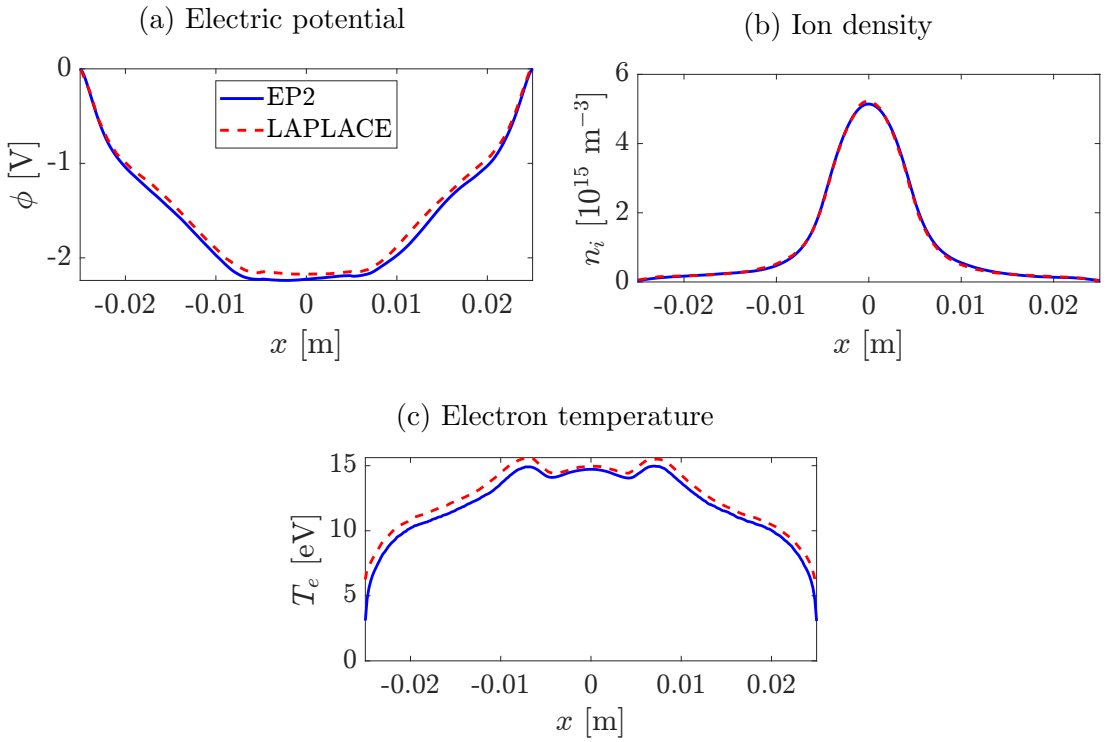

Figure 5.11: Collisionless case. Comparison of cross-section profiles of (a) ϕ, (b) n_i and (c) T_e obtained with LAPLACE and EP2's PIC codes.

5.4.2 Benchmark case with ionization collisions

In this section, results are compared for a simulation case where ions are not injected using volumetric injection algorithms, but generated from ionization collision of electron macroparticles with a neutral background cloud of helium atoms. This benchmark case is less consolidated and shown results are preliminary. A more detailed comparison is left as future work.

The simulation settings and parameters are the same as in the collisionless case, except for the following. As aforementioned, ions are no longer directly injected in the domain. Electrons are still injected uniformly in the same region but the current is $I_e = -5$ mA, they are cold and mono-energetic (not Maxwellian), having energy $\mathcal{E}_e^{(\mathrm{inj})} = 50$ eV (this is greater than the 24.59 eV required to ionize helium atoms) and macroscopic velocity $\boldsymbol{u}_e^{(\mathrm{inj})} = \sqrt{2\mathcal{E}_e^{(\mathrm{inj})}/m_e}\ \mathbf{1}_z$. The neutral background species has density $n_n = 10^{20}$ m^{-3} with no velocity and no temperature.

The collisions are simulated using the MCC method described in subsection

4.4.2. After the benchmark by Turner et al. [122], the model for the ionization cross section $\sigma_{\text{ion}}(\mathcal{E})$ is taken from the compilation Biagi 7.1 [148] and the scattering of the incoming and ejected electrons is done isotropically. The remaining kinetic energy after every collision event is split equally between the two electrons [this is $F = 0.5$ in equations (4.48) and (4.49)].

In figure 5.12, results obtained with EP2 and LAPLACE codes are compared. In this case, we only compare the time evolution of the spatially averaged n_i and the cross-section $y = 0$ of n_i averaged in the interval 200 μs $\leq t <$ 500 μs (i.e., the average of 6,000 snapshots). The matching between the two solutions is successful, verifying the implementation of MCC ionization collisions.

(a) Spatially averaged n_i (b) Cross-section of n_i

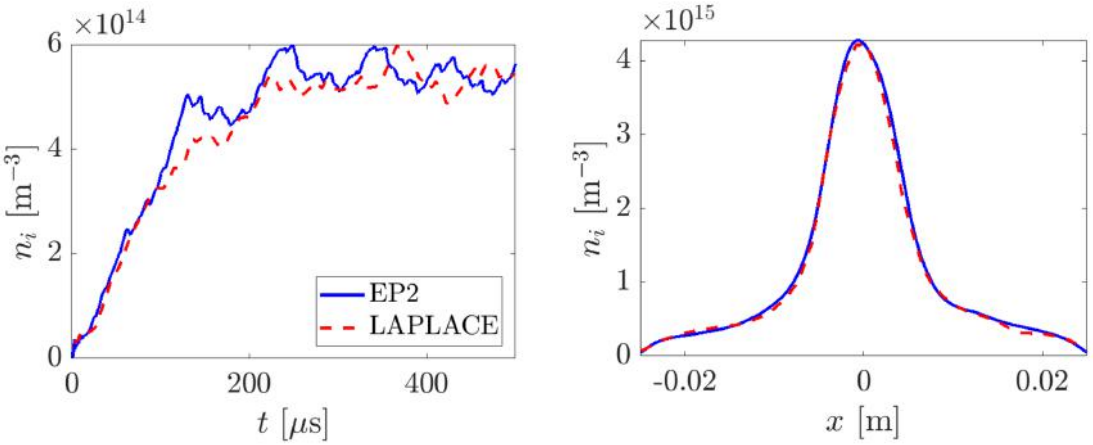

Figure 5.12: Case with ionization collisions. Comparison of (a) time evolution of the spatially averaged n_i and (b) cross-section profile of n_i obtained with LAPLACE and EP2's PIC codes.

Chapter 6

Kinetic instabilities in electrostatic plasmas

This Chapter reproduces the contents of manuscript submitted to a peer-reviewed journal. The typography has been adapted to the style of this Thesis.

Abstract

The electron-cyclotron drift instability (ECDI) has been proposed as one of the main actors behind the anomalous transport of electrons in Hall thruster devices. In this work, we revisit the theory and perform two-dimensional PIC simulations under several conditions to analyze the non-linear behaviour and the induced transport under several boundary conditions. Simulation results with fully-periodic boundaries and conditions faithful to the linear theory show the growth of ECDI modes, ion-wave trapping vortexes and agree with the existing literature in early times. In the long term, however, we observe very mild oscillations and null anomalous current. The evolution towards this new equilibrium is coherent to what can be expected from energy conservation. The quenching of the oscillations seem to be highly related with the distortion of ion-trapping vortexes in phase space after a long-term interaction of ion particles with the electrostatic wave. This result suggests that sustained oscillations and turbulent current could benefit from the renewal of ions by, e.g., removing and injecting particles through axial boundaries instead of applying periodicity. This second type of simulations shows that injection conditions highly impact the late simulation behaviour of ECDI oscillations, where we identify several regimes depending on the value of the ion residence time compared to the characteristic saturation time in the fully periodic case. The intermediate regime, where these two times are close, is the only one providing sustained oscillations and electron transport and seems to be the relevant

one in Hall devices.

6.1 Introduction

The problem of anomalous electron cross-field transport remains as one of big open challenges for the community of $\boldsymbol{E} \times \boldsymbol{B}$ plasmas. In the field of plasma propulsion, this problem has been mainly studied in the context of Hall-thruster discharges and represent one big obstacle on the way towards to predictive efficient numerical models. The large drift of electrons in the azimuthal direction of the Hall thruster is a source of several families of azimuthal oscillations that are potential candidates to explain the anomalous transport and have been observed experimentally [9,15,100,101,149,150]. The classical explanation [8] for the impact of oscillations on transport relies on the correlation of oscillations in density and electric field in the $\boldsymbol{E} \times \boldsymbol{B}$ direction under the presence of a magnetic field.

The amount of articles devoted to the analysis of instabilities and turbulence in Hall thrusters is extensive. With a macroscopic description for ions and electrons, some of the authors of this article have conducted global [38] and local [10] linear stability analyses. In these references two-stream, drift-gradient and drift-dissipative instabilities are discussed. Similar recent studies by other authors are [42,91,92,151,152].

When using a kinetic formulation for the electrons, the analytical studies of instabilities are usually limited to a homogeneous and collisionless plasma. For the conditions of a Hall thruster, where electrons are magnetized but ions are not, the dispersion relation of the electron cyclotron drift instability (ECDI) is obtained [11,12]. This classical instability have been revisited, during the last two decades, by several authors [3,83,87,93,153], in the context of Hall thrusters. Also from the point of view of kinetic simulations [84,93,94,135,154,155] and experiments [15,101,150,156].

Kinetic models aimed to analyze electron turbulence and turbulent transport in the plane perpendicular to the applied magnetic field $\boldsymbol{B}_0$ can be classified in 1D azimuthal [84,154,155] and 2D axial-azimuthal [93,94,135]. The latter case has been the subject of a recent benchmark by several groups [134]. Many 2D simulations include a number of phenomena that makes challenging to compare the results with the ECDI linear theory; such as, inhomogeneous magnetic field, collisions, ionization or electrical connection between anode and cathode. The 1D simulations are closer to the linear theory of the ECDI but they still add effects that are not considered in the dispersion relation, such as refreshing of particle velocities or collisions.

In section 6.2, we revisit the main results from the classical dispersion relation of the ECDI theory. A recently developed in-house two-dimensional PIC code is introduced in section 6.3 and used to analyze the non-linear evolution of the ECDI under several conditions. In every case, a 2D domain perpendicular to $\boldsymbol{B}_0$ is considered; which we will refer to as the axial-azimuthal plane, making the analogy with a Hall discharge geometry. Initially we consider a fully periodic domain and simulate under the assumptions of the classical ECDI theory. These results can be compared with the existing literature [84, 154, 155] on 1D azimuthal simulations of the classical ECDI, but open the possibility to the growth of modes with an axial component. Similar results to those shown elsewhere are found during early simulation times; but our long-term behaviour shows no oscillation capable of driving a turbulent electron transport, which disagrees with the literature. We try to give an explanation from an energy conservation perspective.

Periodic results establish a clear relation between ion-wave trapping behaviour and the existence of electron transport in the long term, what suggests that renewal of ion particles could help to develop sustained ECDI oscillations and axial transport. This motivate us to replace axial boundary conditions from periodic to removal/injection of particles, which mimics the generation and loss of particles in a finite plasma such as the Hall discharge. Results are shown in section 6.4, where we are able to establish a clear relation between the ion velocity (related with the residence time) and the long-term behaviour of short-wavelength oscillations and transport in the plasma.

6.2 The classical ECDI: linear analysis

We attempt to study the stability of a homogeneous, collisionless plasma at equilibrium subjected to mutually perpendicular magnetic $\boldsymbol{B}_0 = B_0\mathbf{1}_x$ and electric $\boldsymbol{E}_0 = E_0\mathbf{1}_z$ fields. Throughout the article subindex '0' and '1' stand for equilibrium and perturbed conditions. Consistent with Hall thruster discharges: the strength of the stationary magnetic field keeps electrons well-magnetized and ions unmagnetized, and the plasma currents are low enough to neglect the contribution of the self-induced magnetic field $\boldsymbol{B}_1$. At equilibrium, electrons have a drifted-Maxwellian velocity distribution function (VDF) with density n_0, temperature T_{e0}, and an $\boldsymbol{E}_0 \times \boldsymbol{B}_0$ drift velocity $\boldsymbol{u}_{e0} = u_{ye0}\mathbf{1}_y$, $u_{ye0} = E_0/B_0$. Equilibrium ions are assumed cold, have a density n_0, and move with a constant velocity $\boldsymbol{u}_{i0} = u_{zi0}\mathbf{1}_z$, parallel to $\boldsymbol{E}_0$. This homogeneous equilibrium disregards the electrostatic acceleration of ions due to $\boldsymbol{E}_0$. From analogy with a Hall-thruster geometry, let us refer throughout the article to the directions of $\boldsymbol{B}_0$, $\boldsymbol{E}_0$ and $\boldsymbol{E}_0 \times \boldsymbol{B}_0$ as radial (x), axial (z) and azimuthal (y).

Next, we summarize the main aspects of the well-known linear stability analysis [3,11,12,83,153]. From the linearly perturbed Vlasov equation, the relation between the electron density and the electric potential perturbations of wavevector $\boldsymbol{k}$ and complex frequency ω, for propagation perpendicular to $\boldsymbol{B}_0$ (i.e., the component of $\boldsymbol{k}$ parallel to $\boldsymbol{B}_0$ is zero), is

$$\frac{n_{e1}}{n_0} = \Big[1 - g(\omega_e, b_e; \omega_{ce})\Big] \frac{e\phi_1}{T_{e0}} \tag{6.1}$$

with

$$g(\omega_e, b_e; \omega_{ce}) = \exp(-b_e)\Big[I_0(b_e) + 2\sum_{m=1}^{\infty} \frac{\omega_e^2 I_m(b_e)}{\omega_e^2 - m^2\omega_{ce}^2}\Big]. \tag{6.2}$$

In these equations $\boldsymbol{E} = -\nabla\phi$, $c_{e0} = \sqrt{T_{e0}/m_e}$ is the electron thermal velocity, $\omega_{ce} = eB_0/m_e$ is the cyclotron frequency, $b_e = k^2\rho_{e0}^2$, $\rho_{e0} = c_{e0}/\omega_{ce}$ is the electron Larmor radius, $\omega_e = \omega - k_y u_{ye0}$ is the electron Doppler-shifted frequency, $\boldsymbol{k} = k_y\mathbf{1}_y + k_z\mathbf{1}_z$, and I_m are the modified Bessel functions of the first kind. According to equation (6.2), the perturbed electron response has resonances at the electron gyrofrequency and its harmonics, i.e. $\omega_e = m\omega_{ce}$.

Next, the density perturbations of cold ions follow

$$\frac{n_{i1}}{n_0} = \frac{k^2 c_{s0}^2}{\omega_i^2} \frac{e\phi_1}{T_{e0}}, \tag{6.3}$$

with $\omega_i = \omega - k_z u_{zi0}$ the ion Doppler-shifted frequency, and $c_{s0} = \sqrt{T_{e0}/m_i}$ the ion sound speed. Using equations (6.1) and (6.3), together with the linearized Poisson equation, yields the two-dimensional dispersion relation

$$1 + k^2\lambda_{D0}^2 = \frac{k^2 c_{s0}^2}{\omega_i^2} + g(\omega_e, b_e; \omega_{ce}). \tag{6.4}$$

This equation is solved for the complex frequencies $\omega = \omega_r + \mathrm{i}\gamma$ with all other parameters fixed, including $\boldsymbol{k}$.

The solutions of the dispersion relation are pairs of modes of three types [12]. First, there is a pair of ion-acoustic modes with $g \ll k^2 c_{s0}^2/\omega_i$ and real-valued frequencies $\omega_i = \pm\omega_{\mathrm{IA}}$; being

$$\omega_{\mathrm{IA}} = \frac{k c_{s0}}{\sqrt{1 + k^2\lambda_{D0}^2}}, \tag{6.5}$$

which include a non-neutral term in the denominator that corrects the quasineutral linear relation $\omega_i = \pm k c_{s0}$. Second, there are electron Bernstein waves [33], with $g \gg k^2 c_{s0}^2/\omega_i$ and real-valued frequencies too, close to the resonances $\omega_e = m\omega_{ce}$. Third, when $g \sim k^2 c_{s0}^2/\omega_i$, Bernstein waves become coupled with the ion acoustic modes, yielding one of them the modified ion acoustic (MIA) pair with frequencies

$$\omega_i = \pm\frac{k c_{s0}}{\sqrt{1 + k^2\lambda_{D0}^2 - g(\omega_e)}}. \tag{6.6}$$

Type	Description and symbol	Value and units
Fundamental plasma parameters	Ion mass, m_i	1 u
	Electric field, E_0	10^4 V/m
	Magnetic field, B_0	200 G
	Plasma density, n_0	10^{17} m^{-3}
	Ion axial velocity, u_{zi0}	2.5 km/s
	Electron temperature, T_{e0}	6 eV
Derived plasma parameters	Electron azimuthal drift, u_{ye0}	500 km/s
	Electron thermal speed, c_{e0}	1027 km/s
	Sound speed, c_{s0}	23.97 km/s
	Debye length, λ_{D0}	57.58 μm
	Electron azimuthal-drift gyroradius, ℓ_{e0}	142.1 μm
	Electron Larmor radius, ρ_{e0}	292.0 μm
	Electron plasma frequency, ω_{pe0}	2.839 GHz
	Electron gyrofrequency, ω_{ce}	0.5600 GHz
	Ion plasma frequency, ω_{pi0}	66.26 MHz
	Lower-hybrid frequency, ω_{lh}	13.07 MHz
Fundamental numerical parameters	Azimuthal domain length, L_y	5.359 mm
	Axial domain length, L_z	2.679 mm
	Number of azimuthal cells, N_y	100
	Number of axial cells, N_z	50
	Number of particles per cell, N_{ppc}	200
	Time steps, Δt	5×10^{-12} s
	Number of time steps, N_t	6×10^5
	Number of time steps between print-outs, N_{print}	1000
Derived numerical parameters	Azimuthal cell size, Δy	53.59 μm
	Axial cell size, Δz	53.59 μm

Table 6.1: Physical and numerical parameters of the reference simulation case. The subscript '0' stands for initial equilibrium conditions. Derived parameter values are included for completeness but can be computed from fundamental ones.

For $g > 1 + k^2\lambda_{D0}^2$, one of MIA modes is unstable leading to the so called ECDI. Since g changes from $-\infty$ to $+\infty$ when crossing the resonance $\omega_e = m\omega_{ce}$ with ω_e increasing, the MIA mode starts becoming unstable at $\omega_e = (m\omega_{ce})^+$ and becomes stable before reaching the $(m+1)$ resonance [3, 83, 153].

Figure 6.1 depicts, for the equilibrium solution of Table 6.1, the complex

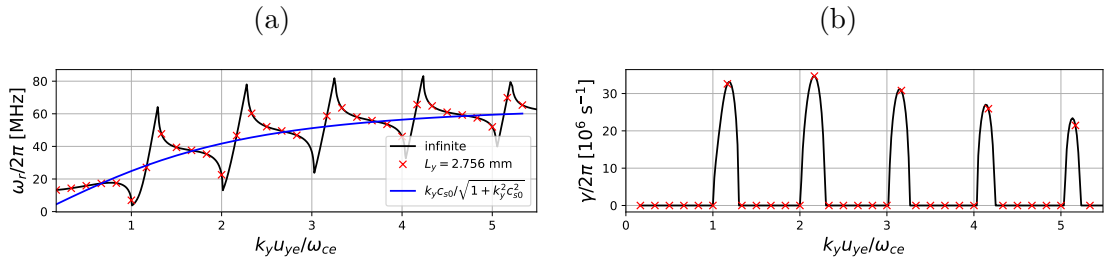

Figure 6.1: ECDI dispersion relation for a hydrogen plasma with $k_{\|} = 0$, $k_z = 0$ and the equilibrium conditions summarized in table 6.1. The black solid line is the solution for an infinite plasma. Red crosses stand for the discrete solutions in a finite plasma with $L_y = 5.359$ mm. The blue solid line is the ion-acoustic frequency ω_{IA}. The dispersion relation has been solved with the same numerical approach than reference [3].

frequency of the purely-azimuthal (i.e. $\boldsymbol{k} = k_y \mathbf{1}_y$) MIA mode, and shows the growth rate of the ECDI linked to each $m\omega_{ce}$; as a function of $k_y \ell_{e0}$, being $\ell_{e0} = u_{ye0}/\omega_{ce}$ the azimuthal-drift gyroradius. The ion-acoustic frequency ω_{IA} is also plotted for comparison with the MIA mode. The same equilibrium solution will be used in the kinetic simulations of the coming sections. For $k_y > 0$, the unstable mode has $\omega_r > 0$, meaning propagation in the $\boldsymbol{E}_0 \times \boldsymbol{B}_0$ direction. Due to symmetry, for $k_y < 0$, the unstable mode has $\omega_r < 0$ (i.e., moving again along $\boldsymbol{E}_0 \times \boldsymbol{B}_0$) and same γ. In the purely azimuthal ECDI, one has $\omega \sim k_y c_s \ll \omega_e \simeq -k_y u_{ye0} \approx -m\omega_{ce}$. Therefore, the electron (Bernstein-type) response is quasi-steady and defines mostly the wavelength of the ECDI. Regarding non-neutral effects the MIA is quasineutral as long as $k_y^2 \lambda_{D0}^2 \ll 1$, i.e.

$$\frac{\lambda_{D0}}{\rho_e} \ll \frac{u_{y_{e0}}}{m c_{e0}} \tag{6.7}$$

and non-neutral effects tend to reduce the complex frequency. This effect is very clearly seen in the curve ω_{IA} in figure 6.1(a), that shows frequencies lowered with respect to a quasineutral ion-acoustic linear relation. The comparison of the MIA and ion-acoustic frequencies demonstrates that they follow the same trend but with significant deviations coming from the coupling with the Bernstein terms.

If the plasma has a finite size L_y along y, there is only a discrete wave spectrum with $k_y = n2\pi/L_y$ and n the number of wavelengths fitting in the domain. Red crosses in Fig. 6.1 show that spectrum for $L_y = 12\pi\ell_{e0} = 5.359$ mm, when resonances correspond to n a multiple of 6. That length has been chosen so that modes $n = 1 + 6m$ capture approximately the peaks in γ associated to each resonance m. For the chosen parameters, the fastest growing mode is $n = 13$, close to the $m = 2$ resonance, with $\gamma/2\pi = 34.7 \times 10^6$ s^{-1}, $k_y \ell_{e0} = 2.167$ and $\omega_r = 46.6$ MHz. In terms of growth rate, the mode $n = 7$, in the band $m = 1$, follows closely with $\gamma/2\pi = 32.6 \times 10^6$ s^{-1}, $k_y \ell_{e0} = 1.167$ and $\omega_r = 27.1$ MHz.

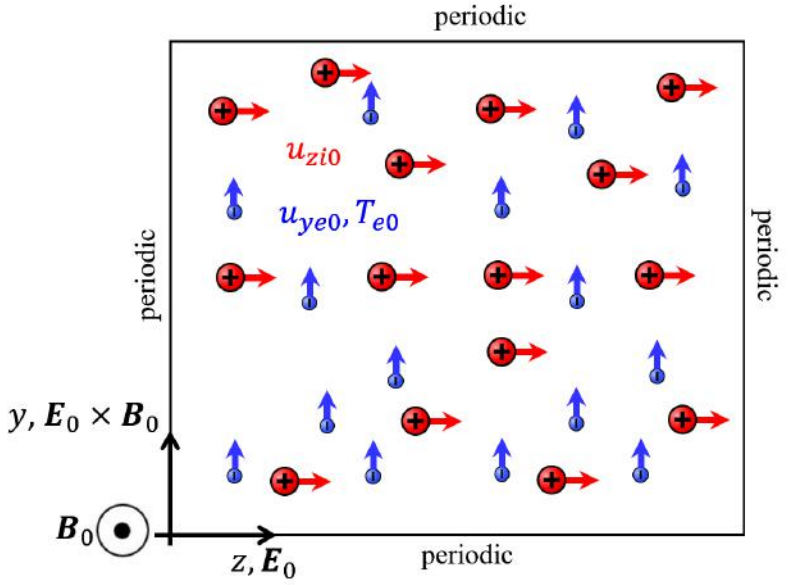

Figure 6.2: Diagram summarizing the simulation axes, boundary conditions and initial equilibrium state for simulations of the classical ECDI. A second type of simulations is considered that substitutes left and right boundary conditions to $\phi = 0$ and injection/absorbing conditions for particles.

The effects of a non-zero (moderate) k_z on the MIA modes are: introducing an ion-Doppler shift $k_z u_{zi0}$ in the frequencies, shifting the unstable bands in k_y, and changing mildly the growth rates (find a more exhaustive analysis in [83]).

To reduce the computational cost, simulations here correspond to a hydrogen plasma. The frequencies for hydrogen are, approximately, one order of magnitude higher than those expected in xenon. This is a reasonable result, since equation (6.4) shows that frequency and growth of the ECDI modes are proportional to kc_{s0} and, thus, scale with $1/\sqrt{m_i}$. This trend is, indeed, retrieved in PIC simulations shown later in this paper. The use of hydrogen instead of xenon in PIC simulations of the ECDI is a computational advantage since it allows us to observe the same physical phenomena but in a shorter time. With the same time step (still limited by the electron dynamics), this means reducing the number of time steps by one order of magnitude.

6.3 The classical ECDI: non-linear evolution

6.3.1 The numerical PIC model

The non-linear evolution and saturation of the classical ECDI is studied with a 2D axial azimuthal, 2D(z, θ), full PIC code developed in-house. The PIC formulation

follows ions and electrons. The electrostatic potential is obtained from a Poisson solver. The numerical codes are implemented in Fortran and use OpenMP shared-memory parallel computing.

The PIC code applies a standard Boris method to move electron and ion macroparticles in the periodic domain, and it employs a particle-decomposition strategy for parallel calculations. Macroparticles have equal and constant weights (i.e., number of real particles per macroparticle). As already pointed out, collisions between particles are totally disregarded.

The Poisson solver is able to use different schemes depending on boundary conditions. When all boundaries are periodic (the case in the present section 6.3), spectral methods are well suited to solve the Poisson equation in the Fourier complex space; here, the FFTW3 library [133] for Fourier and inverse transform operations is used, with a zero average potential. If Neumann or Dirichlet conditions are used in at least one boundary (the case in section 6.4), the Poisson solver uses a second order finite difference scheme for the Laplace operator and electric field, and the discrete linear system is solved with the PARDISO direct-solver routines in the Math Kernel Library of INTEL.

The electric and magnetic fields felt by each species and their initial macroscopic properties comply with the hypotheses and equilibrium state of section 6.2. Electron and ion particles are moved in a periodic domain with electric fields $\boldsymbol{E}_e = \boldsymbol{E}_0 + \boldsymbol{E}_1$ and $\boldsymbol{E}_i = \boldsymbol{E}_1$, respectively, being $\boldsymbol{E}_1 = -\nabla\phi$ the local fluctuation relative to $\boldsymbol{E}_0$ that comes as solution to the Poisson equation with periodic boundary conditions. The treatment of ions has been seen to be troublesome in one-dimensional azimuthal simulations [154,155] and it is even more concerning in the present two-dimensional model that accounts for the axial coordinate. Figure 6.2(a) sketches the simulation setup. At the initial equilibrium state, the axial current of electrons, j_{ze0} is zero. Since the plasma is collisionless, electrons are trapped in magnetic lines. Therefore, any subsequent electron axial current is due exclusively to the cross-field transport generated by the ECDI.

Regarding the simulations in this and next section, Table 6.1 includes both the physical and numerical parameters. Regarding the macroscopic and kinetic results to be shown, they include a moving-average during runtime on a window corresponding to N_{print} time steps. For an arbitrary variable φ, this is defined as

$$\tilde{\varphi}_k = \frac{\tilde{\varphi}_{k-1}(N_{\text{print}} - 1) + \varphi_k}{N_{\text{print}}}, \tag{6.8}$$

being k the time step index, φ_k the instantaneous value of and $\tilde{\varphi}_k$ its time-average value.

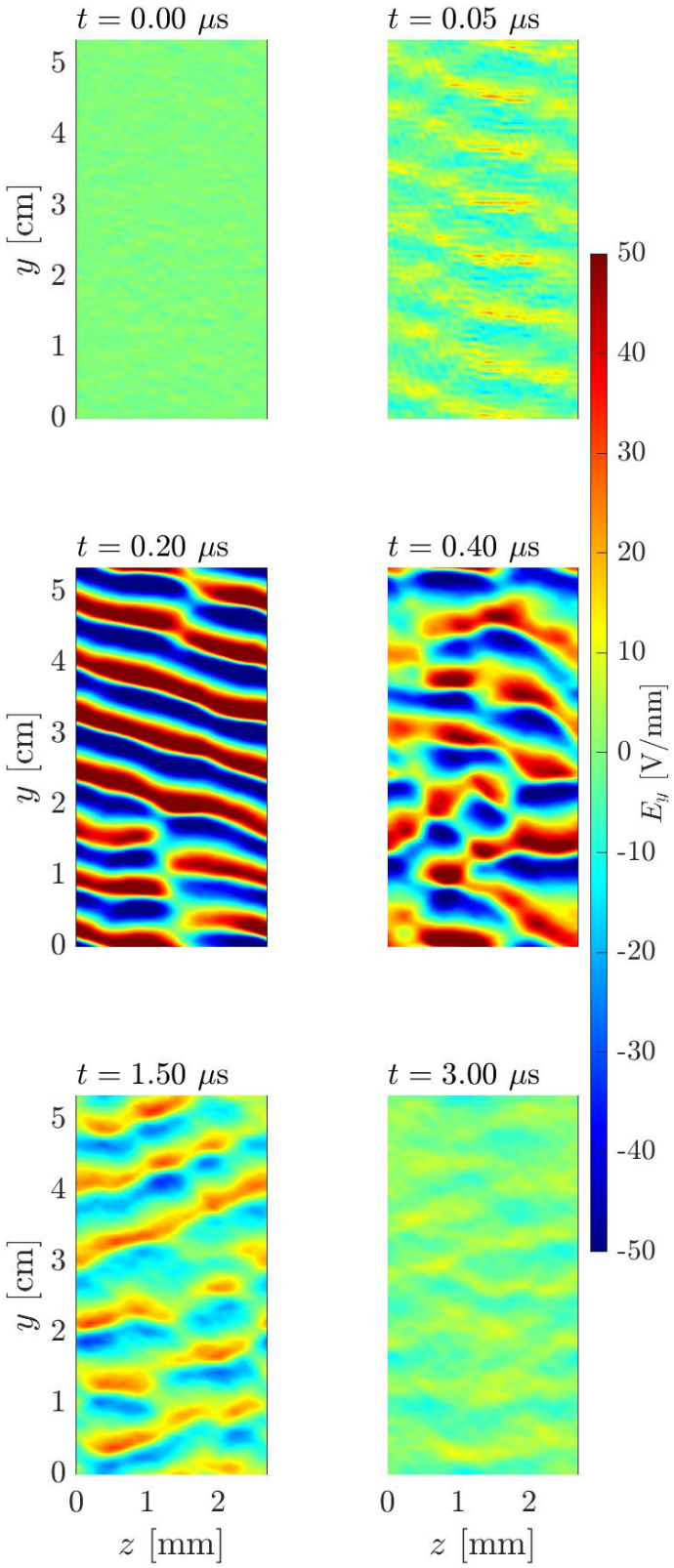

Figure 6.3: Reference case with fully periodic conditions: time-evolution of $E_y(y, z, t)$ in the yz-plane.

(a) $L_y = 2.679$ mm

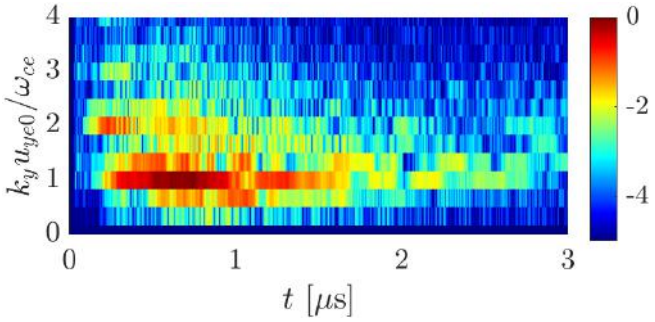

(b) $L_y = 5.359$ mm

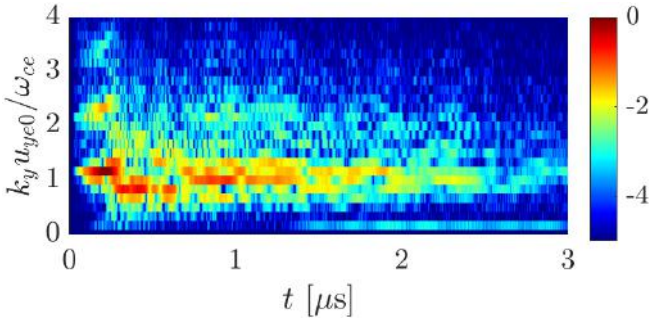

(c) $L_y = 10.72$ mm

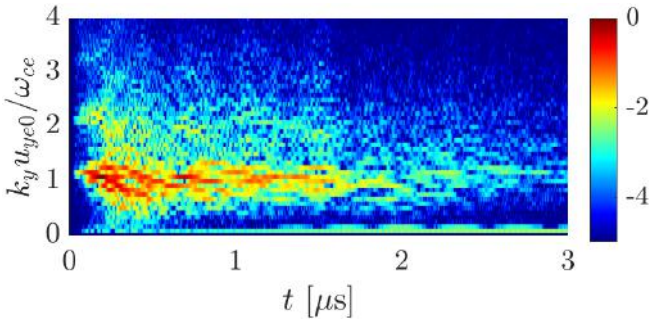

(d) $L_y = 16.08$ mm

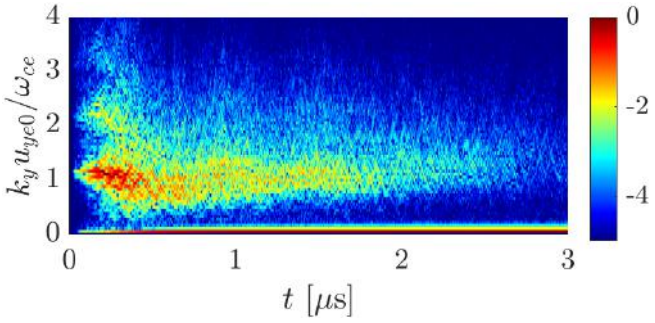

Figure 6.4: Reference case with fully periodic conditions: time-evolution of the logarithm of normalized coefficients from the fast Fourier transform of $E_y(t, y, z^*)$ in coordinate y, at $z^* = 5L_z/6$, for different L_y.

(a) 0 μs $< t <$ 0.20 μs

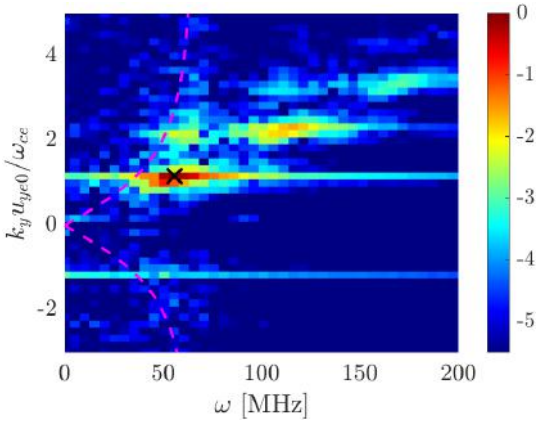

(b) 0.20 μs $< t <$ 0.75 μs

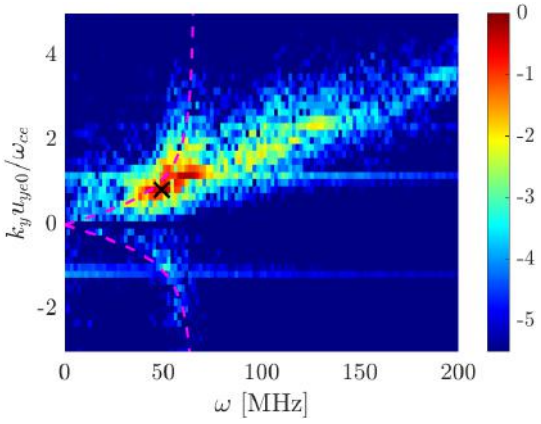

(c) 2.5 μs $< t <$ 3.0 μs

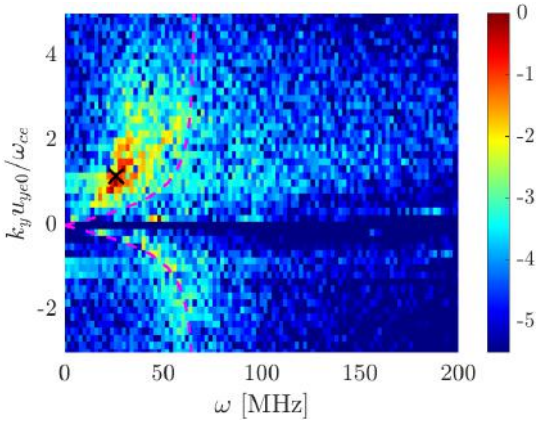

Figure 6.5: Reference case with fully periodic conditions: logarithm of normalized coefficients from the 2D fast Fourier transform of $E_y(t, y, z^*)$ in coordinates y and t, at $z^* = 5L_z/6$, and for 3 different time windows. The absolute maxima are marked with a black cross. Dashed magenta lines stand for ion-acoustic modes $\pm\omega_{\mathrm{IA}}$ with T_{e0} taken as the average value on the considered window: (a) 11.4 eV, (b) 40.1 eV and (c) 58.3 eV.

6.3.2 Onset, saturation, and vanishing of the ECDI

The time evolution in the yz-plane of $E_y(t, y, z)$ is represented in figure 6.3. The initial equilibrium state is unstable and the ECDI start to grow from any perturbation. The time-dependent solution is almost 1D in the azimuthal direction, although an axial component is present in early times, mainly. The oscillation amplitude gets a maximum around 0.2 μs and decreases in later times until eventually a new equilibrium state, different from the initial one, is reached. For $t < 0.2$ μs, wave modes are weakly mixed and the dominant monochromatic waves are easier to observe. The top panels of figure 6.3 indicate that the dominant mode is $n = 7$, which is the closest one to the resonance $m = 1$. For $t > 0.2$ μs, there is more mixing of modes; the bottom panels of figure 6.3 show transitions to $n = 5$ and 6 as dominant modes.

The linear theory showed that mode $m = 2$ has a (slightly) higher growth rate than mode $m = 1$. In fact the Fourier analysis of $E_y(t, y, z)$ in y [depicted in figure 6.4(b) for our simulation with $L_y = 5.359$mm] shows some contribution of mode $m = 2$ to the early time spectrum. However, the fast growth of several modes makes non-linear effects important soon in the simulation, which, together with the noise intrinsic to the PIC formulation, makes tough the exact comparison of early PIC results with the linear results from Vlasov equation [157, 158]. In addition, the long-term dominant modes in the non-linear stage may not coincide with the most unstable modes in the linear dispersion relation [87]. The use of quiet start techniques by other authors [154,158] to minimize the noise of the initial population has not been seen to be completely satisfactory.

The determination of the dominant frequency is more difficult since it depends on time itself. In Figure 6.5, results of the 2D fast Fourier transform in y and t are shown for three different time windows, together with the ion-acoustic curves $\pm\omega_{\mathrm{IA}}$ for the average T_e within the corresponding time interval. Each window represents different stages in the evolution of the ECDI:

(i) $0 < t < 0.20$ μs. The peaks seem to concentrate in bands near $k_y\ell_{e0} = m$, similarly to the theoretical dispersion relation in figure 6.1. The maximum Fourier coefficient is located at $k_y\ell_{e0} = 1.166$ and $\omega_r = 55.6$ MHz, with phase speed $\omega_r/k_y = 42.6$ km/s. This is mode number $n = 7$, near the resonance $m = 1$. There are secondary bands close to $m = 2$ and $m = 3$. The results in this early stage are qualitatively aligned with figure 6.1, but the dominant frequency ω_r is larger than predicted by the linear theory.

(ii) 0.2 μs $< t < 0.75$ μs. The bands of the upper spectrum near the resonances have been blurred and there is an approximately linear relation between k_y and ω_r, resembling a linear ion-acoustic relation. However, some parts of the

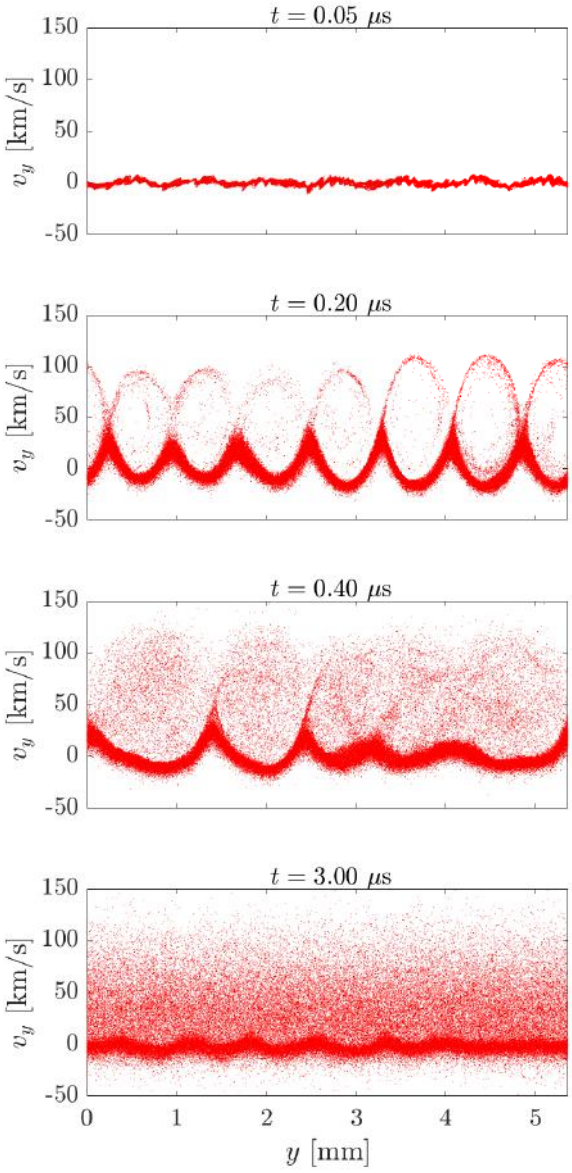

Figure 6.6: Reference case with fully periodic conditions: time evolution, in the phase space (y, v_y), of ions contained in an axial slab of width $0.1L_z$. The formation and blurring of the vortex-like structure characteristic of ion-wave trapping is observed.

upper spectrum seem to follow the non-neutral acoustic frequency ω_{IA}. This is aligned with previous PIC simulations [94, 134] and experiments [101]. The peak in the spectrum is at $k_y \ell_{e0} = 0.8334$; with $n = 5$, $\omega_r = 49.1$ MHz and $\omega_r / k_y = 52.6$ km/s and matches the ion-acoustic curve. Let us note that the lower part of the spectrum (propagation in the $-\boldsymbol{E}_0 \times \boldsymbol{B}_0$ direction), shows some remnants of the counter-propagating ion-acoustic wave with frequency $-\omega_{\mathrm{IA}}$.

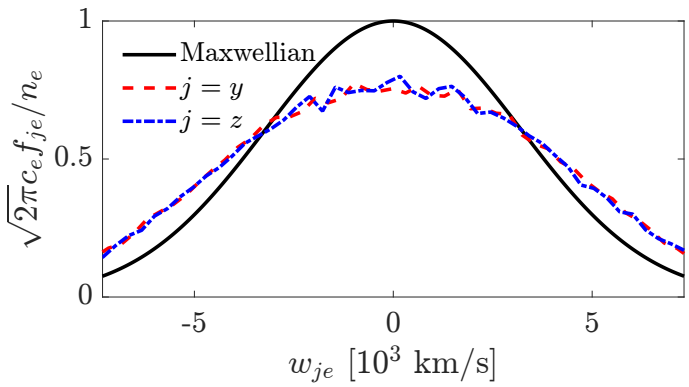

Figure 6.7: Reference case with fully periodic conditions: normalized electron distribution functions f_{je} in the azimuthal ($j = y$, red dashed) and axial ($j = z$, blue dash-dotted) directions, being the abscissa coordinate w_{je} the random velocity of electrons . The Maxwellian curve (black solid) is included for comparison, using local final values of $n_e = 10^{17}$ and $T_e = 58.8$ eV from the PIC simulation.

(iii) 2.5 μs $< t <$ 3 μs. Even if a peak is identifiable at $k_y \ell_{e0} = 1.166$ ($n = 7$), the mixing of different temporal and azimuthal scales result in a messy spectrum without a clear dominant mode. The ion-acoustic behaviour is only seen in the lower part of the spectrum.

At $t \sim 3$ μs, the plasma seems to tend to a new equilibrium with distorted ion and electron VDFs. Figure 6.6 plots the evolution of ion particles, contained within an axial slab of width $0.1L_z$, in phase space (y, v_y). During the growth and saturation of the ECDI (this is $t < 0.2$ μs), vortexes are formed in phase space showing the characteristic behaviour of ion trapping in the electrostatic wave. The vortexes are shifted towards positive velocities, matching the $\boldsymbol{E}_0 \times \boldsymbol{B}_0$ and dominant mode propagation directions. Later times reveal the distortion of those vortex structures until they are fully blurred into a strongly one-sided distribution with a long tail into positive velocities. This process coincides with the quenching of E_y oscillations. Electrons one-dimensional VDFs at the end of the simulation are shown in figure 6.7 to be fairly isotropic and flatter close to the average velocity compared to a Maxwellian, which coincides with [83, 84].

6.3.3 Evolution of the plasma energy

Let us get a further insight on the ECDI by analyzing the plasma energy stored in the plasma. The total energy in the plasma domain has contributions from the electrostatic field, electrons and ions, according to

$$\mathcal{E} = \mathcal{E}_E + \mathcal{E}_e + \mathcal{E}_i, \tag{6.9}$$

(a) Energy

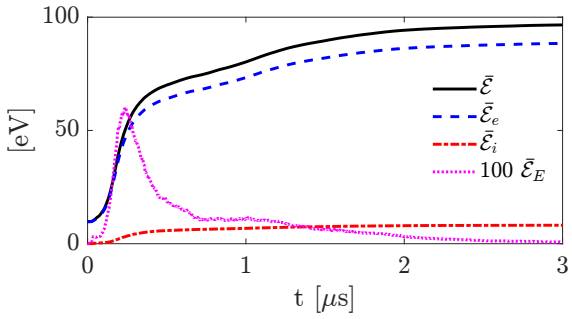

(b) Energy derivative

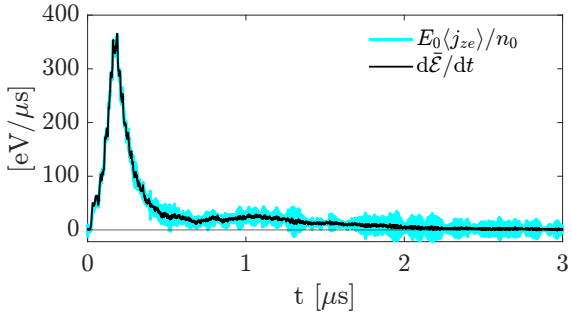

(c) Effect of L_y on $\bar{\mathcal{E}}$

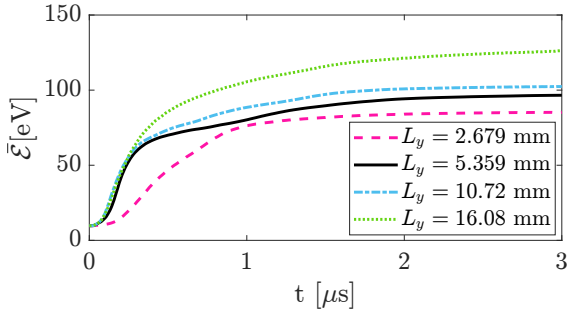

(d) Effect of L_y on $\langle j_{ze}\rangle$

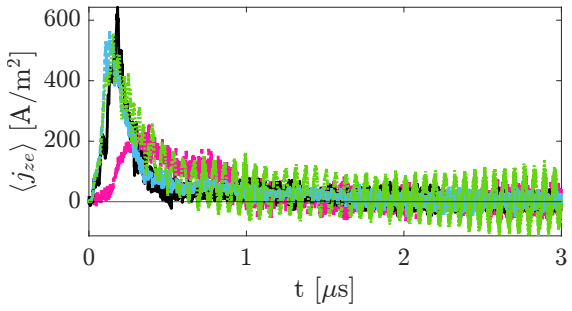

Figure 6.8: Fully-periodic case. Time evolution of (a) the energy time-derivative and (b) the electrostatic, species and total energies per particle (i.e., $\bar{\mathcal{E}} = \mathcal{E}/\langle n\rangle V$. Panels (c) and (d) plot energy per particle and volume-averaged electron axial current for different L_y.

with

$$\mathcal{E}_E = \frac{\varepsilon_0}{2} \int_{\mathcal{V}} E_1^2 \, \mathrm{d}\mathcal{V}. \tag{6.10}$$

the energy of the electromagnetic oscillations,

$$\mathcal{E}_s = \int_{\mathcal{V}} \left[\frac{1}{2} m_s n_s u_s^2 + \frac{3}{2} p_s \right] \mathrm{d}\mathcal{V}, \quad s = e, i \tag{6.11}$$

the total energy of electrons and ions; and $\mathcal{V}$ is the volume of the domain. The energy of each species is approximated in the PIC formulation as

$$\mathcal{E}_s = \sum_p \frac{1}{2} m_s v_p^2 W_p, \tag{6.12}$$

where the sum is on every particle in the domain with v_p and W_p the particle speed and weight, respectively.

In a consistent situation, the work done by the electric field should act as a mechanism that converts species energy on electric-field energy, and the other way around. However, the assumptions behind the linear theory of the ECDI forced us to let ions and electrons feel different electric fields. Because of this non-conventional feature, it can be proved that the total energy changes according to

$$\frac{\partial \mathcal{E}}{\partial t} = \int_{\mathcal{V}} (\boldsymbol{j}_e \cdot \boldsymbol{E}_0) \, \mathrm{d}\mathcal{V} = E_0 \int_{\mathcal{V}} j_{ze} \, \mathrm{d}\mathcal{V} = E_0 \langle j_{ze} \rangle \mathcal{V}, \tag{6.13}$$

with $\boldsymbol{j}_e$ the electron current density and $\langle j_{ze} \rangle$ the volume-averaged j_{ze}. Therefore, this kind of simulation will not show a proper conservation of energy and the equilibrium electric field will pump energy into the isolated system. However, this source of energy requires also an axial electron current j_{ze} to be developed. This means that the energy is conserved initially until the instability is triggered, and any other stationary energy state should satisfy a null $\langle j_{ze} \rangle$, i.e., no turbulent electron transport.

Figure 6.8(a) shows the evolution of electrostatic, species, and total energies in the domain per real particle. Here, average energies per particle $\bar{\mathcal{E}} = \mathcal{E} / \langle n \rangle \mathcal{V}$ are used, being $\langle n \rangle$ the volume-averaged density and $\langle n \rangle \mathcal{V}$ the real number particles in the domain. Initially $\bar{\mathcal{E}}_E = 0$, $\bar{\mathcal{E}}_i = m_i u_{zi0}^2/2 = 0.0324$ eV and $\bar{\mathcal{E}}_e = 3T_{e0}/2 + m_e u_{ye0}^2/2 = 9.71$ eV. Eventually, the total energy saturates and becomes stationary. There is significant heating of electrons and, to a lesser extent, of ions; which is coherent with other works [84, 154, 155, 157]. The electrostatic energy is much lower than those of electrons and ions, and approaches zero for late simulation times, when oscillations are very weak.

The balance (6.13) is evaluated in figure 6.8(b). The rate $\mathrm{d}\bar{\mathcal{E}}/\mathrm{d}t$ is approximated numerically and compared with the source term $E_0 \langle j_{ze} \rangle / n_0$. The two curves show an excellent match apart from the noise inherent to the PIC approach, specially

problematic in the calculation of j_{ze}. The PIC simulation is able to approximately replicate the theoretical energy balance (6.13), which is a good sign of the validity of such simulations. The change in energy shows a peak and then decreases tending to zero for late simulation times, meaning that a new stationary equilibrium state of the plasma is reached. As already said, the energy source is related with the development of a net axial current, so the new equilibrium holds an average j_{ze} equal to zero. However, at mid simulation times, saturated ECDI modes are effective in inducing an axial transport of electrons.

6.3.4 Effect of the domain's azimuthal length

As pointed out in section 6.2, the azimuthal domain length L_y is an important parameter that determines the unstable ECDI modes that can be excited in a finite domain. On the contrary, the effect of L_z has been seen to be small, although the chosen axial length is large enough to allow the formation of waves with axial component fitting L_z. Increasing L_y allows larger scales to develop and increases the spectral resolution in the k_y-space, better capturing the continuous dispersion relation for an infinite plasma. In figure 6.4, the time evolution of azimuthal Fourier coefficients for E_{y1} are represented for several L_y multiples of 2.679 mm, the reference case corresponding to plot 6.4(b). The main trends identified in the shortest case are also recovered in larger domains: modes close to resonant bands $m = 1$ and $m = 2$ are excited in early times, modes close to $m = 1$ dominate at mid times, and oscillations quench after the spectrum peaks are passed. These trends become clearer as longer domains are used. Some differences worth mentioning among cases are: (i) a mode with azimuthal wavelength equal to L_y (i.e. $n = 1$) is present only at long L_y and (ii) the enhanced spectral resolution of longer L_y allows to better capture shorter resonant bands, such as the modes close to $m = 2$. Similar conclusions on these two points are reached in reference [157].

Figure 6.8(c) shows that the energy per real particle increases with parameter L_y, probably due to the greater number of unstable excited modes [157]. With the exception of the shortest case $L_y = 2.679$ mm, which shows a slower energy increase and lower $\langle j_{ze} \rangle$ [most probably due to a poor spectral resolution, unable to properly capture the peaks of the growth rate of Fig 6.1] the rates of energy increase during the growth period are similar for $L_y \geq 5.359$ mm. This suggests that the maximum $\langle j_{ze} \rangle$ and the time to reach it are numerically robust and thus physical. Therefore, results with $L_y = 5.359$ mm are representative of simulations with longer L_y multiples of 5.359 mm. This behaviour disagrees with reference [157], where changes in L_y can drastically change the transients of $\langle j_{ze} \rangle$ and, thus, the energy growth rates.

(a) $m_i = 1\text{u}$

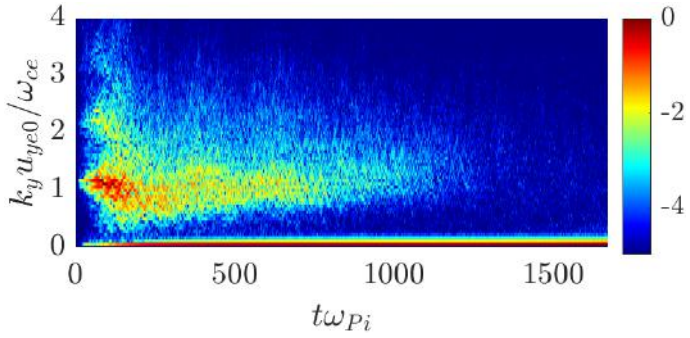

(b) $m_i = 4\text{u}$

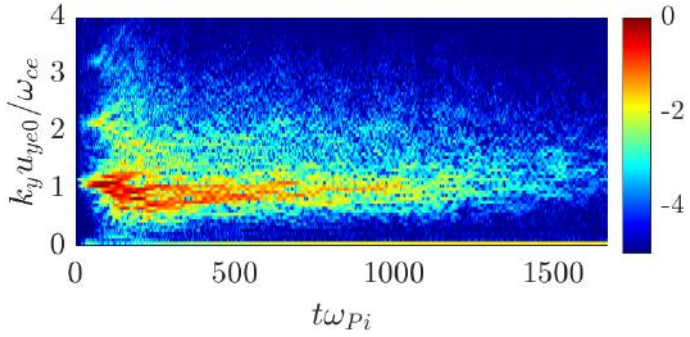

(c) $m_i = 9\text{u}$

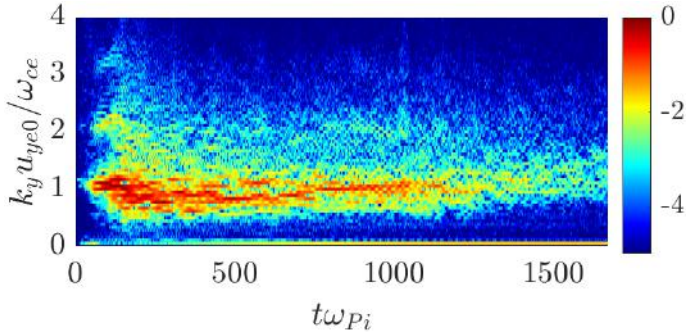

Figure 6.9: Fully-periodic case, Time-evolution of the logarithm of normalized azimuthal Fourier coefficients for different values of m_i.

Since the long term behaviour of $\langle j_{ze} \rangle$ tends to zero in every case, we can conclude that the long-wavelength mode with $n = 1$ that develops with increasing L_y is not effectively producing an axial electron transport. This is consistent with the late evolution of n_e and E_y (not included), which shows completely out of phase oscillations.

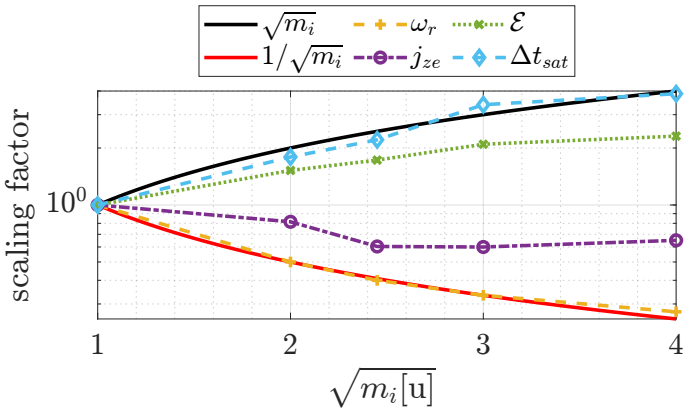

Figure 6.10: Scaling factor, with the ion mass m_i, of several variables: dominant ω_r in the interval $t\omega_{Pi} < 83.15$, peak averaged j_{ze}, final $\mathcal{E}$ and Δt_{sat}. The curves $\sqrt{m_i}$ and $1/\sqrt{m_i}$ are also included for comparison.

6.3.5 Effect of the ion mass

In this subsection, the simulation is repeated for increasing values of the ion mass. While hydrogen mass, m_H has been used in order to speed up the dynamics and minimize the computational cost, the practical cases of interest deal with heavier ions, e.g., xenon or krypton. In addition, an increased azimuthal length $L_y = 16.08$ mm is used to have a proper spectral resolution and a fair comparison, since an increased m_i narrows the unstable bands in the dispersion relation near the resonances what needs an increased spectral resolution.

In the early evolution of the ECDI, the dispersion relation (6.4) shows that the frequency should scale inversely proportional to $\sqrt{m_i}$. However, this does not have to be the case of the non-linear dynamics or other magnitudes. The scaling factors for several quantities, defined as the ratio with respect to the value in the reference case $m_i = 1$ u are computed in figure 6.10: dominant ω_r in the interval $t\omega_{Pi} < 83.15$, peak of $\langle j_{ze} \rangle$, final $\mathcal{E}$ and Δt_{sat}. The observed trends are coherent with results reported in reference [159]. If the dominant frequency is measured in early simulation times, the observed scaling perfectly matches the linear theoretical result. The saturation time Δt_{sat}, defined as the time of maximum average $\langle j_{ze} \rangle$, seems to scale proportional to $\sqrt{m_i}$. The 1D azimuthal Fourier spectra are compared in figure 6.9, where the time axis is normalized with the inverse of the ion plasma frequency ω_{Pi}. While the saturation of the early oscillations produced by the ECDI happens at similar $t\omega_{Pi}$ (as shown by the scaling of Δt_{sat}), the quenching of short wavelength $m = 1$ and $\langle j_{ze} \rangle$ seems to be slightly slower with increasing m_i.

The level of turbulent current, measured by the peak $\langle j_{ze} \rangle$, initially decreases with m_i, which could be explained by the weaker oscillations observed in n_e (not included here), but seems to saturate. The current $\langle j_{ze} \rangle$ decreases, however, slower

than $1/\sqrt{m_i}$ which leads to a final $\mathcal{E}$ increasing with m_i, in accordance with equation (6.13). Extrapolating these results, with xenon we can expect somehow smaller level of transport but dilated in time, what would cause a significant heating such as that observed in similar studies in the literature [87, 154, 157].

6.3.6 Saturation behaviour in previous literature

The results we have shown in this section pursue the simulation of scenarios as close as possible to the classical ECDI. While we observe the growth and saturation of oscillations due to an instability, modes that induce an axial electron transport seem to vanish at long times. The late simulation behaviour differ from other 1D [84, 154, 155, 157] and 2D [93, 94, 134, 135] simulations on similar configurations, which report sustained oscillations not vanishing with time. Even if our model is 2D, we disregard many of the effects included in other 2D works (e.g., inhomogeneous magnetic field, anode-cathode circuit or collisions), which are closer to Hall-discharge-like configurations. A fairer comparison is that with the existing 1D azimuthal models [84, 154, 155, 157], whose sustained oscillation for late simulation times either saturate [154, 155] or forever grow [84, 157], depending on the axial treatment of particles.

As seen in section 6.3.2, the stages observed in the evolution of oscillations are greatly related to the interaction of ions with the electrostatic wave and the distribution of ion particles in phase space. Our approach, similarly to references [84, 157], disregard $\boldsymbol{E}_0$ on the ion motion to prevent the consequent axial inhomogeneity and be able to apply periodic conditions, not only azimuthally, but also axially. Because there is no change in velocity for particles going through boundaries, the change in the VDF of ions and electrons from the initial one is solely a result of the ECDI. On the other hand, references [154, 155] account for a virtual axial dimension, so that particles that leave the domain through axial boundaries after interacting with the electrostatic wave are re-injected with a refreshed velocity sampled from a prescribed VDF. This is, the refreshing axial conditions (and the refreshing rate determined but the axial length) modify the VDF of particles and can have a significant impact on the particle-wave interaction and overall simulation behaviour. This point is extensively analyzed in the next section.

When no virtual axial dimension or refreshing are considered, previous literature [84, 154, 157] observe an unlimited growth of the oscillations and heating. The reasons that explain why they do not see the quenching of short-wavelength waves are still to be investigated, but let us speculate about a couple of possibilities. An explanation could be that the evolution towards a new equilibrium is not inherent to all simulations of this type and depends on the selection of parameters (although

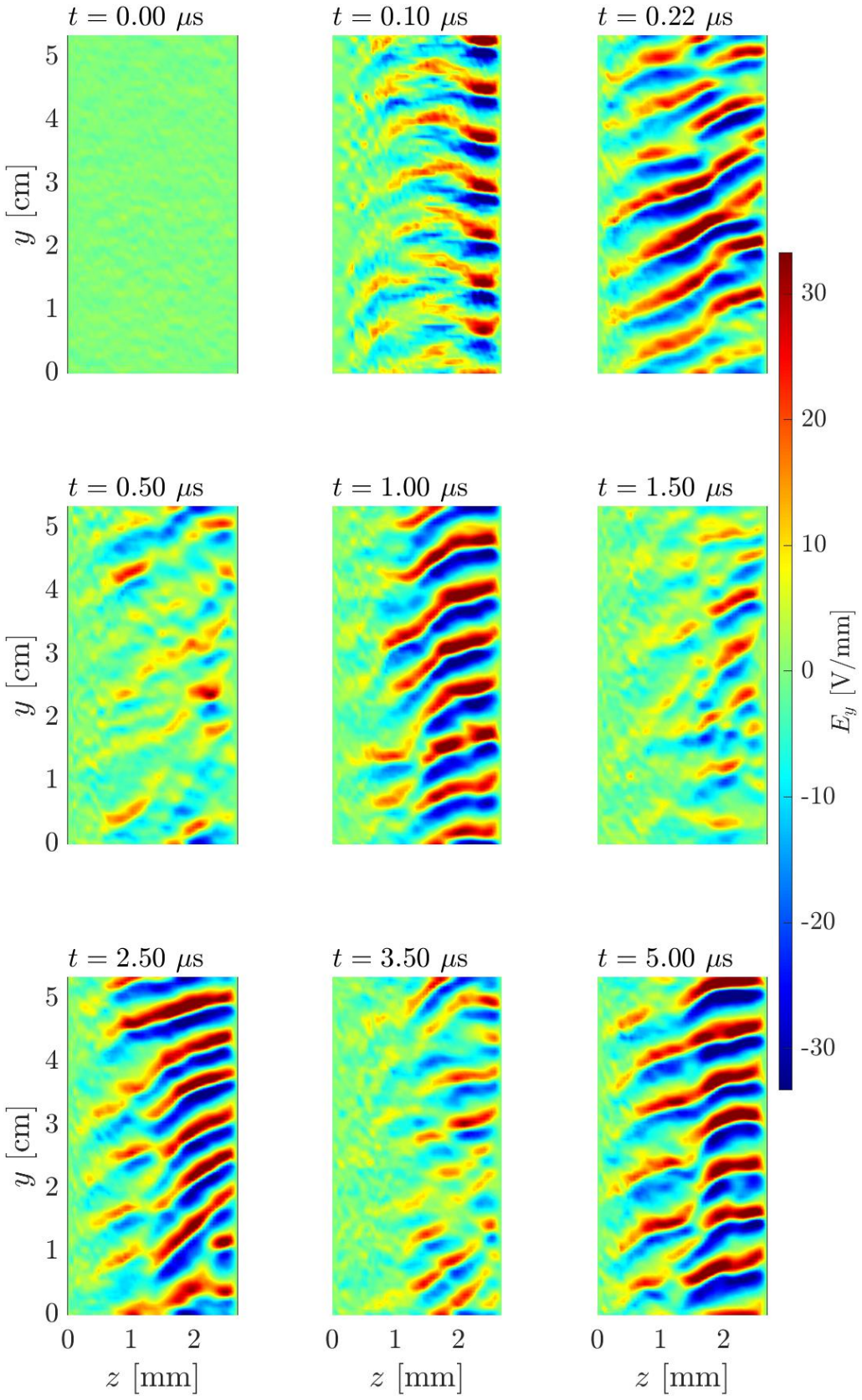

Figure 6.11: Finite plasma with axial injection. Time-evolution of E_y in the yz-plane.

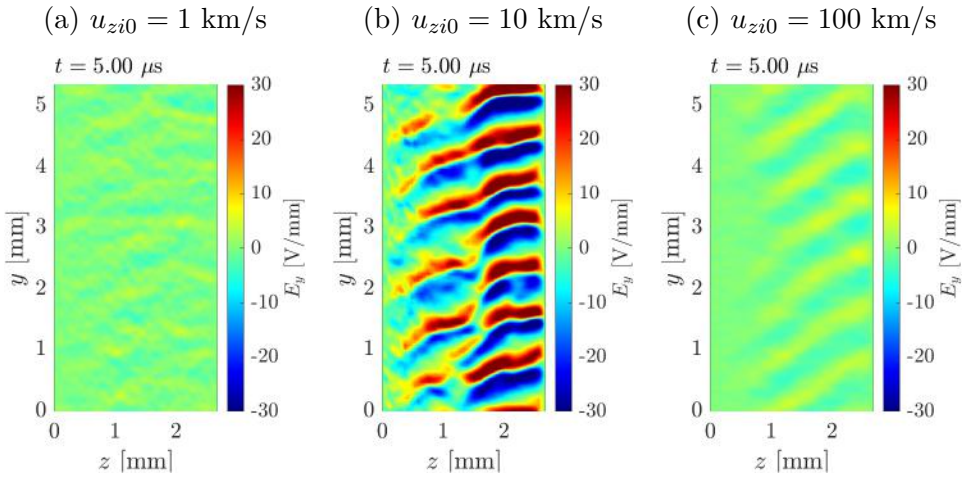

Figure 6.12: Finite plasma with axial injection. Late behaviour (at $t = 5\mu$s) of E_y in the yz-plane, for different u_{zi0}.

this is the behaviour we have seen in all of our simulations). Another possibility, in line with the results in section 6.3.5, could be that more simulation time is needed with xenon than considered in [84, 154, 157] to observe our late simulation stage.

6.4 The ECDI in an axially-injected finite-plasma

In the previous section, we pointed out the possible interaction of particle injection with the ECDI. Fully periodic boundary conditions preserve the VDF of the particles resultant of interacting with the instability. When there is particle removal and injection through boundaries, particles that have already interacted with the wave are removed from the simulation and new particles are injected having a different VDF that could possibly modify the behaviour of the instability.

Following this reasoning, a new simulation setup is presented here that replaces axial periodic conditions by injection ones, while periodic conditions are kept in the azimuthal direction. Any particle leaving the domain though axial boundaries is removed from the simulation. A constant flux of ions $n_0 u_{zi0}$ is injected through the left boundary, with zero temperature and velocity $u_{zi0}\mathbf{1}_z$. Constant fluxes of electrons $\pm n_0 c_{e0}/\sqrt{2\pi}$, corresponding to the one obtained from half-Maxwellian, are injected through left and right boundaries, whose velocities are sampled from a Maxwellian-flux distribution with temperature T_{e0} and velocity $u_{ye0}\mathbf{1}_y$. The injection fluxes are chosen such that they match the amount of ions and electrons leaving the domain in equilibrium conditions, making this equilibrium equivalent to the fully periodic domain. In contrast with the particle refreshing approach used in [154, 155], once the instability arises, the injected fluxes do not need to coincide with fluxes leaving the domain and the number of particles and electric charge are not conserved

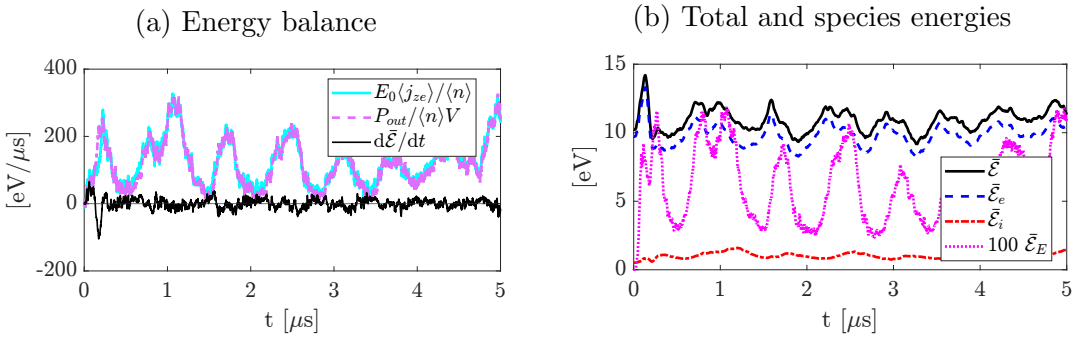

Figure 6.13: Finite plasma with axial injection. Time evolution of (a) energy balance and (b) electrostatic (c), species and total energies; for an axial-injection simulation with $u_{zi0} = 10$ km/s. Values are given per real particle.

any more. For that reason, axial conditions on potential are also changed from periodic to fixed potential $\phi = 0$ and the finite-difference PARDISO version of the Poisson solver is used.

6.4.1 Dependence on the ion residence time

In section 6.3, we showed the usual stages that we observe in the evolution of the ECDI, being the final one the quenching of short-wavelength oscillations. These stages are related with the ion velocity distribution and the formation and blurring of vortex-like structures in phase space. In this sense, adding axial boundaries that inject and absorb particles can have a major impact on the late simulation behaviour since old particles that have interacted with the wave are removed and new, non-trapped particles are injected with the original distribution.

In this scenario with axial injection, more similar to a Hall discharge, the ion residence time

$$\Delta t_{i0} = L_z/u_{zi0} \tag{6.14}$$

(infinite in a fully periodic domain independently of L_z) is the key parameter in maintaining a saturated ECDI, with sustained short-wavelength oscillations and a non-zero axial electron transport. Three regimes will be distinguished depending on Δt_{i0} being much smaller, of the same order, or much higher than the saturation time Δt_{sat} of the full-periodic configuration for the same equilibrium plasma, where $\langle j_{ze}\rangle$ peaks.

We consider again a hydrogen plasma and the reference case of Table 6.1. The saturation time was $\Delta t_{\mathrm{sat}} \sim 0.16$-$0.18$ μs. We run cases with $u_{zi0} = 1$, 5, 10, 15, 20, 25 and 100 km/s, yielding, for $L_z = 2.679$ mm, residence times $\Delta t_{i0} = 2.68$, 0.536, 0.268, 0.179, 0.134, 0.107 and 0.0268 μs, covering the three expected regimes.

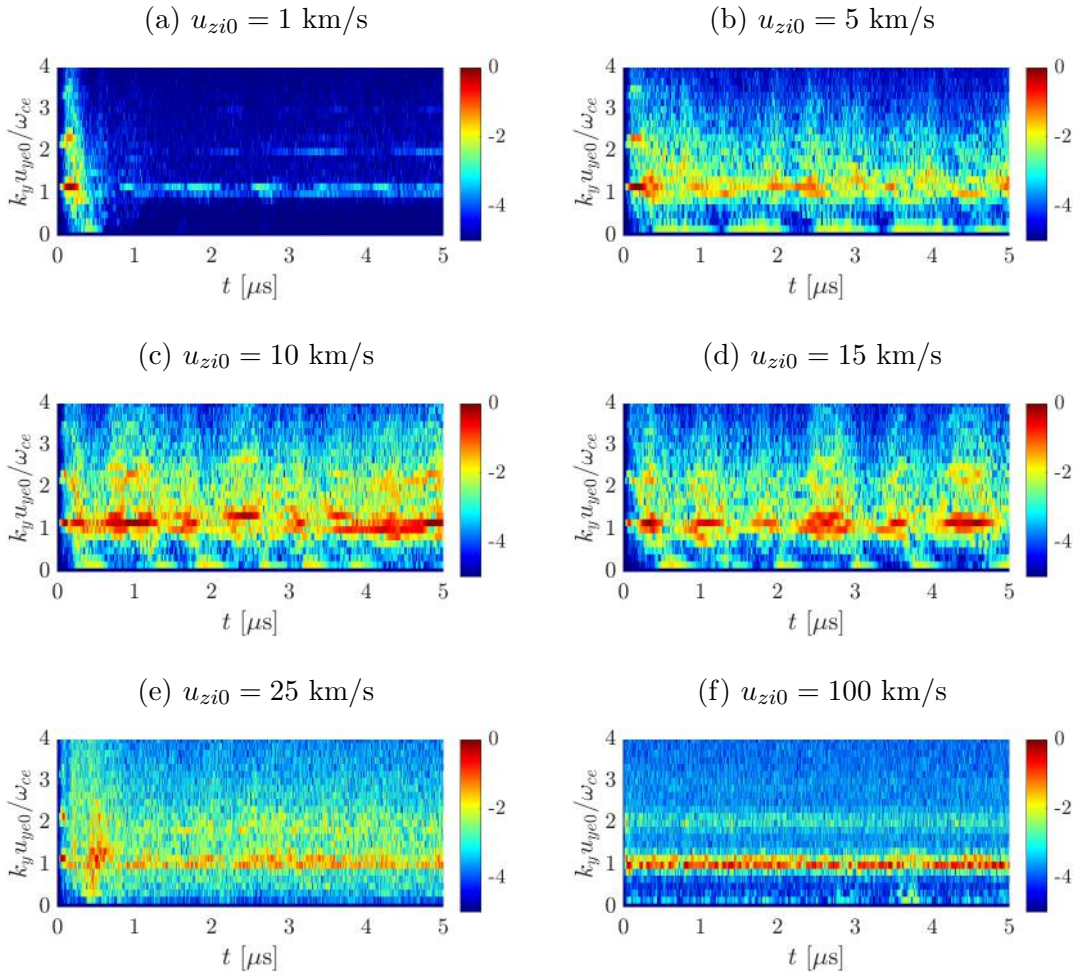

Figure 6.14: Finite plasma with axial injection. Time-evolution of the logarithm of normalized azimuthal Fourier coefficients for different values of u_{zi0}.

The evolution of azimuthal Fourier coefficients in figure 6.14 and the average current j_{ze} in figure 6.15 give an idea of the time evolution, where the transition from one limit regime to the other can be appreciated. The final E_y in the axial-azimuthal plane after 5 μs for cases $u_{zi0} = 1$, 10 and 100 km/s are shown in figure 6.12.

The case having $u_{zi0} = 1$ km/s corresponds to regime $\Delta t_{i0} \gg \Delta t_{\text{sat}}$ and the final E_y resembles the periodic case. Looking at figure 6.14(a), we see that the time evolution of Fourier coefficients is only similar at very early times when the onset of the ECDI on the initial population; after which oscillations are mild. From the energy point of view, the different axial boundary conditions here limit the electron heating and total energy in the domain, which is probably limiting the energy and contributing to the quenching of oscillations after the first ECDI onset. The evolution of $\langle j_{ze} \rangle$ is similar to the periodic case, where the current induced by the onset of the ECDI at early simulation times fades away at large enough times.

On the opposite limit we have the case $u_{zi0} = 100$ km/s with $\Delta t_{i0} \ll \Delta t_{\text{sat}}$,

where the final E_y shows a sustained but very weak short-wavelength oscillation. The azimuthal spectrum shows that dominant modes concentrate around resonances $m = 1$ and, to a lesser extend, $m = 2$. In this regime ECDI modes cannot develop completely since most of the ions leave the domain before full trapping occurs, so that we get an early stage of the ECDI observed with periodic conditions. According to figure 6.15, these mild oscillatory modes induce a weak j_{ze} in the electrons, which is very small compared with values produced by a fully developed ECDI.

In the intermediate regime $\Delta t_{i0} \sim \Delta t_{\text{sat}}$ we consider cases with u_{zi0} between 5 and 25 km/s (always for hydrogen). The plasma behaviour resembles the saturated behaviour of periodic simulation, because the removal and injection of particles happen at the proper rate that keeps feeding ECDI modes and allows them to fully develop, preventing the quenching of the oscillations observed in the regime $\Delta t_{i0} \gg \Delta t_{\text{sat}}$. From these cases, those with $u_{zi0} = 5$ and 25 km/s are halfway between regimes and show features of both limit and intermediate regimes. In every case, the electric field shows sustained oscillations with a clear dominant mode close to the resonance $m = 1$, that effectively induces a significant j_{ze} in the long term. The magnitude of the induced transport depends on the case, being more significant, and comparable to the peak values of the periodic case, for the cases with $u_{zi0} = 10$ and 15 km/s. In these two cases the dominance of modes close to $m = 1$ does not happen at every time and there is some kind of intermittent or pulsed behaviour of long and short wavelength modes, which results in an oscillatory evolution of the average j_{ze}. This intermittency is also observed in the time evolution of figure 6.11 for the case $u_{zi0} = 10$ km/s. For greater and smaller values of ion velocity, j_{ze} gets diminished, which is expected after our observations of null j_{ze} in upper and lower limit regimes.

From the point of view of ion particles in phase space, the final pictures for cases $u_{zi0} = 1$, 10 and 25 km/s are shown in an axial slab $0.7 < z/L_z < 0.75$. Here, it is confirmed that only when $\Delta t_{i0} \sim \Delta t_{\text{sat}}$ the vortex-like structure characteristic of ion-wave trapping is preserved and long-term axial transport exists. The existence of different regimes depending on the ion residence time could also explain why, with a virtual axial length, some groups observe a transition to an ion-acoustic mode [153] while others do not [155, 160].

The sensitivity of these results to L_y has been tested to ensure that the same conclusions apply to larger domains. The evolution of electron currents are plotted in figure 6.17 varying L_y while fixing $u_{zi0} = 10$ km/s. As with fully periodic simulations, the shortest case gives the most different transient but in all cases a large j_{ze} develops and they all show the characteristics of the intermediate regime $\Delta t_{i0} \sim \Delta t_{\text{sat}}$. In light of the fully periodic results, where larger L_y seemed to favour the formation of long domain-size modes, it is surprising that, here, increasing L_y mitigates the intermittency of short and long scales and yields less oscillatory currents. A possible

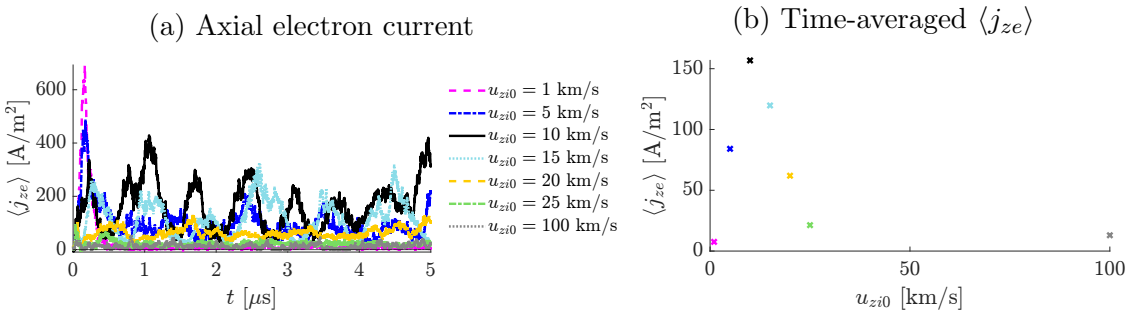

Figure 6.15: Finite plasma with axial injection. (a) Time evolution of the volume-averaged electron axial current $\langle j_{ze} \rangle$ for several u_{zi0} and (b) its time average for $t \geq 2$ μs.

explanation could be that the saturation time is slightly affected by L_y.

Previous results can be extrapolated to xenon in a Hall discharge using the scaling laws suggested in section 6.3.5 and a typical Δt_{i0}. Using an average ion velocity $u_{zi0} = 17$ km/s and anode-to-cathode length $L_z = 3.35$ cm (e.g., from results in [28]), Δt_{i0} is estimated to be 1.95 μs. The value of Δt_{sat} for xenon mass is estimated to be 1.83 to 2.06 μs. This similarity suggests that the intermediate regime of the ECDI in a finite plasma could develop in a conventional Hall discharge and supports the idea of the ECDI possibly being an important actor in the anomalous electron transport.

6.4.2 Energy balance

For the fully periodic case, equation (6.13) shows that the evolution of total energy in the domain is fed by the equilibrium electric field E_0 and is tied to the presence of an average j_{ze}. Therefore, an energetically stationary state does not allow for an axial electron current. This theoretical conclusion is retrieved in our periodic simulations.

Axial injection and removal of particles involve energy inputs and losses through axial boundaries that have to be accounted for in the energy balance, yielding

$$\frac{\mathrm{d}\mathcal{E}}{\mathrm{d}t} = E_0 \langle j_{ze} \rangle \mathcal{V} - P_{\text{out}}, \tag{6.15}$$

where P_{out} gathers the net energy outflow through axial boundaries and can be computed from the energies of removed and injected particles. The new term opens the possibility to have a balance between the energy input by E_0 and boundary losses, allowing for an energetically stationary behaviour and an average j_{ze} at the same time. Any energy loss term, such as inelastic collisions, could play a similar role in the balance.

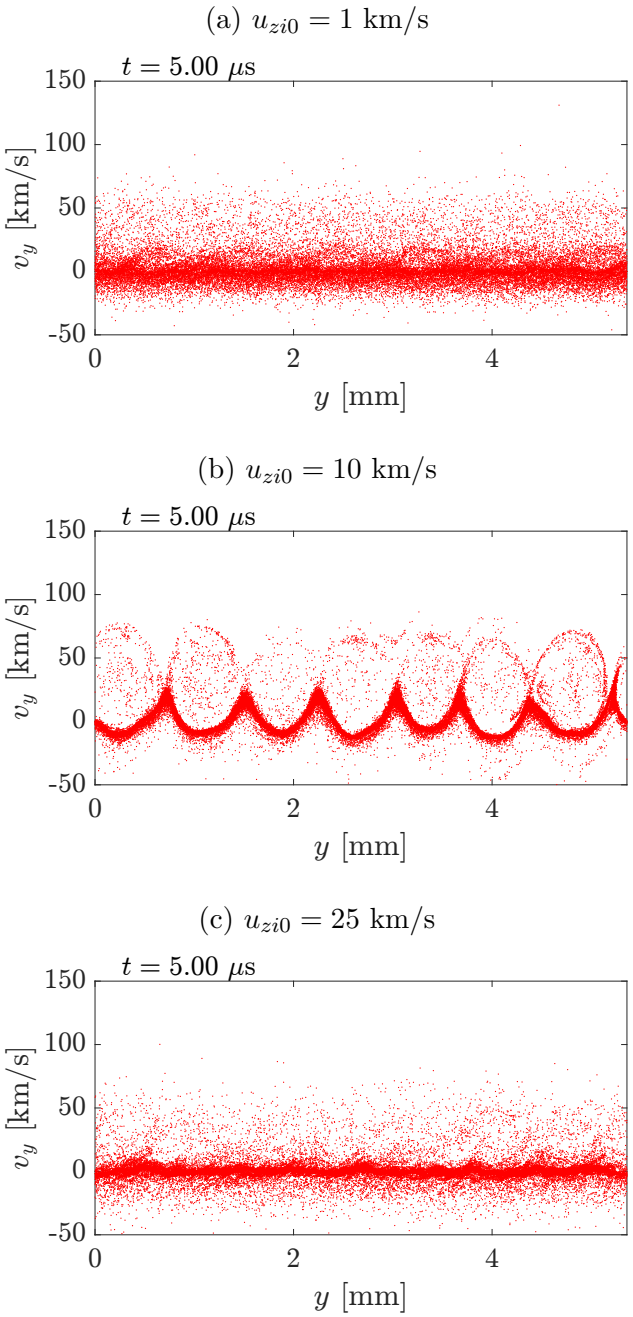

Figure 6.16: Finite plasma with axial injection. Late behaviour (at $t = 5\mu$s) in the phase space plane (y, v_y) of ion particles contained in the axial slab $0.7 \leq z/L_z \leq 0.75$.

The different terms in the balance equation (6.15) are computed and represented in figure 6.13 for the case with $u_{zi0} = 10$ km/s, in the intermediate regime with a net j_{ze}. The balance is approximately fulfilled and the energy is close to stationary. There is, however, small changes in the total energy as well as in the partial energies of ions and electrons. The losses introduced by the axial boundary conditions limit enormously the heating that was observed in the fully periodic cases without losses. Actually, the total and species energies remain within levels close to the initial

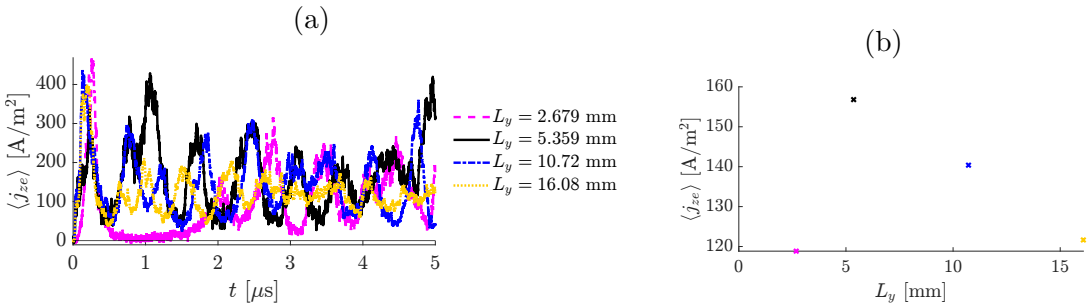

Figure 6.17: Finite plasma with axial injection. (a) Time evolution of the volume-averaged electron axial current $\langle j_{ze} \rangle$ for several L_y and (b) its time average for $t \geq 2$ μs.

population. The electrostatic energy is, again, a minor contribution to the total energy.

6.5 Conclusions

The first part of this article is focused on the simulation of the classical ECDI with the PIC formulation and settings as close as possible to the linear kinetic theory. Unstable short-wavelength modes are seen to grow in the initially homogeneous plasma that fit qualitatively well the features of the theoretical ECDI dispersion relation in early simulation times. Close to saturation, some parts of the Fourier spectra show similarities with ion-acoustic modes. After saturation, the short scale modes vanish and the plasma tends to a new equilibrium with mild or long-wavelength oscillations and much more mode mixing. It is only during the growth and saturation of the ECDI modes that a turbulence-based axial current is induced in the electrons. The initial growth and saturation are related with the ion distribution that yields the characteristic vortex-like structure in phase space. The vanishing of oscillations seemed related with the blurring of those vortexes.

This behaviour differs from the unlimited growth reported in the literature of 1D ECDI simulations with no virtual axial length [84, 154, 157], where the quenching of short modes was not seen. It is possible that the evolution we observe is not inherent to every ECDI simulation and depends on the choice of parameters. Other possibility is that more simulation time is needed in these works to reproduce the full behaviour reported here, which is in line with our parametric analysis on the ion mass.

When axial boundaries are replaced by removal/injection surfaces, the refreshing of particles (mimicking the finite plasma in a Hall discharge) can yield completely different behaviours. These boundary conditions imply that particles that have

interacted with the electrostatic wave are removed from the simulation eventually and new particles with the original distribution are injected. A key parameter is the ion injection velocity u_{zi0}, while its effect is negligible in the ECDI dispersion relation and periodic simulations. The intermediate regime where saturation and ion-residence times are similar is the only one yielding long-term short-scale oscillations and a turbulent-based axial current, and it is the most interesting one in the context of Hall discharges. A rough estimation with typical magnitudes shows that the condition for this regime is likely to happen in a conventional Hall thruster discharge.

Acknowledgements

This work has been supported by the R&D project PID2022-140035OB-I00 (HEEP) funded by MCIN/AEI/10.13039/501100011033 and by "ERDF A way of making Europe". E. Bello-Benítez thanks the financial support by the European Research Council under the European Union's Horizon 2020 research and innovation programme (project ZARATHUSTRA, grant agreement No 950466). A. Marín-Cebrián thanks the financial support by MCIN/AEI/10.13039/501100011033 under grant FPU20/02901. The authors acknowledge useful discussions on this work with J. J. Ramos. This work is part of his PhD thesis, under development, and it will be included as a chapter within it.

Chapter 7

Conclusions and future work

In this Chapter the main contributions of this Thesis are summarized and future steps are suggested. Using a theoretical and numerical-simulation point of view, this Thesis has contributed to the understanding of plasma instabilities and related transport using different formulations (fluid and kinetic) and techniques (linear analyses and non-linear simulations). This thesis also contributes to the stationary multi-fluid modelling of the Hall discharge by extending the 1D-axial model of Ahedo et al. [27, 36, 37]. Most of these contributions have been published in peer-reviewed journals or are currently under revision. One of the main outcomes of this thesis is a functional in-house 2D PIC code that has been thoroughly verified, optimized and benchmarked during a research stay at LAPLACE laboratory. This PIC code is expected to be an important simulation tool for the near future of the EP2 research group. Next, the contributions of this Thesis are summarized in detail and future work is proposed.

7.1 Stationary modelling of the Hall discharge with a fluid model

Main contributions

In Chapter 2, based on the peer-reviewed article [28], the well-known 1D-axial stationary model of Ahedo et al. [27,36,37] is extended with several physical effects: EAI and gyroviscosity, a finite cathode emission region and the physics of the far plume past the cathode. The resulting model also has, from a mathematical point of view, some major differences with respect to previous works [27, 36, 37]: a new singular point close to the cathode where $u_{ze} = 0$, the mathematical coupling of

the channel and far-plume solutions, and the far-plume boundary condition. To better deal with these new mathematical properties, the original Runge-Kutta and shooting schemes in [27, 36, 37] have been replaced by a finite-difference solver for BVPs and non-linear ODEs.

The EAI has a smoothing effect on the axial evolution of the azimuthal velocity u_{ye}, more importantly close to the anode and across the cathode layer. In addition, the EAI cannot be neglected in the far plume once the electrons demagnetize, where the azimuthal drift is progressively lost due to collisions. However, our results show no 'shear-induced' effect of the EAI on the global electron transport. Our estimations also suggest that the gyroviscous force could be of the same order as EAI in some regions.

Even if mathematically coupled, the behaviour of the plasma variables in the channel is fairly independent of the far-plume conditions, cathode layer thickness or magnetic decay. Regarding the plume behaviour, a far-field boundary condition based on the value of T_e (and not on the $\mathrm{d}T_e/\mathrm{d}z$ or q_{ze}) is recommended since it mitigates the sensitivity of the solutions to the domain length, allowing to have shorter domains with almost equivalent results. The solutions to the 1D model are quite sensitive to a strong magnetic field in the plume, which yields significant electron heating and deceleration of ions past the cathode. This could be, however, a limitation of the 1D model since it is not observed in 2D simulations with HYPHEN [67].

Future work

The 1D-axial stationary model, solved with the finite-difference method, has been proved to be a flexible tool to introduce new terms in the fluid equations, test different boundary conditions and doing parametric analyses with small computational effort. In this sense, this 1D model could be used to guide and support the development of more complex and computationally-intensive fluid codes, such as the electron module of HYPHEN. The rigorous comparison of results from HYPHEN and the 1D model in its current state, with the same parameters and turbulent-transport model, could be a starting point in order to evaluate the importance of 2D effects and to check the quantitative and qualitative resemblance. On the other hand, electron gyroviscosity has been seen to be sometimes comparable to EAI, which raises the question of introducing the gyroviscous force as a new term in the fluid equations. This would drastically change the mathematical properties of the model. A first approximation could be to account for this effect as a correction to the leading-order solution. Finally, axial electron inertia is negligible in every solution considered in this Thesis, but it could be relevant to extend the validity of

the model to a wider parametric space (e.g., when the anode sheath is inverted).

7.2 Global stability of the Hall discharge with a fluid model

Main contributions

In Chapter 3, a global linear stability analysis of the Hall discharge is conducted. The global approach is consistent with the highly inhomogeneous nature of the discharge; unlike local techniques, which are best suited to homogeneous (or mildly inhomogeneous) equilibria. In linear stability analyses, the evolution of small perturbations to certain axisymmetric equilibrium solutions are studied. The complete problem is split in two steps: (i) the zeroth-order axial equilibrium problem and (ii) the first-order perturbation problem. Chapter 2 is devoted to the 1D-axial stationary model that is used to solve for equilibrium solutions. The first-order equations governing the perturbations are linear with coefficients that depend on the zeroth-order variables. This Sturm-Liouville problem is solved for each azimuthal wavenumber k_y, yielding the complex frequencies ω and axial behaviour of the oscillatory modes. This type of analyses can be found in the existing literature [39, 40, 42, 91], but the model in this Thesis fully takes into account pressure effects or the effect of electron inertia in the first-order problem.

The perturbation analyses here targets mid to high frequencies ($f > 100$ kHz) and the region from anode to cathode (disregarding the plume past the cathode). Using inertialess zeroth-order solution and perturbation-problem closure $T_{e1} = 0$, two types of modes are found:

1. The dominant NPI mode developing in the near plume region with $f \sim 1$ - 30 MHz, mode numbers $k_y R \sim 10$ - 30 and propagating in the $+E \times B$ direction. This family of modes is mostly electronic, meaning that oscillations of ion-related variables are small compared with electron ones. Also, oscillations seem to be attached to the region of negative magnetic gradient ($\mathrm{d}B/\mathrm{d}z < 0$), being the NPI possibly related to local drift-gradient instabilities [10, 13, 51, 96]. In addition to the dominant NPI, there is a subdominant NPI propagating in the $-E \times B$; this observation is coherent with some experimental evidence [101].

2. The subdominant NAI mode developing mostly close to the anode with $f \sim 100$ - 300 kHz, mode numbers $k_y R \sim 1$ - 10 and with contributions of both electrons and ions.

A second part of Chapter 3, analyses the impact on these modes of changes in the first-order model. Adding EAI to the zeroth-order model and temperature perturbations lead to a much more intricate dispersion relation with several more unstable branches. Even so, the dominant mode is still of the NPI type with higher frequency and wavenumber. Generally speaking, we have found the NPI mode to be quite robust to parametric and model changes, in contrast with the NAI family.

In the last part of Chapter 3, the quasilinear extension of the averaged electron azimuthal momentum equation is used to speculate on the contribution of the NPI and NAI to the electron cross-field transport. This anomalous contribution comes from the correlation of quadratic terms from inertia and electric forces, being both similar in order of magnitude. In order for the turbulent force to be able to compensate the magnetic force, a full non-linear development of the modes is needed with amplitude of the oscillations comparable to zeroth-order variables. The resultant force is highly rippled axially. Such a turbulent force could enhance the role of inertia and gyroviscous force in the equilibrium solutions.

Future work

The next steps in global stability analyses of the Hall discharge can take advantage of the extension of the 1D-axial model of Chapter 2 to the plume region. Given that the NPI modes develop very close to the cathode boundary (specially when including zeroth-order EAI or temperature perturbations), extending the first-order model to the plume region could help to check the reliability and better characterize the NPI modes. In addition, the finite cathode layer introduced in Chapter 2 induces large gradients of u_{ye0}, which could result in new Kelvin-Helmholtz-type instabilities [48]. Finally, the analysis of the turbulent force in this Chapter assumes that the unstable modes keep the linear behaviour once fully developed in the non-linear regime. However, a rigorous analysis of the turbulent transport requires a non-linear fluid model. Solving the non-linear transient version of the fluid equations used in the global analysis would allow to do so and to verify the conclusions from the linear analysis. A first effort has been already done in EP2 by Davide Poli [29] with a 1D axial model.

7.3 Development, optimization and benchmark of the 2D PIC code

Main contributions

One of the main contributions of this Thesis is the development of a functioning 2D PIC and Poisson codes, which can be used to simulate a ample variety of plasma scenarios. The code has been developed together with Alberto Marín-Cebrián and it is being also used as part of his thesis on plasma-wall interaction phenomena in Hall thrusters. The PIC program and its main algorithms and capabilities are described in Chapter 4. The input generation is coded in Python and generates the mesh, the initial particle populations and everything needed in the core program. The initial state of the particles can be generated randomly following a Maxwellian VDF. The core program is coded in Fortran90 and involves standard PIC algorithms [20, 35] to: move macroparticles, simulate surface interaction, inject new macroparticles volumetrically and superficially, simulate scattering and ionization collisions and compute macroscopic properties from macroparticle states. The electric field is calculated as solution to the Poisson equation, given the macroscopic charge density. This is done by calling and in-house Fortran90 Poisson library that internally calls external libraries. Depending on the problem boundary conditions, two different schemes are available: (*i*) a spectral method when all boundaries are periodic and (*ii*) a finite-difference method, otherwise. In the spectral method, the DFT and inverse operation are computed with the FFTW3 library [133]. In the finite-difference approach, used in most applications of interest, the linear system after discretization is solved with PARDISO project [130–132], PARDISO Intel® MKL or LIS [126–129] solvers.

Chapter 5 describes the optimization process and benchmark of the PIC code, performed as part of a research stay at LAPLACE under the supervision of Dr. Laurent Garrigues. The PIC program calculations benefit from shared-memory parallel computing with OpenMP. Having an efficient parallelization is key in order to minimize the high computational cost of the PIC code. The chosen parallelization strategy is particle decomposition with each parallel thread working on private macroparticle lists and macroscopic-property matrices; a reduction operation adds the contributions of every thread to the macroscopic properties. This strategy has allowed to simplify many routines of the program with respect to those before the stay at LAPLACE, which were designed to work on shared variables and implemented more intricate algorithms in order to avoid race conditions. In addition, with the goal of optimizing the use of the processor cache memory, sorting techniques have been tried so that particles close in the domain (i.e., in the same cell) are adjacent in the particle list. However, with the new multiple-list parallelization,

sorting seems to have a minor impact on the computational cost (but it has a significant effect with the old single-list parallelization). Regarding the Poisson finite-difference solver, several linear solvers and configurations have been tested, being the cheapest strategy using the direct solver of PARDISO and doing the factorization step only once at the beginning of the simulation. Other aspects considered that can have a big impact in performance are the chosen compiler (being Intel® Fortran compiler the most efficient for our program and processor) and OpenMP thread affinity (concluding that we should avoid setting no affinity). The final part of Chapter 5 is devoted to show results on a Penning-discharge simulation as part of an international benchmark of 2D PIC codes [41]. Two types of simulations are considered: (*i*) fixed injection of both electrons and ions and (*ii*) fixed injection of electrons while ions are generated through ionization collisions with a neutral background. Here the comparison is limited to this and LAPLACE's codes with an excellent match, which contributes to verify and give credibility to our new in-house PIC code.

Future work

As part of this Thesis, a 2D PIC code and Poisson solvers have been developed (together with Alberto Marín-Cebrián), parallelized and optimized. However, there is still room for improvement from the computational point of view. The use of shared-memory OpenMP parallel computing is a major limiting factor compared to distributed memory when moving towards larger-size problems. At the moment of writing this Thesis, the program can only take advantage of the resources available in a single workstation (in our case, this is two processors Intel®Xeon® Silver 4316 @ 2.30 GHz with 20 cores each), while bigger problems (e.g., a Hall-discharge-like simulation) may require more cores to be affordable in a reasonable amount of time (as seen from the resources and computational times reported by several groups in reference [134]). On the other hand, the fact that the multiple-list approach needs each thread to work on large private variables is very memory intensive and, thus, there is a potential bottleneck in cache memory when a large amount of nodes is used together with a large number of parallel threads. This is a problem of the particle decomposition approach and changing to domain decomposition could be a possible solution (at the cost of a greater algorithmic complexity). However, the two previous points can be solved by adapting the parallelization to a distributed-memory (or hybrid) strategy with MPI, which would potentially increase both the available cores and cache memory if the program is run on a cluster with several nodes; this is the state of the art of parallelization of PIC codes [134]. At its current state, the PIC code with multiple-list parallelization could be adapted to MPI with reasonable amount of effort. A more drastic approach would be the use of parallel computing with a graphics-processing unit (GPU), which are specially designed to

perform parallel calculations efficiently and may have thousands of cores (although generally slower than processor cores). However, a parallelization based on GPUs would certainly imply to rewrite the PIC code.

From the point of view of the physics, the main area of improvement is the modelling of more types of collisional phenomena. At the moment, the capabilities of the PIC code are limited to a simple random scattering (with a prescribed frequency) and ionization collisions using a MCC approach (macroparticles are collided with a target background species). Other types of collisions relevant to Hall discharges are: electron-neutral elastic, electron-ion Coulomb or ion-neutral charge-exchange collisions. The MCC approach is, however, only suitable when the collisions have a negligible impact on the target background species (e.g., events involving an electron macroparticle and a heavy background species). This point can be solved with the implementation of DSMC collisions to simulate directly the collisions of particle pairs. The DSMC technique would allow to take into account, e.g., the effect of intraspecies electron-electron collisions, which could have a thermalizing effect on the electron population.

7.4 Non-linear behaviour of the ECDI

Main contributions

In Chapter 6, the classical ECDI theory is revisited and 2D kinetic simulations are performed with the in-house PIC code under several axial boundary conditions. In order to speed-up the dynamics of the problem, hydrogen ions are assumed. The first part of the Chapter reviews the main aspects of the linear dispersion relation, remarking the interplay of ion-acoustic and Bernstein waves that results in the ECDI. Actually, the dispersion relation can be rewritten in the form of a MIA mode destabilized by electron Bernstein terms close to the resonances of the Doppler-shifted frequency with the harmonics of the gyrofrequency. In the PIC simulations, apart from boundary conditions, the initial plasma equilibrium state and physics comply with the assumptions behind the ECDI linear theory.

Two types of simulation configurations are considered with different boundary conditions in axial boundaries. The first set of simulations is performed in a fully periodic domain. According to the Fourier spectrum, the behaviour of the plasma is as expected from the literature and qualitatively similar to the ECDI dispersion relation. Close to saturation, the discrete nature of the ECDI is lost and the spectrum is similar to regular ion-acoustic modes. In the long-term, however, we observe that the intense short-scale oscillations quench and the plasma converges

to a new equilibrium state with mild oscillations and no turbulent transport. This last phase of the ECDI non-linear evolution has not been reported elsewhere in the literature; which could mean that either it is not intrinsic to every ECDI scenario or longer simulation times are needed. Indeed, the parametric analysis on the ion mass seems to suggest that, with xenon, more simulation time is needed than usually reported in the literature of 1D PIC ECDI simulations without refreshing [84, 157].

The growth, saturation and vanishing of short scale modes in periodic simulations are highly related with ion-wave trapping and the formation and blurring of vortexes in the ion phase space. If particles are not removed and injected (or refreshed), the distribution of particles in phase space is purely a result of the particles interaction with the wave. When axial removal and fixed-injection conditions are used, there is a renewal of particles that can significantly affect the non-linear behaviour of the ECDI. The injection/removal conditions simulate the finite plasma length of a Hall discharge. In this Chapter, we demonstrate the existence of different regimes depending on the value of the ion residence time compared with the characteristic saturation time of the ECDI measured in periodic simulations. The intermediate regime, when these two times are similar, is the only one with short-scale oscillations and a turbulent-based electron transport in the long term. Indeed, according to our estimations, the conditions to observe this regime could be fulfilled in a conventional Hall discharge.

Future work

The simulation and turbulent transport analyses shown in Chapter 6 give a simplified but valuable insight on the role of the ECDI in the turbulent transport in a Hall discharge. Next steps should move in the direction of trying to relate these results with the behaviour observed in Hall-discharge-like simulations. The code is ready to simulate the axial-azimuthal plane of a Hall discharge, just like the benchmark in reference [134] (maybe with augmented vacuum permittivity to reduce the computational cost). In these simulations however, there are many complex physical phenomena acting at the same time and global effects that make the results difficult to analyse and relate to the ECDI behaviour. This complexity can be introduced progressively to the simplified ECDI simulations in a finite plasma: electron collisions, volumetric particle injection or ionization, inhomogeneous magnetic field, a non-zero potential drop between the axial boundaries and the consequent inhomogeneity due to ion acceleration... This approach would allow to easily track the changes in behaviour of the ECDI when adding effects not covered by the existing theory, just as done in Chapter 6 with injection. It would be also interesting to verify in these complex simulations the existence of the different regimes of the ECDI found with injection conditions.

Bibliography

[1] J.P. Boeuf. Tutorial: Physics and modeling of Hall thrusters. *J. Applied Physics*, 121(1):011101, 2017.

[2] K.J Bowers. Accelerating a particle-in-cell simulation using a hybrid counting sort. *Journal of Computational Physics*, 173(2):393–411, 2001.

[3] J. Cavalier, N. Lemoine, G. Bonhomme, S. Tsikata, C. Honoré, and D. Grésillon. Hall thruster plasma fluctuations identified as the exb electron drift instability: Modeling and fitting on experimental data. *PoP*, 20(8):082107, 2013.

[4] R.H. Goddard. *The green notebooks, vol.1. The Dr. Robert H. Goddard Collection at Clark University Archives*. Clark University, 1906.

[5] E.Y. Choueiri. A critical history of electric propulsion: The first 50 years (1906-1956). *Journal of Propulsion and Power*, 20(2):193–203, 2004.

[6] T.M. Mel'kumov. *Pioneers of Rocket Technology: Selected Works, volume 9285.* National Aeronautics and Space Administration, 1965.

[7] D.M. Goebel and I. Katz. *Fundamentals of Electric Propulsion: Ion and Hall Thrusters*. Jet Propulsion Laboratory, Pasadena, CA, 2008.

[8] G.S. Janes and R.S. Lowder. Anomalous electron diffusion and ion acceleration in a low-density plasma. *Physics of Fluids*, 9(6):1115–1123, 1966.

[9] E.Y. Choueiri and J.K. Ziemer. Quasi-steady magnetoplasmadynamic thruster performance database. *Journal of Propulsion and Power*, 17(5):967–976, 2001.

[10] J. J. Ramos, E. Bello-Benítez, and E. Ahedo. Local analysis of electrostatic modes in a two-fluid E x B plasma. *Physics of Plasmas*, 28(5):052115, 2021.

[11] D.W. Forslund, R.L. Morse, and C.W. Nielson. Electron cyclotron drift instability. *Physical Review Letters*, 25:1266–1270, 1970.

[12] H.V. Wong. Electrostatic electron-ion streaming instability. *Physics of Fluids*, 13:757–760, 1970.

[13] A.I. Smolyakov, O. Chapurin, W. Frias, O. Koshkarov, I. Romadanov, T. Tang, M. Umansky, Y. Raitses, I.D. Kaganovich, and V.P. Lakhin. Fluid theory and simulations of instabilities, turbulent transport and coherent structures in partially-magnetized plasmas of ExB discharges. *Plasma Physics and Controlled Fusion*, 59:014041, 2017.

[14] A.A. Litvak and N.J. Fisch. Resistive instabilities in Hall current plasma discharge. *Physics of Plasmas*, 8(2):648–651, 2001.

[15] S. Tsikata and T. Minea. Modulated electron cyclotron drift instability in a high-power pulsed magnetron discharge. *Physical Review Letters*, 114:185001, 2015.

[16] J.A. Bittencourt. *Fundamentals of plasma physics*. Springer, Berlin, Germany, 2004.

[17] M. Martínez-Sánchez, J. Navarro-Cavallé, and E. Ahedo. Electron cooling and finite potential drop in a magnetized plasma expansion. *Physics of Plasmas*, 22(5):053501, 2015.

[18] Mario Merino, Javier Mauriño, and Eduardo Ahedo. Kinetic electron model for plasma thruster plumes. *Plasma Sources Science and Technology*, 27(3):035013, 2018.

[19] Gonzalo Sánchez-Arriaga, Jiewei Zhou, E Ahedo, Manuel Martínez-Sánchez, and Jesús José Ramos. Kinetic features and non-stationary electron trapping in paraxial magnetic nozzles. *Plasma Sources Science and Technology*, 27(3):035002, 2018.

[20] C.K. Birdsall and A.B. Langdon. *Plasma Physics via Computer Simulation*. Institute of Physics Publishing, Bristol, 1991.

[21] F. Taccogna, S. Longo, M. Capitelli, and R. Schneider. Particle-in-cell simulation of stationary plasma thruster. *Contributions to Plasma Physics*, 47(8-9):635–656, 2007.

[22] D. Tskhakaya, K. Matyash, R. Schneider, and F. Taccogna. The particle-in-cell method. *Contributions to Plasma Physics*, 47(8-9):563–594, 2007.

[23] Adrián Domínguez-Vázquez, Francesco Taccogna, and Eduardo Ahedo. Particle modeling of radial electron dynamics in a controlled discharge of a Hall thruster. *Plasma Sources Science and Technology*, 27(6):064006, 2018.

[24] E. Bello-Benítez, A. Marín-Cebrián, J. J. Ramos, and E. Ahedo. Two-dimensional kinetic simulation of electrostatic instabilities in a Hall plasma. In 37^{th} *International Electric Propulsion Conference*, number IEPC-2022-314, Boston, MA, June 19-23, 2022. Electric Rocket Propulsion Society.

[25] Mario Merino, Filippo Cichocki, and Eduardo Ahedo. A collisionless plasma thruster plume expansion model. *Plasma Sources Science and Technology*, 24(3):035006, 2015.

[26] I.G. Mikellides and I. Katz. Numerical simulations of Hall-effect plasma accelerators on a magnetic-field-aligned mesh. *Physical Review E*, 86(4):046703, 2012.

[27] E. Ahedo, J.M. Gallardo, and M. Martínez-Sánchez. Effects of the radial-plasma wall interaction on the axial Hall thruster discharge. *Physics of Plasmas*, 10(8):3397–3409, 2003.

[28] E Bello-Benítez and E Ahedo. Stationary axial model of the Hall thruster plasma discharge: electron azimuthal inertia and far plume effects. *Plasma Sources Science and Technology*, 32(11):115011, 2023.

[29] Davide Poli, Enrique Bello-Benítez, Pablo Fajardo, and Eduardo Ahedo. Time-dependent axial fluid model of the hall thruster discharge and its plume. *Journal of Physics D: Applied Physics*, 2023.

[30] AR Barakat and RW Schunk. Transport equations for multicomponent anisotropic space plasmas: A review. *Plasma Physics*, 24(4):389, 1982.

[31] J.J. Ramos. Fluid formalism for collisionless magnetized plasmas. *Physics of Plasmas*, 12(5):052102, 2005.

[32] Francis F. Chen. *Introduction to Plasma Physics and Controlled Fusion*. Springer International Publishing, 2016.

[33] D.G. Swanson. *Plasma Waves, 2nd Edition*. IOP Publishing, Bristol, UK, 2003.

[34] Ira B. Bernstein. Waves in a plasma in a magnetic field. *Phys. Rev.*, 109:10–21, Jan 1958.

[35] Adrián Domínguez-Vázquez. *Axisymmetric simulation codes for Hall effect thrusters and plasma plumes*. PhD thesis, Universidad Carlos III de Madrid, Leganés, Spain, 2019.

[36] E. Ahedo, P. Martínez-Cerezo, and M. Martínez-Sánchez. One-dimensional model of the plasma flow in a Hall thruster. *Physics of Plasmas*, 8:3058–3068, 2001.

[37] E. Ahedo, J.M. Gallardo, and M. Martínez-Sánchez. Model of the plasma discharge in a Hall thruster with heat conduction. *Physics of Plasmas*, 9(9):4061–4070, 2002.

[38] E. Bello-Benítez and E. Ahedo. Axial-azimuthal, high-frequency modes from global linear-stability model of a Hall thruster. *Plasma Sources Science and Technology*, 30(3):035003, mar 2021.

[39] D. Escobar and E. Ahedo. Low frequency azimuthal stability of the ionization region of the Hall thruster discharge. II. Global analysis. *Physics of Plasmas*, 22:102114, 2015.

[40] D. Escobar and E. Ahedo. Numerical analysis of high-frequency azimuthal oscillations in Hall thrusters. In 34^{th} *International Electric Propulsion Conference*, number IEPC-2015-371, Hyogo-Kobe, Japan, July 6-10, 2015. Electric Rocket Propulsion Society.

[41] L. Garrigues, G. Fubiani, J.P. Boeuf, A.T. Powis, W. Villafana, I. Kaganovich, Y. Raitses, F. Petronio, A. Alvarez-Laguna, A. Bourdon, P. Chabert, G. Vigot, G. Bogopolsky, B. Cuenot, O. Vermorel, D. Sydorenko, M. Zadeh, A. Smolyakov, F. Cichocki, P. Minelli, F. Taccogna, D. Eremin, L. Xu, A. Denig, K. Hara, P. Q. Elias, E. Bello Benítez, A. Marín-Cebrián, E. Ahedo, M. Merino, P. Fajardo, Z. Donko, P. Hartmann, M. Turner, M. Reza, F. Faraji, A. Knoll, P. Parodi, , and T. Magin. Benchmark of particle-in-cell simulations of a Penning-type discharge: Preliminary results. Poster presented in 35^{th} *International Conference on Plasmas and Ionized Gases*. Egmond aan Zee, The Netherlands, July 9–14.

[42] E. A. Sorokina, N. A. Marusov, V. P. Lakhin, and V. I. Ilgisonis. Discharge oscillations in Morozov's stationary plasma thruster as a manifestation of large-scale modes of gradient drift instability. *Plasma Physics Reports*, 45(1):1, 2019.

[43] E. Ahedo. Radial macroscopic model of a plasma flowing along annular dielectric walls. *Physics of Plasmas*, 9(7):3178–3186, 2002.

[44] E. Ahedo. Presheath/sheath model of a plasma with secondary emission from two parallel walls. *Physics of Plasmas*, 9(10):4340–4347, 2002.

[45] E. Ahedo and V. Pablo. Combined effects of electron partial thermalization and secondary emission in Hall thruster discharges. *Physics of Plasmas*, 14:083501, 2007.

[46] E. Ahedo and D. Escobar. Influence of design and operation parameters on Hall thruster performances. *Journal of Applied Physics*, 96(2):983–992, 2004.

[47] E. Ahedo and F.I. Parra. A model of the two-stage Hall thruster discharge. *Journal of Applied Physics*, 98:023303, 2005.

[48] A.A. Litvak and N.J. Fisch. Rayleigh instability in Hall thrusters. *Physics of Plasmas*, 11:1379, 2004.

[49] A. Kapulkin and M.M. Guelman. Low-frequency instability in near-anode region of Hall thruster. *IEEE Transactions on Plasma Science*, 36(5):2082–2087, 2008.

[50] D. Escobar and E. Ahedo. Low frequency azimuthal stability of the ionization region of the Hall thruster discharge. I. Local analysis. *Physics of Plasmas*, 21(4):043505, 2014.

[51] V. P. Lakhin, V. I. Ilgisonis, A. I. Smolyakov, E. A. Sorokina, and N. A. Marusov. Effects of finite electron temperature on gradient drift instabilities in partially magnetized plasmas. *Physics of Plasmas*, 25:012106, 2018.

[52] S. Barral, K. Makowski, Z. Peradzynski, N. Gascon, and M. Dudeck. Wall material effects in stationary plasma thrusters. II. Near-wall and in-wall conductivity. *Phys. Plasmas*, 10(10):4137–4152, 2003.

[53] J.M. Fife, M. Martínez-Sánchez, and J. Szabo. A numerical study of low-frequency discharge oscillations in Hall thrusters. In *33rd Joint Propulsion Conference, Seattle, WA*, AIAA 97-3052, 1997.

[54] S. Barral, K. Makowski, Z. Peradzynski, and M. Dudeck. Transit-time instability in Hall thrusters. *Physics of Plasmas*, 12:073504, 2005.

[55] S. Barral and E. Ahedo. Low-frequency model of breathing oscillations in Hall discharges. *Physical Review E*, 79:046401, 2009.

[56] S. Barral and Z. Peradzyński. Ionization oscillations in Hall accelerators. *Physics of Plasmas*, 17(1):014505, 2010.

[57] R. Martorelli, T. Lafleur, A. Bourdon, and P. Chabert. Comparison between ad-hoc and instability-induced electron anomalous transport in a 1D fluid simulation of Hall-effect thruster. *Physics of Plasmas*, 26(8):083502, 2019.

[58] T. Lafleur, P. Chabert, and A. Bourdon. The origin of the breathing mode in Hall thrusters and its stabilisation. *Journal of Applied Physics*, 130(5):053305, 2021.

[59] Vittorio Giannetti, Manuel Martín Saravia, Luca Leporini, Simone Camarri, and Tommaso Andreussi. Numerical and experimental investigation of longitudinal oscillations in hall thrusters. *Aerospace*, 8:148, 05 2021.

[60] O. Chapurin, A. I. Smolyakov, G. Hagelaar, J.-P. Boeuf, and Y. Raitses. Fluid and hybrid simulations of the ionization instabilities in hall thruster. *Journal of Applied Physics*, 132(5):053301, 2022.

[61] K. Hara. An overview of discharge plasma modeling for Hall effect thrusters. *Plasma Sources Science and Technology*, 28(4):044001, 2019.

[62] E. Ahedo. Using electron fluid models to analyze plasma thruster discharges. *Journal of Electric Propulsion*, 2(1):2, 2023.

[63] E. Ahedo and J.Rus. Vanishing of the negative anode sheath in a Hall thruster. *Journal of Applied Physics*, 98:043306, 2005.

[64] L. Dorf, Y. Raitses, N. Fisch, and V. Semenov. Effect of anode dielectric coating on Hall thruster operation. *Applied Physics Letters*, 84(7):1070–1072, 2003.

[65] E. Ahedo and D. Escobar. Two-region model for positive and negative plasma sheaths and its application to Hall thruster metallic anodes. *Physics of Plasmas*, 15:033504, 2008.

[66] J.M. Haas and A.D. Gallimore. Considerations on the role of the hall current in a laboratory-model thruster. *IEEE Transactions on Plasma Science*, 30(2):687–697, 2002.

[67] Adrián Domínguez-Vázquez, Jiewei Zhou, Pablo Fajardo, and Eduardo Ahedo. Analysis of the plasma discharge in a Hall thruster via a hybrid 2D code. In 36^{th} *International Electric Propulsion Conference*, number IEPC-2019-579, Vienna, Austria, 2019. Electric Rocket Propulsion Society.

[68] M. Cappelli, N.B. Meezan, and N. Gascon. Transport physics in Hall plasma thrusters. In *38th Joint Propulsion Conference, Indianapolis, IN*, AIAA 2002-0485, 2002.

[69] M.K. Scharfe, C.A. Thomas, D.B. Scharfe, N. Gascon, M.A. Cappelli, and E. Fernandez. Shear-based model for electron transport in hybrid Hall thruster simulations. *Plasma Science, IEEE Transactions on*, 36(5):2058–2068, 2008.

[70] J. Fox, A.A. Batishcheva, O.V. Batishchev, and M.Martinez-Sanchez. Adaptively meshed fully-kinetic PIC-Vlasov model for near vacuum Hall thrusters. In *42th Joint Propulsion Conference, Sacramento, CA*, AIAA 2006-4324, 2006.

[71] R. Sahu, A.R. Mansour, and K. Hara. Full fluid moment model for low temperature magnetized plasmas. *Physics of Plasmas*, 27(11):113505, 2020.

[72] Jesús Perales-Díaz, Adrián Domínguez-Vázquez, Pablo Fajardo, Eduardo Ahedo, Farbod Faraji, Maryam Reza, and Tommaso Andreussi. Hybrid plasma simulations of a magnetically shielded Hall thruster. *Journal of Applied Physics*, 131(10):103302, 2022.

[73] V.V. Zhurin, H.R. Kaufman, and R.S. Robinson. Physics of closed drift thrusters. *Plasma Sources Science and Technolgy*, 8:1, 1999.

[74] A. Macmahon. Finite gyro-radius corrections to the hydromagnetic equations for a Vlasov plasma. *Physics of Fluids*, 8:1840, 1965.

[75] R.D. Hazeltine and J.D. Meiss. *Plasma confinement*. Addison-Wesley, Redwood, CA, 1992.

[76] J.J. Ramos. Fluid theory of magnetized plasma dynamics at low collisionality. *Physics of Plasmas*, 14:052506, 2007.

[77] J. Perales-Díaz, A. Domínguez-Vázquez, P. Fajardo, E. Ahedo, T. Andreussi, and A. Piragino. Hybrid 2D plasma simulations of a 20kW-class magnetically shielded Hall effect thruster. In 37^{th} *International Electric Propulsion Conference*, number IEPC-2022-322, Boston, MA, June 19-23, 2022. Electric Rocket Propulsion Society.

[78] J.P. Boeuf and L. Garrigues. Low frequency oscillations in a stationary plasma thruster. *J. Applied Physics*, 84(7):3541–3554, 1998.

[79] Francis F Chen et al. *Introduction to plasma physics and controlled fusion*, volume 1. Springer, 1984.

[80] Ioannis G Mikellides and Alejandro Lopez Ortega. Challenges in the development and verification of first-principles models in Hall-effect thruster simulations that are based on anomalous resistivity and generalized Ohm's law. *Plasma Sources Science and Technology*, 28:014003, 2019.

[81] J.J. Ramos. General expression of the gyroviscous force. *Physics of Plasmas*, 12(11):112301, 2005.

[82] E. Choueiri. Plasma oscillations in Hall thrusters. *Physics of Plasmas*, 8(4):1411–1426, 2001.

[83] A. Ducrocq, J.C. Adam, A. Héron, and G. Laval. High-frequency electron drift instability in the cross-field configuration of Hall thrusters. *Physics of Plasmas*, 13:102111, 2006.

[84] S. Janhunen, A. Smolyakov, O. Chapurin, D. Sydorenko, I. Kaganovich, and Y. Raitses. Nonlinear structures and anomalous transport in partially magnetized ExB plasmas. *Physics of Plasmas*, 25:11608, 2018.

[85] N. A. Krall and P. C. Liewer. Low-frequency instabilities in magnetic pulses. *Physical Review A*, 4:2094–2103, 1971.

[86] J.B. McBride, E. Ott, J.P. Boris, and J.H. Orens. Theory and simulation of turbulent heating by the modified two-stream instability. *The Physics of Fluids*, 15(12):2367–2383, 1972.

[87] S. Janhunen, A. Smolyakov, D. Sydorenko, M. Jimenez, I. Kaganovich, and Y. Raitses. Evolution of the electron cyclotron drift instability in two-dimensions. *Physics of Plasmas*, 25(8):082308, 2018.

[88] A. Kapulkin, J. Ashkenazy, A. Kogan, G. Appelbaum, D. Alkalay, and M. Guelman. Electron instabilities in Hall thrusters: Modeling and application to electric field diagnostics. In *Proceedings of the 28th International Electric Propulsion Conference*, 2003.

[89] A. Kapulkin and M. Guelman. Lower-hybrid instability in Hall thruster. In *Proceedings of the 29th International Electric Propulsion Conference*, IEPC-2005-88, 2005.

[90] N. A. Marusov, E. A. Sorokina, V. I. Ilgisonis, and V. P. Lakhin. Large-scale azimuthal structures in Hall-type plasma discharges. *Physics of Plasmas*, 26(9):090701, 2019.

[91] I. Romadanov, A.I. Smolyakov, Y. Raitses, I.D. Kaganovich, T. Tian, and S. Ryzhkov. Structure of nonlocal gradient-drift instabilities in hall exb discharges. *Physics of Plasmas*, 23:122111, 2016.

[92] W. Frias, A.I. Smolyakov, I.D. Kaganovich, and Y. Raitses. Long wavelength gradient drift instability in Hall plasma devices. I. Fluid theory. *Physics of Plasmas*, 19:072112, 2012.

[93] J.C. Adam, A. Herón, and G. Laval. Study of stationary plasma thrusters using two-dimensional fully kinetic simulations. *Physics of Plasmas*, 11:295–305, 2004.

[94] T. Lafleur and P. Chabert. The role of instability-enhanced friction on 'anomalous' electron and ion transport in Hall-effect thrusters. *Plasma Sources Science and Technology*, 27:015003, 2017.

[95] T. Charoy, T. Lafleur, A. Tavant, P. Chabert, and A. Bourdon. A comparison between kinetic theory and particle-in-cell simulations of anomalous electron transport in ExB plasma discharges. *Physics of Plasmas*, 27(6):063510, 2020.

[96] Y.V. Esipchuk and G.N. Tilinin. Drift instability in a Hall-current plasma accelerator. *Sov. Physics-Tech. Physics*, 21(4):417–423, 1976.

[97] E. Ahedo, P. Martínez-Cerezo, and M. Martínez-Sánchez. Steady and linearly-unsteady analysis of a Hall thruster with an internal sonic point. In *Proc. 36th Joint Propulsion Conference, Huntsville, AL*, AIAA 2000-3655. American Institute of Aeronautics and Astronautics, 2000.

[98] N A Marusov, E A Sorokina, V P Lakhin, V I Ilgisonis, and A I Smolyakov. Gradient-drift instability applied to Hall thrusters. *Plasma Sources Science and Technology*, 28(1):015002, 2019.

[99] M. S. McDonald and A. D. Gallimore. Rotating spoke instabilities in Hall thrusters. *IEEE Transactions on Plasma Science*, 39(11):2952–2953, 2011.

[100] C.L. Ellison, Y. Raitses, and N.J. Fisch. Cross-field electron transport induced by a rotating spoke in a cylindrical Hall thruster. *Physics of Plasmas*, 19(1):013503, 2012.

[101] S. Tsikata, N. Lemoine, V. Pisarev, and D.M. Gresillon. Dispersion relations of electron density fluctuations in a Hall thruster plasma, observed by collective light scattering. *Physics of Plasmas*, 16:033506, 2009.

[102] Y.B. Esipchuk, A.I. Morozov, G.N. Tilinin, and A.V. Trofimov. Plasma oscillations in closed-drift accelerators with an extended acceleration zone. *Soviet Physics-Technical Physics*, 18:928–932, 1974.

[103] A.A. Litvak, Y. Raitses, and N.J. Fisch. Experimental studies of high-frequency azimuthal waves in Hall thrusters. *Physics of Plasmas*, 11:1701, 2004.

[104] C. S. Liu, V. K. Tripathi, and Bengt Eliasson. *High-Power Laser-Plasma Interaction*. Cambridge University Press, 2019.

[105] Adrián Domínguez-Vázquez, Filippo Cichocki, Mario Merino, Pablo Fajardo, and Eduardo Ahedo. Axisymmetric plasma plume characterization with 2D and 3D particle codes. *Plasma Sources Science and Technology*, 27(10):104009, 2018.

[106] Adrián Domínguez-Vázquez, Francesco Taccogna, Pablo Fajardo, and Eduardo Ahedo. Parametric study of the radial plasma-wall interaction in a Hall thruster. *Journal of Physics D: Applied Physics*, 52(47):474003, 2019.

[107] Alberto Marín-Cebrián, Adrián Domínguez-Vázquez, Pablo Fajardo, and Eduardo Ahedo. Macroscopic plasma analysis from 1D-radial kinetic results of a Hall thruster discharge. *Plasma Sources Science and Technology*, 30(11):115011, November 2021.

[108] V. Vahedi and M. Surendra. A Monte Carlo collision model for the particle-in-cell method: applications to argon and oxygen discharges. *Computer Physics Communications*, 87(1-2):179–198, 1995.

[109] G.A. Bird. *Molecular Gas Dynamics and the Direct Simulation of Gas Flows*. The Oxford Engineering Science Series. Oxford University Press, Oxford, UK, 1994.

[110] W. Villafana, B. Cuenot, and O. Vermorel. 3d particle-in-cell study of the electron drift instability in a Hall thruster using unstructured grids. *Physics of Plasmas*, 30(3), 2023.

[111] Andrew T. Powis, Wilca Villafana, and Igor D. Kaganovich. Three-dimensional kinetic simulations of oscillations and anomalous electron transport in a hall thruster. 2022.

[112] Francesco Taccogna and Pierpaolo Minelli. Three-dimensional particle-in-cell model of Hall thruster: The discharge channel. *Physics of Plasmas*, 25(6):061208, 2018.

[113] A Bruce Langdon. Effects of the spatial grid in simulation plasmas. *Journal of Computational Physics*, 6(2):247–267, 1970.

[114] Hideo Okuda. Nonphysical noises and instabilities in plasma simulation due to a spatial grid. *Journal of Computational Physics*, 10(3):475–486, 1972.

[115] Luc Devroye. *Non-Uniform Random Variate Generation*. Springer New York, 1986.

[116] Jay P Boris et al. Relativistic plasma simulation-optimization of a hybrid code. In *Proc. Fourth Conf. Num. Sim. Plasmas*, pages 3–67, 1970.

[117] Charles K Birdsall. Particle-in-cell charged-particle simulations, plus Monte Carlo collisions with neutral atoms, pic-mcc. *IEEE Transactions on plasma science*, 19(2):65–85, 1991.

[118] F. I. Parra, E. Ahedo, J. M. Fife, and M. Martínez-Sánchez. A two-dimensional hybrid model of the Hall thruster discharge. *Journal of Applied Physics*, 100(2):023304, 2006.

[119] R. Santos and E. Ahedo. Implementation of the kinetic Bohm condition in a Hall thruster hybrid code. In *45th Joint Propulsion Conference*, AIAA 2009-4913, Denver, Colorado, August 2-5, 2009. AIAA, Reston, VA.

[120] E. Ahedo, R. Santos, and F. Parra. Fulfillment of the kinetic Bohm criterion in a quasineutral particle-in-cell model. *Physics of Plasmas*, 17(7):073507, 2010.

[121] F.I. Parra. Actualización y mejora de un código pic-fluido bidimensional para el flujo de plasma en motores de efecto Hall. Technical report, http://web.fmetsia.upm.es/ep2/, 2004.

[122] M. M. Turner, A. Derzsi, Z. Donkó, D. Eremin, S. J. Kelly, T. Lafleur, and T. Mussenbrock. Simulation benchmarks for low-pressure plasmas: Capacitive discharges. *Physics of Plasmas*, 20(1), 2013.

[123] C. Opal, W. Peterson, and E. Beaty. Measurements of secondary electron spectra produced by electron impact ionization of a number of simple gases. *J. Chem. Phys*, 55:4100–4106, 1971.

[124] M Surendra, DB Graves, and GM Jellum. Self-consistent model of a direct-current glow discharge: Treatment of fast electrons. *Physical Review A*, 41(2):1112, 1990.

[125] M. Surendra, D. B. Graves, and I. J. Morey. Electron heating in low-pressure rf glow discharges. *Appl. Phys. Lett.*, 56(11):1022–1024, 1990.

[126] H. Kotakemori, H. Hasegawa, and A. Nishida. Performance evaluation of a parallel iterative method library using OpenMP. In *Eighth International Conference on High-Performance Computing in Asia-Pacific Region (HPCA-SIA'05)*. IEEE, 2005.

[127] Akihiro Pujii, Akira Nishida, and Yoshio Oyanagi. Evaluation of parallel aggregate creation orders: Smoothed aggregation algebraic multigrid method. In *High Performance Computational Science and Engineering*, pages 99–122. Springer-Verlag, 2005.

[128] Hisashi Kotakemori, Hidehiko Hasegawa, Tamito Kajiyama, Akira Nukada, Reiji Suda, and Akira Nishida. Performance evaluation of parallel sparse matrix–vector products on SGI altix3700. In *OpenMP Shared Memory Parallel Programming*, pages 153–163. Springer Berlin Heidelberg, 2008.

[129] Akira Nishida. Experience in developing an open source scalable software infrastructure in japan. In *Computational Science and Its Applications – ICCSA 2010*, pages 448–462. Springer Berlin Heidelberg, 2010.

[130] Christie Alappat, Achim Basermann, Alan R Bishop, Holger Fehske, Georg Hager, Olaf Schenk, Jonas Thies, and Gerhard Wellein. A recursive algebraic coloring technique for hardware-efficient symmetric sparse matrix-vector multiplication. *ACM Transactions on Parallel Computing (TOPC)*, 7(3):1–37, 2020.

[131] Matthias Bollhöfer, Aryan Eftekhari, Simon Scheidegger, and Olaf Schenk. Large-scale sparse inverse covariance matrix estimation. *SIAM Journal on Scientific Computing*, 41(1):A380–A401, 2019.

[132] Matthias Bollhöfer, Olaf Schenk, Radim Janalik, Steve Hamm, and Kiran Gullapalli. State-of-the-art sparse direct solvers. In *Parallel Algorithms in Computational Science and Engineering*, pages 3–33. Springer International Publishing, 2020.

[133] Matteo Frigo and Steven G Johnson. The design and implementation of FFTW3. *Proceedings of the IEEE*, 93(2):216–231, 2005.

[134] T Charoy, J P Boeuf, A Bourdon, J A Carlsson, P Chabert, B Cuenot, D Eremin, L Garrigues, K Hara, I D Kaganovich, A T Powis, A Smolyakov, D Sydorenko, A Tavant, O Vermorel, and W Villafana. 2d axial-azimuthal particle-in-cell benchmark for low-temperature partially magnetized plasmas. *Plasma Sources Science and Technology*, 28(10):105010, 2019.

[135] P. Coche and L. Garrigues. A two-dimensional (azimuthal-axial) particle-in-cell model of a hall thruster. *Physics of Plasmas*, 21:023503, 2014.

[136] J.P. Boeuf and B Chaudhury. Rotating instability in low-temperature magnetized plasmas. *Phys. Rev. Lett.*, 111:155005, 2013.

[137] J.P. Boeuf and L. Garrigues. E× b electron drift instability in hall thrusters: Particle-in-cell simulations vs. theory. *Physics of Plasmas*, 25(6), 2018.

[138] Wenjian Yu and Michael Mascagni. *Monte Carlo Methods for Partial Differential Equations With Applications to Electronic Design Automation.* Springer Nature Singapore, 2023.

[139] F. Cichocki. *Analysis of the expansion of a plasma thruster plume into vacuum.* PhD thesis, Universidad Carlos III de Madrid, Leganés, Spain, 2017.

[140] Filippo Cichocki, Adrián Domínguez-Vázquez, Mario Merino, and Eduardo Ahedo. Hybrid 3D model for the interaction of plasma thruster plumes with nearby objects. *Plasma Sources Science and Technology*, 26(12):125008, 2017.

[141] M Surendra. Radiofrequency discharge benchmark model comparison. *Plasma Sources Science and Technology*, 4(1):56–73, 1995.

[142] J. Carlsson, A. Khrabrov, I. Kaganovich, T. Sommerer, and D. Keating. Validation and benchmarking of two particle-in-cell codes for a glow discharge. *Plasma Sources Science and Technology*, 26(1):014003, 2016.

[143] W. Villafana, F. Petronio, A.C. Denig, M.J. Jimenez, D. Eremin, L. Garrigues, F. Taccogna, A. Alvarez-Laguna, J.P. Boeuf, A. Bourdon, P. Chabert, T. Charoy, B. Cuenot, K. Hara, F. Pechereau, A. Smolyakov, D. Sydorenko, A. Tavant, and O Vermorel. 2D radial-azimuthal particle-in-cell benchmark for ExB discharges. *Plasma Sources Science and Technology*, 30(7):075002, 2021.

[144] Johan Carlsson, Igor Kaganovich, Andrew Powis, Yevgeny Raitses, Ivan Romadanov, and Andrei Smolyakov. Particle-in-cell simulations of anomalous transport in a Penning discharge. *Physics of Plasmas*, 25(6), 2018.

[145] A.T. Powis, J.A. Carlsson, I.D. Kaganovich, Y. Raitses, and A. Smolyakov. Scaling of spoke rotation frequency within a penning discharge. *Physics of Plasmas*, 25(7):072110, 2018.

[146] A. Simon. Instability of a partially ionized plasma in crossed electric and magnetic fields. *The Physics of Fluids*, 6(3):382–388, 1963.

[147] F. C. Hoh. Instability of Penning-type discharges. *The Physics of Fluids*, 6(8):1184–1191, 1963.

[148] Stephen Francis Biagi. Cross sections extracted from PROGRAM MAGBOLTZ, version 7.1 june 2004, June 2004. [Online; accessed 5-July-2021].

[149] Natalia A MacDonald, Mark A Cappelli, Stephen R Gildea, Manuel Martinez-Sanchez, and William A Hargus Jr. Laser-induced fluorescence velocity measurements of a diverging cusped-field thruster. *Journal of Physics D: Applied Physics*, 44(29):295203, 2011.

[150] S. Tsikata, A. Héron, and C. Honoré. Hall thruster microturbulence under conditions of modified electron wall emission. *Physics of Plasmas*, 24(5):053519, 2017.

[151] Oleksandr Koshkarov, Andrei Smolyakov, Yevgeny Raitses, and Igor Kaganovich. Self-organization, structures, and anomalous transport in turbulent partially magnetized plasmas with crossed electric and magnetic fields. *Physical Review Letters*, 122:185001, May 2019.

[152] V. Nikitin, D. Tomilin, A. Lovtsov, and A. Tarasov. Gradient-drift and resistive mechanisms of the anomalous electron transport in Hall effect thrusters. *Europhysics Letters*, 117(4):45001, 2017.

[153] T. Lafleur, S.D. Baalrud, and P. Chabert. Theory for the anomalous electron transport in Hall effect thrusters. ii. kinetic model. *Physics of Plasmas*, 23:053503, 2016.

[154] T. Lafleur, S.D. Baalrud, and P. Chabert. Theory for the anomalous electron transport in hall effect thrusters. i. insights from particle-in-cell simulations. *Physics of Plasmas*, 23:053502, 2016.

[155] Zahra Asadi, Francesco Taccogna, and Mehdi Sharifian. Numerical study of electron cyclotron drift instability: Application to hall thruster. *Frontiers in Physics*, 7, 2019.

[156] J.C. Adam, J.P. Boeuf, N. Dubuit, M. Dudeck, L. Garrigues, D. Gresillon, A. Heron, G.J.M. Hagelaar, V. Kulaev, N. Lemoine, et al. Physics, simulation and diagnostics of Hall effect thrusters. *Plasma Physics and Controlled Fusion*, 50:124041, 2008.

[157] Arash Tavassoli, Mina Papahn Zadeh, Andrei Smolyakov, Magdi Shoucri, and Raymond J. Spiteri. The electron cyclotron drift instability: A comparison of

particle-in-cell and continuum Vlasov simulations. *Physics of Plasmas*, 30(3), 2023. 033905.

[158] Arash Tavassoli, Oleksandr Chapurin, Marilyn Jimenez, Mina Papahn Zadeh, Trevor Zintel, Meghraj Sengupta, Lénaïc Couëdel, Raymond J. Spiteri, Magdi Shoucri, and Andrei Smolyakov. The role of noise in pic and Vlasov simulations of the Buneman instability. *Physics of Plasmas*, 28(12), 2021.

[159] Long Chen, Zi-Chen Kan, Wei-Fu Gao, Ping Duan, Jun-Yu Chen, Cong-Qi Tan, and Zuo-Jun Cui. Growth mechanism and characteristics of electron drift instability in Hall thruster with different propellant types. *Chinese Physics B*, 33(1):015203, 2024.

[160] A. Smolyakov, T. Zintel, L. Couedel, D. Sydorenko, A. Umnov, E. Sorokina, and N. Marusov. Anomalous electron transport in one-dimensional electron cyclotron drift turbulence. *Plasma Physics Reports*, 46(5), 2019.